Title

Energetics of Substitution Effects on the Stability of Metal-Organic Frameworks

Permalink

https://escholarship.org/uc/item/9fv0p0st

Author

Novendra, Novendra

Publication Date

2021

Peer reviewed|Thesis/dissertation

Energetics of Substitution Effects on the Stability of Metal-Organic Frameworks

By

NOVENDRA NOVENDRA
DISSERTATION

Submitted in partial satisfaction of the requirements for the degree of

DOCTOR OF PHILOSOPHY

in

Chemical Engineering

in the

OFFICE OF GRADUATE STUDIES

of the

UNIVERSITY OF CALIFORNIA

DAVIS

Approved:

_____
Alexandra Navrotsky, Chair

_____
Roland Faller

_____
Coleman X. Kronawitter

Committee in Charge

2021

Energetics of Substitution Effect on the Stability of Metal-Organic Frameworks

Abstract

Metal-organic frameworks are hybrid materials constructed by inorganic metal nodes and organic linkers. The presence of both organic and inorganic moieties in the structure allows MOFs to have a significant flexibility and tunability in compositions, structures, and functional properties. This in turns enables MOFs to have very desirable and interesting properties, such as very high porosity, very high surface area, multiferroicity, electrical conductivity, proton conductivity and others. Consequently, MOFs have potentials in a wide array of applications, including catalysis, gas storage and separation, energy storage and drug delivery.

Despite the significant amount of research performed on the development and synthesis of MOFs, fundamental study of their intrinsic stability is still fragmentary. The thermodynamic properties of materials are crucial in understanding their properties and evaluating their intrinsic stability. To accelerate the discovery of new MOFs, it is necessary to study the energetics of MOFs systematically to further understand how the compositions and structures affect stability. By relating these composition – structure – energetics relationships to other measurable, calculable, or available chemical properties, it should be possible to predict the stability of new MOFs. Therefore, this dissertation work aims to fulfill this goal of understanding and predicting MOF stability.

Chapter 1 is a general introduction. Chapter 2 discusses the synthesis, characterization and thermodynamic study of mineral paceite $CaCu(OAc)_4 \cdot 6H_2O$ as well as its cadmium-based

analogue CaCd(OAc)$_4\cdot$6H$_2$O. The enthalpy of formation revealed the destabilization introduced by the Cd to the structure. Additionally, it also explained the most possible synthesis route of paceite, which is through the formation of a calcium acetate – acetic acid solvate intermediate.

Chapter 3 presents a systematic study of the energetics of A-site cation substitution on the thermodynamic stability of protonated-amine manganese formate perovskite. This system was chosen representative of a dense MOF system. The measured enthalpy of formation revealed that the stability of hybrid perovskites is not strongly influenced by the structural factor, unlike its inorganic perovskite counterparts. Instead, the stability is governed more by the interaction of the A-site cation with the framework, which further can be explained by the dissolution enthalpy of the cation salts.

Chapter 4 reports the interplay between theoretical calculations and experimental measurements to determine the thermodynamic stability of porous metal organic frameworks, in this case fluorinated zeolitic imidazolate frameworks (ZIFs). The enthalpy of formations revealed the strong influence of ligand functionalization and topology on the stability.

Chapter 5 presents a systematic study of the energetics of ligand substitution on the stability of ZIFs with sodalite structure. Based on the results obtained in Chapter 4, this study was designed to see only the contribution of ligand substitution to stability, while keeping the topology the same. It was found that the stability trend of sodalite ZIF samples with different ligand functionalization can be explained by a tabulated chemical property from physical organic chemistry, namely Hammett σ-para(+) constant.

Lastly, in Chapter 6, all the results are related with summarizing points and suggestions for future research will be presented.

Acknowledgements

First and foremost, I would like to express my utmost gratitude to my PhD advisor, Prof. Alexandra Navrotsky. Alex has been a great advisor and I was lucky to have her guide me during my research. She has been the most supportive, patient and understanding during my graduate study. I appreciate the flexibility that Alex gives to her students, we were able to explore our research ideas and Alex would always help us direct the research with her very valuable insights and expertise. I am also very grateful for all of the discussions that we had both about science and life. The experience working with her would be one of the highlights of my PhD research and words would not be sufficient to express my gratitude to Alex.

I would like to thank Prof. Roland Faller and Prof. Coleman Kronawitter for being part of my dissertation committee and qualifying exam. I am very grateful for their support and invaluable advice. Additionally, I would also like to point out that I am very grateful for their kindness and flexibility despite the very tight schedule with the dissertation writing. I am also thankful to Prof. Yayoi Takamura and Prof. Gang-Yu Liu for their inputs and insightful comments during my qualifying exams.

Next, I would like to thank my wonderful colleagues and friends in our *previously known as* Peter A. Rock Thermochemistry Laboratory. Zamir, thank you for being a wonderful friend. I am very glad that we've known each other since our undergraduate study. I'm very thankful for your help when I first got to the US, you helped me get my feet on the ground and start my study on the right foot. I am very thankful to Bhushan for all of your support and for being my mentor in my first year. Your help during my first project and the scientific discussions that we had have been invaluable. I would like to thank Sergey for all the discussions that we had and your help with

instruments training. I would also like to thank Krasen who helped me so much with problems that occurred with the instruments, the lab would not be running smoothly without Sergey and Krasen. Thank you to Andy and Pinghui for your continuous friendship and support both in the lab and these past few months during our writing support group. I would also like to extend my thank you to Can, Lili, Jiewei, Radha, Casey, Xin, Bin, Anna, Tamil, Albert, Jayanthi, Mykola, Pardha, and Kristina for making a great lab environment and making everyday work in the lab exciting! Special thank you also to Erica, William and Suki for all your help with administrative work!

I would also like to express my gratitude to Prof. Tomislav Friscic and the team at McGill University, Hatem, Joe, and Mihails. We had very interesting and exciting research collaborations together and I enjoyed every part of it. I'm very grateful for every discussion, calls and emails that I had with Prof. Tomislav Friscic, I learned a lot from our work together and this dissertation would not have been possible without it.

A special thank you to my chosen family here, George, Suzie, Dale, Matthew and Aiden! I am so happy that I met George shortly after arriving in the US. I got to meet so many great friends since then and also got to experience so many new and exciting things. Thank you for your continuous support and help, I have grown so much because of you guys. I'm forever indebted to you. I would also like to thank my family back in Indonesia that keeps pushing me to be a better version of myself.

Finally, I would like to thank my partner, Romeo, for his never-ending support and confidence in me. Last year has been very rough, but your smile and laugh kept me going and motivated. I wouldn't have been able to finish this work without your support. I am forever grateful to you.

Table of Contents

List of Tables

List of Figures

Chapter 1:

Introduction

1.1   Metal-Organic Frameworks

1.1.1 Background

Metal-organic frameworks (MOFs) are a class of advanced hybrid materials with extended crystalline structures consisting of inorganic metal nodes interconnected by organic ligands or linkers (see Figure 1.1). Based on the choice of the metal nodes and the linkers used, the type of the framework and the corresponding physical and chemical properties of MOFs can be tuned. The vast number of possible combinations of organic and inorganic moieties allows significant flexibility in their composition, which further allows its structure and functional properties to be tuned for various applications[1–4].

Research on MOFs has mostly concentrated on porous MOFs, and has grown rapidly since the introduction of several important and currently widely utilized MOFs, including the report of HKUST-1 by Williams' group in 1999[5] and the report of ZIF-8 by Yaghi's group in 2006[6]. The main features of these porous MOFs are very high porosity, up to 90 % seen on MOF-200, combined with very high Brunauer-Emmett-Teller (BET) surface areas, exceeding 9000 m^2g^{-1}, which was seen for NU-1501-Al[7–9]. Computationally, it was also demonstrated that MOF surface areas could exceed 14600 m^2g^{-1} [10].
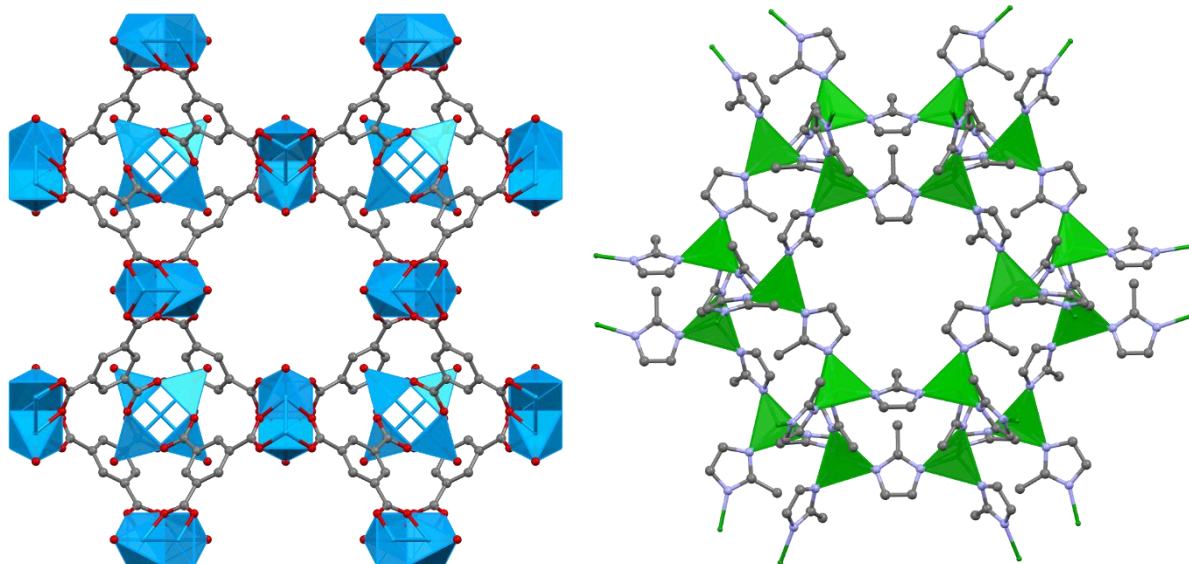
Figure 1-1. Example of porous MOF structures; HKUST-1 (CSD code: FIQCEN) (left) and ZIF-8 (CSD code: VELVOY) (right). Color scheme: Cu is blue, O is red, N is purple, C is gray, and Zn is green.

In addition to porous MOFs, an increasing number of dense hybrid materials are also being synthesized and reported[11,12]. An example of dense MOFs are formate perovskites, a hybrid organic-inorganic material with perovskite structure, such as methylammonium manganese formate ($[CH_3NH_3]Mn[(HCOO)_3]$) and dimethylammonium manganese formate ($[(CH_3)_2NH_2]Mn[(HCOO)_3]$). These materials also have very interesting functional properties, such as ferromagnetism, ferroelectricity, ferroelasticity and multiferroicity[13–17]. Another example of dense MOF is recently discovered naturally occurring MOFs, stepanovite ($[Mg(H_2O)_6][NaFe(C_2O_4)_3]\cdot 3H_2O$) and zhemchuzhnikovite ($[Mg(H_2O)_6][NaFe_{0.6}Al_{0.4}(C_2O_4)_3]\cdot 3H_2O$)[18,19]. These materials were also found to exhibit interesting properties such as high proton conductivity, due to the presence of interstitial water molecules, and stability at elevated temperature, allowing reversible dehydration process.

2

These wide ranges of functional properties allow both porous and dense MOFs to be used in a wide array of application, including catalysis, gas storage and separation, energy storage, drug delivery and others.[20,21].

1.1.2 Synthesis of Metal-Organic Frameworks

Most MOFs are synthesized using the conventional synthesis method of solvothermal synthesis. In this method, the starting materials, the organic ligands and the metal salts react in a closed vessel at elevated temperatures and pressures. This method of synthesis also typically use a large amount of organic solvents, such as N,N-dimethylformamide (DMF), N,N-diethylformamide (DEF) and 1-methyl-2-pyrrolidone (NMP)[22–24]. Several other synthesis methods, such as mechanochemistry, have since been developed to reduce the usage of organic solvents and also lower the energy cost by working at lower temperature and pressure, as well as to make new MOFs not accessible by conventional solvothermal synthesis. Mechanochemistry is a chemical synthesis method that is enabled by mechanical force, typically provided by milling balls in jars made from stainless steel, tungsten carbide or zirconia[25,26]. In addition to making the synthesis more environmentally friendly, it was also shown that it was possible to synthesize new MOFs, such as sodalite $Zn(CF_3Im)_2$. This work has been published[27] and will be discussed further in Chapter 4.

1.1.3 Calorimetric measurements

Development of an in-situ technique to measure the enthalpy associated with every kind of formation reactions would be difficult due to the different conditions where the reaction occurs. Because of this, an alternative pathway to calculate the enthalpy of formation is necessary. Based on the state function property of enthalpy, the value of the enthalpy associated with a specific reaction only depends on the initial and final state, irrespective of the path in which the reactions

occur. It would be then possible to design a thermodynamic cycle that corresponds to this formation reaction, where the enthalpy associated with each step in this cycle can be easily measured.

$$ZnO_{(s)} \quad + \quad 2\ 2\text{-MeImH}_{(s)} \quad \rightarrow \quad Zn(2\text{-MeIm})_{2(s)} \quad + \quad H_2O_{(l)}$$

$$\downarrow \Delta H_1 \qquad\qquad \downarrow \Delta H_2 \qquad\qquad\qquad \downarrow \Delta H_3 \qquad\qquad\quad \downarrow \Delta H_4$$

$$Zn^{2+}{}_{(aq)} + H_2O_{(aq)} \qquad MeIm^-{}_{(aq)} + H^+{}_{(aq)} \qquad Zn^{2+}{}_{(aq)} + 2MeIm^-{}_{(aq)} \qquad H_2O_{(aq)}$$

$$\Delta H_f\ (Zn(2\text{-MeIm})_2) = \Delta H_1 + 2\Delta H_2 - \Delta H_3 - \Delta H_4$$
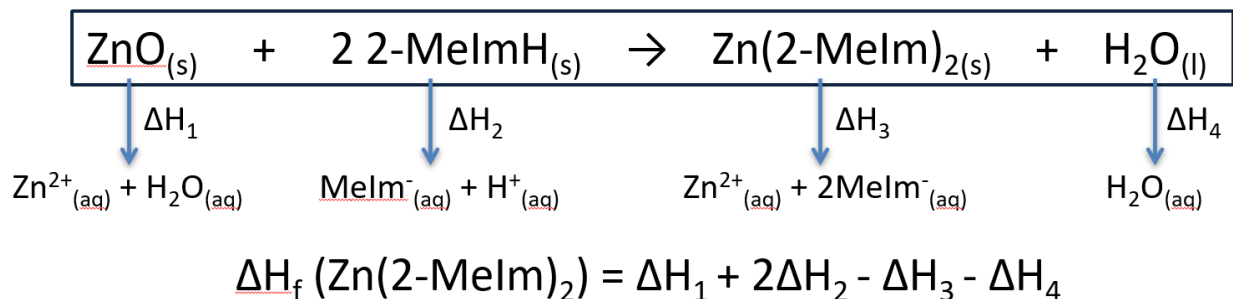
Figure 1-2. Thermodynamic cycle used to calculate the enthalpy of formation of ZIF-8 with respect to its components (ZnO and 2-MeImH)

An example of the thermodynamic cycle for the formation reaction of ZIF-8 ($Zn(2\text{-MeIm})_2$) is shown in the diagram (**Figure 1-2**). The formation reaction of ZIF-8 is given as the reaction of one mole of zinc oxide (ZnO) with 2 moles of 2-methylimidazoles (2-MeImH). In the proposed cycle here, the enthalpy of formation of ZIF-8 (ΔH_f ($Zn(2\text{-MeIm})_2$) is calculated by using the enthalpy of dissolution of each component in an aqueous solution (ΔH_1 - ΔH_4). In this dissertation, the enthalpy of dissolution of the samples are measured in a room temperature solution calorimeter (CSC 4400 isothermal microcalorimeter) (**Figure 1-3**)
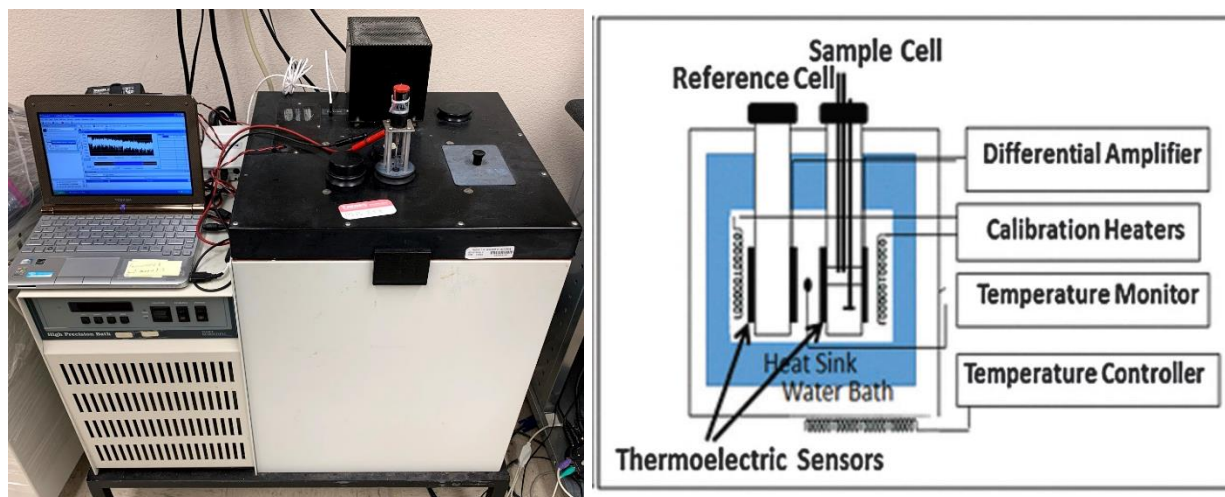
Figure 1-3. Picture and schematic of CSC 4400 isothermal microcalorimeter[28]

1.2 Dissertation Objectives

1.2.1 The Challenges

The immense flexibility that MOFs offer with tunability of structural and functional properties while being their greatest strength, but this is also a drawback. Without the tools to properly predict the stability of MOFs, it would be difficult to target the best compositions for specific applications, while also ensuring their synthesizability. Despite the substantial work on the discovery and synthesis of new MOFs, it has been largely trial and error and the thermodynamic driving force behind the stability of MOFs has not been studied systematically extensively. This can be seen from the most recent report, over 500000 MOFs have been predicted computationally while only over 90000 MOFs have been successfully synthesized so far[29]. This big difference between the predicted and synthesized structures could be attributed to both the need for new and novel synthetic methods and the intrinsic instability of the structures themselves, preventing them from

being synthesized. In addition, trying to synthesize hundreds of thousands of MOFs is a Herculean task, and therefore the synthetic chemist needs further focus and guidance.

It is important to properly understand the relation between MOFs stability and their composition, both the inorganic metal nodes and the organic ligands are important. Based on the currently available thermodynamic stability study of both porous MOFs[30–34] and dense MOFs[35], there is still a lack of experimental data. Additionally, most of the computational study on the stability of MOFs by density functional theory (DFT) has not been experimentally validated[36–40]. Because of this, a further systematic study on MOF stability would be beneficial. Further relating this thermodynamic stability to other relevant and accessible chemical properties would allow the prediction of the stability of not yet synthesized MOFs. The experimentally measured thermodynamic properties would also help validate theoretical calculation models and subsequently improve its accuracy to calculate MOFs stability. This in turn would improve the prediction of MOF stability, significantly reduce the trial-and-error time involved during MOF synthesis and accelerate the development of functional MOFs.

1.2.2 Thermodynamic Study

The purpose of this dissertation is to study the thermodynamic stability of metal-organic frameworks, understand the energetics of substitution effects, and relate it to relevant chemical properties for use as a prediction tool for future syntheses. To achieve this, representative systems of dense and porous MOFs are chosen with different substituents to understand the role of substitution on the resulting thermodynamic stability systematically. First, the system of organic mineral paceite $CaCu(OAc)_4 \cdot 6H_2O$ and its cadmium-based analogue has been studied to investigate the energetics of Cd substitution for Ca in the structure. The calorimetric data will also

be used to explain the possible reaction pathways to form paceite from its starting materials (Chapter 2, a published paper). Then in Chapter 3, a system of protonated-amine manganese formate perovskites (AmineH$^+$-Mn-F) will be studied to explore the energetics of substitution effect on dense MOFs stability. The measured enthalpy of formation will be correlated with relevant properties to create a predictive model. In a similar fashion, in Chapter 4 (a published paper), a system of zeolitic imidazolate frameworks (ZIFs) with different substitutions and framework topologies will be studied. Here, both the role of substitutions and framework topologies on the stability of ZIFs will be investigated. Building from this result, in Chapter 5 (a published paper), a system of isostructural ZIFs with sodalite structure and only different substitutions will be analyzed. The energetics of substitutions on the thermodynamic stability of ZIFs with sodalite structure will be investigated, and the result will be correlated with relevant chemical properties to construct a predictive model.

1.3   References

(1)   Yaghi, O. M.; O'Keeffe, M.; Ockwig, N. W.; Chae, H. K.; Eddaoudi, M.; Kim, J. Reticular Synthesis and the Design of New Materials. *Nature* **2003**, *423*, 705–714.

(2)   James, S. L. Metal-Organic Frameworks. *Chem. Soc. Rev.* **2003**, *32*, 276–288.

(3)   Kalaj, M.; Bentz, K. C.; Ayala, S.; Palomba, J. M.; Barcus, K. S.; Katayama, Y.; Cohen, S. M. MOF-Polymer Hybrid Materials: From Simple Composites to Tailored Architectures. *Chem. Rev.* **2020**, *120*, 8267–8302.

(4)   Rowsell, J. L. C.; Yaghi, O. M. Metal-Organic Frameworks: A New Class of Porous Materials. *Microporous Mesoporous Mater.* **2004**, *73*, 3–14.

(5)   Chui, S. S. Y.; Lo, S. M. F.; Charmant, J. P. H.; Orpen, A. G.; Williams, I. D. A Chemically Functionalizable Nanoporous Material [Cu3(TMA)2 (H2O)3](N). *Science* **1999**, *283*, 1148–1150.

(6)   Park, K. S.; Ni, Z.; Cote, A. P.; Choi, J. Y.; Huang, R.; Uribe-Romo, F. J.; Chae, H. K.; O'Keeffe, M.; Yaghi, O. M. Exceptional Chemical and Thermal Stability of Zeolitic Imidazolate Frameworks. *Proc. Natl. Acad. Sci.* **2006**, *103*, 10186–10191.

(7)   Chen, Z.; Li, P.; Anderson, R.; Wang, X.; Zhang, X.; Robison, L.; Redfern, L. R.; Moribe, S.; Islamoglu, T.; Gómez-Gualdrón, D. A.; Yildirim, T.; Stoddart, J. F.; Farha, O. K. Balancing Volumetric and Gravimetric Uptake in Highly Porous Materials for Clean Energy. *Science* **2020**, *368*, 297–303.

(8)   Furukawa, H.; Ko, N.; Go, Y. B.; Aratani, N.; Choi, S. B.; Choi, E.; Yazaydin, A. O.; Snurr, R. Q.;

O'Keeffe, M.; Kim, J.; Yaghi, O. M. Ultrahigh Porosity in Metal-Organic Frameworks. *Science* **2010**, *329*, 424–428.

(9)   Zhang, X.; Chen, Z.; Liu, X.; Hanna, S. L.; Wang, X.; Taheri-Ledari, R.; Maleki, A.; Li, P.; Farha, O. K. A Historical Overview of the Activation and Porosity of Metal-Organic Frameworks. *Chem. Soc. Rev.* **2020**, *49*, 7406–7427.

(10)   Farha, O. K.; Eryazici, I.; Jeong, N. C.; Hauser, B. G.; Wilmer, C. E.; Sarjeant, A. A.; Snurr, R. Q.; Nguyen, S. T.; Yazaydın, A. Ö.; Hupp, J. T. Metal–Organic Framework Materials with Ultrahigh Surface Areas: Is the Sky the Limit? *J. Am. Chem. Soc.* **2012**, *134*, 15016–15021.

(11)   Cheetham, A. K.; Rao, C. N. R. There's Room in the Middle. *Science* **2007**, *318*, 58–59.

(12)   Tominaka, S.; Coudert, F. X.; Dao, T. D.; Nagao, T.; Cheetham, A. K. Insulator-to-Proton-Conductor Transition in a Dense Metal-Organic Framework. *J. Am. Chem. Soc.* **2015**, *137*, 6428–6431.

(13)   Pato-Doldán, B.; Gómez-Aguirre, L. C.; Hansen, A. P.; Mira, J.; Castro-García, S.; Sánchez-Andújar, M.; Señarís-Rodríguez, M. A.; Zapf, V. S.; Singleton, J. Magnetic Transitions and Isotropic versus Anisotropic Magnetic Behaviour of [CH$_3$NH$_3$][M(HCOO)$_3$] M = Mn^{2+}, Co^{2+}, Ni^{2+}, Cu^{2+} Metal–Organic Perovskites. *J. Mater. Chem. C* **2016**, *4*, 11164–11172.

(14)   Jain, P.; Dalal, N. S.; Toby, B. H.; Kroto, H. W.; Cheetham, A. K. Order-Disorder Antiferroelectric Phase Transition in a Hybrid Inorganic-Organic Framework with the Perovskite Architecture. *J. Am. Chem. Soc.* **2008**, *130*, 10450–10451.

(15)   Li, W.; Zhang, Z.; Bithell, E. G.; Batsanov, A. S.; Barton, P. T.; Saines, P. J.; Jain, P.; Howard, C. J.; Carpenter, M. A.; Cheetham, A. K. Ferroelasticity in a Metal-Organic Framework Perovskite; Towards a New Class of Multiferroics. *Acta Mater.* **2013**, *61*, 4928–4938.

(16)   Rogez, G.; Viart, N.; Drillon, M. Multiferroic Materials: The Attractive Approach of Metal-Organic Frameworks (MOFs). *Angew. Chem., Int. Ed..* **2010**, *49*, 1921–1923.

(17)   Vinod, K.; Deepak, C. S.; Sharma, S.; Sornadurai, D.; Satya, A. T.; Ravindran, T. R.; Sundar, C. S.; Bharathi, A. Magnetic Behavior of the Metal Organic Framework [(CH$_3$)$_2$NH$_2$]Co(HCOO)$_3$. *RSC Adv.* **2015**, *5*, 37818–37822.

(18)   Huskić, I.; Pekov, I. V.; Krivovichev, S. V.; Friščić, T. Minerals with Metal-Organic Framework Structures. *Sci. Adv.* **2016**, *2*, e1600621–e1600621.

(19)   Huskić, I.; Novendra, N.; Lim, D. W.; Topić, F.; Titi, H. M.; Pekov, I. V.; Krivovichev, S. V.; Navrotsky, A.; Kitagawa, H.; Friščić, T. Functionality in Metal-Organic Framework Minerals: Proton Conductivity, Stability and Potential for Polymorphism. *Chem. Sci.* **2019**, *10*, 4923–4929.

(20)   Kirchon, A.; Feng, L.; Drake, H. F.; Joseph, E. A.; Zhou, H. C. From Fundamentals to Applications: A Toolbox for Robust and Multifunctional MOF Materials. *Chem. Soc. Rev.* **2018**, *47*, 8611–8638.

(21)   Furukawa, H.; Cordova, K. E.; O'Keeffe, M.; Yaghi, O. M. The Chemistry and Applications of Metal-Organic Frameworks. *Science* **2013**, *341*, 1230444.

(22)   Zhang, B.; Zhang, J.; Liu, C.; Sang, X.; Peng, L.; Ma, X.; Wu, T.; Han, B.; Yang, G. Solvent Determines the Formation and Properties of Metal-Organic Frameworks. *RSC Adv.* **2015**, *5*, 37691–37696.

(23)   Stock, N.; Biswas, S. Synthesis of Metal-Organic Frameworks (MOFs): Routes to Various MOF Topologies, Morphologies, and Composites. *Chem. Rev.* **2012**, *112*, 933–969.

(24)   Yuan, S.; Feng, L.; Wang, K.; Pang, J.; Bosch, M.; Lollar, C.; Sun, Y.; Qin, J.; Yang, X.; Zhang, P.; Wang, Q.; Zou, L.; Zhang, Y.; Zhang, L.; Fang, Y.; Li, J.; Zhou, H.-C. Stable Metal-Organic Frameworks: Design, Synthesis, and Applications. *Adv. Mater.* **2018**, *30*, 1704303.

(25)   Do, J. L.; Friščić, T. Mechanochemistry: A Force of Synthesis. *ACS Cent. Sci.* **2017**, *3*, 13–19.

(26)   Stolar, T.; Užarević, K. Mechanochemistry: An Efficient and Versatile Toolbox for Synthesis, Transformation, and Functionalization of Porous Metal-Organic Frameworks. *CrystEngComm* **2020**, *22*, 4511–4525.

(27)   Arhangelskis, M.; Katsenis, A. D.; Novendra, N.; Akimbekov, Z.; Gandrath, D.; Marrett, J. M.; Ayoub, G.; Morris, A. J.; Farha, O. K.; Friščić, T.; Navrotsky, A. Theoretical Prediction and Experimental Evaluation of Topological Landscape and Thermodynamic Stability of a Fluorinated Zeolitic Imidazolate Framework. *Chem. Mater.* **2019**, *31*, 3777–3783.

(28)   Akimbekov, Z.; Wu, D.; Brozek, C. K.; Dincə, M.; Navrotsky, A. Thermodynamics of Solvent Interaction with the Metal-Organic Framework MOF-5. *Phys. Chem. Chem. Phys.* **2015**, *18*, 1158–1162.

(29)   Moosavi, S. M.; Nandy, A.; Jablonka, K. M.; Ongari, D.; Janet, J. P.; Boyd, P. G.; Lee, Y.; Smit, B.; Kulik, H. J. Understanding the Diversity of the Metal-Organic Framework Ecosystem. *Nat. Commun.* **2020**, *11*, 1–10.

(30)   Hughes, J. T.; Bennett, T. D.; Cheetham, A. K.; Navrotsky, A. Thermochemistry of Zeolitic Imidazolate Frameworks of Varying Porosity. *J. Am. Chem. Soc.* **2013**, *135*, 598–601.

(31)   Hughes, J. T.; Navrotsky, A. MOF-5: Enthalpy of Formation and Energy Landscape of Porous Materials. *J. Am. Chem. Soc.* **2011**, *133*, 9184–9187.

(32)   Akimbekov, Z.; Katsenis, A. D.; Nagabhushana, G. P.; Ayoub, G.; Arhangelskis, M.; Morris, A. J.; Friščić, T.; Navrotsky, A. Experimental and Theoretical Evaluation of the Stability of True MOF Polymorphs Explains Their Mechanochemical Interconversions. *J. Am. Chem. Soc.* **2017**, *139*, 7952–7957.

(33)   Akimbekov, Z.; Navrotsky, A. Little Thermodynamic Penalty for the Synthesis of Ultraporous Metal Organic Frameworks. *ChemPhysChem* **2016**, *17*, 468–470.

(34)   Wu, D.; Navrotsky, A. Thermodynamics of Metal-Organic Frameworks. *J. Solid State Chem.* **2015**, *223*, 53–58.

(35)   Nagabhushana, G. P.; Shivaramaiah, R.; Navrotsky, A. Thermochemistry of Multiferroic Organic–Inorganic Hybrid Perovskites [(CH$_3$)$_2$NH$_2$][M(HCOO)$_3$] (M = Mn, Co, Ni, and Zn). *J. Am. Chem. Soc.* **2015**, *137*, 10351–10356.

(36)   Coudert, F.-X.; Fuchs, A. H. Computational Characterization and Prediction of Metal–Organic Framework Properties. *Coord. Chem. Rev.* **2016**, *307*, 211–236.

(37)   Schröder, C. A.; Baburin, I. A.; Van Wüllen, L.; Wiebcke, M.; Leoni, S. Subtle Polymorphism of Zinc Imidazolate Frameworks: Temperature-Dependent Ground States in the Energy Landscape Revealed by Experiment and Theory. *CrystEngComm* **2013**, *15*, 4036–4040.

(38)   Baburin, I. A.; Leoni, S. The Energy Landscapes of Zeolitic Imidazolate Frameworks (ZIFs): Towards Quantifying the Presence of Substituents on the Imidazole Ring. *J. Mater. Chem.* **2012**, *22*, 10152–10154.

(39)   Witman, M.; Ling, S.; Gladysiak, A.; Stylianou, K. C.; Smit, B.; Slater, B.; Haranczyk, M. Rational Design of a Low-Cost, High-Performance Metal-Organic Framework for Hydrogen Storage and Carbon Capture. *J. Phys. Chem. C* **2017**, *121*, 1171–1181.

(40)   Galvelis, R.; Slater, B.; Chaudret, R.; Creton, B.; Nieto-Draghi, C.; Mellot-Draznieks, C. Impact of Functionalized Linkers on the Energy Landscape of ZIFs. *CrystEngComm* **2013**, *15*, 9603–9612.

Chapter 2:

Mechanochemical Synthesis, Accelerated Aging and Thermodynamic Stability of the Organic Mineral Paceite and Its Cadmium Analogue

This chapter is presented based on the following previously published paper with additions on the thermal analysis and calorimetry section:

Li, S.; Huskić, I.; Novendra, N.; Titi, H. M.; Navrotsky, A.; Friščić, T. Mechanochemical Synthesis, Accelerated Aging, and Thermodynamic Stability of the Organic Mineral Paceite and Its Cadmium Analogue. *ACS Omega* **2019**, *4*, 5486–5495.

Note: My contributions to this work are on the thermal analysis experiments, calorimetric measurements, and discussion of the energetics of the system.

2.1   Abstract

We demonstrate the use of ball milling mechanochemistry for rapid, simple, and materials-efficient synthesis of the organic mineral paceite $CaCu(OAc)_4 \cdot 6H_2O$ (where OAc^- is the acetate ion), composed of coordination polymer chains containing alternating Ca^{2+} and Cu^{2+} ions, as well as its cadmium-based analogue $CaCd(OAc)_4 \cdot 6H_2O$. While the synthesis of paceite in aqueous solutions requires a high excess of the copper precursor, mechanochemistry permits the use of stoichiometric amounts of reagents, as well as the use of poorly soluble and readily accessible

calcium carbonate or hydroxide reactants. As established by thermochemical measurements, enthalpies of formation of both synthetic paceite and its cadmium analogue relevant to the mechanochemical reactions are highly exothermic. Reactions can also be conducted using accelerated aging, a synthetic technique that mimics geological processes of mineral weathering. Accelerated aging reactivity involving copper(II) acetate monohydrate (hoganite) and calcium carbonate (calcite) provides a potential explanation of how complex organic minerals like paceite could form in a geological environment.

2.2 Introduction

Over the past 10 years, structural studies of geological samples have identified an increasing number of organic minerals, broadly defined as carbon-bearing mineral species other than carbonates and carbon allotropes.[1,2] Principal representatives of such organic minerals are transition metal and lanthanide oxalates,[3,4] as well as metal formates,[5] mellitates,[6] acetates,[1,2] and organic molecules such as uric acid.[7−9] The search for organic minerals and a deeper understanding of their structures and origins have been additionally promoted by the recent "Carbon Mineral Challenge" initiative, which considers organic minerals, while extremely poorly investigated, as nevertheless central to understanding mineral evolution and carbon cycle on Earth and other planetary systems.[10,11] The vibrant investigations of organic minerals have recently led to the structural characterization of geoporphyrins,[12] discovery of naturally occurring metal−organic frameworks (MOFs),[13,14] and proposed geological appearance of organic cocrystals[15] in extraterrestrial environments such as Titan.[16]

Recent additions to the library of organic minerals are copper(II) acetate monohydrate, $Cu(OAc)_2 \cdot H_2O$, found as the mineral hoganite in the Potosi Mine in New South Wales (Australia),

and paceite, the related double salt of calcium copper(II) acetate hexahydrate, $CaCu(OAc)_4 \cdot 6H_2O$, found as dark blue crystals growing on the surface of hoganite specimens.[17] The minerals found in gossan were goethite, hematite, quartz, linarite, malachite, azurite, cuprian smithsonite, and cerussite. Gossan was located at a depth of approximately 20 m and in the vicinity of a decomposing leaf litter, providing a potential source of acetate ion. The structures of both minerals are unique in the context of organic minerals, representing the first identified acetate minerals,[17] and are also of relevance to modern metal−organic materials chemistry. In particular, hoganite consists of the well-known copper(II) acetate "paddlewheel" dimers (**Figure 2-1**), which are also important secondary building units in the design and synthesis of coordination polymers and metal−organic frameworks (MOFs).[18] Calcium copper(II) acetate hexahydrate is a synthetic compound that has been known since at least 1960,[19] and its single crystal X-ray diffraction structure was reported first by Langs and Hare in 1967,[20] who described the structure without detailed crystallographic data. The structure was subsequently redetermined by Klop et al.[21] and by El-Bali and Bolte[22] and consists of one-dimensional coordination polymer chains of alternating square-coordinated copper(II) ions and hydrated octahedrally coordinated calcium ions bridged by acetate ions. Such regular alternation of metal ions is also of relevance for the development of metal−organic materials based on more than one type of metal ion. In particular, while a number of designs have recently emerged for such mixed-metal materials,[23,24] these are usually based on the formation of solid solutions in which different metal ions are randomly distributed over specific crystallographic sites.[25] The potentially broader relevance of this structure in metal−organic chemistry is highlighted by its cadmium- and calcium-based analogue, $CaCd(OAc)_4 \cdot 6H_2O$. This compound was described by Balarew and Stoilova,[26] as well as by Langs and Hare, who also

12

conducted structural characterization.[20] The compound was reported to be isomorphous to CaCu(OAc)$_4$·6H$_2$O, but detailed crystallographic information was never provided.

Consequently, we recognized paceite and its synthetic cadmium analogues as excellent targets for our ongoing investigation of the properties and potential origin of naturally occurring metal−organic materials.[13,27] Specifically, we targeted the structure, thermal, and thermodynamic stability of synthetic paceite and its cadmium analogue, as well as potential routes through which such materials could assemble from geologically relevant precursors, via mechanochemical[28] or accelerated aging[29] reactions.
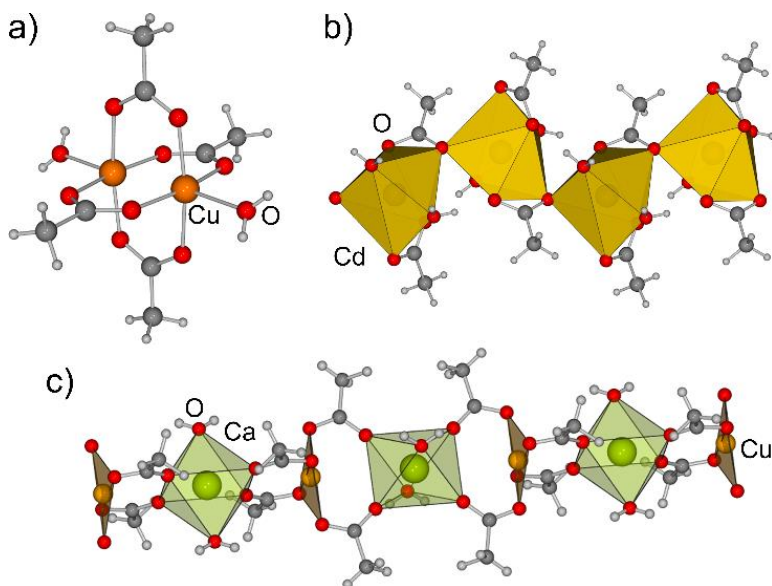
Figure 2-1. a) Structure of the paddlewheel unit found in the crystal structure of Cu(OAc)$_2$·H$_2$O (hoganite mineral) and b) fragment of the crystal structure of Cd(OAc)$_2$·2H$_2$O, with coordination environments around cadmium ions shown as yellow polyhedra. c) Fragment of a single bimetallic coordination polymer chain in the crystal structure of paceite, CdCa(OAc)$_2$·6H$_2$O, with calcium and cadmium ion coordination environments shown as green and yellow polyhedra, respectively.

2.3   Experimental Section

Mechanochemical syntheses were conducted using either a Retsch MM200 mixer mill operating at 25 Hz or a Form-Tech Scientific 1000 shaker mill operating at 30 Hz. All reactions were performed using stainless steel milling media, including a milling jar of 15 mL volume equipped with two milling balls of 7 mm diameter (1.37 g each). A detailed mechanochemical reaction procedure for each compound is given in the appendix.

Differential scanning calorimetry coupled with thermogravimetric analysis (DSC-TG) was performed on a Netzsch 449 instrument to determine the water content of the samples. In each experiment, the samples were heated from 25 to 800 °C under an O_2 atmosphere (heating rate 10 °C/min, platinum crucible).

Fourier transform infrared attenuated total reflectance (FTIR-ATR) spectra were obtained using a Bruker Platinum ATR spectrometer. In situ PXRD monitoring of aging reactions was performed on a PROTO AXRD Benchtop diffractometer equipped with a DECTRIS Mythen 1K strip detector. Data were collected using a custom designed sample holder.[30] A homogenized mixture of $Ca(OH)_2$ and $Cu(OAc)_2 \cdot H_2O$ was placed in the middle, and 200 mL of 50% aqueous solution (by volume) of acetic acid was placed in the sample holder grooves. Consecutive powder diffractograms were collected over the course of 12 h with a time resolution of 5 min and 50 s between scans. Rietveld fitting was performed in the TOPAZ6 analytical program.[31]

Single crystal X-ray diffraction data were collected on a Bruker D8 Advance diffractometer with a Photon 200 CMOS area detector and an IμS microfocus X-ray source (Madison, WI) using Mo Kα radiation. The single crystal was coated with paraffin oil, and data were collected at room

temperature. The Apex3 software suite (Madison, WI) was used for data collection, reduction, and unit cell assignment.

The enthalpy of dissolution of the samples was measured using a CSC (Calorimetry Sciences Corporation) 4400 isothermal microcalorimeter at 25 °C. In each experiment, 5−15 mg of the sample was hand-pressed to form a pellet and dropped into a Teflon cell in the calorimeter filled with 25 g of 5 N HCl solvent. All weight measurements were done using a Mettler microbalance with an accuracy of 10 μg. The solvent was isothermally equilibrated for at least 3 h under mechanical stirring before the introduction of the sample, and the sample was allowed to dissolve in the cell for at least 3 h, ensuring the return of baseline back to the initial position. For each experiment, the solvent in the cell was replaced with a new fresh solvent. The collected data were integrated with a baseline correction and converted to joules using a calibration factor to obtain the total heat effect due to the dissolution of the sample. To obtain the calibration factor, the NIST standard reference material KCl was used. The calibration was done by dissolving 15 mg of KCl pellet into 25 g of H_2O, which corresponds to a reference concentration of 0.008 mol/kg at 25 °C. The calibration factor was obtained by correlating the integrated data with a known enthalpy of dissolution and dilution of 0.008 mol/kg KCl. For each sample, at least four measurements were performed, and their average was reported as the final value. The uncertainties given in the result represent 95% confidence interval. This experimental method is the same as the one used in our earlier study of metal−organic frameworks.[32]

2.4 Results and Discussion

2.4.1 Mechanochemical Synthesis of Synthetic Paceite and Its Cadmium Analogue.

Synthesis of artificial paceite from water was described in 1960 by Holden and Singer using copper(II) acetate monohydrate and calcium acetate as starting materials.[19] The synthesis is a textbook example of noncongruent cocrystallization, as the aqueous solubility of calcium acetate is significantly higher than that of $Cu(OAc)_2 \cdot H_2O$, which requires the two components to be used in a non-stoichiometric approximately 4:1 ratio. Mechanochemistry by ball milling has been demonstrated to provide access to solubility-independent reactions in which the stoichiometric composition of the product can be readily controlled by the composition of the reaction mixture.[33,34] Such stoichiometry control was observed for mechanochemistry by neat (dry) milling, as well as by liquid-assisted grinding (LAG), a methodology that uses a small amount of a liquid phase (measured in the form of η, the ratio of liquid additive to reactant weight) to enable and accelerate mechanochemical reactions.[32] Consequently, we decided to explore whether mechanochemistry can be used to obtain synthetic paceite samples using stoichiometric amounts of Cu^{2+} and Ca^{2+} precursors.

For that purpose and with the intention to explore potential routes through which paceite could be formed in a geological environment, we envisaged a two-step synthetic protocol that would use mineral-like substances as precursors. We chose copper(II) acetate monohydrate, $Cu(OAc)_2 \cdot H_2O$, as a source of Cu^{2+} ions, while the calcium acetate material required for the synthesis would be obtained in a mechanochemical reaction of either $CaCO_3$ or $Ca(OH)_2$ in combination with acetic

16

acid (AcOH) (reactions 1 and 2). The resulting hydrated calcium acetate was then expected to form paceite in a mechanochemical reaction with 1 equiv of $Cu(OAc)_2 \cdot H_2O$ (reaction 3).

$$CaCO_{3(s)} + 2AcOH_{(l)} \rightarrow Ca(OAc)_2 \cdot H_2O_{(s)} + CO_{2(g)} \qquad (1)$$

$$Ca(OH)_{2(s)} + 2AcOH_{(l)} \rightarrow Ca(OAc)_2 \cdot H_2O_{(s)} + H_2O_{(g)} \qquad (2)$$

$$Ca(OAc)_2 \cdot H_2O_{(s)} + Cu(OAc)_2 \cdot H_2O_{(s)} + 4H_2O_{(l)} \rightarrow CaCu(OAc)_4 \cdot 6H_2O_{(s)} \qquad (3)$$
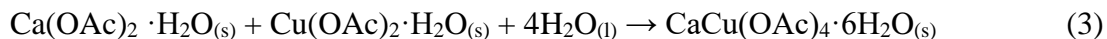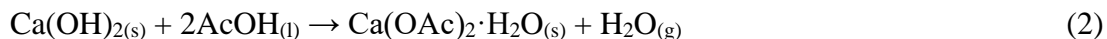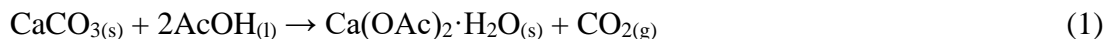
All mechanochemical reactions were performed by the LAG methodology[35] using a small amount of water as an additive (typically 10−12 μL), and analysis of reactants by PXRD confirmed that the used $CaCO_3$ was in the calcite form. The LAG reactions of either $Ca(OH)_2$ or $CaCO_3$ with a small excess (under 5 mol %) of glacial acetic acid led to the formation of calcium acetate monohydrate as the sole crystalline product. In particular, milling 0.5 mmol of $Ca(OH)_2$ for 30 min with 60 μL of AcOH and 10 μL of water led to the complete disappearance of the solid reactant and formation of hydrated calcium acetate of the formula $Ca(OAc)_2 \cdot H_2O$ (CSD code CEJLIM), identified by powder X-ray diffraction (PXRD) and thermogravimetric analysis (TGA) (**Figure 2-2** and **Figure 2-9**). In contrast, complete conversion of $CaCO_3$ into $Ca(OAc)_2 \cdot H_2O$ required 80 min of milling on the 1 mmol scale. Shorter milling times revealed the formation of a mixed hydrate and acetic acid solvate of calcium acetate, of composition $Ca(OAc)_2 \cdot H_2O \cdot AcOH$, which was identified by PXRD reflections matching those simulated for the published structure (CSD code COKJUH), along with unreacted $CaCO_3$. Upon longer milling, the initially formed $Ca(OAc)_2 \cdot H_2O \cdot AcOH$ reacted with remaining $CaCO_3$ to provide $Ca(OAc)_2 \cdot H_2O$.

In the next step, 1 equiv of $Cu(OAc)_2 \cdot H_2O$ was added to the mechanochemically prepared $Ca(OAc)_2 \cdot H_2O$ and the reaction mixture was milled for an additional 30 min. Analysis by PXRD revealed the complete disappearance of Bragg reflections of the starting materials and appearance

of new reflections consistent with the diffraction pattern calculated for the crystal structure of paceite. Identical outcomes were obtained regardless of whether the Ca^{2+} source in this two-step process was calcium carbonate or hydroxide (**Figure 2-2**). The formation of the paceite structure was also possible in a one-pot one-step process by milling calcium carbonate or hydroxide and acetic acid in the presence of equimolar amounts of $Cu(OAc)_2 \cdot H_2O$ and water. After 30 min of milling, the PXRD pattern of the reaction mixture exhibited only X-ray reflections of the mixed coordination polymer $CuCa(OAc)_4 \cdot 6H_2O$ (**Figure 2-2**). The formation of paceite by both one-and two-step mechanochemical routes was also confirmed by Fourier transform infrared attenuated total reflectance (FTIR-ATR) spectra, which were identical for the products of both synthetic methods.

The described two-step and one-step mechanochemical routes to $CuCa(OAc)_4 \cdot 6H_2O$ clearly demonstrate that the synthesis of this material can be readily performed through LAG using only stoichiometric amounts of metal precursors.

Ca(**OAc**)$_2$·H$_2$O by milling from Ca(OH)$_2$

Ca(**OAc**)$_2$·H$_2$O by milling from CaCO$_3$

simulated for Ca(OAc)$_2$·H$_2$O (**CSD** CEJLIM)

CaCu(**OAc**)$_4$·6H$_2$O
two-step mechanosynthesis from Ca(OH)$_2$

CaCu(**OAc**)$_4$·6H$_2$O
two-step synthesis from CaCO$_3$

CaCu(**OAc**)$_4$·6H$_2$O
one-step synthesis from Ca(OH)$_2$

CaCu(**OAc**)$_4$·6H$_2$O
one-step synthesis from CaCO$_3$

simulated for CaCu(**OAc**)$_4$·6H$_2$O
(**CSD** CACUAC01)

Cu(**OAc**)$_2$·H$_2$O reagent

Ca(OH)$_2$ reagent

CaCO$_3$ reagent

2θ / °
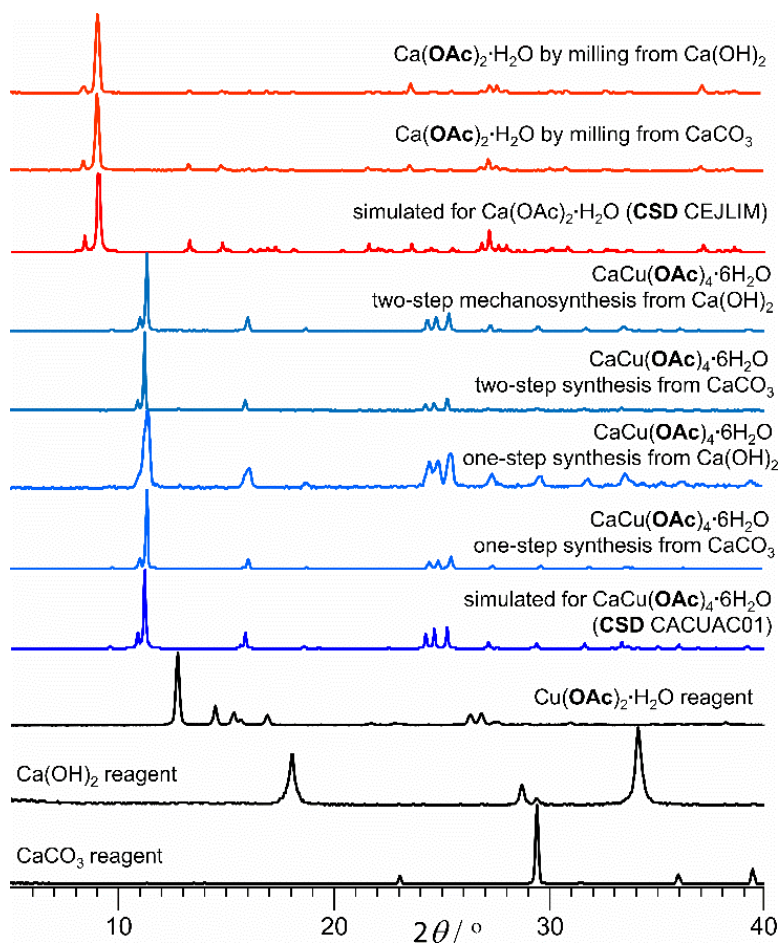
Figure 2-2. PXRD patterns for Ca(OAc)$_2$·H$_2$O and CaCu(OAc)$_4$·6H$_2$O mechanochemically prepared from Ca(OH)$_2$ or CaCO$_3$, to relevant patterns of reactants and simulated patterns.

19

2.4.2 Stoichiometric Control in Mechanochemical Synthesis of Calcium Acetate Solvates.

The observed formation of $Ca(OAc)_2 \cdot H_2O \cdot AcOH$ as an intermediate in the mechanochemical synthesis of $Ca(OAc)_2 \cdot H_2O$ from $CaCO_3$ is consistent with previously reported formation of highly solvated compounds as intermediates in mechanochemical synthesis of coordination compounds and MOFs.[36–38] It also suggests the possibility for selective synthesis of different solvates of calcium acetate, $Ca(OAc)_2 \cdot H_2O$ or $Ca(OAc)_2 \cdot H_2O \cdot AcOH$, depending on the stoichiometric composition of the reaction mixture. Specifically, we speculated that simply using the calcium-based precursor and acetic acid in the respective stoichiometric ratio of 1:3 should enable the selective formation of $Ca(OAc)_2 \cdot H_2O \cdot AcOH$. Indeed, milling of 1 mmol of $Ca(OH)_2$ with 3 mmol of AcOH led to the complete disappearance of Bragg reflections of the solid reactant in the PXRD pattern of the reaction mixture and the appearance of reflections of $Ca(OAc)_2 \cdot H_2O \cdot AcOH$ (**Figure 2-3**). The formation of $Ca(OAc)_2 \cdot H_2O \cdot AcOH$ was also verified by TGA (**Figure 2-9**). Similarly, milling of $CaCO_3$ with 3 equiv of AcOH led to quantitative conversion within 60 min of milling. Energetic constraints on these reactions and observed intermediates are discussed below from the point of view of thermochemical data.

The demonstrated ability to selectively obtain either $Ca(OAc)_2 \cdot H_2O \cdot AcOH$ or $Ca(OAc)_2 \cdot H_2O$ provides an additional illustration of the effectiveness of mechanochemical methods in controlling the stoichiometric composition of products.
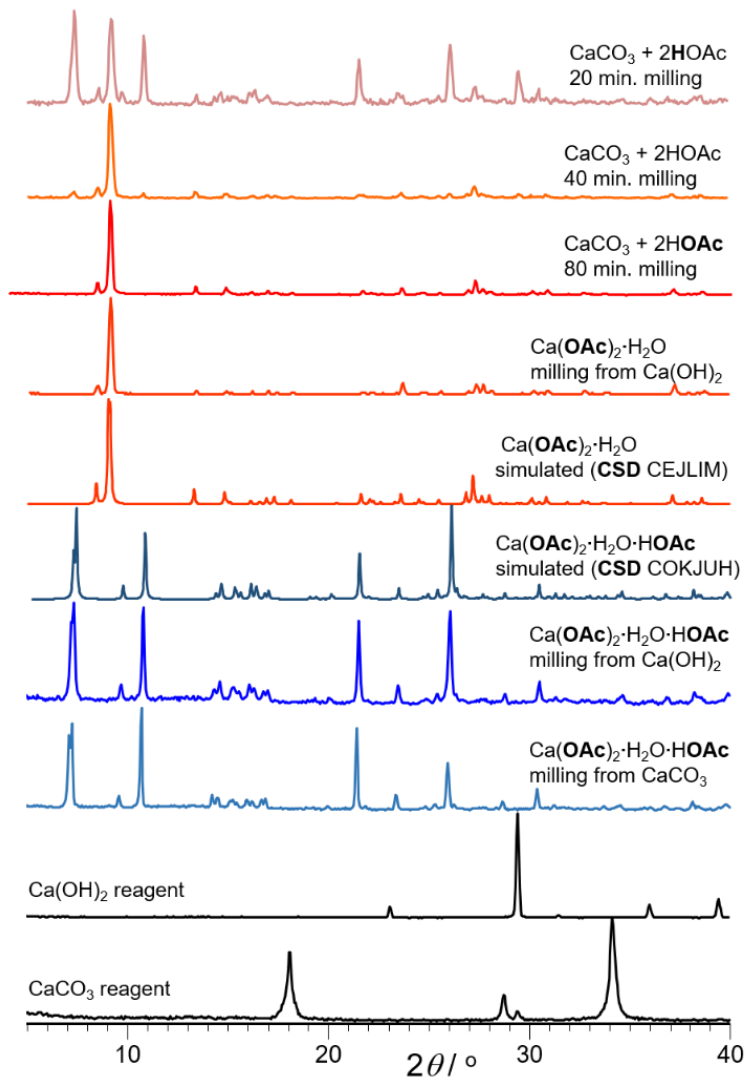
Figure 2-3. PXRD patterns for Ca(OAc)$_2$·H$_2$O·AcOH mechanochemically synthesized from Ca(OH)$_2$ or CaCO$_3$ to relevant patterns of reactants and simulated patterns.

2.4.3 Formation of Paceite by Accelerated Aging: A Potential Route for Geochemical Synthesis.

The formation of paceite by two-step or one-step milling reaction of $CaCO_3$ and $Cu(OAc)_2 \cdot H_2O$, both of which are known mineral species, suggests a possible geochemical route to paceite either through mechanical impact[39] or through mineral weathering reactions. In order to explore this possibility, we conducted accelerated aging reactions[40] inspired by mineral weathering processes[41] in which the exposure of inorganic minerals to small organic molecules under suitable conditions of temperature and atmosphere leads to the formation of organic minerals.

Two designs of accelerated aging reactions were explored. In one design, the reaction mixtures of either $Ca(OH)_2$ or $CaCO_3$ with 1 equiv of $Cu(OAc)_2 \cdot H_2O$ were manually mixed, followed by addition of a slight excess (10 mol %) of liquid AcOH, and then left to age for 7 days in 100% relative humidity (100% RH, i.e., saturated water vapor). In the second reaction design, the mixtures of $Cu(OAc)_2 \cdot 2H_2O$ with either $CaCO_3$ or $Ca(OH)_2$ as the calcium source were left to age for 7 days in an atmosphere saturated by vapors of a 50% aqueous solution of acetic acid (v/v). The reactions were conducted either at room temperature or in an incubator set to 45 °C. Visual observation of reaction mixtures over time in most cases revealed partial deliquescence and change in reaction mixture color to blue, consistent with paceite formation (**Figure 2-4**). The exceptions were reactions in which mixtures of $Cu(OAc)_2 \cdot H_2O$ with $CaCO_3$ or $Ca(OH)_2$ were left to age in vapors of the 50% aqueous acetic acid solution. Even after 7 days, these mixtures clearly consisted of a white powder with dispersed dark green particles of the $Cu(OAc)_2 \cdot H_2O$ reactant. The visual observations are confirmed by PXRD analysis of the aged reaction mixtures (**Figure 2-5**), which were briefly manually ground before recording a diffractogram. The analysis revealed the

formation of the paceite structure in all experiments, except in the aforementioned reactions of aging in vapors of 50% aqueous AcOH solution (v/v) at room temperature. Importantly, while reaction mixtures exhibited deliquescence, in no case was complete dissolution of samples observed.
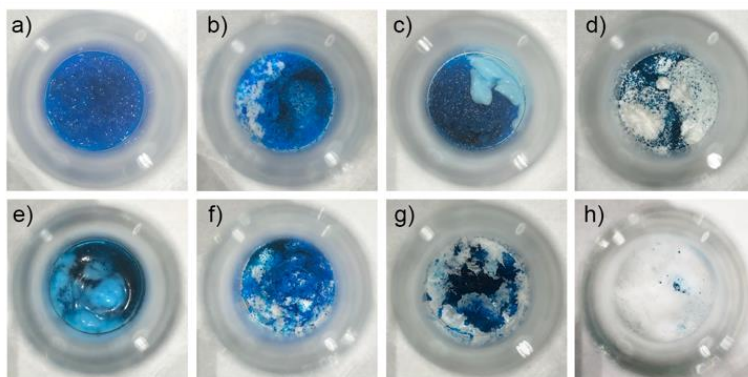
Figure 2-4. Optical images of equimolar mixtures of $Cu(OAc)_2 \cdot H_2O$ and either $Ca(OH)_2$ or $CaCO_3$ upon six days of aging under different conditions: a) $Cu(OAc)_2 \cdot H_2O$ and $Ca(OH)_2$ with 1.1 equivalent of AcOH added directly to the mixture, and aged at 100% RH and 45 ºC; b) $Cu(OAc)_2 \cdot H_2O$ and $Ca(OH)_2$ with 1.1 equivalent of AcOH added directly to the mixture, and aged at 100% RH and room temperature; c) $Cu(OAc)_2 \cdot H_2O$ and $Ca(OH)_2$, aged in vapors of 50% aqueous AcOH at 45 ºC; d) $Cu(OAc)_2 \cdot H_2O$ and $Ca(OH)_2$, aged in vapors of 50% aqueous AcOH at room temperature; e) $Cu(OAc)_2 \cdot H_2O$ and $CaCO_3$ with 1.1 equivalent of AcOH added directly to the mixture, and aged at 100% RH and 45 ºC; f) $Cu(OAc)_2 \cdot H_2O$ and $CaCO_3$ with 1.1 equivalent of AcOH added directly to the mixture, and aged at 100% RH and room temperature; g) $Cu(OAc)_2 \cdot H_2O$ and $CaCO_3$, aged in vapors of 50% aqueous AcOH at 45 ºC and h) $Cu(OAc)_2 \cdot H_2O$ and $CaCO_3$, aged in vapors of 50% aqueous AcOH at room temperature.

In addition to paceite, the reaction mixtures also exhibited X-ray reflections consistent with different amounts of $Ca(OAc)_2 \cdot H_2O$ or $Ca(OAc)_2 \cdot H_2O \cdot AcOH$. The observation that both of these phases participate in the solid-state formation of paceite was verified by real-time monitoring of the reaction of $Cu(OAc)_2 \cdot H_2O$ with $Ca(OH)_2$ in an atmosphere containing vapors of water and AcOH. An analogous measurement was not possible for $CaCO_3$ as the calcium source due to formation of the gaseous CO_2 in the reaction. A detailed description of the experimental setup and its use in monitoring cocrystal formation have been recently published.[30,42]

Real-time in situ X-ray diffraction monitoring of changes in a mixture of equimolar amounts of $Ca(OH)_2$ and $Cu(OAc)_2 \cdot H_2O$ upon exposure to vapors of acetic acid and water revealed (**Figure 2-6**) the interconversion of at least five crystalline phases: $Ca(OH)_2$, $Cu(OAc)_2 \cdot H_2O$, paceite, calcium acetate monohydrate (CSD code CEJLIM), and $Ca(OAc)_2 \cdot H_2O \cdot AcOH$ (CSD code COKJUH). Rietveld refinement of in situ PXRD data revealed a continuous drop in the content of $Ca(OH)_2$ and $Cu(OAc)_2 \cdot H_2O$ reactants over approximately 14 h. The first new crystalline phase observed in the reaction is the mixed hydrate and acetic acid solvate $Ca(OAc)_2 \cdot H_2O \cdot AcOH$, which is detected already in the first experimental data sets. The crystalline monohydrate $Ca(OAc)_2 \cdot H_2O$ appears considerably later in the reaction, after approximately 3.5 h of aging, and is soon followed by the appearance of the paceite structure after approximately 5 h of aging. The initial formation of $Ca(OAc)_2 \cdot H_2O \cdot AcOH$, followed by $Ca(OAc)_2 \cdot H_2O$, is consistent with previous general observations on mechanochemical reactions of oxides with carboxylic acids, which reveal the initial formation of the more solvated intermediate phases.
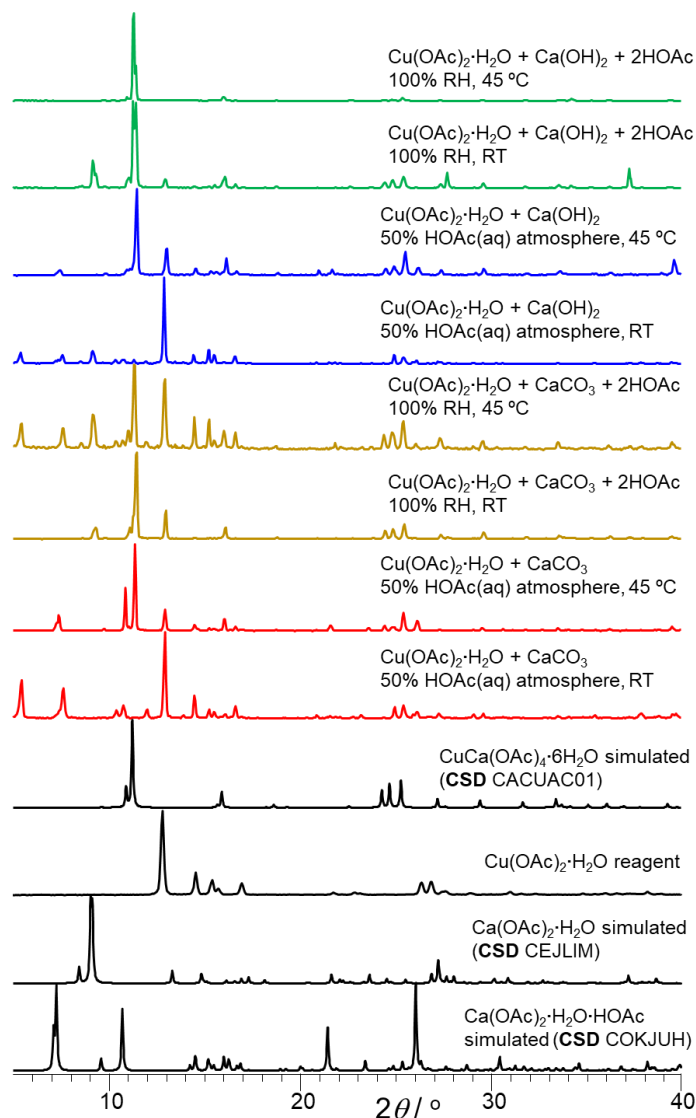
Figure 2-5. PXRD patterns for mixtures of $Cu(OAc)_2·H_2O$ after seven days aging under different conditions, to relevant patterns of reactants and simulated patterns.

Rietveld analysis suggests that the disappearance of $Ca(OH)_2$ takes place faster than that of $Cu(OAc)_2·H_2O$. While quantitative analysis is hindered by significant potential for preferred orientation and crystal size effects in such a nonmixed reaction system, these observations may be explained by multiple possible reaction pathways available for calcium hydroxide, forming three different calcium-containing products, in contrast to copper(II) acetate converting only to paceite.

25
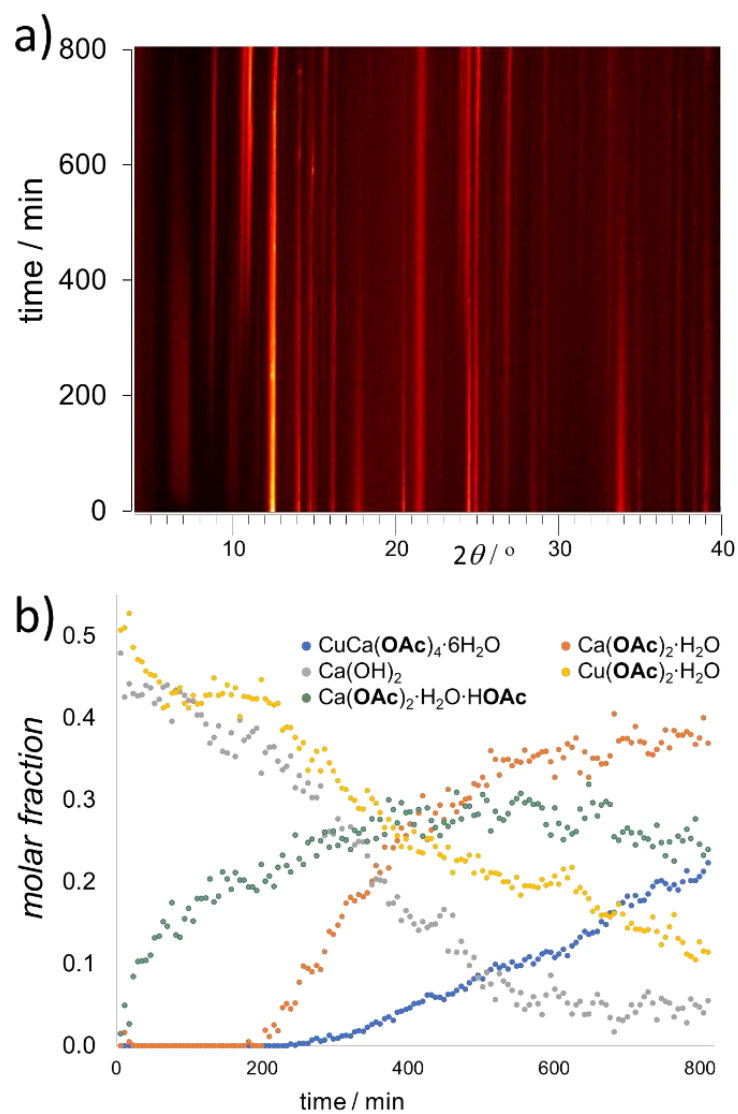
Figure 2-6. a) Time-resolved X-ray powder diffractogram for the aging reaction of $Ca(OH)_2$ and $Cu(OAc)_2 \cdot H_2O$ in an atmosphere of water and acetic acid and b) corresponding reaction profile based on Rietveld refinement of the PXRD data.

2.4.4 Cadmium Analogue of Paceite.

We next explored the potential to use analogous reactivity to synthesize the previously reported cadmium analogue of paceite.[20] Indeed, the two-step mechanochemical reactions involving milling of $Ca(OH)_2$ or $CaCO_3$ in the presence of a small excess of acetic acid, followed by milling of resulting $Ca(OAc)_2 \cdot H_2O$ with commercially available $Cd(OAc)_2 \cdot 2H_2O$, led to the quantitative formation of the targeted $CaCd(OAc)_4 \cdot 6H_2O$ paceite analogue (**Figure 2-7**). Formation of $CaCd(OAc)_4 \cdot 6H_2O$ was verified by PXRD pattern analysis, which revealed a product isostructural to paceite. As observed in the case of synthetic paceite, its cadmium analogue could also be obtained by a one- pot mechanochemical procedure starting from either $CaCO_3$ or $Ca(OH)_2$ in the presence of commercial $Cd(OAc)_2 \cdot 2H_2O$, acetic acid, and a small amount of water. Again, the formation of $CaCd(OAc)_4 \cdot 6H_2O$ was confirmed by PXRD analysis (**Figure 2-7**), as well as TGA (**Figure 2-9**). In this case also, the formation of the same product by both one- and two-step mechanochemical routes was confirmed by FTIR-ATR spectroscopy.
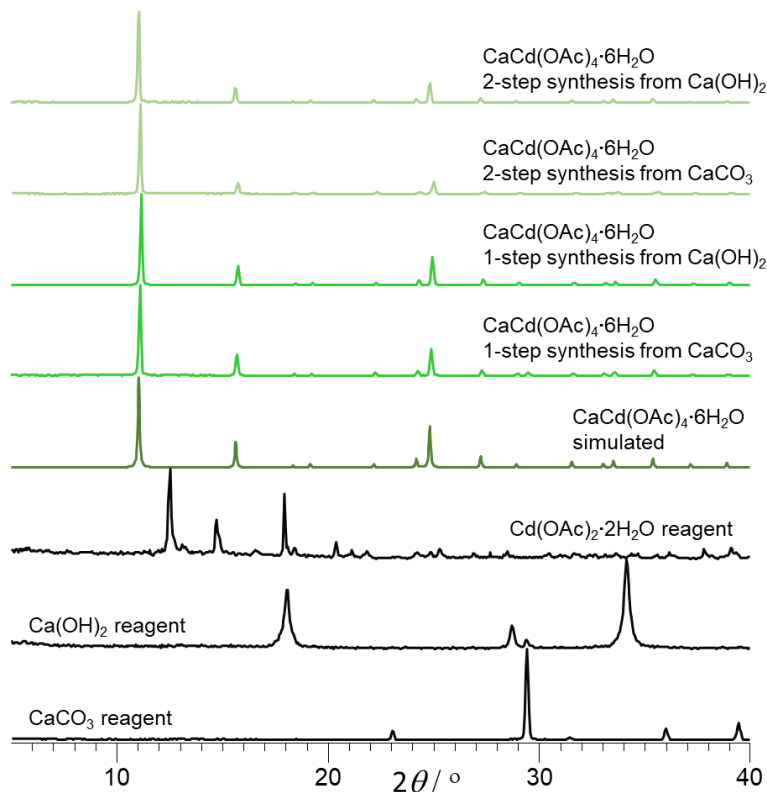
Figure 2-7. PXRD patterns for $CaCd(OAc)_4 \cdot 6H_2O$ prepared from $Ca(OH)_2$ or $CaCO_3$ to relevant patterns of reactants and simulated patterns.

As the crystallographic data for $CaCd(OAc)_4 \cdot 6H_2O$ have previously not been reported, we also conducted a single crystal X-ray diffraction study of the structure of this mixed- metal coordination polymer (**Table 2-1**). Single crystals for $CaCd(OAc)_4 \cdot 6H_2O$ were obtained through an accelerated aging process from a deliquescent mixture of equimolar amounts of $Ca(OH)_2$, $Cd(OAc)_2 \cdot 2H_2O$, and a small excess (10%) of acetic acid that was aged over 2 days at 45 °C and 100% RH. Crystal structure analysis revealed coordination polymer chains of alternating Cd^{2+} and Ca^{2+} ions propagating along the 4_1-screw axis parallel to the crystallographic c-axis (**Figure 2-8**). The chains are isostructural to those of copper(II)- and calcium-based chains found in paceite.

Similar to paceite, Ca^{2+} ions adopt an octahedral coordination geometry involving four equatorial acetate ions. However, in the $CaCd(OAc)_4 \cdot 6H_2O$ structure, the oxygen atom of each acetate ion associated with a Ca^{2+} ion was found to be disordered over two sites, whose relative occupational parameters were established as 0.51 and 0.49 using least- squares refinement. The disorder gives rise to two Ca$\cdots$O distances of 2.31 and 2.33 Å, respectively. As in the paceite structure, each acetate ion forms a bridge to one of the two nearest-neighbor Cd^{2+} ions in a chain (Cd$\cdots$O distance 2.29 Å). The apical coordination positions on each Ca^{2+} ion are occupied by oxygen atoms of two water molecule ligands (Ca$\cdots$O distances 2.34 Å). Also analogous to Cu^{2+} ions, the Cd^{2+} ions in the structure of $CaCd(OAc)_4 \cdot 6H_2O$ adopt a roughly square-planar coordination geometry (O$\cdots$Cd$\cdots$O angle 90.7°), established through four monodentate oxygen ligands, each coming from a different acetate ion, which is also associated with a nearest-neighbor Ca^{2+} ion.

Table 2-1. Crystallographic and general data for CaCd(OAc)$_2$·6H$_2$O.

Formula	C$_4$H$_{12}$Ca$_{0.5}$Cd$_{0.5}$O$_7$
Mr	248.4
T / K	298(2)
crystal system	tetragonal
space group	I4/m
a / Å	11.3440(4)
c / Å	16.0488(6)
V / Å^3	2065.3(2)
Z	8
ρcalc / g/cm^3	1.598
μ / mm^{-1}	1.362
F(000)	1008
crystal size / mm^3	0.3 × 0.15 × 0.15
λ / Å	0.71073 (MoKα)
2θ range for data collection / °	7.18 - 66.21
No. reflections	17744
No. independent reflections	1825
No. restraints	8
No. parameters	79
S	0.990
R1, wR2 (I≥2σ(I))	0.028, 0.070
R1, wR2 (all data)	0.056, 0.087
Largest difference electron density peak/hole / e Å^{-3}	0.31; –0.27

Each of the two water ligands on a Ca^{2+} ion also acts as a hydrogen bond donor to two neighboring water molecules (O−H···O distance 2.77 Å), which are further hydrogen-bonded to their symmetry-related counterparts (O−H···O separation 2.78 Å) across a 4_1-screw axis to form 12-membered cages based on O−H···O hydrogen bonds.
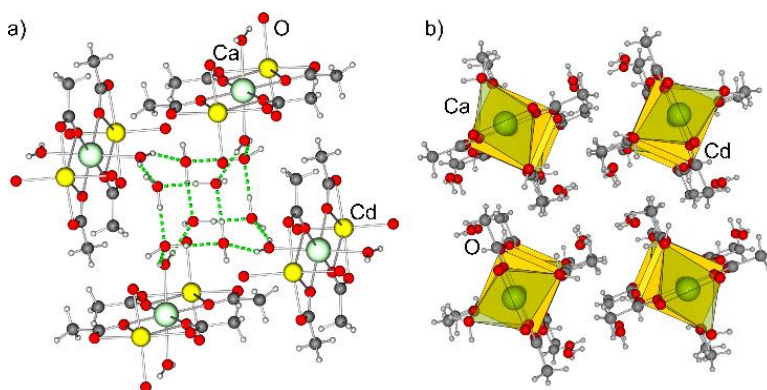
Figure 2-8. The CaCd(**OAc**)$_4$·6H$_2$O crystal structure viewed along the 4_1 screw axis parallel to the crystallographic *c*-direction: a) highlighting the hydrogen-bonded (H$_2$O)$_{12}$ cluster situated between four bimetallic coordination polymer chains and b) similar orientation of the structure, with metal coordination polyhedra outlined (Cd:yellow, Ca:green). For clarity, the disorder of the acetate ion is not shown.

2.4.5 Thermal analysis for water content determination

DSC-TG curves of all the samples are shown in **Figure 2-9**. Both copper and cadmium acetate samples showed an endothermic mass loss process at 100-200 ºC which corresponds to the dehydration process. This water loss was followed by the loss of the acetate at around 250-350ºC to form the corresponding oxides. Similar behavior was seen with calcium acetate, except that there was an additional mass loss step after the dehydration process where calcium carbonate formation occurs, which was then finally followed by the formation of calcium oxide. The mass

loss observed for each step for both copper and cadmium acetates agrees within 0.5 % with what is expected corresponding to the stoichiometric amount of water. For calcium acetate sample, the water content measured was slightly higher than expected, namely 1.1mol of H_2O per mole of calcium acetate. This composition was the one used for the subsequent calorimetry measurements and enthalpy calculations involving calcium acetate. The mass loss behavior of the acetic acid solvated calcium acetate sample was similar to that of the non-solvated calcium acetate sample, except that during the dehydration process there was also the loss of acetic acid solvent, followed by the formation of calcium carbonate and calcium oxide at the last step. The mass loss observed for each step also agrees within 0.5 % with what is expected for the stoichiometric amount of water. For calcium carbonate, there was no mass loss until 650 ^{o}C, which indicates that there was no water on the sample. This was further confirmed by absence of water peak on the sample's FTIR-ATR spectrum.

For the paceite and cadmium analog of paceite ($CaCd(OAc)_4 \cdot 6H_2O$) samples, a three-step mass loss process was observed, similar to the one observed with calcium acetate. The dehydration process started earlier at 50-200°C, followed by the loss of mass to form copper oxide and calcium carbonate for the paceite and to form cadmium oxide and calcium carbonate for the $CaCd(OAc)_4 \cdot 6H_2O$. Finally, at the last mass loss step, CO_2 was released to form the binary oxides. Here the mass loss observed in each step for both paceite and its cadmium analogue agrees within 0.5 % with what is expected for the stoichiometric amount of water. The calculated water content of each sample and the expected mass loss value is summarized in **Table 2-2**.
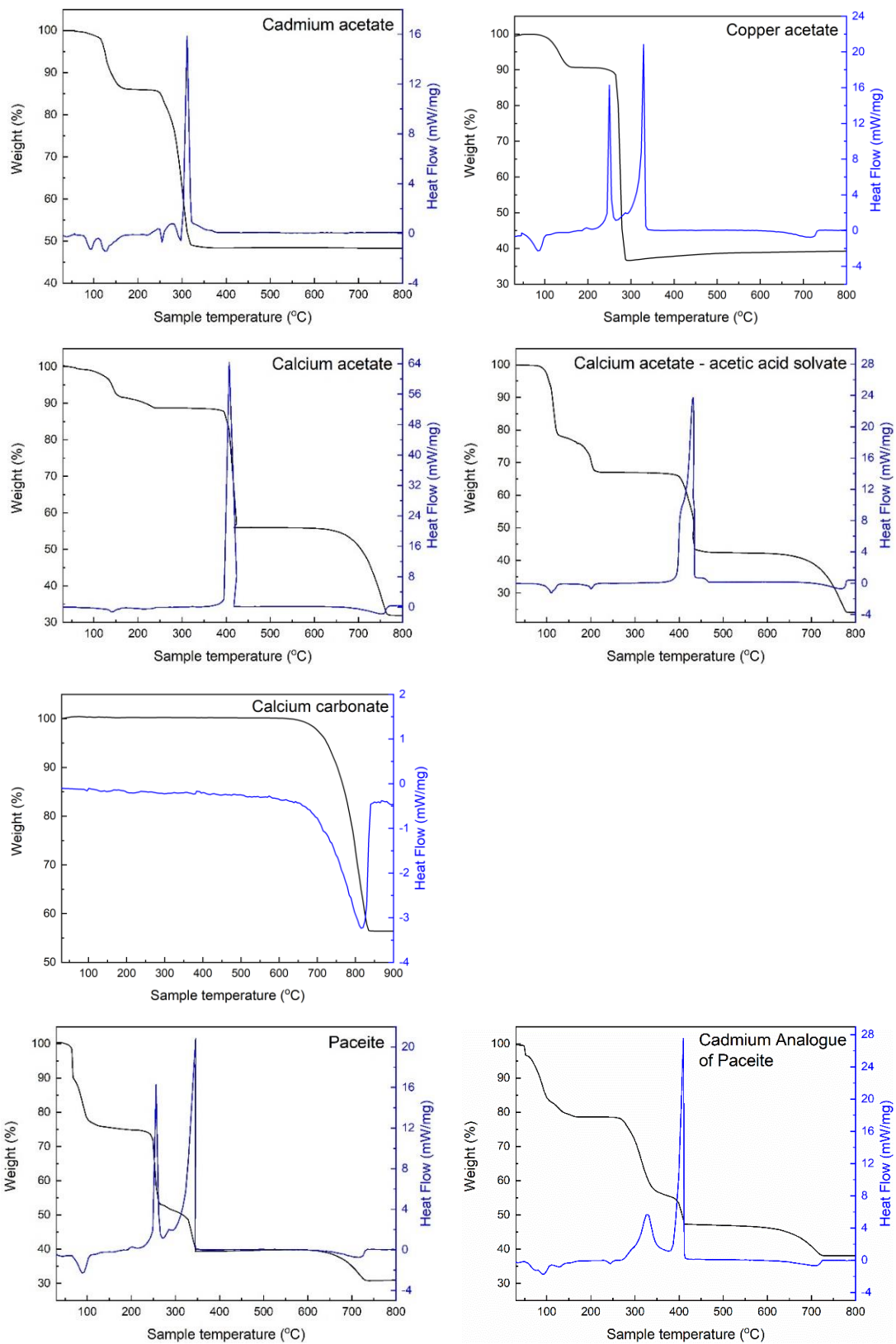
Figure 2-9. DSC-TG curves of all studied samples.

Table 2-2. Summary of sample composition, the expected stoichiometric mass loss and the experimental mass loss observed from DSC-TG measurements

Sample	Mass loss (weight %)			
	First step (complete dehydration)	Expected value	Total (formation of binary oxides)	Expected value
$Cu(OAc)_2.H_2O$	9.06	9.02	60.55	60.16
$Cd(OAc)_2.2H_2O$	13.70	13.52	51.40	51.82
$Ca(OAc)_2.1.1H_2O$	11.55	11.06	68.09	68.47
$Ca(OAc)_2.1H_2O.AcOH$	32.94	33.05	75.89	76.26
$CdCa(OAc)_4.6H_2O$	21.34	21.76	62.00	62.86
$CuCa(OAc)_4.6H_2O$	24.3	24.13	69.28	69.72

2.4.6 Enthalpies of Formation of Paceite Structures and Thermodynamic Driving Force for the Mechanochemical and Aging Formation of Paceite Structures from $CaCO_3$.

In order to achieve deeper insight into the formation of paceite and its cadmium analogue from calcium carbonate, we evaluated the enthalpies of formation (ΔH_f) for both $CaCu(OAc)_4 \cdot 6H_2O$ and $CaCd(OAc)_4 \cdot 6H_2O$ using acid dissolution calorimetry[43] in 5 N aqueous hydrochloric acid as the solvent. For this purpose, dissolution enthalpies for both $CaCu(OAc)_4 \cdot 6H_2O$ and $CaCd(OAc)_4 \cdot 6H_2O$, as well as for $Cu(OAc)_2 \cdot H_2O$, $Cd(OAc)_2 \cdot 2H_2O$, $Ca(OAc)_2.1.1H_2O$, $Ca(OAc)_2 \cdot H_2O \cdot AcOH$, and $CaCO_3$, were experimentally determined at 25 °C.

For the calorimetric measurements, it was necessary to ensure that there was no variation in the final state for an accurate thermochemical cycle. Since the reactions occurred in an aqueous

solution rather than in a molten salt solvent, we had less experience and need to test consistency of final state more systematically by performing the following experiments:

- Subsequent dissolution of several samples with the same composition into a batch of the same solvent.

- Dissolution of a sample into a solvent containing other samples.

- Dissolution of mechanical mixture of samples, and

- Dissolution of samples with different masses

The tests were performed using $Ca(OAc)_2.1.1H_2O$, $Cu(OAc)_2.H_2O$, and $CaCO_3$ samples and the detailed measured solution enthalpy data for all of the samples is given in **Table 2-3**.

Table 2-3. Solution enthalpy data from acid calorimetry in 5 N HCl at different conditions[a]

Sample: Paceite **$(CaCu(OAc)_4.6H_2O)$**					
Weight (mg)	ΔH_s (kJ/mol)	Solute present in the solution	Weight (mg)	ΔH_s (kJ/mol)	Solute present in the solution
9.90	2.83	-	10.61	2.79	-
10.95	2.86	-	10.42	2.58	-
Average ΔH_s (kJ/mol) = **2.77 ± 0.13 kJ/mol (4)**					

Table 2-3. Continued

Sample: **CaCd(OAc)₄.6H₂O**

Weight (mg)	ΔH_s (kJ/mol)	Solute present in the solution	Weight (mg)	ΔH_s (kJ/mol)	Solute present in the solution
11.14	-24.53	-	10.24	-24.67	-
10.13	-24.49	-	9.91	-24.59	-
9.91	-25.18	-			

Average ΔH_s (kJ/mol) = **-24.69 ± 0.25 kJ/mol (5)**

Sample: Cu-acetate **(Cu(OAc)₂.H₂O)**

Weight (mg)	ΔH_s (kJ/mol)	Solute present in the solution	Weight (mg)	ΔH_s (kJ/mol)	Solute present in the solution
11.43	2.46	-	9.89	2.46	9.76mg Cu(OAc)₂.H₂O
9.63	2.39	-	7.12	2.89	9.65mg Cu(OAc)₂.H₂O
11.49	2.75	-	9.98	2.58	19.64mg Cu(OAc)₂.H₂O
9.88	2.54	-	9.60	2.29	16.77mg Cu(OAc)₂.H₂O
13.60	2.63	-	12.65	3.25	29.62mg Cu(OAc)₂.H₂O
9.76	2.86	-	9.44	2.90	26.37mg Cu(OAc)₂.H₂O
9.65	2.88	-			

Average ΔH_s (kJ/mol) = **2.68 ± 0.15 (13)**

Sample: Cd-acetate **(Cd(OAc)₂.2H₂O)**

Weight (mg)	ΔH_s (kJ/mol)	Solute present in the solution	Weight (mg)	ΔH_s (kJ/mol)	Solute present in the solution
15.49	-14.02	-	13.24	-14.25	-
12.96	-14.03	-	14.43	-14.25	-

Average ΔH_s (kJ/mol) = **-14.14 ± 0.13 (4)**

Table 2-3. Continued

Sample: Ca-carbonate $(CaCO_3)$

Weight (mg)	ΔH_s (kJ/mol)	Solute present in the solution	Weight (mg)	ΔH_s (kJ/mol)	Solute present in the solution
10.08	-25.98	-	4.90	-25.77	4.76mg $CaCO_3$
10.22	-25.78	-	4.97	-24.99	9.86mg $CaCO_3$
10.34	-26.25	-	4.92	-24.74	9.96mg $CaCO_3$
9.87	-26.05	-	4.98	-24.82	9.66mg $CaCO_3$
10.77	-25.76	-	9.76	-25.71	10.07mg $CaCO_3$
10.07	-25.63	-	4.90	-24.87	14.88mg $CaCO_3$
4.98	-24.99	-	4.84	-24.47	14.63mg $CaCO_3$
5.08	-25.10	-	4.86	-24.84	19.78mg $CaCO_3$
4.97	-24.89	-	4.94	-24.15	19.47mg $CaCO_3$
4.95	-24.54	-	4.96	-25.07	18.61mg $(Cu(OAc)_2.H_2O + Ca(OAc)_2.1.1H_2O)$
4.76	-25.22	-	4.89	-25.53	18.61mg $(Cu(OAc)_2.H_2O + Ca(OAc)_2.1.1H_2O) + 4.96mg\ CaCO_3$
4.88	-26.58	4.98mg $CaCO_3$	4.97	-24.90	18.61mg of $(Cu(OAc)_2.H_2O + Ca(OAc)_2.1.1H_2O) + 9.84mg\ CaCO_3$
5.26	-25.65	5.08mg $CaCO_3$	5.21	-24.31	42.27mg $Cu(OAc)_2.H_2O$ + 9.92mg $Ca(OAc)_2.1.1H_2O$
4.90	-25.16	4.97mg $CaCO_3$	4.92	-25.13	35.81mg $Cu(OAc)_2.H_2O$ + 9.99mg $Ca(OAc)_2.1.1H_2O$
5.01	-24.82	4.95mg $CaCO_3$			

Average ΔH_s (kJ/mol) = **-25.23 ± 0.22 (29)**

Table 2-3. Continued

Sample: Ca-acetate $(\mathbf{Ca(OAc)_2 \cdot 1.1H_2O})$

Weight (mg)	ΔH_s (kJ/mol)	Solute present in the solution	Weight (mg)	ΔH_s (kJ/mol)	Solute present in the solution
9.99	-29.90	-	9.36	-29.88	-
10.16	-29.95	-	9.92	-29.89	42.27mg $Cu(OAc)_2 \cdot H_2O$
9.47	-30.34	-	9.99	-30.06	35.81mg $Cu(OAc)_2 \cdot H_2O$

Average ΔH_s (kJ/mol) = **-30.00± 0.15 (6)**

Sample: Cu- and Ca-acetate mechanical mixture $(\mathbf{Cu(OAc)_2 \cdot H_2O + Ca(OAc)_2 \cdot 1.1H_2O})$

Weight (mg)	ΔH_s (kJ/mol)	Solute present in the solution	Weight (mg)	ΔH_s (kJ/mol)	Solute present in the solution
9.81	-27.53	-	8.80	-26.64	9.81mg $(Cu(OAc)_2 \cdot H_2O + Ca(OAc)_2 \cdot 1.1H_2O)$

Average ΔH_s (kJ/mol) = **-27.08 ± 0.89 (2)**

Sample: Ca-acetate-acetic acid solvate $(\mathbf{Ca(OAc)_2 \cdot H2O \cdot AcOH})$

Weight (mg)	ΔH_s (kJ/mol)	Solute present in the solution	Weight (mg)	ΔH_s (kJ/mol)	Solute present in the solution
9.75	-9.23	-	9.86	-9.28	-
10.51	-9.21	-			

Average ΔH_s (kJ/mol) = **-9.24 ± 0.04 (3)**

The error is two standard deviations of the mean; the values in brackets are the numbers of experiments performed; weight refers to the weight of the sample pellet that was dropped to the solvent; ΔH_s is the measured dissolution enthalpy; and the solute present in the solution refers to the solute that was already dissolved in the solvent before the sample drop was performed.

From the data in **Table 2-3**, it can be seen that the dissolution enthalpy values of the samples at different conditions were consistent and did not depend on the concentrations of other dissolved samples in the range used. Changing both the weight and the nature of the solute already present in the solvent resulted in no appreciable difference in the measured dissolution enthalpy. This indicates that the dissolved ions in the solvent interact similarly with each other and with the solvent independent of concentration in the range used. Additionally, the dissolution enthalpy value observed for the mechanical mixture of $Cu(OAc)_2 \cdot H_2O$ and $Ca(OAc)_2.1.1H_2O$ was -27.08 ± 0.89 kJ/mol, which agrees with the expected value calculated from their individual dissolution enthalpy, 27.38 ± 0.18 kJ/mol. This further confirmed that the final state of sample and its constituents after calorimetric measurement are the same.

Having confirmed the consistency of the final state on the calorimetric measurements, together with the measured and literature values for the dissolution enthalpies of glacial acetic acid and water, these enabled the evaluation of ΔH_f for $CaCu(OAc)_4 \cdot 6H_2O$ and $CaCd(OAc)_4 \cdot 6H_2O$ from reacting the corresponding transition metal acetates either with $CaCO_3$ and acetic acid or with hydrated calcium acetate. The calculations were performed following the thermodynamic cycle presented in **Table 2-4** and the summary of the enthalpy values is given in **Table 2-5**:

Table 2-4. Thermodynamic cycle used to calculate the formation enthalpy of the paceite and cadmium analogue of the paceite

Formation from $CaCO_3$ and $M(OAc)_2 \cdot xH_2O$	
Reactions	Enthalpy (ΔH, kJ mol^{-1})
$MCa(OAc)_4.6H_2O_{(s)} \rightarrow M^{2+}_{(aq)} + Ca^{2+}_{(aq)} + 4OAc^-_{(aq)} + 6H_2O_{(aq)}$	ΔH_1
$M(OAc)_2.xH_2O_{(s)} \rightarrow M^{2+}_{(aq)} + 2OAc^-_{(aq)} + xH_2O_{(aq)}$	ΔH_2
$CaCO_{3(s)} + 2H^+_{(aq)} \rightarrow Ca^{2+}_{(aq)} + H_2O_{(aq)} + CO_{2(g)}$	ΔH_3
$AcOH_{(l)} \rightarrow OAc^-_{(aq)} + H^+_{(aq)}$	ΔH_4
$H_2O_{(l)} \rightarrow H_2O_{(aq)}$	ΔH_5
$M(OAc)_2.H_2O_{(s)} + CaCO_{3(s)} + 2AcOH_{(l)} + (5-x)H_2O_{(l)} \rightarrow$ $MCa(OAc)_4.6H_2O_{(s)} + CO_{2(g)}$	$\Delta H_6 = \Delta H_f = -\Delta H_1 + \Delta H_2$ $+ \Delta H_3 + 2\Delta H_4 + (5-x)\Delta H_5$

Formation from $Ca(OAc)_2.1.1H_2O$ and $M(OAc)_2 \cdot xH_2O$	
Reactions	Enthalpy (ΔH, kJ mol^{-1})
$MCa(OAc)_4.6H_2O_{(s)} \rightarrow M^{2+}_{(aq)} + Ca^{2+}_{(aq)} + 4OAc^-_{(aq)} + 6H_2O_{(aq)}$	ΔH_1
$M(OAc)_2.xH_2O_{(s)} \rightarrow M^{2+}_{(aq)} + 2OAc^-_{(aq)} + xH_2O_{(aq)}$	ΔH_2
$Ca(OAc)_2.1.1H_2O_{(s)} \rightarrow Ca^{2+}_{(aq)} + 2OAc^-_{(aq)} + 1.1H_2O_{(aq)}$	ΔH_7
$H_2O_{(l)} \rightarrow H_2O_{(aq)}$	ΔH_5
$M(OAc)_2.H_2O_{(s)} + Ca(OAc)_2.1.1H_2O_{(s)} + (4.9-x)H_2O_{(l)} \rightarrow$ $MCa(OAc)_4.6H_2O_{(s)}$	$\Delta H_8 = \Delta H_f = -\Delta H_1 + \Delta H_2$ $+ \Delta H_7 + (4.9-x)\Delta H_5$

[a]$M = $ Cu and Cd; $x = 1$ for Cu and 2 for Cd

Table 2-5. Thermodynamic data obtained and calculated from acid solution calorimetry in 5N HCl

Compound	ΔH_s (kJ/mol)	ΔH_f (kJ/mol)	
		From carbonate	From acetate
$CuCa(OAc)_4 \cdot 6H_2O_{(s)}$ (synthetic paceite)	2.77 ± 0.13 (4)	-27.14 ± 0.30^a	-31.45 ± 0.25^b
$CdCa(OAc)_4 \cdot 6H_2O_{(s)}$	-24.69 ± 0.25 (5)	-16.14 ± 0.36^c	-20.46 ± 0.32^d
$Ca(OAc)_2 \cdot 1.1H_2O_{(s)}$	-30.00 ± 0.15 (6)		
$Cu(OAc)_2 \cdot H_2O_{(s)}$	2.68 ± 0.15 (13)		
$Cd(OAc)_2 \cdot 2H_2O_{(s)}$	-14.14 ± 0.13 (4)		
$Ca(OAc)_2 \cdot H_2O \cdot AcOH_{(s)}$	-9.24 ± 0.04 (3)		
$(Cu(OAc)_2 \cdot H_2O + Ca(OAc)_2 \cdot 1.1H_2O)$ (mechanical mixture)	-27.08 ± 0.89 (2)		
$CaCO_{3(s)}$	-25.23 ± 0.22 (29)		
$AcOH_{(l)}$	-0.21 ± 0.01^e		
$H_2O_{(l)}$	-0.35^f		

Reactions corresponding to each enthalpy of formation values:

[a] $Cu(CH_3COO)_2.H_2O_{(s)} + CaCO_{3(s)} + 2CH_3COOH_{(l)} + 4H_2O_{(l)} \rightarrow CuCa(CH_3COO)_4.6H_2O_{(s)} + CO_{2(g)}$

[b] $Cu(CH_3COO)_2.H_2O_{(s)} + Ca(CH_3COO)_2.1.1H_2O_{(s)} + 3.9H_2O_{(l)} \rightarrow CuCa(CH_3COO)_4.6H_2O_{(s)}$

[c] $Cd(CH_3COO)_2.2H_2O_{(s)} + CaCO_{3(s)} + 2CH_3COOH_{(l)} + 3H_2O_{(l)} \rightarrow CdCa(CH_3COO)_4.6H_2O_{(s)} + CO_{2(g)}$

[d] $Cd(CH_3COO)_2.2H_2O_{(s)} + Ca(CH_3COO)_2.1.1H_2O_{(s)} + 2.9H_2O_{(l)} \rightarrow CdCa(CH_3COO)_4.6H_2O_{(s)}$
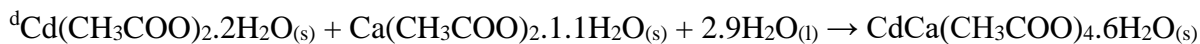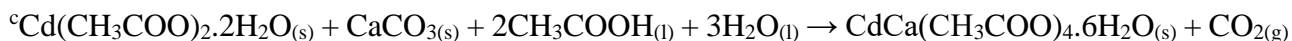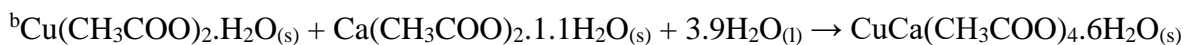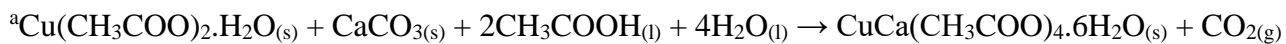
[e] Ref 42; [f] Calculated from dilution enthalpy of HCl[43] Error is two standard deviations of the mean, value in brackets is number of experiments performed.

The calculated enthalpies of formations reveal that the formation of copper(II)- and cadmium-based paceite structures was clearly exothermic, which agrees with the ease of forming $CaCu(OAc)_4 \cdot 6H_2O$ and $CaCd(OAc)_4 \cdot 6H_2O$ by mechanochemical milling of corresponding metal acetates. The ΔH_f values for the formation of $CaCu(OAc)_4 \cdot 6H_2O$ and $CaCd(OAc)_4 \cdot 6H_2O$ from $Ca(OAc)_2 \cdot H_2O$ are more exothermic than values when starting from $CaCO_3$, which might be related to the high stability of the carbonate reactant.

The measured thermodynamic data also reveal that the ΔH_f for the formation of synthetic paceite is in each case more exothermic than for its cadmium-based analogue, indicating a destabilization effect introduced by the incorporation of cadmium. The other important distinction is that the reference states for the formation reactions of $CaCu(OAc)_4 \cdot 6H_2O$ and $CaCd(OAc)_4 \cdot 6H_2O$ are not identical, as well as that the crystal structures of the starting materials $Cu(OAc)_2 \cdot H_2O$ and $Cd(OAc)_2 \cdot 2H_2O$ are different and have different water contents.

Tentatively, the difference in ΔH_f for synthetic paceite and its cadmium analogue might be attributed to the difference in the change of transition metal coordination during the reaction: in the $Cu(OAc)_2 \cdot H_2O$ starting material, the Cu^{2+} ions are five-coordinated with oxygen-based ligands, whereas in $Cd(OAc)_2 \cdot 2H_2O$, the Cd^{2+} ions adopt a coordination number of 7.[46,47] However, in $CaCu(OAc)_4 \cdot 6H_2O$ and $CaCd(OAc)_4 \cdot 6H_2O$, the transition metal ions adopt a coordination number of 4. Consequently, cadmium ions undergo a more significant change in coordination number upon transformation into the paceite structure compared to copper(II) ions.[20] Such a difference might be a significant factor contributing to a diminished exothermic enthalpy of formation of $CaCd(OAc)_4 \cdot 6H_2O$ compared to synthetic paceite.

The measurement of enthalpies of dissolution also enabled the calculation of ΔH_f for $CaCu(OAc)_4 \cdot 6H_2O$ and $CaCd(OAc)_4 \cdot 6H_2O$ from hydrated calcium acetate, in a process corresponding to the second step of the herein reported two-step mechanochemical synthesis starting from either $CaCO_3$ or $Ca(OH)_2$. The calculation of the enthalpy of formation of the intermediates and the enthalpy of formation of $CaCu(OAc)_4 \cdot 6H_2O$ and $CaCd(OAc)_4 \cdot 6H_2O$ from the intermediates were performed following the thermodynamic cycle presented in **Table 2-6**:

Table 2-6. Thermodynamic cycle used to calculate the formation enthalpy of the intermediates and $CaCu(OAc)_4 \cdot 6H_2O$ and $CaCd(OAc)_4 \cdot 6H_2O$ from intermediates

Formation of $Ca(OAc)_2.H_2O.AcOH$ intermediate from $CaCO_3$	
Reactions	Enthalpy (ΔH, kJ mol^{-1})
$Ca(OAc)_2.H_2O.AcOH_{(s)} \rightarrow Ca^{2+}_{(aq)} + 3\ OAc^-_{(aq)} + H_2O_{(aq)} + H^+_{(aq)}$	ΔH_1
$CaCO_{3(s)} + 2H^+_{(aq)} \rightarrow Ca^{2+}_{(aq)} + H_2O_{(aq)} + CO_{2(g)}$	ΔH_2
$AcOH_{(l)} \rightarrow OAc^-_{(aq)} + H^+_{(aq)}$	ΔH_3
$CaCO_{3(s)} + 3AcOH_{(l)} \rightarrow Ca(OAc)_2.H_2O.AcOH_{(s)} + CO_{2(g)}$	$\Delta H_f = -\Delta H_1 + \Delta H_2 + 3\Delta H_3$

Formation of $Ca(OAc)_2.1.1H_2O$ intermediate from $CaCO_3$	
Reactions	Enthalpy (ΔH, kJ mol^{-1})
$Ca(OAc)_2.1.1H_2O_{(s)} \rightarrow Ca^{2+}_{(aq)} + 2OAc^-_{(aq)} + 1.1H_2O_{(aq)}$	ΔH_1
$CaCO_{3(s)} + 2H^+_{(aq)} \rightarrow Ca^{2+}_{(aq)} + H_2O_{(aq)} + CO_{2(g)}$	ΔH_2
$AcOH_{(l)} \rightarrow OAc^-_{(aq)} + H^+_{(aq)}$	ΔH_3
$H_2O_{(l)} \rightarrow H_2O_{(aq)}$	ΔH_4
$CaCO_{3(s)} + 3AcOH_{(l)} \rightarrow Ca(OAc)_2.H_2O.AcOH_{(s)} + CO_{2(g)}$	$\Delta H_f = -\Delta H_1 + \Delta H_2 + 2\Delta H_3 + 0.1\Delta H_4$

Table 2-6. Continued

Formation of $Ca(OAc)_2.1.1H_2O$ from $Ca(OAc)_2.H_2O.AcOH$

Reactions	Enthalpy (ΔH, kJ mol^{-1})
$Ca(OAc)_2.1.1H_2O_{(s)} \rightarrow Ca^{2+}_{(aq)} + 2OAc^-_{(aq)} + 1.1H_2O_{(aq)}$	ΔH_1
$Ca(OAc)_2.H_2O.AcOH_{(s)} \rightarrow Ca^{2+}_{(aq)} + 3\,OAc^-_{(aq)} + H_2O_{(aq)} + H^+_{(aq)}$	ΔH_2
$AcOH_{(l)} \rightarrow OAc^-_{(aq)} + H^+_{(aq)}$	ΔH_3
$H_2O_{(l)} \rightarrow H_2O_{(aq)}$	ΔH_4
$Ca(OAc)_2.H_2O.AcOH_{(s)} + 0.1H_2O_{(l)} \rightarrow Ca(OAc)_2.1.1H_2O_{(s)} +$ $AcOH_{(l)}$	$\Delta H_f = -\Delta H_1 + \Delta H_2 - \Delta H_3 +$ $0.1\Delta H_4$

Formation of $MCa(OAc)_4.6H_2O$ from $Ca(OAc)_2.H_2O.AcOH$ intermediate

Reactions	Enthalpy (ΔH, kJ mol^{-1})
$MCa(OAc)_4.6H_2O_{(s)} \rightarrow M^{2+}_{(aq)} + Ca^{2+}_{(aq)} + 4\,OAc^-_{(aq)} + 6H_2O_{(aq)}$	ΔH_1
$Ca(OAc)_2.H_2O.AcOH_{(s)} \rightarrow Ca^{2+}_{(aq)} + 3\,OAc^-_{(aq)} + H_2O_{(aq)} + H^+_{(aq)}$	ΔH_2
$M(OAc)_2.xH_2O_{(s)} \rightarrow M^{2+}_{(aq)} + 2OAc^-_{(aq)} + xH_2O_{(aq)}$	ΔH_3
$AcOH_{(l)} \rightarrow OAc^-_{(aq)} + H^+_{(aq)}$	ΔH_4
$H_2O_{(l)} \rightarrow H_2O_{(aq)}$	ΔH_5
$Ca(OAc)_2.H_2O.AcOH_{(s)} + M(OAc)_2.xH_2O_{(s)} + (5-x)H_2O_{(l)} \rightarrow$ $MCa(OAc)_4.6H_2O_{(s)} + AcOH_{(l)}$	$\Delta H_f = -\Delta H_1 + \Delta H_2 + \Delta H_3$ $- \Delta H_4 + 4\Delta H_5$

^{a}M = Cu and Cd; x = 1 for Cu and 2 for Cd

An energy diagram explaining the reaction steps that occur during the formation of $CaCu(OAc)_4 \cdot 6H_2O$ is given in **Figure 2-10**. It is drawn to conserve mass in all the reactions; thus, excess acetic acid and carbon dioxide appear in the final products together with the paceite. The top diagram shows the reaction steps when $CaCO_3$ is first milled with acetic acid to form $Ca(OAc)_2 \cdot H_2O \cdot AcOH$, followed by formation of $Ca(OAc)_2 \cdot 1.1H_2O$, which is then followed by

subsequent milling with $Cu(OAc)_2 \cdot H_2O$ to form paceite. Formation of the first intermediate $Ca(OAc)_2 \cdot H_2O \cdot AcOH$ was seen after short milling times, and the ease of this reaction is supported here by the exothermic enthalpy change (-16.62 ± 0.23 kJ/mol). The formation of $Ca(OAc)_2 \cdot 1.1H_2O$ is accompanied by an endothermic enthalpy change (20.94 ± 0.35 kJ/mol), which results in an intermediate that has higher energy than the reactants. The highly endothermic enthalpy is consistent with longer milling times required for the synthesis of calcium acetate monohydrate and with the loss of CO_2 gas or other volatile reaction components, where a large positive entropy can compensate for the positive enthalpy to make the overall reaction favorable in free energy. The last step of paceite formation from $Ca(OAc)_2 \cdot 1.1H_2O$ is accompanied by a strong exothermic enthalpy change of -31.45 ± 0.25 kJ/mol.
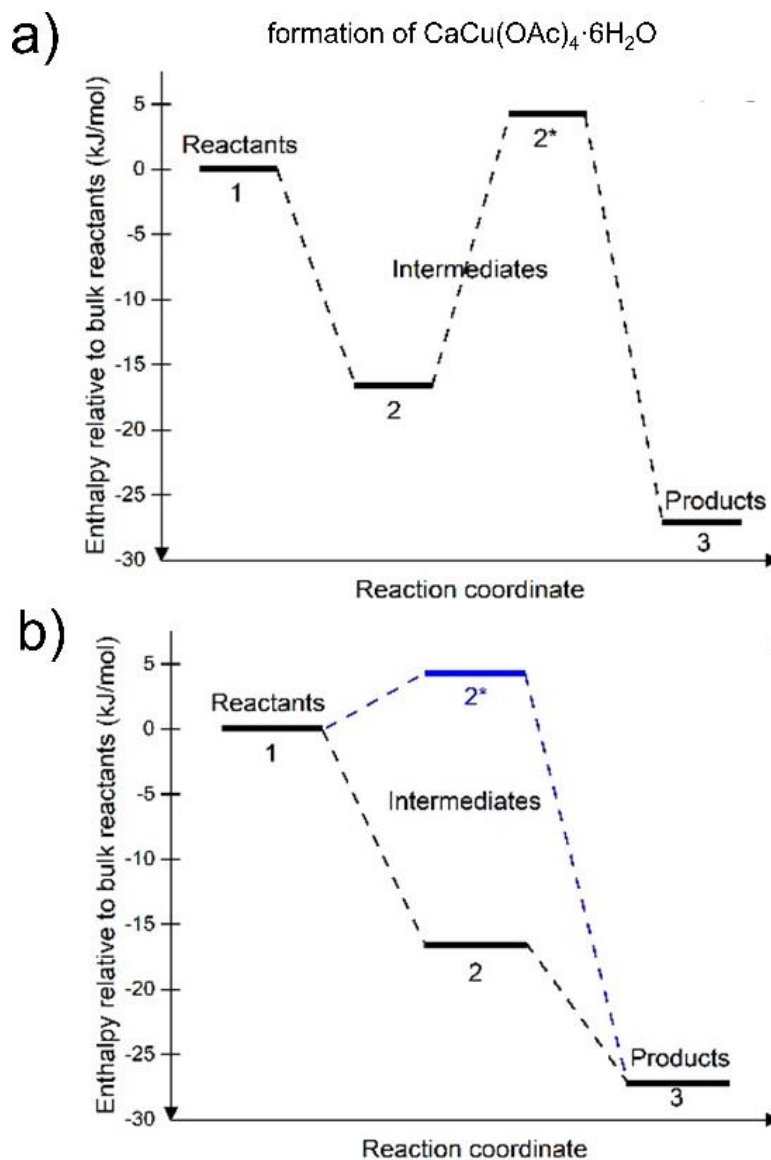
Figure 2-10. Energy diagram for the formation reaction of $CaCu(OAc)_2 \cdot 6H_2O$ from $CaCO_3$ and $Cu(OAc)_2 \cdot H_2O$ by considering the participation of either: (top) both intermediates or (bottom) one intermediate. Each step corresponds to one of the following compositions:

(1) $Cu(OAc)2 \cdot H2O(s) + CaCO_{3(s)} + 3AcOH_{(l)} + 4H_2O_{(l)}$;

(2) $Cu(OAc)2 \cdot H2O(s) + Ca(OAc)_2 \cdot H_2O \cdot AcOH_{(s)} + CO_{2(g)} + 4H_2O_{(l)}$;

(2*) $Cu(OAc)2 \cdot H2O(s) + Ca(OAc)_2 \cdot 1.1H_2O_{(s)} + CO_{2(g)} + \quad AcOH_{(l)} + 3.9H_2O_{(l)}$ and

(3) $CuCa(OAc)4 \cdot 6H2O(s) + AcOH_{(l)} + CO_{2(g)}$.
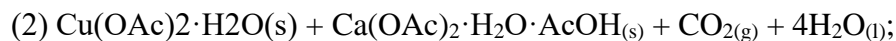
Comparison of the formation of paceite directly from either of the intermediates can be seen in the bottom diagram in **Figure 2-10**. There, the black line indicates the formation through the $Ca(OAc)_2 \cdot H_2O \cdot AcOH$ intermediate, while the blue line indicates the formation through the $Ca(OAc)_2 \cdot 1.1H_2O$ intermediate. It can be seen that the $Ca(OAc)_2 \cdot 1.1H_2O$ intermediate has higher enthalpy than the bulk reactants, compared to the other intermediate that has lower enthalpy than the reactants. The formation of $Ca(OAc)_2 \cdot 1.1H_2O$ is accompanied by a small positive enthalpy change of 4.32 ± 0.27 kJ/mol. Based on these two figures, the pathway with the formation of $Ca(OAc)_2 \cdot H_2O \cdot AcOH$ appears to be the more favorable one because the intermediate lies energetically between the reactants and the products, slightly closer to the products. The reactions proceed toward lower energy and more stable forms, where the first reaction step forming the intermediate is accompanied by an enthalpy change of -16.62 ± 0.23 kJ/mol and the subsequent step of paceite formation is accompanied by an enthalpy change of -10.51 ± 0.20 kJ/mol.

Analogous diagrams for the cadmium analogue of paceite are given in **Figure 2-11**. The intermediates also have the same energy as previously, because their formation does not depend on the presence of copper(II) or cadmium acetate. In the bottom diagram, an interesting behavior is observed. The product has essentially the same enthalpy as the $Ca(OAc)_2 \cdot H_2O \cdot AcOH$ intermediate or perhaps slightly higher. The formation reaction of the product from $Ca(OAc)_2 \cdot H_2O \cdot AcOH$ is accompanied by an enthalpy change of 0.48 ± 0.29 kJ/mol, that is, essentially zero. Thus, while $Ca(OAc)_2 \cdot H_2O \cdot AcOH$ is indeed an intermediate in enthalpy between reactants and products in the case of $CaCu(OAc)_4 \cdot 6H_2O$, for $CaCd(OAc)_4 \cdot 6H_2O$ it appears to be essentially the same in enthalpy as the final product. The reason for this difference is not yet clear.
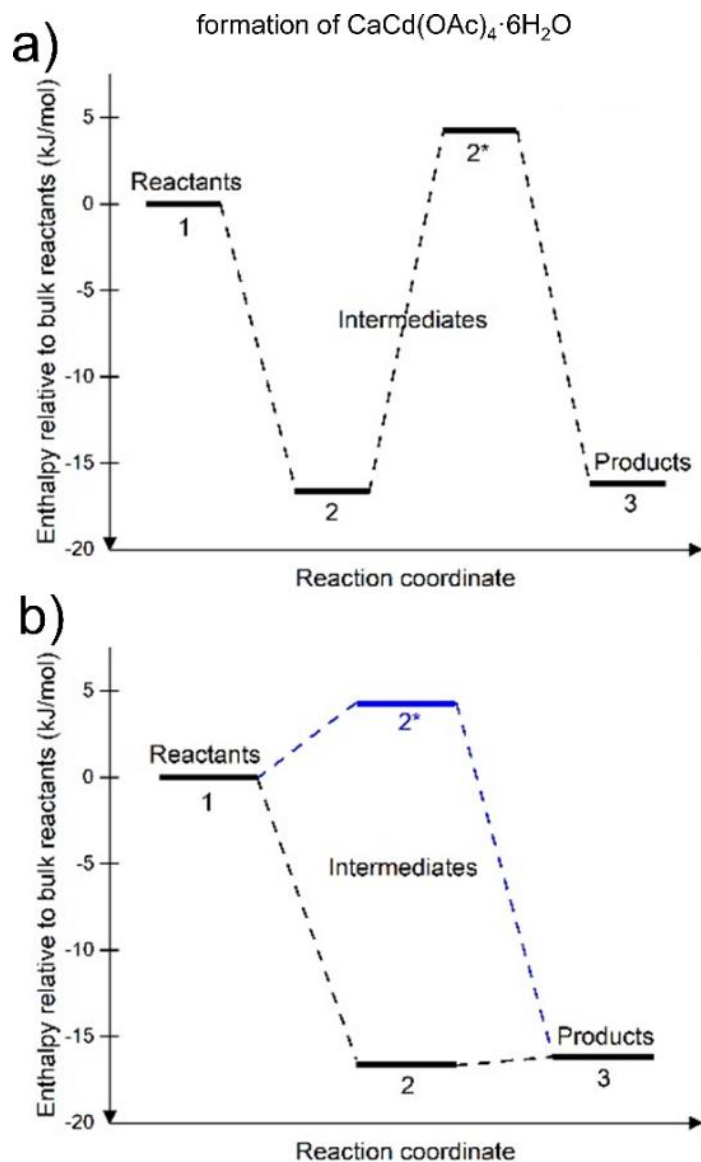
Figure 2-11. Energy diagram of the formation reaction of $CaCd(OAc)_2 \cdot 6H_2O$ from $CaCO_3$ and $Cd(OAc)_2 \cdot 2H_2O$ by considering the participation of either: (top) both intermediates or (bottom) one intermediate. Each step corresponds to one of the following compositions:

(1) $Cd(OAc)2 \cdot 2H2O(s) + CaCO_{3(s)} + 3AcOH_{(l)} + 3H_2O_{(l)}$;

(2) $Cd(OAc)2 \cdot 2H2O(s) + Ca(OAc)_2 \cdot H_2O \cdot AcOH_{(s)} + CO_{2(g)} + 3H_2O_{(l)}$;

(2*) $Cd(OAc)2 \cdot 2H2O(s) + Ca(OAc)_2 \cdot 1.1H_2O_{(s)} + CO_{2(g)} + AcOH_{(l)} + 2.9H_2O_{(l)}$;

(3) $CdCa(OAc)4 \cdot 6H2O(s) + AcOH_{(l)} + CO_{2(g)}$.

48
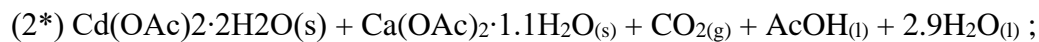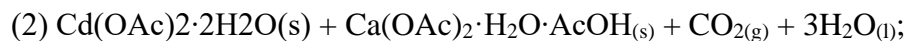
2.5   Conclusions

We have demonstrated the use of mechanochemistry for the rapid, simple, and materials-efficient preparation of synthetic samples of the organic mineral paceite and its cadmium analogue, $CaCd(OAc)_4 \cdot 6H_2O$. Importantly, while the synthesis of synthetic paceite from aqueous solutions containing copper(II) acetate and calcium acetate requires the use of an approximately 4-fold excess of the calcium reagent, mechanochemistry permits the synthesis of this material using only stoichiometric amounts of metal precursors. Furthermore, the use of mechanochemical techniques also permitted the use of readily available calcium hydroxide or carbonate as a source of Ca^{2+}, which would be difficult to achieve using simple solution-based chemistry. Consequently, the described mechanochemical approaches illustrate the benefits of ball milling mechanochemistry in improving the control over product stoichiometry in the synthesis of coordination polymers based on two different types of metal centers and in expanding the scope of starting materials in such syntheses to poorly soluble solids. At the same time, these syntheses of synthetic paceite illustrate a poorly explored, but fast, simple, and efficient route for making synthetic samples of organic minerals. This is expected to be of high value for studies of very rare mineral species, such as hoganite, paceite, and other organic minerals. The exploration of mechanochemical reactivity also led to hints at how analogous reactions could take place in a non- agitated system by aging of reactant mixtures at high humidity and mild temperature. Such accelerated aging experiments, which mimic mineral weathering processes in a geological environment, provide a potential route for the formation of organic minerals. Importantly, thermodynamic studies based on acid dissolution calorimetry confirm that the mechanochemical syntheses of synthetic paceite and analogous aging reactions, involving known mineral species $Cu(OAc)_2 \cdot H_2O$ (hoganite) and $CaCO_3$

(calcite), are highly exothermic. It is expected that the exothermic nature of such transformations provides sufficient driving force for the formation of paceite in a natural environment.

2.6   Acknowledgments

2.7   References

(1)   Echigo, T.; Kimata, M. Crystal chemistry and genesis of organic minerals: a review of oxalate and polycyclic aromatic hydrocarbon minerals. *Canad. Mineral.* **2010**, *48*, 1329-1358.

(2)   Huskić, I.; Friščić, T. Understanding geology through crystal engineering: coordination complexes, coordination polymers and metal-organic frameworks as minerals. *Acta Crystallogr. B.* **2018**, *74*, 539-559.

(3)   Clarke, R. M,.; Williams, I. R. Moolooite, a naturally occurring hydrated copper oxalate from Western Australia. *Min. Mag.***1986**, *50*, 295-298.

(4)   Guastoni, A.; Nestola, F.; Gentile, P.; Zorzi, F.; Alvaro, M.; Lanza, A.; Perutto, L.; Shiazza, M.; Casati, N. M. Deveroite-(Ce): a new REE-oxalate from Mount Cervandone, Devero Valley, Western-Central Alps, Italy. *Min. Mag.* **2013**, *77*, 3019-3026.

(5)   Vranova, V.; Rejsek, K.; Formanek, P. *Sci. World J.* **2013**, 524239.

(6)   Giacovazzo, C.; Menchetti, S; Scordari, F. The crystal structure of mellite. *Acta Crystallogr. Sect. B*. **1973**, *29*, 26–31.

(7)   Bridge, P. J. Guanine and uricite, two new organic minerals from Peru and Western Australia. *Min. Mag.* **1974**, *39*, 889-890.

(8)   Pekov, I.V.; Chukanov, N.V.; Belakovskiy, D.I.; Lykova, I.S.; Yapaskurt, V.O.; Zubkova, N.V.; Shcherbakova, E.P.; Britvin, S.N. Tinnunculite, IMA 2015-021a. CNMNC Newsletter No. 29, February 2016, page 202. *Min. Mag.* **2016**, *80*, 199–205.

(9)   Piro, O. E.; Baran, E. J. Crystal chemistry of organic minerals – salts of organic acids: the synthetic approach. *Crystallogr. Rev.* **2018**, *24*, 149-175.

(10)   Hazen, R. M.; Hummer, D. R.; Hystad, G.; Downs, R. T.; Golden, J. J. Carbon mineral ecology: predicting the undiscovered minerals of carbon. *Amer. Mineral.* **2016**, *101*, 889-906.

(11)   https://mineralchallenge.net/ Webpage accesed: Jan 21st 2019

(12)   Hummer, D. R.; Noll, B. C.; Hazen, R. M.; Downs, R. T. Crystal structure of abelsonite, the only known crystalline geoporphyrin. *Amer. Mineral.* **2017**, *102*, 1129-1132.

(13)   Huskić, I.; Pekov, I. V.; Krivovichev, S. V.; Friščić, T. Minerals with metal-organic framework structures. *Sci. Adv.* **2016**, *2*:e1600621.

(14) Piro, O. E.; Echeverría, G. A.; González-Baró, A. C.; Baran, E. J. Crystal and molecular structure and spectroscopic behavior of isotypic synthetic analogs of the oxalate minerals stepanovite and zhemchuzhnikovite. *Phys. Chem. Min.* **2016**, *43*, 287-300.

(15) Friščić, T. Supramolecular concepts and new techniques in mechanochemistry: cocrystals, cages, rotaxanes, open metal-organic frameworks. *Chem. Soc. Rev.* **2012**, *41*, 3493-3510.

(16) Maynard-Casely, H. E.; Hodyss, R.; Cable, M. L.; Vu, T. H.; Rahm, M. A co-crystal between benzene and ethane: a potential evaporite material for Saturn's moon Titan. *IUCrJ*, **2016**, *3*, 192–199.

(17) Hibbs, D.E.; Kolitsch, U.; Leverett, P.; Sharpe, J. L.; Williams, P. A. Hoganite and paceite, two new acetate minerals from the Potosi mine, Broken Hill, Australia. *Min. Mag.* **2002**, *66*, 459–464.

(18) Furukawa, H.; Cordova, K. E.; O'Keeffe, M.; Yaghi, O. M. The chemistry and applications of metal-organic frameworks. *Science*, **2013**, *341*, 974.

(19) Holden, A.; Singer, P. Crystals and crystal growing. Anchor Books, Doubleday, Garden City, New York (1960).

(20) Langs, D. A; Hare, C. R. The crystal structure of calcium copper acetate hexahydrate and its isomorph calcium cadmium acetate hexahydrate. *Chem. Commun.* **1967**, 890-891.

(21) Klop, A. E.; Duisenberg, A. J. M.; Spek, A. L. Reinvestigation of the structure of calcium copper acetate hexahydrate, $CaCu(C_2H_3O_2).6H_2O$. *Acta Cryst. C*, **1983**, *39*, 1342-1344.

(22) El-Bali, B.; Bolte, M. Redetermination of $[CaCu(C_2H_3O_2)_4(H_2O)_2]\cdot6H_2O$ at 173 K. *Acta Cryst. C*, **1999**, *55*, IUC9900015.

(23) Furukawa, H.; Müller, U.; Yaghi, O. M. "Heterogeneity within Order" in Metal–Organic Frameworks. *Angew. Chem. Inter. Ed*. **2015,** *54*, 3417-3430.

(24) Wang, L. J.; Deng, H.; Furukawa, H.; Gándara, F.; Cordova, K. E.; Peri, D.; Yaghi, O. M. Synthesis and characterization of metal-organic framework-74 containing 2, 4, 6, 8, and 10 different metals. *Inorg. Chem.* **2014,** *53*, 5881-5883.

(25) Castillo-Blas, C.; de la Peña, V. A.; Puente-Orech, I.; de Paz, J. R.; Sáez-Puche, R.; Gutiérrez-Puebla, E.; Gándara, F.; Monge, Á. Addressed realization of multication complex arrangements in metal-organic frameworks. *Sci. Adv.* **2017**, *3*:e1700773.

(26) Balarew, C.; Stoilova, D. R elation between the crystal structures of some salts of the type $Me(OCOCH_3)_2\cdot nH_2O$ and their ability to form mixed crystals or double salts (Me^{2+} = Mg, Ca, Mn, Co, Ni, Cu, Zn, Cd). *J. Solid State Chem.* **1981**, *38*, 192-198.

(27) Huskić, I.; Friščić, T. Naturally occuring metal-organic frameworks. *Acta Cryst. A*, **2015**, *71*, s57-s58.

(28) James, S. L.; Adams, C. J.; Bolm, C.; Braga, D.; Collier, P.; Friščić, T.; Grepioni, F.; Harris, K. D. M.; Hyett, G.; Jones, W.; Krebs, A.; Mack, J.; Maini, L.; Orpen, A. G.; Parkin, I. P.; Shearouse, W. C.; Steed, J. W.; Waddell, D. C. Mechanochemistry: opportunities for new and cleaner synthesis. *Chem. Soc. Rev.* **2012**, *41*, 413-447.

(29) Mottillo, C.; Friščić, T. Advances in solid-state transformations of coordination bonds: from the ball mill to the aging chamber. *Molecules* **2017**, *22*, 144.

(30) Huskic, I.; Christopherson, J.-C.; Uzarevic, K.; Friščić, T. In situ monitoring of vapour-induced assembly of pharmaceutical cocrystals using a benchtop powder X-ray diffractometer. *Chem. Commun*. **2016**, *52*, 5120−5123.

(31) Coelho, A. TOPAS-Academic: Version 6; Coelho Software: Brisbane, Australia July, 2016

(32)   Akimbekov, Z.; Katsenis, A. D.; Nagabhushana, G. P.; Ayoub, G.; Arhangelskis, M.; Morris, A. J.; Friščić, T.; Navrotsky, A. Experimental and theoretical evaluation of the stability of true MOF polymorphs explains their mechanochemical interconversions. *J. Am. Chem. Soc.* **2017**, *139*, 7952−7957

(33)   Štrukil, V.; Fábián, L.; Reid, D. G.; Duer, M. J.; Jackson, G. J.; Eckert-Maksić, M.; Friščić, T. Towards an environmentally-friendly laboratory: dimensionality and reactivity in the mechanosynthesis of metal-organic compounds. *Chem. Commun.* **2010**, *46*, 9191-9193.

(34)   Karki, S.; Friščić, T.; Jones, W. Control and interconversion of cocrystal stoichiometry by grinding: stepwise mechanism for the formation of a hydrogen-bonded cocrystal. *CrystEngComm* **2009**, *11*, 470-481

(35)   Friščić, T.; Childs, S. L.; Rizvi, S. A. A.; Jones, W. The role of solvent in mechanochemical and sonochemical cocrystal formation: a solubility-based approach for predicting cocrystallisation outcome. *CrystEngComm* **2009**, *11*, 418-426.

(36)   Friščić, T.; Halasz, I.; Strobridge, F. C.; Dinnebier, R. E.; Stein, R. S.; Fábián, L.; Curfs, C. A rational approach to screen for hydrated forms of the pharmaceutical derivative magnesium naproxen using liquid-assisted grinding. *CrystEngComm* **2011**, *13*, 3125-3129.

(37)   Strobridge, F. C.; Judaš, N.; Friščić, T. A stepwise mechanism and the role of the liquid phase in the liquid-assisted grinding synthesis of metal-organic materials. *CrystEngComm* **2010**, *12*, 2409-2418.

(38)   Beldon, P. J.; Fábián, L.; Stein, R. S.; Thirumurugan, A.; Cheetham, A.K.; Friščić, T. Rapid room-temperature synthesis of zeolitic imidazolate frameworks using mechanochemistry. *Angew. Chem. Int. Ed.* **2010**, *49*, 9640-9643.

(39)   Bolm, C.; Mocci, R.; Schumacher, C.; Turberg, M.; Puccetti, F.; Hernández, J. G. Mechanochemical activation of iron cyano complexes: a prebiotic impact scenario for the synthesis of α-amino acid derivatives. *Angew. Chem. Int. Ed.* 2018, *57*, 2423-2426.

(40)   Qi, F.; Stein, R. S.; Friščić, T. Mimicking mineral neogenesis for the clean synthesis of metal-organic materials from mineral feedstocks: coordination polymers, MOFs and metal oxide separation. *Green Chem.* **2014*, 16,* 121-132

(41)   Banfield, J. F.; Barker, W. W.; Welch, S. A.; Taunton, A. Biological impact on mineral dissolution: Application of the lichen model to understanding mineral weathering in the rhizosphere. *Proc. Natl. Acad. Sci. U. S. A.* **1999**, *96*, 3404–3411.

(42)   Lisac, K.; Nemec, V.; Topić, F.; Arhangelskis, M.; Hindle, P.; Tran, R.; Huskić, I.; Friščić, T.; Cinčić, D. Experimental and theoretical investigation of structures, stoichiometric diversity and bench stability of cocrystals with a volatile halogen bond donor. *Cryst. Growth Des.* **2018**, *18*, 2387-2396.

(43)   Hughes, J. T.; Bennett, T. D.; Cheetham, A. K.; Navrotsky, A. Thermochemistry of Zeolitic Imidazolate Frameworks of Varying Porosity. *J. Am. Chem. Soc*. **2013**, 135, 2, 598–601.

(44)   Hughes, J. T.; Navrotsky, A. Enthalpy of Formation of Zinc Acetate Dihydrate. *J. Chem. Thermodyn*. **2011**, 43, 6, 980–982.

(45)   Parker, V. B. Thermal Properties of Aqueoues Uni-Univalent Electrolytes; Dept. of Commerce, National Bureau of Standards: Washington, D.C., U.S., **1965**.

(46)   Harrison, W.; Trotter, J. Crystal and Molecular Structure of Cadmium Diacetate Dihydrate. *J. Chem. Soc. Dalt. Trans*. **1972**, No. 8–9, 956–960.

(47)   Brown, G. M.; Chidambaram, R. Dinuclear Copper(II) Acetate Monohydrate: A Redetermination of the Structure by Neutron-Diffraction Analysis. *Acta Crystallogr. B* **1973**, 29, 11, 2393–2403.

Chapter 3:

Thermodynamics of Hybrid Manganese Formate Perovskites

Novendra, N.; Nagabhushana, G. P.; Navrotsky, A *(in preparation)*

3.1   Abstract

Hybrid organic-inorganic materials, both dense and porous, have gained significant attention in recent years due to their extreme tunability in both compositions and functional properties. A deep understanding of their intrinsic stability would be crucial to accelerate the discovery of new compositions that are not only functional but also thermodynamically stable. Here, we report the first systematic experimental study on the effect of A-site cations on the thermodynamic stability of hybrid perovskites using a series of manganese formate perovskites $[AmineH^+]Mn[HCOO]_3$ with $AmineH^+ = NH_4^+$, $CH_3NH_3^+$, $(CH_3)_2NH_2^+$, $(CH_2)_3NH_2^+$, $CH(NH_2)_2^+$, and $C(NH_2)_3^+$. Their thermodynamic stability is presented as the enthalpy of formations, calculated based on the measurement performed on a room temperature acid solution calorimetry. The stability trend of this protonated-amine manganese formate perovskite series was found to be independent of their tolerance factors, unlike what has been seen previously with other inorganic perovskites. We show that the perovskite enthalpy of formation correlates linearly to their corresponding A-site cation salts enthalpy of dissolution, suggesting that the interactions between the A-site cation and the framework dominate the energetics of the perovskite stability, rather than the geometric factor.

3.2 Introduction

The term perovskite has been accepted for a wide class of materials that have a similar structure to the mineral $CaTiO_3$. This structure has a general formula of ABX_3, where A is a cation located at the cavities of the framework constructed by the B cation and X anions, typically halogens or oxygen. In this structure, the A-site cation is twelve-coordinated, while the B-site cation is six-coordinated by the X-site anion to form a BX_6 octahedron. These octahedrons are corner shared, forming the 3D framework[1]. Hybrid organic-inorganic perovskites (HOIP) can be defined as a subset of the perovskite family in which the cation in A-site and/or the anion in X-site is replaced by organic amine cations and/or organic linkers respectively. The introduction of organic components to this structure provides new functionalities and structural flexibilities that are previously unattainable with inorganic perovskites[2–4]. Additionally, the introduction of more organic components to the X-site allows the structure to be also characterized as a dense metal-organic framework.

The first discovered and characterized hybrid perovskite structure was cubic methylammonium lead halide ($MAPbX_3$, X=Cl, Br or I)[5,6]. This structure gained massive popularity in the following years due to the promising properties of high optical absorption, benign grain boundaries, high carrier mobility and narrow bandgap, which together allow its application in high-performance photovoltaic operations. Since then, several different types of other HOIPs have been synthesized with different organic amine cations in the A-site, such as methylammonium ($CH_3NH_3^+$), formamidinium ($CH(NH_2)_2^+$), and dimethylammonium ($(CH_3)_2NH_2^+$), and molecular linkers on the X-site, such as azide (N_3^-), cyanide (CN^-), formate ($HCOO^-$) and borohydride (BH_4^-)[2,7–10].

Different thermodynamic studies have been performed on hybrid perovskites, both experimentally and theoretically, to understand their stability and the effect of their compositions on the overall stability[11–17]. However, throughout these studies, the effect of molecular A-site cation on the thermodynamic stability of the hybrid perovskite has not been explored systematically. AmineH$^+$ cation on the A-site has been shown to have an interesting contribution to the hybrid perovskite properties, affecting the crystal structure due to the different cation sizes and charge compensation, modifying the electronic properties due to the mobility of the cation, and changing the mechanical properties due to the presence of hydrogen bonding.[18–22] In this study, the role of the AmineH$^+$ cation on the resulting stability of the hybrid perovskite was studied systematically using room temperature isothermal acid solution calorimetry for the first time. The system chosen for this study is a manganese formate perovskite series with formate ion (HCOO$^-$) on the X site, or [AmineH$^+$]Mn[HCOO]$_3$ (**Figure 3-1**). This class of materials has very interesting functional properties, such as ferromagnetism, ferroelectricity, ferroelasticity and multiferroicity[23–27]. The presence of medium-sized formate anions on the [AmineH$^+$]Mn[HCOO]$_3$ (indicated by AmineH$^+$-Mn-F from this point forward) allows the incorporation of a wider array of AmineH$^+$ into the structure. Here we report the synthesis, characterization, and calculation of enthalpy of formations of different AmineH$^+$-Mn-F structures, where AmineH$^+$ = ammonium (AM) (NH$_4^+$), methylammonium (MA) (CH$_3$NH$_3^+$), dimethylammonium (DMA) ((CH$_3$)$_2$NH$_2^+$), azetidinium (AZE) ((CH$_2$)$_3$NH$_2^+$), formamidinium (FA) (CH(NH$_2$)$_2^+$), and guanidinium (GUA) (C(NH$_2$)$_3^+$). The energetics revealed that the stability of hybrid perovskites, unlike their inorganic counterpart, is not influenced strongly by the geometric mismatch explained by the tolerance factor. Instead, we show that the stability is more strongly related to the interaction between the cation and the framework, and this could be related simply to the dissolution enthalpy of the cation salts on HCl.

55
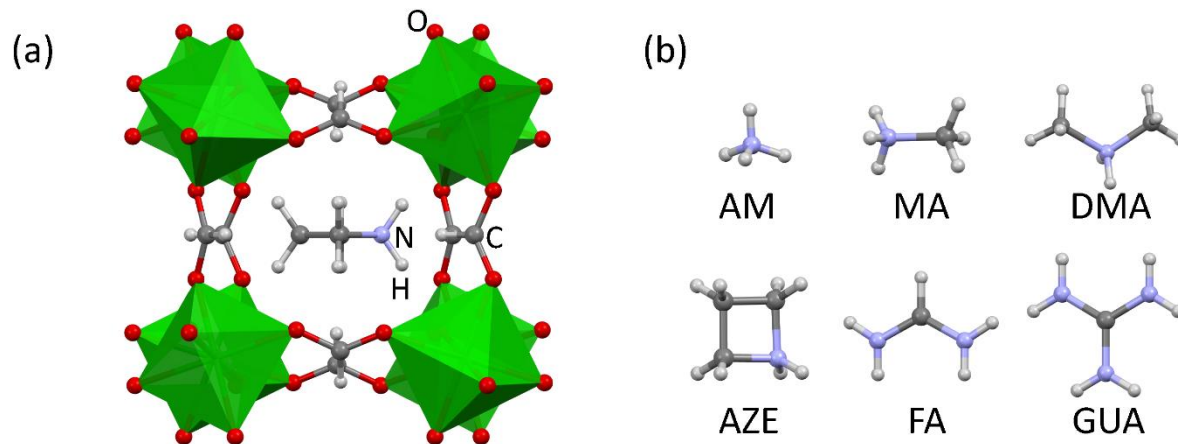
Figure 3-1. (a) Perovskite framework structure of AZE-Mn-F. (b) AmineH$^+$ cations studied in this work: ammonium (AM) (NH$_4^+$), methylammonium (MA) (CH$_3$NH$_3^+$), dimethylammonium (DMA) ((CH$_3$)$_2$NH$_2^+$), azetidinium (AZE) ((CH$_2$)$_3$NH$_2^+$), formamidinium (FA) (CH(NH$_2$)$_2^+$), and guanidinium (GUA) (C(NH$_2$)$_3^+$). Color scheme: Mn is green, O is red, N is purple, C is gray, and H is white.

3.3   Experimental Methods

3.3.1 Synthesis

All chemicals used for the synthesis process were commercially available and used without any further purification. We previously reported the synthesis, characterization and calorimetric measurements of DMA-Mn-F[14], and those calorimetric data are used in this report. AM-Mn-F was synthesized by the reaction of MnCl$_2$·4H$_2$O solution in methanol with ammonium hydroxide and formic acid solution in methanol. In a typical experiment, 203 mg of MnCl$_2$·4H$_2$O was dissolved in 10 mL of methanol and mixed with 5.5 ml 0.8 M solution of [NH$_4$][HCOO] in methanol (prepared by mixing 0.29 ml of ammonium hydroxide and 0.22 ml of formic acid with 4.99 ml of

methanol). The mixed solution was left covered and undisturbed. The crystals were obtained after 1 day and washed with methanol[28].

MA-Mn-F and AZE-Mn-F samples were synthesized with a solution diffusion method. In a typical experiment, 5 ml methanol solution of 0.5 M formic acid and 0.5 M of methylamine or azetidine respectively was placed at the bottom of a glass tube. 2 ml of methanol was layered on top of this solution carefully and on the upmost layer, 8 ml of 0.1 M $MnCl_2$ solution in methanol was placed carefully. The tube was sealed and left undisturbed. The crystals were collected after a week and washed with methanol[29].

FA-Mn-F was prepared by a solvothermal method. In a typical experiment, 1.05 g of $MnCl_2 \cdot 4H_2O$ was dissolved in a mixture of 0.5 ml of ethanol, 0.5 ml of water, and 0.15 ml of formic acid with 10 ml of formamide. The solution was sealed and kept undisturbed at 130 ^{o}C. Crystals formation were observed after a day and the crystals were collected after 2 days and washed with formamide. This synthesis method is an adaptation of the previously reported synthesis of DMA-Mn-F[14].

GUA-Mn-F was prepared by mixing 10 ml aqueous solution of 1.0mmol $Mn(ClO_4)_2 \cdot 6H_2O$ with 20 ml aqueous solution of 8.7 mmol formic acid and 4.2 mmol $[C(NH_2)_3]_2CO_3$. The mixture was left undisturbed and let to evaporate over time. The crystals were collected after 3 days and washed with ethanol[30].

3.3.2 Characterization

Powder X-ray diffraction (PXRD) data of the samples were recorded at room temperature by Bruker-AXS D8 Advance diffractometer using Cu-Kα radiation (λ = 1.54060 Å) operated at 40 kV and 40 mA. The scans were collected in the range of 10 to 70 ^{O} 2θ with a step size of 0.02 ^{O} by using a zero-background sample holder. Thermogravimetric analysis (TG) was conducted by

57

using Netzsch 449 TG/DSC system. The measurement was done in a platinum crucible at a temperature range of 30-600 $^{\circ}$C and a heating rate of 10 $^{\circ}$C·min^{-1} under a mixture of argon and oxygen atmosphere (40 ml·min^{-1} flow rate). Fourier transform infrared spectroscopy (FTIR) measurement was done with a Bruker Equinox 55 system and the data were collected in the range of 400 - 4000 cm^{-1}.

3.3.3 Isothermal Acid Solution Calorimetry

Room temperature solution calorimetry measurement was conducted using a CSC (Calorimetry Sciences Corporation) 4400 isothermal microcalorimeter at 25 $^{\circ}$C. The data collection and device operation were done by using IMC data acquisition software. In each experiment, typically 15 mg of the sample was hand pressed to form a pellet and dropped into a Teflon cell in the calorimeter, filled with 25.0 g of 5M HCl solvent. All weight measurements were done using a Mettler microbalance with an accuracy of 10 µg. The solvent was isothermally equilibrated for at least 3 hours under mechanical stirring before the introduction of the sample, and the sample was allowed to dissolve in the cell for at least 3 hours, ensuring the return of signal back to its initial position. After each experiment, the cell was reassembled with fresh solvent.

The collected data was integrated with a baseline correction in OriginPro 8.5 software, which was then converted to joules using a calibration factor, to obtain the total heat effect due to the dissolution of the sample. To obtain the calibration factor, a NIST standard reference material KCl was used. The calibration was done by dissolving a 15 mg KCl pellet into 25 g of H_2O, which corresponds to a reference concentration of 0.008 mol·kg^{-1} at 25 $^{\circ}$C. The calibration factor was obtained by correlating the integrated data with a known enthalpy of dissolution and dilution of 0.008 mol·kg^{-1} KCl[31]. For each sample, at least 4 measurements were performed, and their average

was reported as the final value. The uncertainties given represents the 95 % confidence interval. This experimental method is the same as the one used in our earlier study of metal-organic frameworks[14,32,33].

3.4 Results and Discussion

The characterization of AM-Mn-F, MA-Mn-F, AZE-Mn-F, FA-Mn-F and GUA-Mn-F will be discussed in detail here, while the result for DMA-Mn-F was previously reported[14]. PXRD analysis was performed on the synthesized samples to confirm the formation of the intended phase, and the PXRD patterns of all [AmineH$^+$]Mn[HCOO]$_3$ samples are given in **Figure 3-2**. Whole pattern fitting using the published crystal structures of each sample was performed using MDI Jade 6.5 software. The result confirmed the formation of single phases, and the lattice parameters are given in Table 3-1.

Table 3-1. Lattice parameters of the AmineH$^+$-Mn-F samples.

Sample	Space Group	a ($\dot{A}$)	b ($\dot{A}$)	c ($\dot{A}$)	R^2 value (%)
AM-Mn-F	P6$_3$22	7.362	7.362	8.484	5.37
MA-Mn-F	Pnma	8.684	11.943	8.161	3.35
AZE-Mn-F	Pnma	8.681	12.313	8.882	5.86
FA-Mn-F	C2/c	13.819	8.702	8.477	4.21
GUA-Mn-F	Pnna	8.524	11.980	9.058	6.35

The compounds crystallized in different space groups depending on the size of the [AmineH$^+$] cations, which confirms the effect of the A-site cation on the structure. The smallest cation, [NH$_4^+$]

resulted in the formation of a structure that belongs to the hexagonal space group, while mid-sized cations ($[CH_3NH_3^+]$, $[(CH_2)_3NH_2^+]$, $[CH(NH_2)_2^+]$, $[C(NH_2)_3^+]$) led to the formation of compounds with perovskite structure. For samples with perovskite structure, albeit with different space groups, each sample shares the common feature of a perovskite structure, which is the existence of face centered cubic framework of $Mn[HCOO]_3^-$ and the [AmineH$^+$] cation that occupies the cavity.
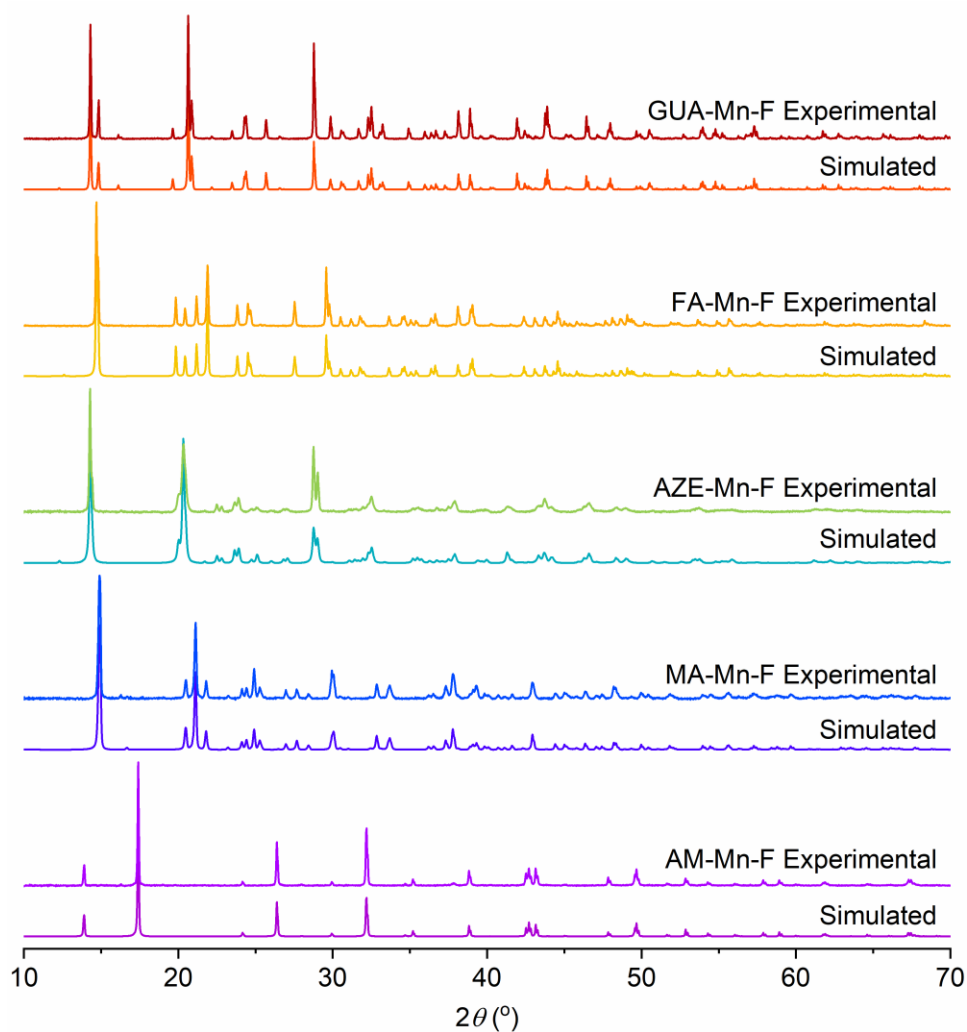
Figure 3-2. PXRD patterns for all synthesized AmineH$^+$-Mn-F samples in this work and their respective simulated patterns.

Further analysis of the purity of the sample was done with infrared spectroscopy (FTIR), and the FTIR patterns of all samples are given in Figure 3-3. The purity of the samples was confirmed by the absence of the starting material signals on the collected FTIR spectra. Additionally, the FTIR spectra of all samples are quite similar to each other, where every pattern shows the characteristic band for the $HCOO^-$ group and the respective [AmineH$^+$] cations. On all samples, the symmetric bending and stretching and asymmetric stretching modes of O-C-O were observed at ~793 cm^{-1}, 1355 cm^{-1}, and 1575 cm^{-1} respectively. Other different characteristic bands for the corresponding [AmineH$^+$] cations are indicated in the figure.
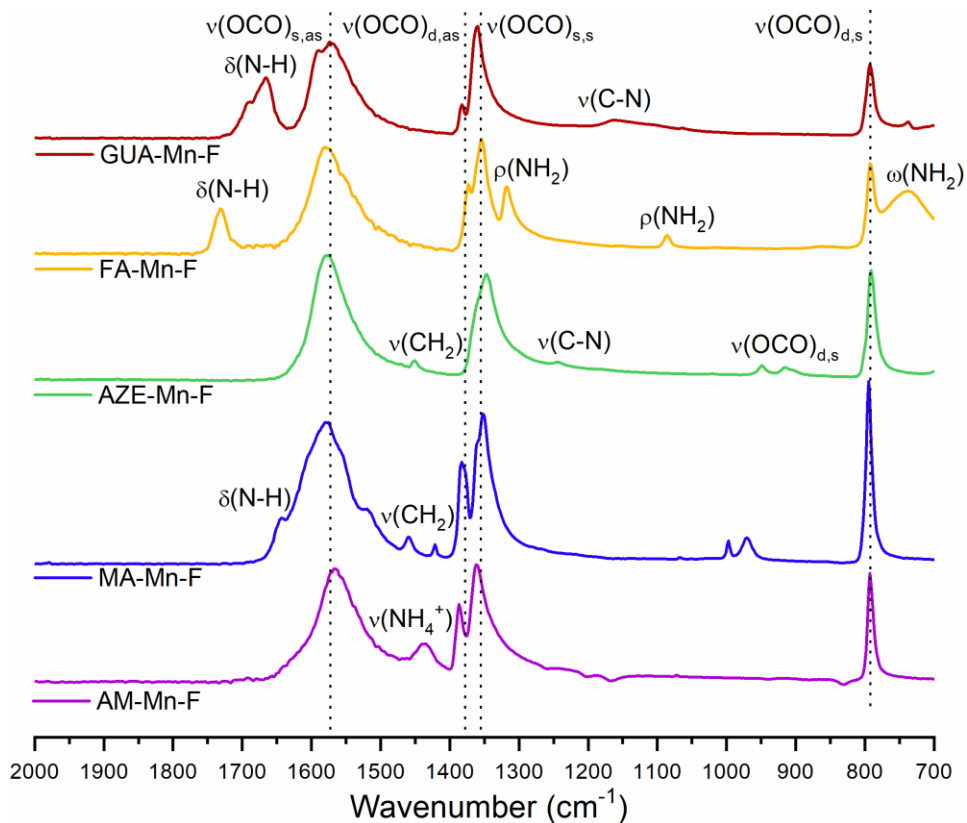
Figure 3-3. FTIR patterns of all AmineH$^+$-Mn-F samples

The thermal stability of the samples was investigated with thermal gravimetric analysis (TGA) and the TGA curve of all the samples are given in Figure 3-4. Under Argon, four of the samples, AM-

Mn-F, MA-Mn-F, AZE-Mn-F and FA-Mn-F showed a distinct two-step mass loss, while GUA-Mn-F showed only one step mass loss instead of two. Also, it can be seen that among all the species, GUA-Mn-F has a significantly higher decomposition temperature of 291.5°C compared to the other species, which indicates that GUA-Mn-F has the highest thermal stability. This is followed by FA-Mn-F which starts decomposing at 250.4°C, MA-Mn-F at 204.4°C, AZE-Mn-F at 191.8°C, and lastly, AM-Mn-F which started to decompose the earliest at 181.7°C, indicating the lowest thermal stability.

For the species that showed two-step mass loss, the first mass loss step corresponds to the loss of one formic acid and one amine per formula unit, which resulted in the formation of $Mn[HCOO]_2$ in each case. The experimental and calculated stoichiometric (in parentheses) weight loss percentages are 30.33 (29.83), 34.46 (34.26), 39.26 (41.16), and 37.11 (38.32) for AM-Mn-F, MA-Mn-F, AZE-Mn-F and FA-Mn-F respectively. The second mass loss step corresponds to the decomposition of $Mn[HCOO]_2$ to the final form of binary manganese oxides, which is confirmed by PXRD analysis of the residue. The total experimental weight loss percentages are 63.09, 66.97, 68.91, and 67.24 for AM-Mn-F, MA-Mn-F, AZE-Mn-F and FA-Mn-F respectively. In the case of GUA-Mn-F, only one step mass loss was observed, which indicates that the loss of one formic acid and one amine, and the decomposition of the resulting $Mn[HCOO]_2$ occurs simultaneously. The total experimental weight loss percentage for GUA-Mn-F is 69.17.
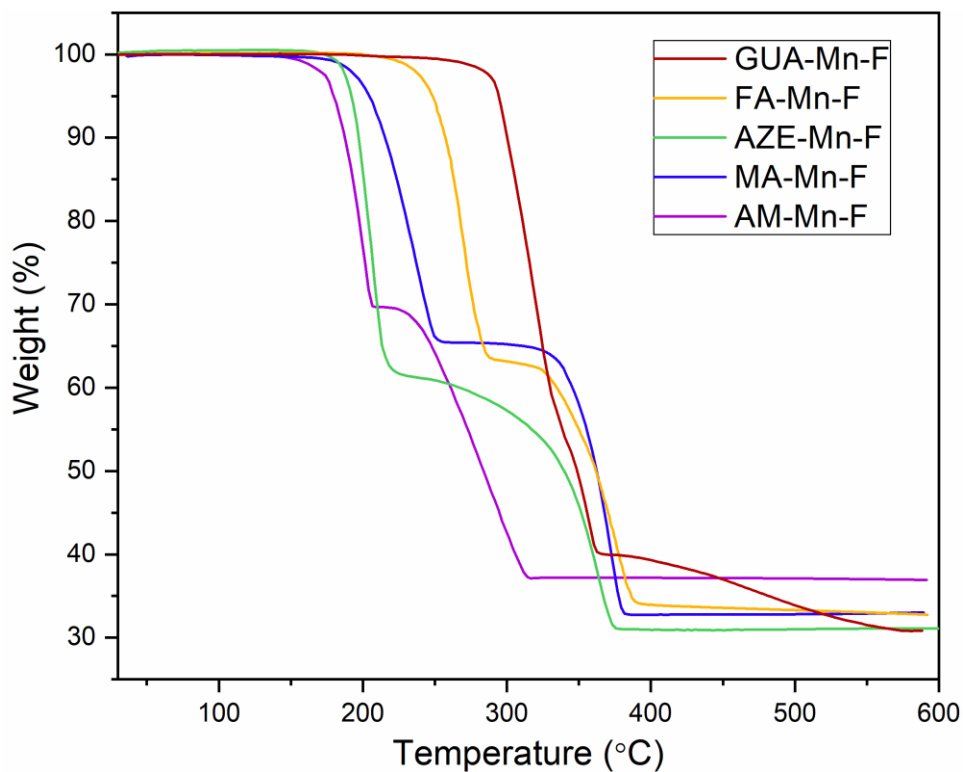
Figure 3-4. TGA patterns of all AmineH$^+$-Mn-F samples

To assess the thermodynamic stability of AmineH$^+$-Mn-F samples, room temperature isothermal acid solution calorimetry measurement was performed. The dissolution enthalpy (ΔH_{ds}) of the samples and its components in 5.0M HCl were collected and used to calculate the enthalpy of formation (ΔH_f) of the AmineH$^+$-Mn-F samples using thermochemical cycle described in Table 3-2. The measured ΔH_{ds}, calculated ΔH_f of AmineH$^+$-Mn-F samples and other thermochemical data needed for the calculation are summarized in Table 3-3.

Table 3-2. Thermocycle used to calculate the formation enthalpy of AmineH$^+$-Mn-F (AmineH$^+$ = AM, MA, DMA[14], AZE, FA, and GUA)

Reactions	Enthalpy (ΔH)
[AmineH$^+$]Mn(HCOO)$_{3(s)}$ → Mn$^{2+}_{(aq)}$ + AmineH$^+_{(aq)}$ + 3HCOO$^-_{(aq)}$	ΔH_1
MnCl$_{2(s)}$ + 2H$^+$ → Mn$^{2+}_{(aq)}$ + 2HCl$_{(5M\ HCl,\ aq)}$	ΔH_2
[AmineH$^+$]·Cl$_{(s)}$ + H$^+_{(aq)}$ → AmineH$^+_{(aq)}$ + HCl$_{(5M\ HCl,\ aq)}$	ΔH_3
HCOOH · xH$_2$O$_{(l)}$ → HCOO$^-_{(aq)}$ + H$^+_{(aq)}$ + xH$_2$O$_{(aq)}$	ΔH_4
xH$_2$O$_{(l)}$ → xH$_2$O$_{(aq)}$	ΔH_5
MnCl$_{2(s)}$ + [AmineH$^+$]· Cl$_{(s)}$ + 3 HCOOH · xH$_2$O$_{(l)}$ → [AmineH$^+$]Mn(HCOO)$_{3(s)}$ + 3HCl$_{(5M\ HCl,\ aq)}$ + 3xH$_2$O$_{(l)}$	$\Delta H_6 = \Delta H_{f,} = -\Delta H_1 + \Delta H_2 + \Delta H_3 + 3\Delta H_4 - 3\Delta H_5$
x = 0.07670 per formula unit	

Table 3-3. Thermochemical data used for the calculation of enthalpy of formation of AmineH$^+$-Mn-F (AmineH$^+$ = AM, MA, DMA, AZE, FA, and GUA)

Compound	ΔH_{ds} (kJ·mol^{-1})[a]	ΔH_f (kJ·mol^{-1})
HCOOH	-0.84 ± 0.17[b] (4)	
H$_2$O	-0.35[b]	
MnCl$_2$	-48.06 ± 1.01[b] (4)	
AM·Cl	17.99 ± 0.16 (4)	
MA·Cl	8.96 ± 0.15 (5)	
DMA·Cl	2.83 ± 0.20 (6)	
AZE·Cl	0.04 ± 0.01 (5)	
FA·Cl	9.29 ± 0.44 (7)	
GUA·Cl	16.58 ± 0.16 (4)	
AM-Mn-F	-10.32 ± 0.09 (4)	-22.20 ± 1.15
MA-Mn-F	4.73 ± 0.05 (5)	-46.35 ± 1.14
DMA-Mn-F	-5.29 ± 0.06[b] (4)	-42.38 ± 1.15[b]
AZE-Mn-F	-7.68 ± 0.09 (4)	-42.86 ± 1.14
FA-Mn-F	8.43 ± 0.12 (7)	-49.72 ± 1.22
GUA-Mn-F	24.97 ± 0.29 (6)	-58.97 ± 1.18

[a]Values given in parentheses are the number of experiments performed. The uncertainties given in the result represent a 95% confidence interval. [b]Reference [14,31,33]

The calculated ΔH_f values show that all AmineH$^+$-Mn-F samples studied here have exothermic heat of formation from their components, AmineH$^+\cdot$Cl and MnCl$_2$ salts. This exothermic enthalpy of formation values indicates their overall thermodynamic stability and also explains that the formation reaction is thermodynamically driven. Among all of the studied samples, AM-Mn-F showed the least exothermic heat of formation of -22.20 $\pm$ 1.15 kJ$\cdot$mol^{-1}, indicating the lowest stability among all of the AmineH$^+$-Mn-F samples in the series. As mentioned before in the PXRD result discussion, AM-Mn-F was the only sample that has a different structure compared to other AmineH$^+$-Mn-F samples, having a non-perovskite structure due to the much smaller size of NH$_4^+$ cation. Forming a perovskite structure with NH$_4^+$ cation, which is the less favourable structure, would lead to less exothermic or even endothermic heat of formation. It was also observed that AM-Mn-F sample decomposed rather quickly when left to sit at room temperature compared to the other samples.

Among all of the studied samples with the perovskite structure, GUA-Mn-F has the most exothermic enthalpy of formation, indicating the most thermodynamically stable sample in this series, followed by FA-Mn-F, MA-Mn-F, AZE-Mn-F, and DMA-Mn-F. There is an appreciable change in enthalpy of formation between each sample, confirming the important role of [AmineH$^+$] cations in the thermodynamic stability of the structures.

To further understand the role of the [AmineH$^+$] cations in the overall stability of the structure, several factors that are influenced by the change of the cations will be examined. Goldschmidt tolerance factor is a very extensively used parameter to explain the formation enthalpy behaviour of perovskites, especially inorganic perovskites[34,35]. This parameter explains the degree of

distortion of the structure from an ideal cubic perovskite structure. The value is calculated from the ratio of the ionic radii of the cations and the anion and is given by:

$$t = (r_A + r_O)/\sqrt{2}(r_B + r_O) \tag{1}$$

where r_A, r_B, and r_O corresponds to the ionic radii of the cations and the anion (oxygen) of ABO_3 perovskite. The ideal perovskite structure will have a tolerance factor value of 1. The application of the Goldschmidt tolerance factor to an inorganic perovskite is straightforward due to the availability of ionic radius data, while the presence of molecular cations and anions in hybrid perovskite introduced another layer of difficulty to the calculation. It is difficult to define the ionic radius of a molecular ion due to the presence of hydrogen bonding that causes the bond lengths to vary. Kieslich et.al.[36,37] tried to estimate the effective radii of the organic ions by using available crystallographic data of hybrid perovskites to overcome this problem. Additionally, the organic cations were assumed to be a rigid sphere having free rotational freedom around the mass, while the ions that have high anisotropy (such as $HCOO^-$) was assumed to be a rigid cylinder. With this model, the effective ionic radius (or effective ion height for anisotropic ion case) was defined as the sum of the distance between the center of the mass of the ion to the farthest atom from the center of mass, excluding hydrogen atom, and the ionic radius of said atom. This is given by:

$$r_{A,eff} = r_{mass} + r_{ion} \tag{2}$$

And the modified tolerance factor equation is given by:

$$t = (r_{A,eff} + r_{X,eff})/\sqrt{2}(r_B + 0.5h_{X,eff}) \tag{3}$$

For formate ion, the effective radius $r_{X,eff} = 136\ pm$ while the effective height $h_{X,eff} = 447\ pm$. The effective radius of the [AmineH⁺] cations and the calculated tolerance factor for each structure is summarized in Table 3-4.

Table 3-4. Size of AmineH⁺ cations and the calculated tolerance factor of AmineH⁺-Mn-F samples

	AmineH⁺ cation size (pm)[a]	Tolerance factor (t)	ΔH_f (kJ·mol⁻¹)
AM-Mn-F	146	0.65	-22.20 ± 1.15
MA-Mn-F	217	0.81	-46.35 ± 1.14
DMA-Mn-F	272	0.94	-42.38 ± 1.15[a]
AZE-Mn-F	250	0.89	-42.86 ± 1.14
FA-Mn-F	253	0.90	-49.72 ± 1.22
GUA-Mn-F	278	0.96	-58.97 ± 1.18

[a]Reference [14,37]

The calculated tolerance factors show that the modified equation produced a result that agrees with the trend seen in inorganic perovskites. The samples that have perovskite structure show tolerance factors ranging between 0.81-0.96, which are in the acceptable range to form a perovskite structure. AM-Mn-F, which has been shown to have a non-perovskite structure, has a tolerance factor of 0.65, which is lower than the commonly accepted limit to form a perovskite structure (<0.8)[38].

To be able to properly assess the effect of the [AmineH⁺] cations on the overall stability and to rule out the contribution of structural changes to the stability, only the samples with perovskite structure will be analyzed. Additionally, DMA-Mn-F, which has a similar structure and whose

enthalpy of formation was studied previously[14], will be included in the discussion. The correlation between the enthalpy of formation of AmineH$^+$-Mn-F and the tolerance factor is shown in **Figure 3-5.**
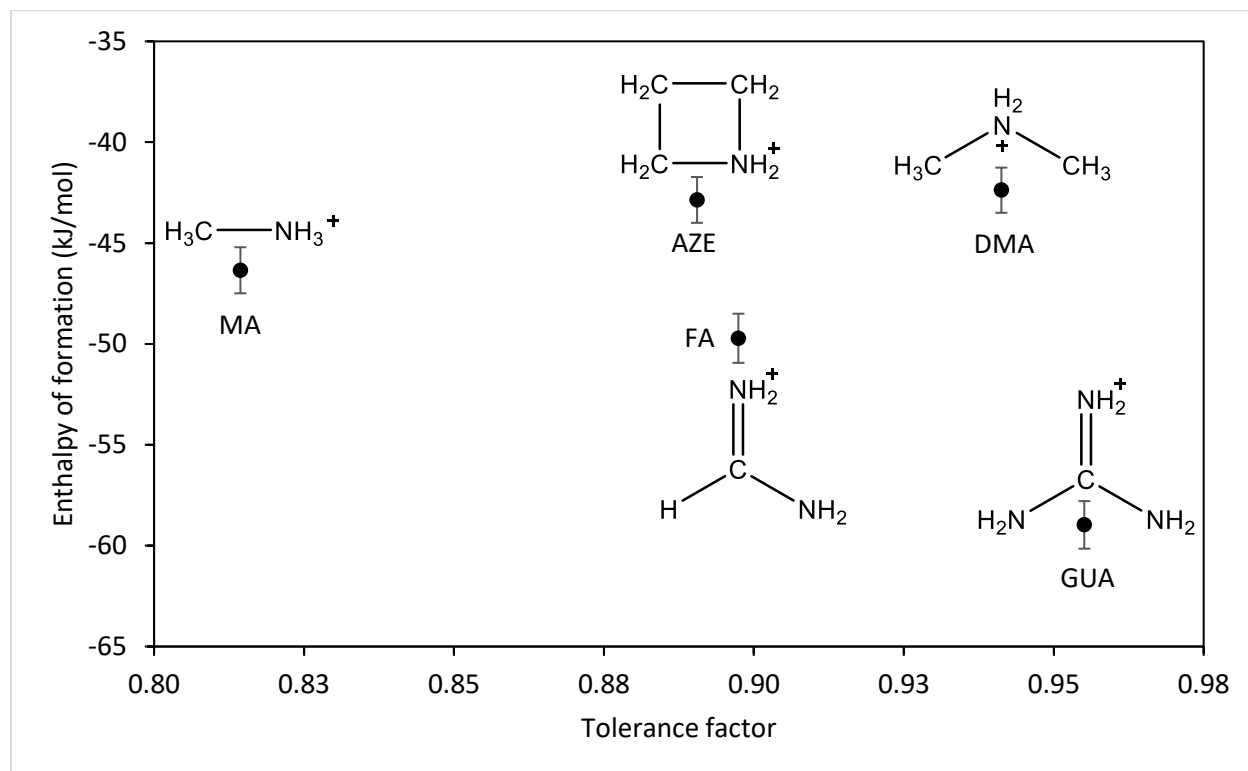
Figure 3-5. Enthalpy of formation of AmineH$^+$-Mn-F (AmineH$^+$ = MA, DMA, AZE, FA, and GUA) as a function of tolerance factor

From the figure, the enthalpy of formation of AmineH$^+$-Mn-F changes as the tolerance factor changes, however, there is no obvious clear trend that explains the relation between them. Comparing the cations with similar number of carbon atoms but different number of nitrogen atoms, the enthalpy of formation becomes more exothermic as the number of nitrogen atoms increases, in order of MA-Mn-F, FA-Mn-F and GUA-Mn-F. However, the same is not seen for the cations with the same number of nitrogen atoms but different number of carbon atoms. AZE-

Mn-F shows lower stability than MA-Mn-F while having a larger tolerance factor and belonged in the same space group. Additionally, AZE-Mn-F and FA-Mn-F, while having very similar cation size and similar tolerance factor, show a significantly different enthalpy of formation. This is also seen when comparing DMA-Mn-F with GUA-Mn-F. This is surprising when compared to the behaviour of inorganic perovskites, where it has been shown that the enthalpy of formation becomes more exothermic as the tolerance factor increases and approaches unity (the structure become more ideal)[34,39–43]. This indicates that the geometric mismatch represented by the tolerance factor is not the major component that affects the resulting thermodynamic stability of hybrid perovskites.

Unlike inorganic perovskites, the cation in hybrid perovskite is a molecular cation, specifically in this case protonated amine. In addition to the electrostatic interaction, the presence of N-H and C-H moieties in the cation structure provides a convenient hydrogen bonding between the cation in the cavity and the oxygen atom in the framework of the perovskite, both strong N-H$\cdots$O hydrogen bonds and weak C-H$\cdots$O hydrogen bonds[18,44]. Due to the different structures and compositions of the cations, it is imperative to expect that the hydrogen bonding interaction between the cation and the framework would affect the thermodynamic stability of the overall structure.

Here, a convenient way to estimate the relative strength of the hydrogen bond is proposed by the means of the calorimetric measurements themselves. From the available crystal structure of some AmineH$^+$·Cl salts, the chlorine atoms and the AmineH$^+$ groups are linked together by means of hydrogen bonds[45–47]. Because of this, the enthalpy associated with the dissolution reaction of AmineH$^+$·Cl in HCl presented in the following reaction:

$$[\text{AmineH}^+]\cdot\text{Cl}_{(s)} + \text{H}^+_{(aq)} \rightarrow \text{AmineH}^+_{(aq)} + \text{HCl}_{(5M\ HCl,\ aq)} \qquad (4)$$

70
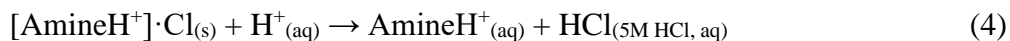
would be equivalent to the enthalpy required to break the hydrogen bonds between the AmineH$^+$ and the Cl atoms in the salt structure. One would expect that the relative strength of the hydrogen bonds in AmineH$^+$·Cl salts would also translate to the relative strength of the hydrogen bonds between the AmineH$^+$ cations and the surrounding frameworks in the AmineH$^+$-Mn-F perovskites. This AmineH$^+$·Cl salt dissolution enthalpy value in HCl was previously measured, and this would allow the comparison with the enthalpy of formation of the perovskites, as presented in **Figure 3-6**:
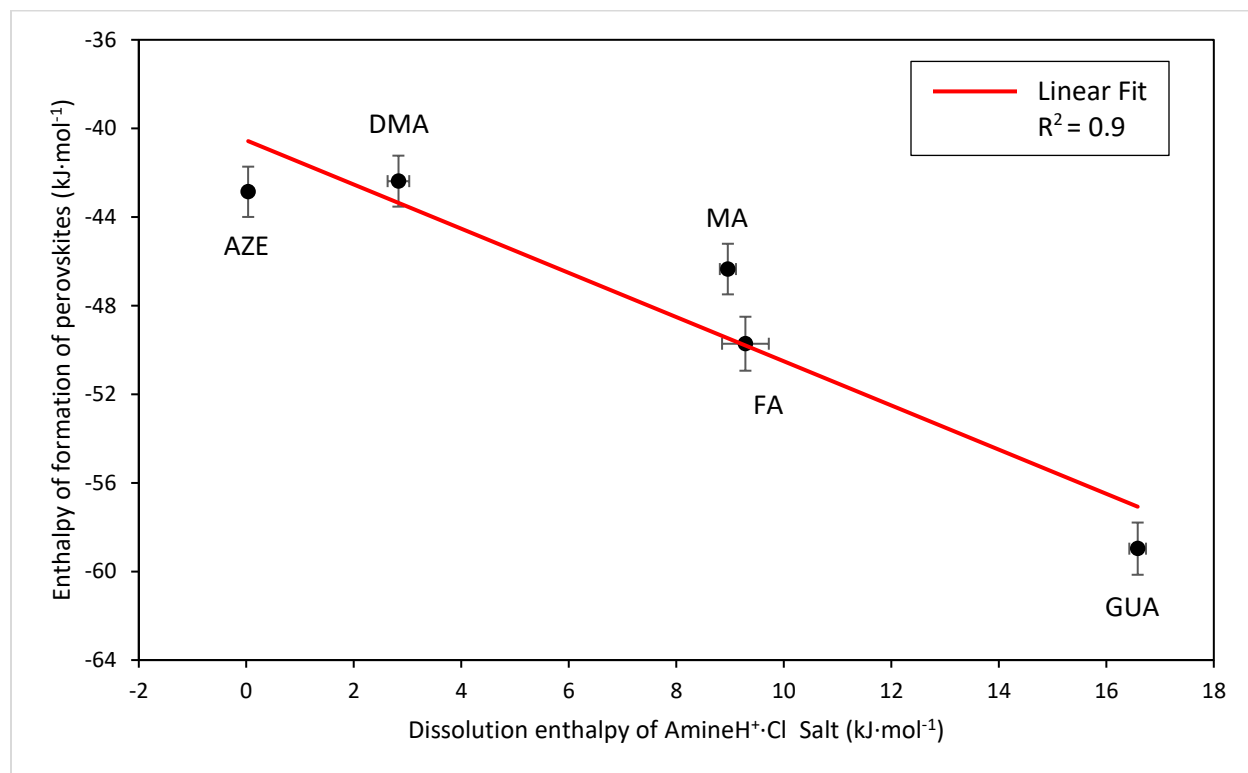
Figure 3-6. Enthalpy of formation of AmineH$^+$-Mn-F (AmineH$^+$ = MA, DMA, AZE, FA, and GUA) as a function of drop solution enthalpy of AmineH$^+$·Cl salt

Figure 3-6 shows that there is a strong linear correlation between the perovskite enthalpy of formation and the dissolution enthalpy of the cation salts. As the solution enthalpy of the cation

salts becomes more endothermic, the corresponding perovskite enthalpy of formation becomes more exothermic. This seems to be very intuitive in that the harder it is to protonate the salt to form the cation, the stronger is the hydrogen bonding between the AmineH$^+$ groups and Cl atoms. Consequently, this results in stronger hydrogen bonding between AmineH$^+$ cations and the surrounding frameworks on the perovskite structure. This result also agrees with the relative magnitude of hydrogen bonding energies between the cations and the framework that was previously calculated computationally for DMA, AZE and GUA-Mn-F, where it was found that the hydrogen bonding energy is the strongest for GUA-Mn-F, followed by DMA-Mn-F and AZE-Mn-F.[18,44]

This linear relationship would also provide an opportunity to predict the stability of other hybrid perovskites based only on the property of the A-site cation. For example, here the slope of the currently observed linear correlation between perovskite enthalpy of formation and the dissolution enthalpy of the cation salts is 1 kJ·mol^{-1}, indicating that the perovskite stability would change by 1 kJ·mol^{-1} per unit of cation salt dissolution enthalpy. Extending this result to other hybrid perovskite systems with a molecular A-site cation, it would be possible to predict the stability of the perovskite structures just by the dissolution enthalpy of the A-site cation salts and predict the most viable sample compositions for synthesis.

3.5 Conclusions

We present a systematic study on the effect of A-site cation substitution on the thermodynamic stability of AmineH$^+$-Mn-F (AmineH$^+$ = AM, MA, DMA, AZE, FA and GUA), a hybrid organic-inorganic perovskite system. Calorimetric measurements using a room temperature isothermal acid solution calorimetry were performed to measure the solution enthalpies of the samples, which

are then used to calculate their formation enthalpies. The usage of NH_4^+ as the organic cation resulted in the formation of a non-perovskite structure and was found to be the least stable structure, thermally and thermodynamically, in the series. Among other synthesized AmineH$^+$-Mn-F perovskites, GUA-Mn-F perovskite was found to be the most stable both thermally and thermodynamically, followed by FA-Mn-F, MA-Mn-F, and lastly AZE-Mn-F and DMA-Mn-F with similar stability. Unlike inorganic perovskite structures, the stability of hybrid perovskite was found to be governed more by the interaction between the A-site cation and the framework, mostly through hydrogen bonding, rather than the distortion degree of the structure calculated by the tolerance factor. It was found that it was possible to measure the relative strength of this hydrogen bonding energy by a simple dissolution enthalpy measurement of the cation salts and it was found that this energy correlates linearly with the perovskite enthalpy of formation. In the vast number of different possible composition combinations in hybrid perovskite systems, this relationship would be a very useful tool to predict the stability and accelerate the discovery of samples that are feasible for experimental synthesis.

3.6 Acknowledgement

3.7 References

(1) Johnsson, M.; Lemmens, P. Crystallography and Chemistry of Perovskites. *Handb. Magn. Adv. Magn. Mater.* **2007**, 11.

(2) Li, W.; Wang, Z.; Deschler, F.; Gao, S.; Friend, R. H.; Cheetham, A. K. Chemically Diverse and Multifunctional Hybrid Organic-Inorganic Perovskites. *Nat. Rev. Mater.* **2017**, *2*, 16099.

(3) Saparov, B.; Mitzi, D. B. Organic-Inorganic Perovskites: Structural Versatility for Functional Materials Design. *Chem. Rev.* **2016**, *116*, 4558–4596.

(4) Grancini, G.; Nazeeruddin, M. K. Dimensional Tailoring of Hybrid Perovskites for Photovoltaics. *Nat. Rev. Mater.* **2019**, *4*, 4–22.

(5)   Green, M. A.; Ho-Baillie, A.; Snaith, H. J. The Emergence of Perovskite Solar Cells. *Nat. Photonics* **2014**, *8*, 506–514.

(6)   Chen, Q.; De Marco, N.; Yang, Y.; Song, T. Bin; Chen, C. C.; Zhao, H.; Hong, Z.; Zhou, H.; Yang, Y. Under the Spotlight: The Organic-Inorganic Hybrid Halide Perovskite for Optoelectronic Applications. *Nano Today* **2015**, *10*, 355–396.

(7)   Trzebiatowska, M.; Gagor, A.; MacAlik, L.; Peksa, P.; Sieradzki, A. Phase Transition in the Extreme: A Cubic-to-Triclinic Symmetry Change in Dielectrically Switchable Cyanide Perovskites. *Dalt. Trans.* **2019**, *48*, 15830–15840.

(8)   Schouwink, P.; Ley, M. B.; Tissot, A.; Hagemann, H.; Jensen, T. R.; Smrčok, ̦ubomír; Černý, R. Structure and Properties of Complex Hydride Perovskite Materials. *Nat. Commun.* **2014**, *5*, 1–10.

(9)   Møller, K. T.; Ley, M. B.; Schouwink, P.; Černý, R.; Jensen, T. R. Synthesis and Thermal Stability of Perovskite Alkali Metal Strontium Borohydrides. *Dalt. Trans.* **2016**, *45*, 831–840.

(10)   Trzebiatowska, M.; Maczka, M.; Ptak, M.; Giriunas, L.; Balciunas, S.; Simenas, M.; Klose, D.; Banys, J. Spectroscopic Study of Structural Phase Transition and Dynamic Effects in a [(CH3)2NH2][Cd(N3)3] Hybrid Perovskite Framework. *J. Phys. Chem. C* **2019**, *123*, 11840–11849.

(11)   Senocrate, A.; Kim, G. Y.; Grätzel, M.; Maier, J. Thermochemical Stability of Hybrid Halide Perovskites. *ACS Energy Lett.* **2019**, *4*, 2859–2870.

(12)   Nagabhushana, G. P.; Shivaramaiah, R.; Navrotsky, A. Direct Calorimetric Verification of Thermodynamic Instability of Lead Halide Hybrid Perovskites. *Proc. Natl. Acad. Sci.* **2016**, *113*, 7717–7721.

(13)   Nagabhushana, G. P.; Shivaramaiah, R.; Navrotsky, A. Thermochemistry of the Simplest Metal Organic Frameworks: Formates [M(HCOO)2]·xH2O (M = Li, Mg, Mn, Co, Ni, and Zn). *J. Chem. Thermodyn.* **2018**, *118*, 325–330.

(14)   Nagabhushana, G. P.; Shivaramaiah, R.; Navrotsky, A. Thermochemistry of Multiferroic Organic–Inorganic Hybrid Perovskites [(CH$_3$)$_2$NH$_2$][M(HCOO)$_3$] (M = Mn, Co, Ni, and Zn). *J. Am. Chem. Soc.* **2015**, *137*, 10351–10356.

(15)   Tenuta, E.; Zheng, C.; Rubel, O. Thermodynamic Origin of Instability in Hybrid Halide Perovskites. *Nat. Publ. Gr.* **2016**, No. July, 1–8.

(16)   Ivanov, I. L.; Steparuk, A. S.; Bolyachkina, M. S.; Tsvetkov, D. S.; Safronov, A. P.; Zuev, A. Y. Thermodynamics of Formation of Hybrid Perovskite-Type Methylammonium Lead Halides. *J. Chem. Thermodyn.* **2018**, *116*, 253–258.

(17)   Hutter, E. M.; Muscarella, L. A.; Wittmann, F.; Versluis, J.; McGovern, L.; Bakker, H. J.; Woo, Y. W.; Jung, Y. K.; Walsh, A.; Ehrler, B. Thermodynamic Stabilization of Mixed-Halide Perovskites against Phase Segregation. *Cell Reports Phys. Sci.* **2020**, *1*, 100120.

(18)   Li, W.; Thirumurugan, A.; Barton, P. T.; Lin, Z.; Henke, S.; Yeung, H. H. M.; Wharmby, M. T.; Bithell, E. G.; Howard, C. J.; Cheetham, A. K. Mechanical Tunability via Hydrogen Bonding in Metal-Organic Frameworks with the Perovskite Architecture. *J. Am. Chem. Soc.* **2014**, *136*, 7801–7804.

(19)   Wang, Z.; Hu, K.; Gao, S.; Kobayashi, H. Formate-Based Magnetic Metal-Organic Frameworks Templated by Protonated Amines. *Adv. Mater.* **2010**, *22*, 1526–1533.

(20)   Motta, C.; Mellouhi, F. El; Kais, S.; Tabet, N.; Alharbi, F.; Sanvito, S. Revealing the Role of Organic Cations in Hybrid Halide Perovskites CH3NH3PbI3. *Nat. Commun.* **2014**, *6*, 1–7.

(21)   Myung, C. W.; Yun, J.; Lee, G.; Kim, K. S. A New Perspective on the Role of A-Site Cations in Perovskite Solar Cells. *Adv. Energy Mater.* **2018**, *8*.

(22)   Zhang, C.; Wang, Y.; Lin, X.; Wu, T.; Han, Q.; Zhang, Y.; Han, L. Effects of A Site Doping on the

Crystallization of Perovskite Films. *J. Mater. Chem. A* **2021**, *9*, 1372–1394.

(23)   Pato-Doldán, B.; Gómez-Aguirre, L. C.; Hansen, A. P.; Mira, J.; Castro-García, S.; Sánchez-Andújar, M.; Señarís-Rodríguez, M. A.; Zapf, V. S.; Singleton, J. Magnetic Transitions and Isotropic versus Anisotropic Magnetic Behaviour of [CH $_3$ NH $_3$][M(HCOO) $_3$] M = Mn $^{2+}$, Co $^{2+}$, Ni $^{2+}$, Cu $^{2+}$ Metal–Organic Perovskites. *J. Mater. Chem. C* **2016**, *4*, 11164–11172.

(24)   Jain, P.; Dalal, N. S.; Toby, B. H.; Kroto, H. W.; Cheetham, A. K. Order-Disorder Antiferroelectric Phase Transition in a Hybrid Inorganic-Organic Framework with the Perovskite Architecture. *J. Am. Chem. Soc.* **2008**, *130*, 10450–10451.

(25)   Li, W.; Zhang, Z.; Bithell, E. G.; Batsanov, A. S.; Barton, P. T.; Saines, P. J.; Jain, P.; Howard, C. J.; Carpenter, M. A.; Cheetham, A. K. Ferroelasticity in a Metal-Organic Framework Perovskite; Towards a New Class of Multiferroics. *Acta Mater.* **2013**, *61*, 4928–4938.

(26)   Rogez, G.; Viart, N.; Drillon, M. Multiferroic Materials: The Attractive Approach of Metal-Organic Frameworks (MOFs). *Angew. Chem., Int. Ed..* **2010**, *49*, 1921–1923.

(27)   Vinod, K.; Deepak, C. S.; Sharma, S.; Sornadurai, D.; Satya, A. T.; Ravindran, T. R.; Sundar, C. S.; Bharathi, A. Magnetic Behavior of the Metal Organic Framework [(CH $_3$) $_2$ NH $_2$]Co(HCOO) $_3$. *RSC Adv.* **2015**, *5*, 37818–37822.

(28)   Wang, Z.; Zhang, B.; Inoue, K.; Fujiwara, H.; Otsuka, T.; Kobayashi, H.; Kurmoo, M. Occurrence of a Rare 49·66structural Topology, Chirality, and Weak Ferromagnetism in the [NH4][MII(HCOO)3] (M = Mn, Co, Ni) Frameworks. *Inorg. Chem.* **2007**, *46*, 437–445.

(29)   Wang, Z.; Zhang, B.; Otsuka, T.; Inoue, K.; Kobayashi, H.; Kurmoo, M. Anionic NaCl-Type Frameworks of [MnII(HCOO)3−], Templated by Alkylammonium, Exhibit Weak Ferromagnetism. *J. Chem. Soc. Dalt. Trans.* **2004**, *4*, 2209–2216.

(30)   Hu, K. L.; Kurmoo, M.; Wang, Z.; Gao, S. Metal-Organic Perovskites: Synthesis, Structures, and Magnetic Properties of [C(NH2)3][MII(HCOO)3] (M=Mn, Fe, Co, Ni, Cu, and Zn; C(NH2)3=guanidinium). *Chem. - Eur. J.* **2009**, *15*, 12050–12064.

(31)   Parker, V. B. Thermal Properties of Aqueoues Uni-Univalent Electrolytes. *Nsrds-Nbs 2* **1965**, 1–66.

(32)   Akimbekov, Z.; Wu, D.; Brozek, C. K.; Dincə, M.; Navrotsky, A. Thermodynamics of Solvent Interaction with the Metal-Organic Framework MOF-5. *Phys. Chem. Chem. Phys.* **2015**, *18*, 1158–1162.

(33)   Novendra, N.; Marrett, J. M.; Katsenis, A. D.; Titi, H. M.; Arhangelskis, M.; Friščić, T.; Navrotsky, A. Linker Substituents Control the Thermodynamic Stability in Metal–Organic Frameworks. *J. Am. Chem. Soc.* **2020**.

(34)   Navrotsky, A. Thermochemistry of Complex Perovskites. *AIP Conf. Proc.* **2000**, *535*, 288–296.

(35)   Navrotsky, A. Thermodynamics of Solid Electrolytes and Related Oxide Ceramics Based on the Fluorite Structure. *J. Mater. Chem.* **2010**, *20*, 10577–10587.

(36)   Kieslich, G.; Sun, S.; Cheetham, A. K. An Extended Tolerance Factor Approach for Organic-Inorganic Perovskites. *Chem. Sci.* **2015**, *6*, 3430–3433.

(37)   Kieslich, G.; Sun, S.; Cheetham, A. K. Solid-State Principles Applied to Organic–Inorganic Perovskites: New Tricks for an Old Dog. *Chem. Sci.* **2014**, *5*, 4712–4715.

(38)   Travis, W.; Glover, E. N. K.; Bronstein, H.; Scanlon, D. O.; Palgrave, R. G. On the Application of the Tolerance Factor to Inorganic and Hybrid Halide Perovskites: A Revised System. *Chem. Sci.* **2016**, *7*, 4548–4556.

(39)   Feng, D.; Navrotsky, A. Thermochemistry of Rare Earth Perovskites. *MRS Adv.* **2016**, *1*, 2695–2700.

(40)   Zlotnik, S.; Sahu, S. K.; Navrotsky, A.; Vilarinho, P. M. Pyrochlore and Perovskite Potassium Tantalate: Enthalpies of Formation and Phase Transformation. *Chem. - Eur. J.* **2015**, *21*, 5231–5237.

(41)   Qi, J.; Guo, X.; Mielewczyk-Gryn, A.; Navrotsky, A. Formation Enthalpies of LaLnO$_3$ (Ln=Ho, Er, Tm and Yb) Interlanthanide Perovskites. *J. Solid State Chem.* **2015**, *227*, 150–154.

(42)   Sahu, S. K.; Maram, P. S.; Navrotsky, A. Thermodynamics of Nanoscale Calcium and Strontium Titanate Perovskites. *J. Am. Ceram. Soc.* **2013**, *96*, 3670–3676.

(43)   Wang, B.; Navrotsky, A. Thermodynamics of Cesium Lead Halide (CsPbX3, X= I, Br, Cl) Perovskites. *Thermochim. Acta* **2021**, *695*, 178813.

(44)   Svane, K. L.; Forse, A. C.; Grey, C. P.; Kieslich, G.; Cheetham, A. K.; Walsh, A.; Butler, K. T. How Strong Is the Hydrogen Bond in Hybrid Perovskites? *J. Phys. Chem. Lett.* **2017**, *8*, 6154–6159.

(45)   Lindgren, J.; Olovsson, I. Hydrogen Bond Studies. XVII. The Crystal Structure of Dimethylammonium Chloride. *Acta Crystallogr. Sect. B* **1968**, *24*, 549–553.

(46)   Haas, D. J.; Harris, D. R.; Mills, H. H. The Crystal Structure of Guanidinium Chloride. *Acta Crystallogr.* **1965**, *19*, 676–679.

(47)   Petrov, A. A.; Goodilin, E. A.; Tarasov, A. B.; Lazarenko, V. A.; Dorovatovskii, P. V; Khrustalev, V. N. Formamidinium Iodide: Crystal Structure and Phase Transitions. *Acta Crystallogr. Sect. E, Crystallogr. Commun.* **2017**, *73*, 569–572.

Chapter 4:

Theoretical Prediction and Experimental Evaluation of Topological Landscape and Thermodynamic Stability of a Fluorinated Zeolitic Imidazolate Framework

This chapter is presented based on the following previously published paper:

Arhangelskis, M.; Katsenis, A. D.; Novendra, N.; Akimbekov, Z.; Gandrath, D.; Marrett, J. M.; Ayoub, G.; Morris, A. J.; Farha, O. K.; Friščić, T.; Navrotsky, A. Theoretical Prediction and Experimental Evaluation of Topological Landscape and Thermodynamic Stability of a Fluorinated Zeolitic Imidazolate Framework. *Chem. Mater.* **2019**, *31*, 3777–3783.

Note: My contributions to this work are on the thermal analysis experiments, calorimetric measurements, and discussion of the energetics of the system.

4.1   Abstract

The prediction of topological preferences and polymorph stability remains a challenge for the design of metal−organic frameworks exhibiting a rich topological landscape, such as zeolitic imidazolate frameworks (ZIFs). Here, we have used mechanochemical screening and calorimetry to test the ability of dispersion-corrected periodic density functional theory (DFT) to accurately survey the topological landscape, as well as quantitatively evaluate polymorph stability, for a

previously not synthesized ZIF composition. Theoretical calculations were used to obtain an energy ranking and evaluate energy differences for a set of hypothetical, topologically distinct structures of a fluorine-substituted ZIF. Calculations were then experimentally validated via mechanochemical screening and calorimetry, which confirmed two out of three theoretically anticipated topologies, including a fluorinated analogue of the popular ZIF-8, while revealing an excellent match between the measured and theoretically calculated energetic differences between them. The results, which speak strongly in favor of the ability of dispersion-corrected periodic DFT to predict the topological landscape of new ZIFs, also reveal the ability to use peripheral substituents on the organic linker to modify the framework thermodynamic stability.

4.2   Introduction

The experimental and computational design of metal-organic frameworks (MOFs)[1-4] has focused largely on the assembly of nodes and linkers of controlled size and rigid geometry.[5-10] While the influence of linker substituents on MOF properties has recently been explored,[11] theoretical studies of how the substituents affect the topological landscape and thermodynamic stability of MOFs are rare and generally not experimentally validated.[12-15] Such studies are especially relevant for zeolitic imidazolate frameworks (ZIFs), azolate MOFs[16] analogous to zeolites. Like zeolites, ZIFs readily form polymorphs, often with a rich topological landscape that depends strongly on the choice and positioning of linker substituents. For example, zinc 2-methylimidazolate Zn(**MeIm**)$_2$ forms a family of increasingly dense and stable frameworks with sodalite (SOD), katsenite (kat) and diamondoid (dia) topologies. Zinc 2-ethylimidazolate Zn(**EtIm**)$_2$ yields ZIFs of zeolite rho (RHO), analcime (ANA) and quartz (qtz) topologies,[17-20] while unsubstituted imidazolate yields at least 15 polymorphs.[21] Periodic density functional theory (DFT) has been extensively used to

model ZIF polymorphism[12-15,22-25] and generally predict MOF structures and properties.[71,72] Our recent theoretical and experimental study shows[20] that periodic DFT with semi-empirical dispersion correction (SEDC) can provide not only the correct energy ranking of Zn(**MeIm**)$_2$ and Zn(**EtIm**)$_2$ polymorphs, but also a reasonable evaluation of energy differences between them. This opens a route to use dispersion-corrected DFT to survey topological preferences of novel ZIFs by evaluating relative stabilities of topologically different hypothetical structures.[28]
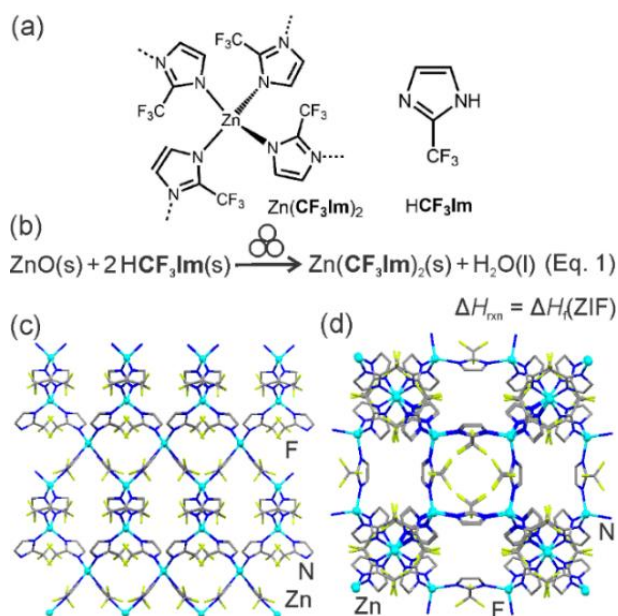
Figure 4-1. (a) Schematic representation of Zn(**CF₃Im**)$_2$ and ligand 2-trifluoromethylimidazole (H**CF₃Im**); (b) synthesis of Zn(**CF₃Im**)$_2$ from ZnO. Crystal structures of herein predicted and observed: (c) *qtz*-Zn(**CF₃Im**)$_2$ and (d) SOD-Zn(**CF₃Im**)$_2$.

We now test this approach by computationally screening and experimentally evaluating the topological preferences and stability for a previously not reported ZIF, zinc 2-trifluoromethylimidazolate (Zn(**CF₃Im**)$_2$, **Figure 4-1**). We selected this model system because of the recent high interest in fluorinated MOF materials.[29-37] Importantly, previous attempts to

synthesize this material from solution were unsuccessful,[38] prompting us to explore mechanochemical methodologies known to offer access to otherwise inaccessible phases.[39]

4.3 Computational and Experimental Methods

4.3.1 Computational Methods

Computational screening, conducted prior to any experiments, was limited to putative $Zn(\mathbf{CF_3Im})_2$ structures based on dia, kat, SOD, qtz, ANA, RHO, zni and cag-topologies that are often found in ZIFs. Structures were generated from ZIFs found in the Cambridge Structural Database (CSD),[40] by removing any guest molecules, inserting CF_3 groups into the 2-position of imidazolate linkers and replacing any 4- and 5-substituents with hydrogens. Some of the resulting structures exhibited short "head-to-head" or "tail-to-tail" $F \cdots F$ contacts, notably those with SOD-, kat-, ANA- and RHO-topologies in which substituents in a 4-ring are in close vicinity (**Figure 4-2**a,b), and dia-$Zn(CF_3Im)_2$ where such contacts result from close packing. To minimize such contacts, neighboring -CF_3 groups were oriented into a head-to-tail arrangement (**Figure 4-2**c). This was readily done for dia-$Zn(CF_3Im)_2$, but not for SOD-, kat-, ANA- and RHO-structures where the alignment of substituents is constrained by space group symmetry. For those topologies two structural models were evaluated, one considering full crystallographic symmetry of the parent CSD structure, and the other with space group symmetry constraints removed to form a disordered $P1$ structure in which the relative orientations of -CF_3 groups could be independently manipulated.

80
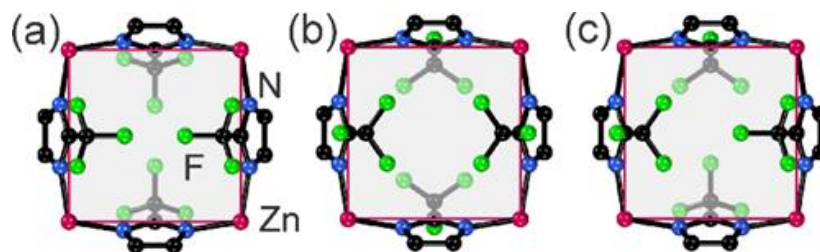
Figure 4-2. Illustration of different relative orientations of -CF$_3$ groups across a 4-ring: (a) head-to-head; (b) tail-to-tail; (c) head-to-tail.

Structures were geometry-optimized using periodic plane wave DFT code CASTEP 16.11.,[41] using the PBE functional with Grimme D2 SEDC.[42] The I-centered structures (zni, SOD, ANA, RHO) were transformed to corresponding primitive structures, reducing the cell volume and computational cost, while preserving all symmetry operations of the original structures. Optimized structures were also used for single point calculations with the many-body dispersion (PBE+MBD*)[43-45] energy model. While the Grimme D2 scheme relies on a parameterization of the pairwise atom-atom interactions to compute dispersion energies, MBD* approach computes the interaction parameters from the energy density of a structure while including the many-body terms beyond the pairwise interaction. The plane wave basis set was truncated at 750 eV cutoff, and norm-conserving pseudopotentials were used for the core regions of electron density. The Brillouin zone was sampled with a 0.03 Å^{-1} Monkhorst-Pack k-point grid.[46] Each structure was geometry optimized to an energy minimum with respect to unit cell dimensions and atom coordinates, subject to space group constraints. One exception to this protocol was the computationally-expensive RHO-Zn(**CF₃Im**)$_2$ in P1 space group, generated from the optimized Im-3m structure. Due to high computational cost, only the positions of atoms in -CF$_3$ groups were optimized, keeping the remaining atoms and unit cell parameters fixed from the optimization with symmetry constraints. The applied strategy provided putative structures without any unusually

short F···F contacts (see **Table 4-1**). Analysis of the contribution of dispersion correction to calculated energies of MOF structures (see the SI) reveals that it becomes increasingly important for structures of high density, especially for PC values higher than ca. 0.5.

The electronic density of states (DOS) were calculated for the optimized ZIF structures, to assess any potential relationships between topological connectivity and electronic properties of Zn(**CF₃Im**)₂ polymorphs. The DOS plots were calculated using the code OptaDOS.[47,48] Further computational details are provided in the SI.

Table 4-1. Topologies, calculated relative energies ($E_{rel,c}$, kJ mol^{-1}), volumes per formula unit (V, Å^3), packing coefficients (PC) and shortest F$\cdots$F distance ($d_{F\cdots F}$, Å) for putative $Zn(CF_3Im)_2$ polymorphs.

Topology	Space group	$E_{rel,c}$		V	PC	$d_{F\cdots F}$
		PBE+D2	PBE+MBD*			
qtz	P6$_4$	0.00	0.00	270.5	0.66	3.06[c]
dia	$P2_1/c$ [a]	11.29	13.49	265.9	0.74	2.74
SOD[a]	$P1$[a]	19.01	15.93	436.4	0.45	2.89[d]
	I-43m	25.17	20.90	442.0	0.44	3.49[d]
kat	$P1$[a]	26.20	27.02	280.4	0.70	2.63
	P-42c	35.59	36.84	282.7	0.69	2.54
RHO	Im-3m	34.60	33.47	534.6	0.36	2.53
	$P1$[a]	34.75	34.14	534.6	0.36	2.53
ANA	I-3ad	43.87	45.25	409.0	0.47	2.87
	$P1$[a]	44.31	45.24	408.7	0.47	2.75
cag[b]	$Pbca$	121.81	116.99	409.0	0.49	2.58
zni[b]	I4$_1$cd	182.15	181.58	296.1	0.65	2.41

[a]-CF$_3$ groups across a 4-ring were placed in a "head-to-tail" orientation; [b]optimization was not successful, leading to structure disruption; [c]the shortest F$\cdots$F distance in subsequently established experimental structure is 3.08 Å; [d]the shortest F$\cdots$F distance in subsequently established disordered experimental structure is 3.75 Å.

4.3.2 Synthesis and Sample Characterization

The experimentally determined structures for qtz- and SOD-Zn(CF$_3$Im)$_2$ frameworks, as well as for the ligand H**CF$_3$Im**, have been deposited with the Cambridge Crystallographic Data Centre (CCDC codes 1859151−1859153).

Details of all experimental techniques, sample analysis, as well as examples of individual mechanochemical experiments are provided in the SI. In a typical mechanochemical experiment, reaction components were placed in a stainless steel jar of 10 mL volume, along with a milling liquid (50 µL per 0.1 mmol of each reactant, which maintained the liquid-to-solid ratio η^{49} below 0.25 µL.mg^{-1}) and two stainless steel balls of 7 mm diameter (1.34 g weight each), mounted on a Retsch MM400 mill. The mill was operated at 30 Hz in all cases. All samples of metal-organic frameworks were washed three times with methanol (MeOH) and dried under vacuum at room temperature. The samples were all analyzed using powder X-ray diffraction (PXRD) and Fourier-transform infrared attenuated total reflectance (FTIR-ATR) spectroscopy. Selected samples were also analyzed using thermogravimetric analysis (TGA) and nitrogen sorption at 77 K (see SI). The crystal structure of the ligand H**CF$_3$Im** was also determined using single crystal X-ray diffraction (see SI).

4.3.3 Calorimetric Measurements

Dissolution enthalpies of Zn(**CF$_3$Im**)$_2$ frameworks were measured with a CSC 4400 isothermal microcalorimeter operating at 25 ℃. A pellet (3-5 mg) of each chemical used in the thermodynamic cycle (**Table 4-2**) was hand-pressed, weighed using a Mettler microbalance, and dropped into 25.0 g of isothermally equilibrated 5 M HCl aqueous solution inside a 50 mL Teflon cell of the calorimeter. After each experiment the cell was reassembled with fresh solvent. The sample was

allowed to dissolve in the cell for at least 3 hours under mechanical stirring at approximately ½ Hz in all experiments. We have used a similar methodology in our previous thermochemical ZIF studies.[20,50]

Table 4-2. Thermodynamic cycle used to calculate the formation enthalpy of ZIFs with respect to ZnO and H**CF₃Im**.

Reactions	Enthalpy (ΔH, kJ·mol^{-1})
$\text{Zn}(\textbf{CF}_3\textbf{Im})_{2(s)} \rightarrow \text{Zn}^{2+}{}_{(aq)} + 2\ \textbf{CF}_3\textbf{Im}^-{}_{(aq)}$	$\Delta H_1 = \Delta H_s(\text{Zn}(\textbf{CF}_3\textbf{Im})_2)$
$\text{ZnO}_{(s)} + 2\text{H}^+{}_{(aq)} \rightarrow \text{Zn}^{2+}{}_{(aq)} + \text{H}_2\text{O}_{(aq)}$	$\Delta H_2 = \Delta H_s(\text{ZnO})$
$\text{H}\textbf{CF}_3\textbf{Im}_{(s)} \rightarrow \textbf{CF}_3\textbf{Im}^-{}_{(aq)} + \text{H}^+{}_{(aq)}$	$\Delta H_3 = \Delta H_s(\text{H}\textbf{CF}_3\textbf{Im})$
$\text{H}_2\text{O}_{(l)} \rightarrow \text{H}_2\text{O}_{(aq)}$	$\Delta H_4 = \Delta H_{dil}(\text{H}_2\text{O})$
$\text{ZnO}_{(s)} + 2\text{H}\textbf{CF}_3\textbf{Im}_{(s)} \rightarrow \text{Zn}(\textbf{CF}_3\textbf{Im})_{2(s)} + \text{H}_2\text{O}_{(l)}$	$\Delta H_5 = \Delta H_f = -\Delta H_1 + \Delta H_2 + 2\Delta H_3 - \Delta H_4$

4.4   Results and discussion

4.4.1 Results of computational screening

Both SEDC approaches gave an identical ranking of putative Zn(**CF₃Im**)₂ frameworks (**Table 4-1**), which is consistent with our previous comparative study[28] of different SEDC schemes in calculating MOF stability. Both MBD*- and D2-based calculations indicate that the most stable form of Zn(**CF₃Im**)₂ should be a non-porous qtz-framework. Experimental studies on Zn(**MeIm**)₂ and Zn(**EtIm**)₂ polymorphs, as well as other systems, indicate that open structures with a calculated energy ($E_{rel,c}$) up to ~25-30 kJ mol^{-1} above the lowest-energy one might be observable.[20,51] Therefore, it is reasonable to assume that qtz-, dia- and SOD-Zn(**CF₃Im**)₂, with

calculated energies under 20 kJ mol^{-1}, could be experimentally accessible. While $E_{rel,c}$ for kat-Zn(**CF₃Im**)$_2$ is just under 30 kJ mol^{-1}, this phase might be difficult to observe as it is a high-energy densely-packed structure (packing coefficient PC=0.70) that cannot be stabilized by guest inclusion.

Calculations reveal a striking effect of -CF$_3$ group orientation on ZIF stability: switching from the ordered *P*-42*c* structure for kat-Zn(**CF₃Im**)$_2$, in which -CF$_3$ groups are arranged "head-to-head" (**Figure 4-2**a), to the *P*1 model with -CF$_3$ groups in the "head-to-tail" orientation (**Figure 4-2**c) produced an energy gain of ~10 kJ mol^{-1} using either PBE+D2 or PBE+MBD* method. Corresponding difference for the less dense SOD-Zn(**CF₃Im**)$_2$ was between 5.0 and 6.2 kJ mol^{-1}, and under 1 kJ mol^{-1} for low-density ANA- and RHO-Zn(**CF₃Im**)$_2$. These results show that the orientation and potential disorder of -CF$_3$ groups can be an important factor in ZIF stability. Attempts to optimize zni- and cag-Zn(**CF₃Im**)$_2$, based on topologies found in ZIFs containing the unsubstituted imidazolate linker, were unsuccessful. Modeling led to significant, unrealistic distortions, involving the rupture of Zn-N bonds and the formation of Zn-F bonds involving -CF$_3$ groups. This suggests that a -CF$_3$ group cannot be easily accommodated within structural models based on the unsubstituted imidazole ligand.
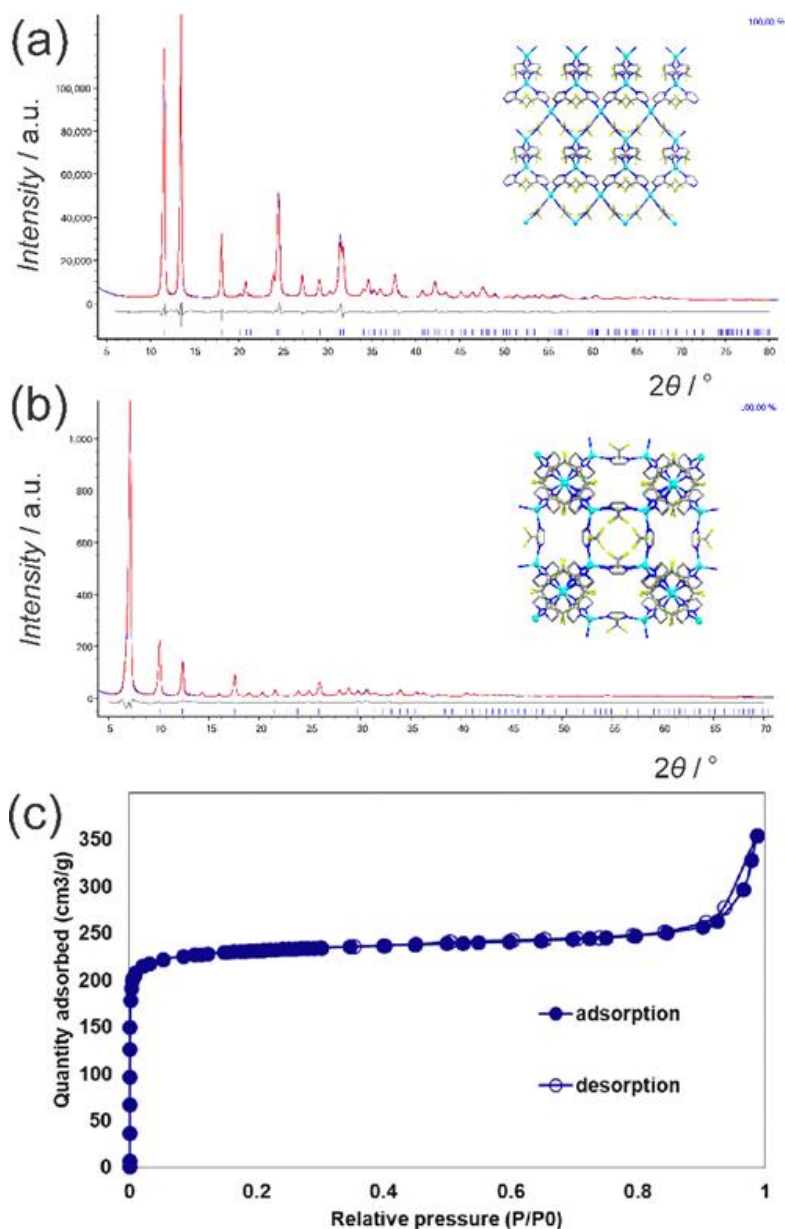
Figure 4-3. Final Rietveld refinement fits for: (a) qtz-Zn(**CF₃Im**)₂ and (b) SOD-Zn(**CF₃Im**)₂. (c) Nitrogen sorption isotherm measured at 77K for SOD-Zn(**CF₃Im**)₂.

To investigate the effects of crystal packing on the electronic properties of Zn(**CF₃Im**)₂, electronic density of states (DOS) plots were calculated for all predicted structures. Despite the differences in lattice energy and packing density, all structures displayed a remarkable similarity in their DOS

plots and calculated band gaps (see SI). It is evident that the electron distribution in ZIFs mostly depends on the nature of nodes and ligands, rather than their network topology.

4.4.2 Results of mechanochemical synthesis

Previous attempts to synthesize Zn(**CF₃Im**)₂ from solution were reported to be unsuccessful, instead leading to the precipitation of ZnO and/or the formation of oxo-bridged coordination polymers.[38] We based our synthesis on mechanochemical ion- and liquid-assisted grinding (ILAG),[52-54] *i.e.* ball milling of stoichiometric amounts of ZnO and **HCF₃Im** (see SI) in the presence of a liquid additive and a catalytic amount of a protic salt (NH₄NO₃, 10 mol% relative to ZnO). Powder X-ray diffraction analysis of reaction mixtures after 20 minutes of milling revealed different phases depending on the choice of liquid: CHCl₃, methanol, N,N-dimethylformamide (DMF) and 1,1,1-trifluoroethanol gave a new crystalline phase with characteristic Bragg reflections at 2θ of 11.5° and 13.5°. The PXRD pattern of the product obtained with DMF did not exhibit any reflections of reactants, indicating complete conversion, and on visual inspection was an excellent match to the computationally generated qtz-Zn(**CF₃Im**)₂ Structure and composition of qtz-Zn(**CF₃Im**)₂ were confirmed by Rietveld refinement (**Figure 4-3**a) and TGA in air (see SI for detailed experimental data).

In contrast, ILAG with ethanol or dioxane for 20 min gave a product whose PXRD pattern was consistent with a mixture of qtz-Zn(**CF₃Im**)₂ and a material isostructural to the putative SOD-Zn(**CF₃Im**)₂ phase. This phase was also observed for all liquid additives if ILAG was conducted for only 10 minutes (see SI), indicating that the mechanochemical reaction of ZnO and **HCF₃Im** proceeds over two stages, yielding first the open SOD-Zn(**CF₃Im**)₂, followed by the close-packed qtz-Zn(**CF₃Im**)₂. Such transformations of open to increasingly dense phases upon

mechanochemical ZIF synthesis have previously been noted.[20,39,53,54] Transformation to the qtz-polymorph made the synthesis of phase-pure SOD-Zn(**CF₃Im**)₂ challenging and, subsequently, a reliable synthesis was accomplished by milder liquid-assisted grinding (LAG)[49,55] of the more reactive[56] basic zinc carbonate $[ZnCO_3]_2[Zn(OH)_2]_3$, conducted in the presence of ethanol and without any protic salts that would encourage the structural rearrangement to the qtz-phase. After methanol washing and evacuation, the composition of SOD-Zn(**CF₃Im**)₂ was confirmed by TGA and Rietveld refinement (**Figure 4-3**b). Nitrogen sorption at 77 K revealed a surface area of 923 m^2/g, in good agreement with the value calculated from the crystal structure (1017 m^2 g^{-1}, **Figure 4-3**c, also see SI). The qtz-Zn(**CF₃Im**)₂ phase was non-porous, with measured surface area of 29 m^2 g^{-1}.

4.4.3 Results of thermochemical measurements

Availability of phase-pure samples allowed us to evaluate the enthalpies of formation (ΔH_f, Equation 1 in **Figure 4-1**b, **Table 4-3**) of qtz- and SOD-Zn(**CF₃Im**)₂ from ZnO and H**CF₃Im**, using dissolution enthalpies (ΔH_{ds}, **Table 4-3**) obtained by acid solution calorimetry.[20,50,51]

All measured ΔH_f are exothermic, indicating that the formation of both frameworks from ZnO is thermodynamically driven. However, ΔH_f for SOD-Zn(**CF₃Im**)₂ is very small, which provides a tentative explanation for the formation of ZnO in attempts to obtain this material from solution.[38] The difference in ΔH_f for SOD-and qtz-Zn(**CF₃Im**)₂ is 15.63 kJ mol^{-1}, suggesting that the observed two-step mechanosynthesis mechanism, in which the initially formed SOD-phase transforms to qtz-Zn(**CF₃Im**)₂, follows Ostwald's rule of stages.[58]

Table 4-3. Dissolution (ΔH_{ds}), Formation (ΔH_f) and Transition (ΔH_{trans}) Enthalpies for qtz-$Zn(CF_3Im)_2$, SOD-$Zn(CF_3Im)_2$ and related reaction components (kJ mol^{-1}).

Compound	ΔH_{ds}	ΔH_f	ΔH_{trans}
ZnO	-72.29 ± 0.17[a]	-	-
HCF$_3$Im	-0.82 ± 0.03	-	-
H$_2$O	-0.35[a]	-	-
qtz-Zn(**CF₃Im**)$_2$	-53.97 ± 0.20	-19.60 ± 0.27	27.10 ± 1.04
SOD-Zn(**CF₃Im**)$_2$	-69.61 ± 0.54	-3.97 ± 0.57	42.73 ± 1.15

[a]references 20, [b]Calculated from dilution enthalpy of HCl[57]

The ΔH_f difference between SOD- and qtz-polymorphs of Zn(**CF₃Im**)$_2$ is remarkably close to the $E_{rel,c}$ for SOD-Zn(**CF₃Im**)$_2$ obtained using the MBD* method (15.93 kJ mol^{-1}, **Table 4-1**), and is only 3.4 kJ mol^{-1} different from that obtained using D2. Such an excellent agreement validates the use of SEDC, and particularly the MBD* method, in calculating ZIF stability. This led us to revisit stabilities of Zn(**MeIm**)$_2$ polymorphs using PBE+MBD*, revealing excellent agreement with experiment (**Table 4-4**).[20]

Table 4-4 Relative stabilities calculated using PBE+D2[a] and PBE+MBD* methods ($E_{rel,c}$, kJ mol^{-1}) and experimental ΔH_{rel} (kJ mol^{-1}) for Zn(MeIm)$_2$ polymorphs.

Framework	$E_{rel,c}$ (PBE+D2)[a]	$E_{rel,c}$ (PBE+MBD*)	ΔH_{rel}
dia-Zn(**MeIm**)$_2$	0.0	0.0	0.0
kat-Zn(**MeIm**)$_2$	7.1	4.7	2.3
SOD-Zn(**MeIm**)$_2$	15.2	11.2	10.6

[a]from reference 20.

The ΔH_f was used to obtain the transition enthalpy (ΔH_{trans}, **Table 4-3**),[20,51,59] a measure of enthalpic changes associated with pore formation from a hypothetical nonporous dense state. The ΔH_{trans} was calculated by subtracting from ΔH_f the enthalpic effects (previously evaluated as -46.7 ± 1.0 kJ mol^{-1}) related to the change in metal coordination environment from oxygen- to a nitrogen-based one. The resulting ΔH_{trans} values for qtz- and SOD-Zn(**CF$_3$Im**)$_2$ are positive, indicating that the change in metal coordination environment is the principal reason for ZIF formation from ZnO. The comparison of ΔH_{trans} for SOD- and qtz-Zn(**CF$_3$Im**)$_2$ to those previously reported[20] for polymorphs of Zn(**MeIm**)$_2$ and Zn(**EtIm**)$_2$ reveals an unexpected effect of peripheral ligand substituent on ZIF stability (**Figure 4-4**). Namely, switching between -CH$_3$, -C$_2$H$_5$ and -CF$_3$ substituents yields sets of ZIFs of similar network density (number of nodes per nm^3) but with significant energy differences. For example, the network densities of SOD-Zn(**CF$_3$Im**)$_2$, SOD-Zn(**MeIm**)$_2$ and ANA-Zn(**EtIm**)$_2$ are close, but the frameworks span an energetic stability range of experimentally measured enthalpies of 27.7 kJ mol^{-1}. Similarly, qtz-Zn(**CF$_3$Im**)$_2$, kat-Zn(**MeIm**)$_2$ and qtz-Zn(**EtIm**)$_2$ have similar network densities, but with measured enthalpies over a range of 21.7 kJ mol^{-1}. In both sets of materials, the framework stability

falls in the sequence -CF$_3$ < -CH$_3$ < C$_2$H$_5$. A similar effect is observed for pairs of ZIFs with identical topologies, e.g. SOD-Zn(**CF₃Im**)$_2$ vs SOD-Zn(**MeIm**)2 and qtz-Zn(**CF₃Im**)$_2$ vs qtz-Zn(**EtIm**)2. In both pairs the -CF$_3$ substituent produces a material with ca. 20 kJ mol^{-1} more endothermic ΔH_f and ΔH_{trans} compared to the hydrocarbon one.
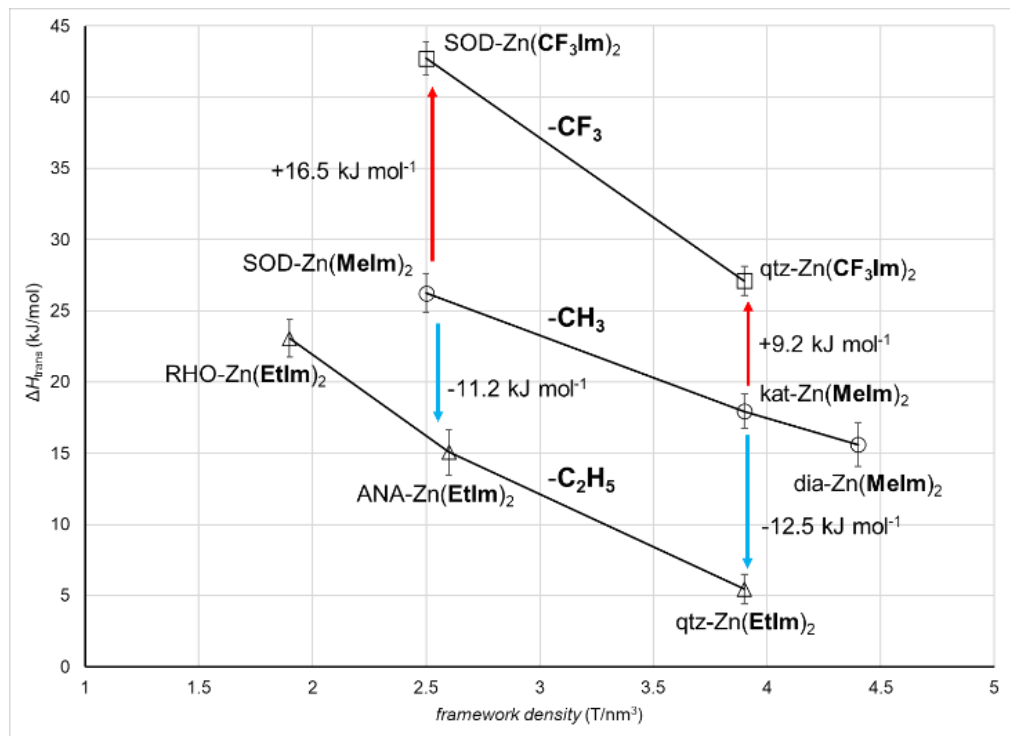
Figure 4-4. ΔH_{trans} for polymorphs of Zn(**CF₃Im**)$_2$ (this work), Zn(**MeIm**)$_2$,[20] and Zn(**EtIm**)$_2$,[20] highlighting energy differences between structures of similar framework density.

This is a remarkable result which indicates that hydrocarbon groups can notably increase the stability of a ZIF, while a fluorine-bearing substituent leads to destabilization. The presented results suggest a means to at least partially decouple the substituent effects on framework stability from its topology or network density. Qualitatively, the reduction in the stability of the ZIF structures upon introducing a trifluoromethyl substituent can be rationalized by several factors, including changes in Zn-N bond strength, repulsion between -CF$_3$ substituents, as well as the

ability of hydrocarbon groups to form C-H···π interactions to adjacent imidazolate linkers. The herein observed reduction in MOF stability upon introducing a fluorinated substituent is in contrast to a previous report describing an enhancement in MOF stability upon fluorination. However, the previously reported stabilization was partially rationalized by short H···F intermolecular interactions involving hydrocarbon and fluorocarbon moieties in the MOF. Such a mechanism is not likely to be significant in the herein determined $Zn(CF_3Im)_2$ structures, as the SOD-polymorph does not exhibit any H···F contacts shorter than the sum of van der Waals radii for hydrogen and fluorine (2.57 Å),[60] while the qtz-form exhibits only one such contact (2.53 Å).

4.5   Conclusions

In summary, this combined synthetic, theoretical and calorimetric study demonstrates the ability of dispersion-corrected periodic DFT to correctly model and anticipate the topological preferences for a previously not synthesized ZIF. Comparison of computational and thermochemical data shows that MBD* correction within periodic DFT CASTEP calculations also offers high accuracy in determining relative stabilities of ZIFs polymorphs, within 0.3-2.6 kJ mol^{-1} from the experiment. This study also reveals a surprising difference in stability between ZIFs exhibiting similar network density, but a different choice of linker substituents, suggesting a potential route to manipulate the thermodynamic stability of MOFs. While the calculations suggest that a dia-$Zn(CF_3Im)_2$ phase should also be accessible, the inability to observe it could be related to experimental limitations, similar to kat-Zn(**MeIm**)$_2$ which was observed years after SOD- and dia-forms. In that context, it is important to highlight the efficiency of mechanochemistry, which rapidly produced two polymorphs of previously not accessible[38] Zn(**CF₃Im**)$_2$. Overall, the herein demonstrated match between theory and experimental results is excellent and stands as a further benchmark for the

modeling community — where the direct evaluation through experimental calorimetry[20,59,61] remains rare.

4.6   Acknowledgment

4.7   References

(1)   Farha, O. K.; Hupp, J. T. Rational Design, Synthesis, Purification, and Activation of Metal−Organic Framework Materials. Acc. Chem. Res. 2010, 43, 1166–1175.

(2)   Furukawa, H.; Cordova, K. E.; O'Keeffe, M.; Yaghi, O. M. The Chemistry and Applications of Metal-Organic Frameworks. Science 2013, 341, 1230444–1230444.

(3)   Rungtaweevoranit, B.; Diercks, C. S.; Kalmutzki, M. J.; Yaghi, O. M. Spiers Memorial Lecture: : Progress and Prospects of Reticular Chemistry. Faraday Discuss. 2017, 201, 9–45.

(4)   Coudert, F.-X.; Fuchs, A. H. Computational Characterization and Prediction of Metal–organic Framework Properties. Coord. Chem. Rev. 2016, 307, 211–236.

(5)   Wilmer, C. E.; Leaf, M.; Lee, C. Y.; Farha, O. K.; Hauser, B. G.; Hupp, J. T.; Snurr, R. Q. Large-Scale Screening of Hypothetical Metal–organic Frameworks. Nat. Chem. 2012, 4, 83–89.

(6)   Chung, Y. G.; Gómez-Gualdrón, D. A.; Li, P.; Leperi, K. T.; Deria, P.; Zhang, H.; Vermeulen, N. A.; Stoddart, J. F.; You, F.; Hupp, J. T.; Farha, O. K.; Snurr, R. Q. In Silico Discovery of Metal-Organic Frameworks for Precombustion CO_2 Capture Using a Genetic Algorithm. Sci. Adv. 2016, 2, e1600909.

(7)   Witman, M.; Ling, S.; Anderson, S.; Tong, L.; Stylianou, K. C.; Slater, B.; Smit, B.; Haranczyk, M. In Silico Design and Screening of Hypothetical MOF-74 Analogs and Their Experimental Synthesis. Chem. Sci. 2016, 7, 6263–6272.

(8)   Moghadam, P. Z.; Islamoglu, T.; Goswami, S.; Exley, J.; Fantham, M.; Kaminski, C. F.; Snurr, R. Q.; Farha, O. K.; Fairen-Jimenez, D. Computer-Aided Discovery of a Metal–organic Framework with Superior Oxygen Uptake. Nat. Commun. 2018, 9, 1378.

(9)   Witman, M.; Ling, S.; Gladysiak, A.; Stylianou, K. C.; Smit, B.; Slater, B.; Haranczyk, M. Rational Design of a Low-Cost, High-Performance Metal–Organic Framework for Hydrogen Storage and Carbon Capture. J. Phys. Chem. C 2017, 121, 1171–1181.

(10) Borboudakis, G.; Stergiannakos, T.; Frysali, M.; Klontzas, E.; Tsamardinos, I.; Froudakis, G. E. Chemically Intuited, Large-Scale Screening of MOFs by Machine Learning Techniques. npj Comput. Mater. 2017, 3, 40.

(11) Collins, S. P.; Daff, T. D.; Piotrkowski, S. S.; Woo, T. K. Materials Design by Evolutionary Optimization of Functional Groups in Metal-Organic Frameworks. Sci. Adv. 2016, 2, e1600954.

(12) Mellot-Draznieks, C.; Kerkeni, B. Exploring the Interplay between Ligand and Topology in Zeolitic Imidazolate Frameworks with Computational Chemistry. Mol. Simul. 2014, 40, 25–32.

(13) Galvelis, R.; Slater, B.; Chaudret, R.; Creton, B.; Nieto-Draghi, C.; Mellot-Draznieks, C. Impact of Functionalized Linkers on the Energy Landscape of ZIFs. CrystEngComm 2013, 15, 9603–9612.

(14) Baburin, I. A.; Leoni, S. The Energy Landscapes of Zeolitic Imidazolate Frameworks (ZIFs): Towards Quantifying the Presence of Substituents on the Imidazole Ring. J. Mater. Chem. 2012, 22, 10152–10154.

(15) Liu, W.-G.; Truhlar, D. G. Computational Linker Design for Highly Crystalline Metal–Organic Framework NU-1000. Chem. Mater. 2017, 29, 8073–8081.

(16) Zhang, J.-P.; Zhang, Y.-B.; Lin, J.-B.; Chen, X.-M. Metal Azolate Frameworks: From Crystal Engineering to Functional Materials. Chem. Rev. 2012, 112, 1001–1033.

(17) Park, K. S.; Ni, Z.; Cote, A. P.; Choi, J. Y.; Huang, R.; Uribe-Romo, F. J.; Chae, H. K.; O'Keeffe, M.; Yaghi, O. M. Exceptional Chemical and Thermal Stability of Zeolitic Imidazolate Frameworks. Proc. Natl. Acad. Sci. 2006, 103, 10186–10191.

(18) Huang, X. C.; Lin, Y. Y.; Zhang, J. P.; Chen, X. M. Ligand-Directed Strategy for Zeolite-Type Metal-Organic Frameworks: Zinc(II) Imidazolates with Unusual Zeolitic Topologies. Angew. Chem. Int. Ed. 2006, 45, 1557–1559.

(19) He, C.-T.; Jiang, L.; Ye, Z.-M.; Krishna, R.; Zhong, Z.-S.; Liao, P.-Q.; Xu, J.; Ouyang, G.; Zhang, J.-P.; Chen, X.-M. Exceptional Hydrophobicity of a Large-Pore Metal–Organic Zeolite. J. Am. Chem. Soc. 2015, 137, 7217–7223.

(20) Akimbekov, Z.; Katsenis, A. D.; Nagabhushana, G. P.; Ayoub, G.; Arhangelskis, M.; Morris, A. J.; Friščić, T.; Navrotsky, A. Experimental and Theoretical Evaluation of the Stability of True MOF Polymorphs Explains Their Mechanochemical Interconversions. J. Am. Chem. Soc. 2017, 139, 7952–7957.

(21) Schröder, C. A.; Baburin, I. A.; van Wüllen, L.; Wiebcke, M.; Leoni, S. Subtle Polymorphism of Zinc Imidazolate Frameworks: Temperature-Dependent Ground States in the Energy Landscape Revealed by Experiment and Theory. CrystEngComm 2013, 15, 4036–4040.

(22) Baburin, I. A.; Leoni, S.; Seifert, G. Enumeration of Not-yet-Synthesized Zeolitic Zinc Imidazolate MOF Networks: A Topological and DFT Approach. J. Phys. Chem. B 2008, 112, 9437–9443.

(23) Lewis, D. W.; Ruiz-Salvador, A. R.; Gómez, A.; Rodriguez-Albelo, L. M.; Coudert, F.-X.; Slater, B.; Cheetham, A. K.; Mellot-Draznieks, C. Zeolitic Imidazole Frameworks: Structural and Energetics Trends Compared with Their Zeolite Analogues. CrystEngComm 2009, 11, 2272–2276.

(24) Galvelis, R.; Slater, B.; Cheetham, A. K.; Mellot-Draznieks, C. Comparison of the Relative Stability of Zinc and Lithium-Boron Zeolitic Imidazolate Frameworks. CrystEngComm 2012, 14, 374–378.

(25) Schweinefuß, M. E.; Springer, S.; Baburin, I. A.; Hikov, T.; Huber, K.; Leoni, S.; Wiebcke, M. Zeolitic Imidazolate Framework-71 Nanocrystals and a Novel SOD-Type Polymorph: Solution Mediated Phase Transformations, Phase Selection via Coordination Modulation and a Density Functional Theory Derived Energy Landscape. Dalton Trans. 2014, 43, 3528–3536.

(26) Nazarian, D.; Camp, J. S.; Chung, Y. G.; Snurr, R. Q.; Sholl, D. S. Large-Scale Refinement of Metal-Organic Framework Structures Using Density Functional Theory. Chem. Mater. 2017, 29, 2521–2528.

(27) Rosen, A. S.; Notestein, J. M.; Snurr, R. Q. Identifying Promising Metal–organic Frameworks for Heterogeneous Catalysis via High-throughput Periodic Density Functional Theory. J. Comput. Chem. 2019, DOI: 10.1002/jcc.25787.

(28) Arhangelskis, M.; Katsenis, A. D.; Morris, A. J.; Friščić, T. Computational Evaluation of Metal Pentazolate Frameworks: Inorganic Analogues of Azolate Metal–organic Frameworks. Chem. Sci. 2018, 9, 3367–3375.

(29) Zhang, D.-S.; Chang, Z.; Li, Y.-F.; Jiang, Z.-Y.; Xuan, Z.-H.; Zhang, Y.-H.; Li, J.-R.; Chen, Q.; Hu, T.-L.; Bu, X.-H. Fluorous Metal-Organic Frameworks with Enhanced Stability and High H_2/CO_2 Storage Capacities. Sci. Rep. 2013, 3, 3312.

(30) Cadiau, A.; Belmabkhout, Y.; Adil, K.; Bhatt, P. M.; Pillai, R. S.; Shkurenko, A.; Martineau-corcos, C.; Maurin, G.; Eddaoudi, M. Hydrolytically Stable Fluorinated Metal-Organic Frameworks for Energy-Efficient Dehydration. Science 2017, 356, 731–735.

(31) Noro, S.; Nakamura, T. Fluorine-Functionalized Metal–organic Frameworks and Porous Coordination Polymers. NPG Asia Mater. 2017, 9, e433.

(32) Bhatt, P. M.; Belmabkhout, Y.; Cadiau, A.; Adil, K.; Shekhah, O.; Shkurenko, A.; Barbour, L. J.; Eddaoudi, M. A Fine-Tuned Fluorinated MOF Addresses the Needs for Trace CO2 Removal and Air Capture Using Physisorption. J. Am. Chem. Soc. 2016, 138, 9301–9307.

(33) Pachfule, P.; Chen, Y.; Jiang, J.; Banerjee, R. Fluorinated Metal-Organic Frameworks: Advantageous for Higher H_2 and CO_2 Adsorption or Not? Chem. Eur. J. 2012, 18, 688–694.

(34) Chen, T.-H.; Popov, I.; Kaveevivitchai, W.; Chuang, Y.-C.; Chen, Y.-S.; Jacobson, A. J.; Miljanić, O. Š. Mesoporous Fluorinated Metal-Organic Frameworks with Exceptional Adsorption of Fluorocarbons and CFCs. Angew. Chem. Int. Ed. 2015, 54, 13902–13906.

(35) Belmabkhout, Y.; Bhatt, P. M.; Adil, K.; Pillai, R. S.; Cadiau, A.; Shkurenko, A.; Maurin, G.; Liu, G.; Koros, W. J.; Eddaoudi, M. Natural Gas Upgrading Using a Fluorinated MOF with Tuned H_2S and CO_2 Adsorption Selectivity. Nat. Energy 2018, 3, 1059–1066.

(36) Liu, G.; Cadiau, A.; Liu, Y.; Adil, K.; Chernikova, V.; Carja, I. D.; Belmabkhout, Y.; Karunakaran, M.; Shekhah, O.; Zhang, C.; Itta, A. K.; Yi, S.; Eddaoudi, M.; Koros, W. J. Enabling Fluorinated MOF-Based Membranes for Simultaneous Removal of H_2S and CO_2 from Natural Gas. Angew. Chem. Int. Ed. 2018, 57, 14811–14816.

(37) Tchalala, M. R.; Belmabkhout, Y.; Adil, K.; Chappanda, K. N.; Cadiau, A.; Bhatt, P. M.; Salama, K. N.; Eddaoudi, M. Concurrent Sensing of CO_2 and H_2O from Air Using Ultramicroporous Fluorinated Metal–Organic Frameworks: Effect of Transduction Mechanism on the Sensing Performance. ACS Appl. Mater. Interfaces 2019, 11, 1706–1712.

(38) Mondal, S. S.; Hovestadt, M.; Dey, S.; Paula, C.; Glomb, S.; Kelling, A.; Schilde, U.; Janiak, C.; Hartmann, M.; Holdt, H.-J. Synthesis of a Partially Fluorinated ZIF-8 Analog for Ethane/Ethene Separation. CrystEngComm 2017, 19, 5882–5891.

(39) Katsenis, A. D.; Puškarić, A.; Štrukil, V.; Mottillo, C.; Julien, P. A.; Užarević, K.; Pham, M.-H.; Do, T.-O.; Kimber, S. A. J.; Lazić, P.; Magdysyuk, O.; Dinnebier, R. E.; Halasz, I.; Friščić, T. In Situ X-Ray Diffraction Monitoring of a Mechanochemical Reaction Reveals a Unique Topology Metal-Organic Framework. Nat. Commun. 2015, 6, 6662.

(40) Cambridge Structural Database (CSD), version 5.39 (February 2018).

(41) Clark, S. J.; Segall, M. D.; Pickard, C. J.; Hasnip, P. J.; Probert, M. I. J.; Refson, K.; Payne, M. C. First Principles Methods Using CASTEP. Z. Kristallogr. 2005, 220, 567–570.

(42) Grimme, S. Semiempirical GGA-Type Density Functional Constructed with a Long-Range Dispersion Correction. J. Comput. Chem. 2006, 27, 1787–1799.

(43) Tkatchenko, A.; DiStasio Jr, R. A.; Car, R.; Scheffler, M. Accurate and Efficient Method for Many-Body van Der Waals Interactions. Phys. Rev. Lett. 2012, 108, 236402.

(44) Ambrosetti, A.; Reilly, A. M.; DiStasio, R. A.; Tkatchenko, A. Long-Range Correlation Energy Calculated from Coupled Atomic Response Functions. J. Chem. Phys. 2014, 140, 18A508.

(45) Reilly, A. M.; Tkatchenko, A. Van Der Waals Dispersion Interactions in Molecular Materials: Beyond Pairwise Additivity. Chem. Sci. 2015, 6, 3289–3301.

(46) Monkhorst, H. J.; Pack, J. D. Special Points for Brillouin-Zone Integrations. Phys. Rev. B 1976, 13, 5188–5192.

(47) Nicholls, R. J.; Morris, A. J.; Pickard, C. J.; Yates, J. R. OptaDOS - a New Tool for EELS Calculations. J. Phys. Conf. Ser. 2012, 371, 012062.

(48) Morris, A. J.; Nicholls, R. J.; Pickard, C. J.; Yates, J. R. OptaDOS: A Tool for Obtaining Density of States, Core-Level and Optical Spectra from Electronic Structure Codes. Comput. Phys. Commun. 2014, 185, 1477–1485.

(49) Friščić, T.; Childs, S. L.; Rizvi, S. A. A.; Jones, W. The Role of Solvent in Mechanochemical and Sonochemical Cocrystal Formation: A Solubility-Based Approach for Predicting Cocrystallisation Outcome. CrystEngComm 2009, 11, 418–426.

(50) Hughes, J. T.; Bennett, T. D.; Cheetham, A. K.; Navrotsky, A. Thermochemistry of Zeolitic Imidazolate Frameworks of Varying Porosity. J. Am. Chem. Soc. 2013, 135, 598–601.

(51) Akimbekov, Z.; Navrotsky, A. Little Thermodynamic Penalty for the Synthesis of Ultraporous Metal Organic Frameworks. ChemPhysChem 2016, 17, 468–470.

(52) Do, J.-L.; Friščić, T. Mechanochemistry: A Force of Synthesis. ACS Cent. Sci. 2017, 3, 13–19.

(53) Beldon, P. J.; Fabian, L.; Stein, R. S.; Thirumurugan, A.; Cheetham, A. K.; Friščić, T. Rapid Room-Temperature Synthesis of Zeolitic Imidazolate Frameworks by Using Mechanochemistry. Angew. Chem., Int. Ed. 2010, 49, 9640−9643.

(54) Friščić, T.; Halasz, I.; Beldon, P. J.; Belenguer, A. M.; Adams, F.; Kimber, S. A. J.; Honkimäki, V.; Dinnebier, R. E. Real-time and in situ monitoring of mechanochemical milling reactions. Nat. Chem. 2013, 5, 66−73.

(55) Friščić, T. New Opportunities for Materials Synthesis Using Mechanochemistry. J. Mater. Chem. 2010, 20, 7599–7605.

(56) Yuan, W.; Friščić, T.; Apperley, D.; James, S. L. High Reactivity of Metal-Organic Frameworks under Grinding Conditions: Parallels with Organic Molecular Materials. Angew. Chem. Int. Ed. 2010, 49, 3916–3919.

(57) Parker, V. B. Thermal Properties of Aqueous Uni-Univalent Electrolytes; Dept. of Commerce, National Bureau of Standards: Washington, D. C., 1965.

(58) Burley, J. C.; Duer, M. J.; Stein, R. S.; Vrcelj, R. M. Enforcing Ostwald's Rule of Stages: Isolation of Paracetamol Forms III and II. Eur. J. Pharm. Sci. 2007, 31, 271–276.

(59) Wu, D.; Navrotsky, A. Thermodynamics of Metal-Organic Frameworks. J. Solid State Chem. 2015, 223, 53–58.

(60) Mantina, M.; Chamberlin, A. C.; Valero, R.; Cramer, C. J.; Truhlar, D. G. Consistent van der Waals Radii for the Whole Main Group. J. Phys. Chem. A 2009, 113, 5806−5812.

(61) Akimbekov, Z.; Wu, D.; Brozek, C. K.; Dincă, M.; Navrotsky, A. Thermodynamics of Solvent Interaction with the Metal–organic Framework MOF-5. Phys. Chem. Chem. Phys. 2016, 18, 1158–1162.

Chapter 5:

Linker Substituents Control the Thermodynamic Stability in Metal-Organic Frameworks

This chapter is presented based on the following previously published paper:

Novendra, N.; Marrett, J. M.; Katsenis, A. D.; Titi, H. M.; Arhangelskis, M.; Friščić, T.; Navrotsky, A. Linker Substituents Control the Thermodynamic Stability in Metal–Organic Frameworks. *J. Am. Chem. Soc.* **2020**, *142*, 52, 21720-21729

Note: My contributions to this work are on the sample characterizations (thermogravimetric analysis, powder X-ray diffraction analysis, surface area measurements), calorimetric measurements, and discussion of the energetics of the system.

5.1   Abstract

We report the first systematic experimental and theoretical study of the relationship between linker functionalization and thermodynamic stability of metal-organic frameworks (MOFs), using a model set of eight isostructural zeolitic imidazolate frameworks (ZIFs) based on 2-substituted imidazolate linkers. The frameworks exhibit a significant (30 kJ·mol^{-1}) variation in the enthalpy of formation depending on the choice of substituent, which is accompanied by only a small change in molar volume. These energetics were readily reproduced by density functional theory (DFT) calculations. We show that these variations in the enthalpy of MOF formation are in linear

99

correlation to readily accessible properties of the linker substituent, such as the Hammett σ-constant or electrostatic surface potential. These results provide the first quantifiable relationship between MOF thermodynamics and linker structure, suggesting a route to design and tune MOF stability.

5.2 Introduction

Metal-organic frameworks (MOFs) are advanced materials whose modular structure permits combining high microporosity with a range of functional properties.[1–19] Whereas MOF development has led to sophisticated functional materials, achieving thermodynamic stability by design remains a challenge.[20–22] For example, while sensitivity of MOFs to hydrolytic degradation by water is a topic of high interest,[23,24] most studies have focused on kinetic aspects of the process, *e.g.* by introducing hydrophobic substituents[25–27] or changing MOF design to increase the strength of metal-linker bonds.[27–31] In contrast, thermodynamic driving forces behind MOF stability remain largely unexplored and poorly understood. We have previously explored the relationship between thermodynamic stability and topology of zeolitic imidazolate frameworks (ZIFs),[32–36] a class of MOFs with topological diversity akin to zeolites.[37–39] This enabled quantitative evaluation of structure-related energy differences between MOF polymorphs, and indicated periodic density functional theory (DFT)[40–44] with semi-empirical dispersion correction (SEDC)[45–47] as an accurate tool to calculate relative thermodynamic stabilities of MOFs.

We now reveal that the enthalpy of formation of MOFs can be strongly and predictably influenced by peripheral substitution on the linker, providing a rational route to tune the framework thermodynamic stability without large-scale changes to MOF topology or design. Specifically, we present a systematic experimental and theoretical study of the enthalpies of formation for eight

100

isostructural, microporous ZIFs of sodalite (SOD) topology bearing different groups in the 2-position of the imidazolate linker (**Figure 5-1**, R = CH$_3$, CH=CH$_2$, C≡CH, CHO, CF$_3$, Cl, Br, I). Experimental calorimetry measurements show that the enthalpy of MOF formation with respect to the metal oxide can be varied over a wide range (~30 kJ·mol^{-1}) simply by replacing the substituent on the linker (**Table 5-1).** It was previously shown that an accurate calculation[33,34] and even prediction[48,49] of MOF stability can be achieved by using extensive periodic DFT calculations. Here we show that the substituent-related variations in MOF stability are in a linear and quantifiable relationship with readily accessible parameters such as the Hammett σ-constants or electrostatic surface potentials (ESPs) of the linker substituent. This linear relationship between framework thermodynamics and easily accessible substituent properties opens the door for strategies to control MOF stability *via* peripheral modifications of the linker, in contrast with current approaches that involve significant changes to the metal node, linker structure, framework density and/or topology.[22,50–53] In such a scenario, the linker becomes an active contributor not only to MOF functionality, but also to its thermodynamic stability.
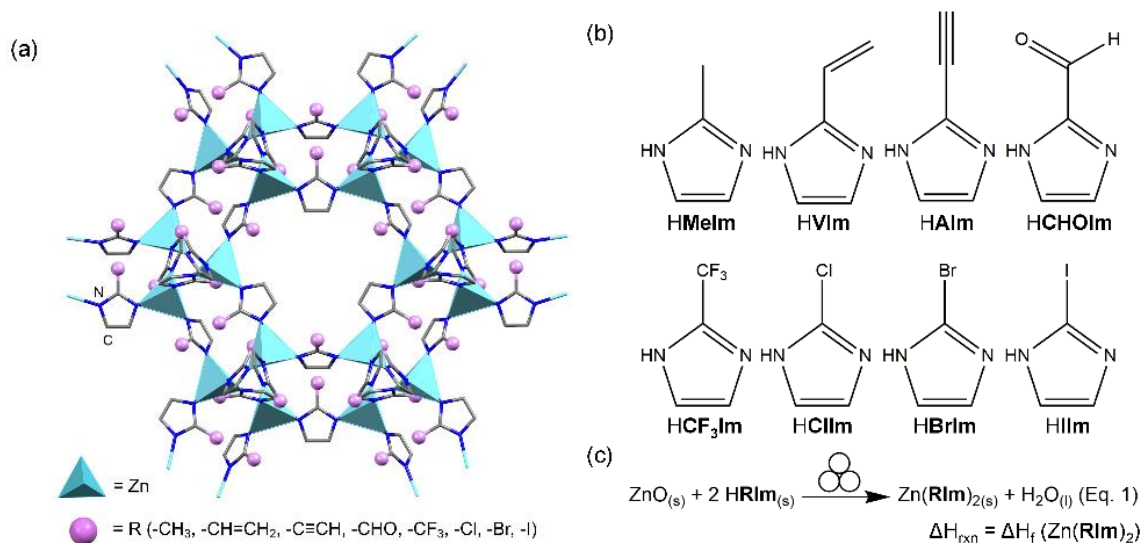
Figure 5-1. (a) A SOD-topology ZIF structure, highlighting the linker 2-substituent (**R**); (b) used imidazoles: 2-methyl- (**HMeIm**), 2-vinyl- (**HVIm**), 2-acetylene- (**HAIm**), 2-carbaldehyde- (**HCHOIm**), 2-trifluoromethyl- (**HCF₃Im**), 2-chloro- (**HClIm**), 2-bromo- (**HBrIm**), and 2-iodoimidazole (**HIIm**), (c) Formation of SOD-Zn(**RIm**)$_2$ ZIFs from ZnO, and the associated thermodynamic parameter.

5.3 Experimental Section

Details of experimental techniques and sample characterizations are provided in the appendix.

5.3.1 Thermodynamic Measurements

Dissolution enthalpies (ΔH_s) were measured with a CSC 4400 isothermal microcalorimeter operating at 25 ℃. Small sample sizes (around 5 mg) were used to ensure that the concentration of dissolved ions is sufficiently low to avoid enthalpy contribution from ion mixing. Additionally, several experimental trials using mechanical mixtures of samples, which gave enthalpy values consistent with mechanical mixtures, confirmed that the measured enthalpies of dissolution were

additive for the components, so any contribution from possible ion complex formation can be neglected. In each experiment, ca. 5 mg of sample used in the thermodynamic cycle (**Table 5-1**) was hand-pressed to form a pellet and dropped into 25.0 g of isothermally equilibrated 5 N HCl aqueous solution inside a 50 mL Teflon cell of the calorimeter. All weight measurements were done using a Mettler microbalance with an accuracy of 10 μg. The solvent was isothermally equilibrated for at least 3 hours under mechanical stirring before the sample was introduced and was then allowed to dissolve in the cell for at least 3 hours, ensuring the return of the baseline back to the initial position. After each experiment, the cell was reassembled with fresh solvent. We have used a similar methodology in our previous thermochemical MOF studies.[32–34] The uncertainties given in the results represent a 95% confidence interval.

5.3.2 Theoretical Calculations

Periodic DFT calculations were performed using the plane-wave DFT code CASTEP 19.1.[54] The experimental CIFs of sodalite MOFs and the corresponding linkers were converted into CASTEP input format using the program cif2cell.[55] Calculations were performed with the PBE functional,[56] combined with the many-body dispersion (MBD*)[57–59] SEDC model, which has shown superior performance in our previous computational studies of MOF topological polymorphism.[34] The plane-wave basis set was truncated at an 800 eV cutoff, and the ultrasoft on-the-fly pseudopotentials were used to attenuate the Coulomb potentials within the core regions of electron density. The electronic 1st Brillouin zone was sampled with a $2\pi \times 0.05$ Å^{-1} Monkhorst-Pack k-point grid.[60] The structures were geometry-optimized with respect to atom coordinates and unit cell parameters, subject to space group symmetry constraints. The calculations were deemed converged upon satisfying the following criteria: a total energy change of 10^{-5} eV·atom^{-1}; a

maximum atomic displacement 10^{-3} Å; a maximum atomic force 0.05 eV·Å^{-1} and residual stress 0.05 GPa. The calculated energies were used to compute the relative energy of formation ($E_{f,rel}$) for a SOD-topology ZIF based on an imidazolate linker bearing the general substituent **R** in the 2-position, with respect to the corresponding 2-methyl-substituted framework Zn(**MeIm**)$_2$ (ZIF-8), following the equation:

$$E_{f,rel}(Zn(\mathbf{RIm})_2) = E(Zn(\mathbf{RIm})_2) - E(Zn(\mathbf{MeIm})_2) - 2[E(H\mathbf{RIm}) - E(H\mathbf{MeIm})] \qquad \text{(Eq. 2)}$$

where $E(Zn(\mathbf{RIm})_2)$, $E(Zn(\mathbf{MeIm})_2)$, $E(H\mathbf{RIm})$ and $E(H\mathbf{MeIm})$ are calculated energies of the 2-substituted ZIFs, ZIF-8, 2-substituted imidazoles and H**MeIm** in the solid state, respectively.

Molecular DFT calculations of electrostatic surface potentials (ESPs) for substituents on imidazolate anions were performed using GAUSSIAN 16 version A.03.[61] The imidazolate anions were geometry-optimized using the PBE/6-311G(d,p) level of theory. The PBE functional was selected for consistency with the periodic DFT calculations. The substituent ESP values were calculated at the 0.002 a. u. isosurface of electron density.

Table 5-1. Thermodynamic cycle used to calculate the formation enthalpy of ZIFs with respect to ZnO and HRIm.

Reactions	Enthalpy (ΔH, kJ·mol^{-1})
Zn(**RIm**)$_{2(s)}$ → Zn^{2+}$_{(aq)}$ + 2 **RIm**$^-$$_{(aq)}$	$\Delta H_1 = \Delta H_s(\text{Zn}(\textbf{RIm})_2)$
ZnO$_{(s)}$ + 2H$^+$$_{(aq)}$ → Zn^{2+}$_{(aq)}$ + H$_2$O$_{(aq)}$	$\Delta H_2 = \Delta H_s(\text{ZnO})$
H**RIm**$_{(s)}$ → **RIm**$^-$$_{(aq)}$ + H$^+$$_{(aq)}$	$\Delta H_3 = \Delta H_s(\text{H}\textbf{RIm})$
H$_2$O$_{(l)}$ → H$_2$O$_{(aq)}$	$\Delta H_4 = \Delta H_{dil}(\text{H}_2\text{O})$
ZnO$_{(s)}$ + 2H**RIm**$_{(s)}$ → Zn(**RIm**)$_{2(s)}$ + H$_2$O$_{(l)}$	$\Delta H_5 = \Delta H_f = -\Delta H_1 + \Delta H_2 + 2\Delta H_3 - \Delta H_4$

5.4 Results and Discussion

5.4.1 Synthesis and Characterization of SOD-topology ZIFs

Based on the previously reported crystal structures or PXRD patterns, all herein explored MOFs are isostructural to ZIF-8 and adopt the SOD topology.[34,38,62–68] This provides a unique opportunity to evaluate changes to thermodynamic stability of ZIFs with variation of the linker substituent, without having to consider differences to framework topology or crystal structure. All eight ZIFs were obtained mechanochemically,[69–71] by liquid-assisted grinding (LAG) of either zinc oxide (ZnO, **Figure 5-1**c), or basic zinc carbonate (3Zn(OH)$_2$·2ZnCO$_3$),[72] with the appropriate amount of imidazole ligand: 2-methyl- (H**MeIm**), 2-trifluoromethyl- (H**CF$_3$Im**), 2-vinyl- (H**VIm**), 2-acetylene- (H**AIm**), 2-chloro- (H**ClIm**), 2-bromo- (H**BrIm**), 2-iodoimidazole (H**IIm**), and imidazole-2-carbaldehyde (H**CHOIm**). We have previously reported the mechanochemical syntheses and calorimetric characterization of ZIF-8 and Zn(**CF$_3$Im**)$_2$,[33,34] and that data is used in

this report. For all other cases, the varying of reaction parameters (amount of liquid additive,[73] milling time) enabled quantitative conversion of starting materials to the SOD-frameworks, as evidenced by the absence of reactant signals from the PXRD patterns and Fourier-transform infrared attenuated total reflectance (FTIR-ATR) spectra of the final products (see SI). The mechanochemically prepared materials were washed and evacuated before any further characterization, using previously described procedures (see SI).

Isostructurality of all prepared ZIFs to ZIF-8 was confirmed by comparison of powder X-ray diffraction (PXRD, **Figure 5-2**) patterns of the obtained materials to those calculated for ZIF-8 (CSD code VELVOY) and/or the corresponding ZIF. While the structures of ZIF-8,[38,62] ZIF-90,[63] SOD-Zn(**CF₃Im**)$_2$,[34] SOD-Zn(**VIm**)$_2$,[64,65] SOD-Zn(**AIm**)$_2$,[66] SOD-Zn(**ClIm**)$_2$,[67,68] and SOD-Zn(**BrIm**)$_2$[67,68] have previously been reported (**Table 5-3**), the structure of SOD-Zn(**IIm**)$_2$ was determined from PXRD data, using a model derived from the known SOD-Zn(**BrIm**)$_2$ structure by replacement of bromine with iodine atoms. The iodine-substituted ZIF structure revealed orientational disorder of the imidazolate linker, analogous to that previously observed in SOD-Zn(**ClIm**)$_2$, and SOD-Zn(**BrIm**)$_2$. The absence of included solvent in all prepared MOFs after washing and evacuation was confirmed by thermogravimetric analysis (TGA). Metal content was analyzed for samples of Zn(**BrIm**)$_2$, Zn(**IIm**)$_2$ and Zn(**AIm**)$_2$ using inductively coupled plasma mass spectrometry (ICP-MS), giving outcomes in excellent agreement with theoretically expected values. Zn(**CHOIm**)$_2$ was additionally characterized by ^{13}C cross-polarization magic angle spinning solid-state nuclear magnetic resonance spectroscopy (CP-MAS ssNMR), producing a spectrum that was an excellent match to that previously reported (see SI).[63] Microporosity was verified by nitrogen sorption measurements (**Table 5-3**) which gave Brunauer-Emmett-Teller (BET) surface areas consistent with previously published values (see SI).[34,38,62–67,74,75]

5.4.2 Thermodynamic Measurements

Enthalpies of formation (ΔH_f) for the ZIFs (**Table 5-3**) were calculated from the measured ΔH_s values for the ZIFs, imidazoles and ZnO, following the thermodynamic cycle of **Table 5-1**. The ΔH_f values for the formation of ZIFs by reaction of ZnO with two equivalents of the imidazole (Equation 1) are negative in all cases except ZIF-90, whose formation was endothermic by ca. 37 kJ·mol^{-1} (**Table 5-1**). ΔH_f values for other ZIFs were negative in the range from -4 kJ·mol^{-1} (for the -CF$_3$ substituent) to -20 kJ·mol^{-1} (for -CH$_3$ and -C≡CH substituents). While the exothermic nature of the reactions explains the generally observed ease of making ZIFs from the metal oxide using mechanochemistry or other types of processes, the ΔH_f values also provide an immediate and quantitative measure of ZIF stability to hydrolysis (Equation 3).

$$Zn(\mathbf{RIm})_{2(s)} + H_2O_{(l)} \rightarrow ZnO_{(s)} + 2H\mathbf{RIm}_{(s)} \text{ (Eq. 3)}$$
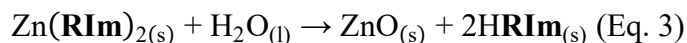
As the hydrolysis reaction is a process reverse to ZIF formation from the metal oxide, the associated reaction enthalpies must be endothermic and opposite to herein measured ΔH_f values, consistent with overall ZIF hydrolytic stability.[24,38,64,76,77]
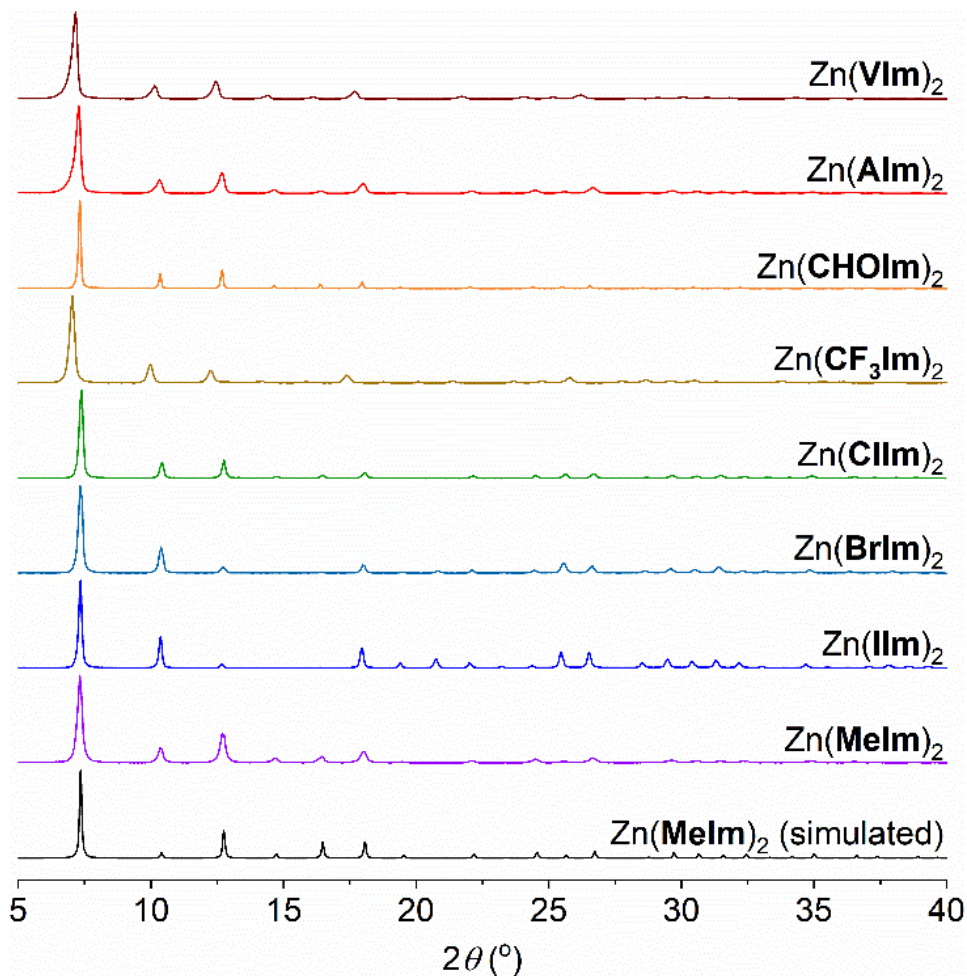
Figure 5-2. Comparison of PXRD patterns for mechanochemically prepared SOD-topology ZIFs, compared to the calculated pattern for ZIF-8 (CSD code VELVOY).

The endothermic ΔH_{f} for ZIF-90 (36.65 ± 1.03 kJ·mol^{-1}) is likely related to the unique structure of the **HCHOIm** ligand which was found to be dimeric in the solid state. With the exception of **HAIm** and **HBrIm**, whose crystal structures are not yet known, the measured PXRD patterns of solid imidazoles are an excellent match to those simulated for the crystal structures of imidazoles that were reported previously (**HCHOIm**, **HMeIm**, **HCF₃Im**)[34,78,79] or determined in this work (**HVIm**, **HClIm**, **HIIm**). All imidazoles are monomers in the solid state, with the exception of

HCHOIm whose crystal structure consists of tricyclic (**HCHOIm**)$_2$ dimers (CSD code YASSAN) (**Figure 5-3**).[79]
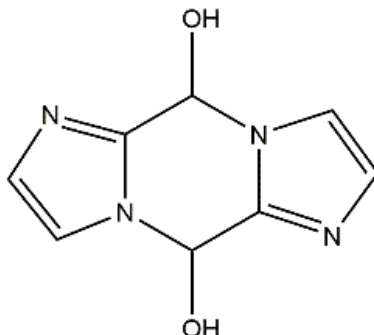
Figure 5-3. Molecular structure of the (HCHOIm)$_2$ dimer in the solid state.

To account for the dimeric structure of **HCHOIm** in the solid state, the corresponding ΔH_s must be recalculated (**Table 5-3**, line 4). Moreover, a new thermodynamic cycle must be constructed to properly include the ligand dimer structure into the ΔH_f calculation (**Table 5-2**). This new cycle would use the dimer dissociation enthalpy, $\Delta H_{dis}((\text{HCHOIm})_2)$, which requires measuring the ΔH_s for the ligand monomer which, to the best of our knowledge, has never been observed. Our repeated attempts to isolate the **HCHOIm** monomer by recrystallization from different solvents have so far been unsuccessful. To at least approximately account for the effect of ligand dimer structure on ΔH_f of ZIF-90, we calculated the energy for gas-phase dissociation of the **HCHOIm** dimer into two monomers (+26.64 kJ mol^{-1}). Including this calculated dissociation energy into the thermodynamic cycle gave a new corrected value for the enthalpy of ZIF-90 formation ($\Delta H_{f,cor}$) of ca. +10 kJ·mol^{-1} (**Table 5-1**). While this value is still endothermic, it is substantially smaller in magnitude than the initially calculated ΔH_f. We suspect that the actual enthalpy of ZIF-90 formation is probably even less endothermic than this, or even exothermic, but the true value cannot be calculated without knowing the ΔH_s for the still inaccessible **HCHOIm** monomer solid.

Table 5-2. Thermodynamic cycle used to calculate the formation enthalpy of ZIF-90 with respect to ZnO and (H**CHOIm**)$_2$ dimer ligand and consequent correction with dimer dissociation enthalpy.

Reactions	Enthalpy (ΔH, kJ·mol^{-1})
Zn(**CHOIm**)$_{2(s)}$ → Zn$^{2+}_{(aq)}$ + 2 **CHOIm**$^-_{(aq)}$	$\Delta H_1 = \Delta H_s(Zn(\mathbf{CHOIm})_2)$
ZnO$_{(s)}$ + 2H$^+_{(aq)}$ → Zn$^{2+}_{(aq)}$ + H$_2$O$_{(aq)}$	$\Delta H_2 = \Delta H_s(ZnO)$
(H**CHOIm**)$_{2\,(s)}$ → 2**CHOIm**$^-_{(aq)}$ + 2H$^+_{(aq)}$	$\Delta H_3 = \Delta H_s((H\mathbf{CHOIm})_2)$
H$_2$O$_{(l)}$ → H$_2$O$_{(aq)}$	$\Delta H_4 = \Delta H_{dil}(H_2O)$
ZnO$_{(s)}$ + (H**CHOIm**)$_{2\,(s)}$ → Zn(**CHOIm**)$_{2(s)}$ + H$_2$O$_{(l)}$	$\Delta H_5 = \Delta H_f = -\Delta H_1 + \Delta H_2 + 2\Delta H_3 - \Delta H_4$
(H**CHOIm**)$_{2\,(s)}$ → 2H**CHOIm**$_{(s)}$	$\Delta H_6 = \Delta H_{dis}((H\mathbf{CHOIm})_2)$
ZnO$_{(s)}$ + 2H**CHOIm**$_{(s)}$ → Zn(**CHOIm**)$_{2(s)}$ + H$_2$O$_{(l)}$	$\Delta H_7 = \Delta H_{f,cor} = \Delta H_5 - \Delta H_6$

Table 5-3. Selected structural information and thermodynamic data derived from acid solution calorimetry: unit cell

parameter (a, Å),[a] BET surface area (BET, $m^2 \cdot g^{-1}$), framework density in tetrahedral centers (T) per unit volume (FD,

$T \cdot nm^{-3}$)[a] and molar volume (MV, $cm^3 \cdot (mol\ Zn)^{-1}$) for herein explored ZIFs, as well as measured enthalpy of dissolution

(ΔH_s, $kJ \cdot mol^{-1}$), enthalpy of formation (ΔH_f, $kJ \cdot mol^{-1}$) and transition enthalpy (ΔH_{trans}, $kJ \cdot mol^{-1}$).

Compound	a (Å)[a]	BET area $m^2 \cdot g^{-1}$	FD[a] $T \cdot nm^{-3}$	MV[a] $cm^3 \cdot mol\ Zn^{-1}$	ΔH_s[b] $kJ \cdot mol^{-1}$	ΔH_f[c] $kJ \cdot mol^{-1}$	ΔH_{trans} $kJ \cdot mol^{-1}$
ZnO[33]	-	-	-	-	-72.29 ± 0.17	-	-
H$_2$O	-	-	-	-	-0.35	-	-
HCHOIm[d]	-	-	-	-	-8.26 ± 0.20	-	-
(HCHOIm)$_2$ (dimer)	-	-	-	-	-16.53 ± 0.40	-	-
HVIm	-	-	-	-	-27.91 ± 0.27	-	-
HAIm	-	-	-	-	-14.52 ± 0.17	-	-
HClIm	-	-	-	-	-5.49 ± 0.16	-	-
HBrIm	-	-	-	-	-5.45 ± 0.10	-	-
HIIm	-	-	-	-	-10.86 ± 0.14	-	-

Table 5-3. Continued

Compound	a (Å)[a]	BET area m^2·g^{-1}	FD[a] T·nm^{-3}	MV[a] cm^3·mol Zn^{-1}	ΔH_s[b] kJ·mol^{-1}	ΔH_f[c] kJ·mol^{-1}	ΔH_trans kJ·mol^{-1}
Zn(**MeIm**)$_2$[33]	16.9910(12)	1578 ± 42	2.50	240.99	-137.5 ± 0.83	-20.45 ± 0.94	26.25 ± 1.37
Zn(**CHOIm**)$_2$	17.2715(4)	1225 ± 62	2.33	258.55	-125.12 ± 0.94	36.65 ± 1.03[e] 10.01 ± 1.03[f]	83.35 ± 1.44[e] 56.71 ± 1.44[f]
Zn(**VIm**)$_2$	17.1473(6)	1009 ± 154	2.38	253.01	-111.19 ± 0.97	-16.58 ± 1.11	30.12 ± 1.50
Zn(**AIm**)$_2$	17.0454(11)	949 ± 73	2.42	248.53	-80.68 ± 0.82	-20.31 ± 0.90	26.39 ± 1.35
Zn(**ClIm**)$_2$	16.9824(4)	1114 ± 10	2.45	245.79	-63.44 ± 0.57	-19.48 ± 0.67	27.22 ± 1.20
Zn(**BrIm**)$_2$	17.065(2)	847 ± 31	2.41	249.39	-76.66 ± 0.43	-6.19 ± 0.50	40.51 ± 1.12
Zn(**IIm**)$_2$	17.1900(6)	721 ± 24	2.36	254.91	-87.21 ± 0.72	-6.44 ± 0.79	40.26 ± 1.28
Zn(**CF$_3$Im**)$_2$[34]	17.5317(12)	914 ± 25	2.23	270.41	-69.61 ± 0.54	-3.82 ± 0.57	42.88 ± 1.15

[a]Crystallographic parameter a, FD and MV were obtained from previously published or herein reported (for SOD-Zn(**IIm**)$_2$) crystal structures of ZIFs; [b]Measured enthalpy of dissolution in 5 N HCl at 298 K; [c]Calculated enthalpy of formation based on the formation reaction in **Table 5-1**; [d]Enthalpy of dissolution value before ligand dimer consideration; [e]calculated before ligand dimer consideration ; [f]with dimer consideration and after correcting for the dissociation of the linker dimer (**Table 5-2**).

The obtained ΔH_f values reflect a combination of the heat effects related to the formation of a porous MOF structure, and to the change in the local bonding environment of zinc ions from an oxygen-based one in ZnO to a nitrogen-based one in the ZIFs, accompanied by the release of water. The energetic effect of the change in local zinc coordination environment was previously established to be -46.7 ± 1.0 kJ·mol^{-1}.[32] Subtracting this value from the measured ΔH_f makes it possible to evaluate the energetic effect associated with the formation of a porous SOD-topology structure. The resulting values correspond to the enthalpy of transition (ΔH_{trans}, **Table 5-3**), a normalized value of enthalpy that describes the transition of a hypothetical non-porous dense state to the experimentally observed open ZIF structure. The ΔH_{trans} values are endothermic in all cases, which indicates that the porous structures are metastable relative to a hypothetical dense state, and that the principal driving force behind the formation of ZIF structures from ZnO is a change in zinc local bonding.

5.4.3 Theoretical calculations

We have previously shown[33,34] that periodic DFT calculations can offer excellent agreement with experiment in ranking the enthalpies of formation for ZIF polymorphs, based on identical linkers. Here, we explore the accuracy of such calculations for evaluating the effect of linker substitution on the stability of ZIFs with chemically distinct linkers. The prerequisite for such calculations, until methodologies for crystal structure prediction (CSP)[48] of MOFs becomes more general, is the knowledge of the experimental crystal structures for MOFs and corresponding linkers. We have used the plane wave DFT code CASTEP, performing the calculations with the PBE functional in combination with MBD* SEDC. The role of dispersion corrections for accurate prediction of MOF

stability has been verified previously, with the MBD* model showing superior performance to alternative SEDC schemes.[34,66]

Table 5-4. Comparison of the calculated ($\Delta E_{f,rel}$) and experimental ($\Delta H_{f,rel}$) enthalpies of formation of herein explored ZIFs, relative to ZIF-8.

Framework	$\Delta H_{f,rel}$ (kJ·mol^{-1}) (experimental)	$\Delta E_{f,rel}$ (kJ·mol^{-1}) (calculated)
Zn(**MeIm**)$_2$	0.0	0.0
Zn(**VIm**)$_2$	3.87 ± 1.45	1.06
Zn(**ClIm**)$_2$	0.97 ± 1.15	-2.74
Zn(**IIm**)$_2$	14.01 ± 1.23	8.10
Zn(**CF₃Im**)$_2$	16.63 ± 1.10	14.54
Zn(**CHOIm**)$_2$	57.10 ± 1.39	50.21

The crystal structures of imidazole ligands required for calculations were either determined in this work by single crystal X-ray diffraction (H**VIm**, H**ClIm**, H**IIm**) (see SI) or are available from the Cambridge Structural Database (CSD) (H**CF₃Im**: CSD code XOPLEW; H**MeIm**: CSD code FULPIM; H**CHOIm**: CSD code YASSAN). Crystal structure data was not available only for the H**AIm** and H**BrIm** linkers. Structural information on the linkers enabled the calculation of enthalpies of formation relative to ZIF-8 ($\Delta E_{f,rel}$) for all ZIFs except Zn(**AIm**)$_2$ and Zn(**BrIm**)$_2$ (**Table 5-4**). The $\Delta E_{f,rel}$ values showed excellent correlation with the experimentally measured ΔH_f (**Figure 5-4**, **Table 5-4**), with 2-methyl, -vinyl and -chloro substituted ZIFs showing similar $\Delta E_{f,rel}$, followed by ZIFs bearing the 2-iodo, -CF$_3$ and -CHO substituents. The match between

experimental and calculated enthalpy of formation of ZIF-90 is noteworthy: since the calculations were made assuming the dimer structure of the **HCHOIm** ligand in the solid state, the match is consistent with the assumption that the unusually high ΔH_f of ZIF-90 is due to the additional energy required for the dissociation of the linker dimer.
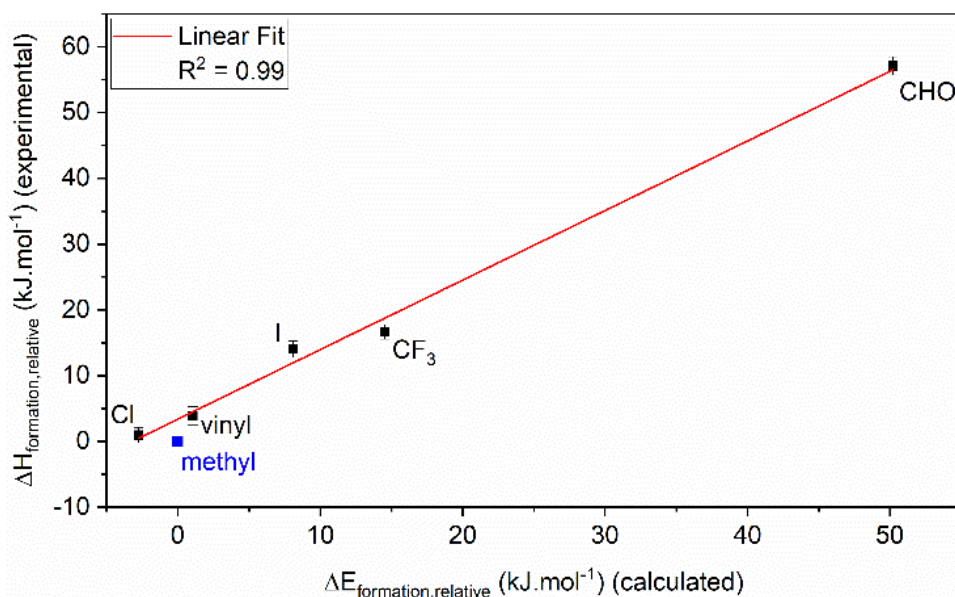
Figure 5-4. Comparison of the calculated ($\Delta E_{f,rel}$) and experimental ($\Delta H_{f,rel}$) enthalpies of formation. Both calculated and experimental values are defined relative to Zn(**MeIm**)$_2$, for which the formation enthalpy is set to zero and excluded from linear fitting.

5.4.4 Stability trends

The isostructurality of the eight ZIFs offers an opportunity to examine how MOF thermodynamic stability changes with respect to composition, independent of framework structure or topology. In particular, ZIF stability is likely to be related to the strength of Zn-N bonds, which depends on the electronic properties of the framework linker. A well-established, readily accessible parameter that describes how different functional groups affect the electronic properties of small molecules is the

Hammett σ-constant.[80–84] While Hammett σ-constants have been explored mostly for substituted benzenes, the values established for *meta-* (σ-*meta* constants) and *para*-substituted (σ-*para* constants) phenyl systems have also been found applicable to other chemically distinct systems, for example pK_a values of imidazole derivatives.[85,86] Consequently, we were encouraged to evaluate a potential relationship between ΔH_f and either σ-*meta* or σ-*para* Hammett parameters. This is the first time, to our knowledge, that Hammett parameters have been related to the stability of framework solids.

Plotting the ΔH_f values for herein explored ZIFs against tabulated[81] Hammett σ-*meta* constants for the corresponding linker substituent groups revealed a clear linear correlation with a coefficient of determination (R^2) of 0.46 (**Figure 5-5**a). A weaker, but still significant linear correlation ($R^2 = 0.35$) was also observed when plotting ΔH_f against Hammett σ-*para* constants (**Figure 5-5**b). Linear correlation between the ΔH_f values of ZIF materials and Hammett parameters is novel and also surprising, as the σ-constants are generally used to describe small molecules in dilute solution or gas phase. We suggest that the strong linear relationship between σ-values and the thermodynamics of ZIFs is due to the open, microporous structure of the frameworks, which reduces the importance of non-covalent interactions between individual linkers.
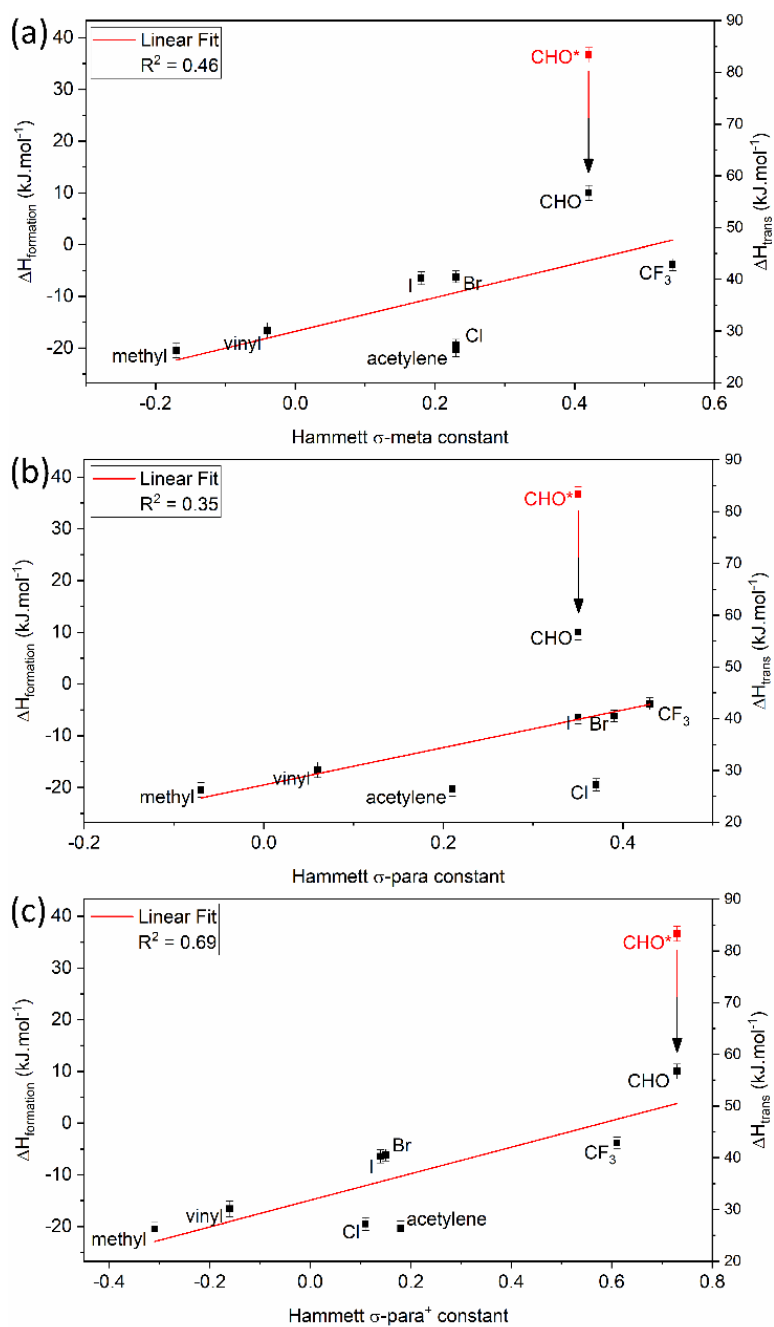
Figure 5-5. Correlation of ZIF ΔH_f and ΔH_{trans} to the Hammett σ-constants reported for: (a) *meta*-substitution; (b) *para*-substitution (bottom) and (c) *para*-substitution with σ-*para(+)* parameters used. Red label and star indicate the ΔH_f and ΔH_{trans} for ZIF-90 before correction for linker dimer dissociation.

117

The most notable discrepancies from a linear fit of ΔH_f to the Hammett σ-parameter are observed for ZIFs with acetylene- and chloro-substituted linkers. These discrepancies are unlikely to have resulted from an experimental error, as the measured ΔH_f value for the Cl-substituted MOF agrees with the energy calculated by periodic DFT. Both the -C≡CH and -Cl substituents can readily participate in the resonant electronic structure of the linker. Considering that the linker in the ZIF structure formally exhibits the electronic structure of an imidazolium cation,[66] and that the 2-substituent is in the direct vicinity of the Zn-N bond, we decided to explore how the correlation would be affected by considering the modified *σ-para(+)* Hammett constants.[81] Notably, this modified version of the Hammett constant has been developed to account for the ability of the substituent to delocalize positive charge close to a reactive part of the molecule.[81,87] Gratifyingly, the *σ-para(+)* constants yielded a strong correlation to measured ΔH_f values, with R^2 of ca. 0.7 (**Figure 5-5**c).

A particularly interesting observation to be made here is that the *σ-para(+)* constant for the -CHO substituent is larger than that of the -CF_3 group. This is opposite to the behavior seen for the *σ-meta* and the *σ-para* constants and contributes significantly to the much-improved linear correlation of the data. The stability-substituent correlations reveal that the ΔH_f for ZIFs becomes less exothermic, *i.e.* the materials should become less thermodynamically stable, with increasing Hammett parameter. This is consistent with the expectation that framework stability should be lower for linkers with electron-withdrawing substituents, which diminish the electron-donating ability of the linker and weaken the Zn-N bonds.

Because the Hammett σ-constants reflect the electronic effects of a substituent, it is possible that other related parameters could be useful in quantifying ZIF stability. Electrostatic surface potential

(ESP) has previously been used to evaluate electron-donating and -accepting abilities of functional groups, notably for rationalizing the formation of hydrogen- or halogen-bonded cocrystals.[88–90] To explore ESPs as a potential descriptor of ZIF stability, we calculated this parameter for substituents on isolated imidazolate anions in the gas phase. Plotting ΔH_f against such calculated ESP values again revealed a strong linear correlation ($R^2 = 0.60$, **Figure 5-6**a) In this correlation, the linkers with the highest (least negative) substituent ESP values (vinyl, acetylene) were found to provide the greatest ZIF stabilization, while the linkers bearing groups with most negative ESP (trifluoromethyl, aldehyde) produced the least stable ZIFs.

The described correlations represent the first quantitative relationships between the thermodynamic stability of a complex three-dimensional framework structure, and fundamental, measurable, or readily calculated properties of the linker substituent. In the context of MOF design, the relationship between ΔH_f and substituent σ-parameter or ESP value provides an opportunity to predict the stability of SOD-topology ZIFs based on the properties of the linker alone. For example, the slope of the best currently observed linear correlation between Hammett constant and the enthalpy of formation is 25.7 ± 7.1 kJ·mol^{-1}, indicating that ZIF stability should change by almost 26 kJ·mol^{-1} per σ-para(+) unit.
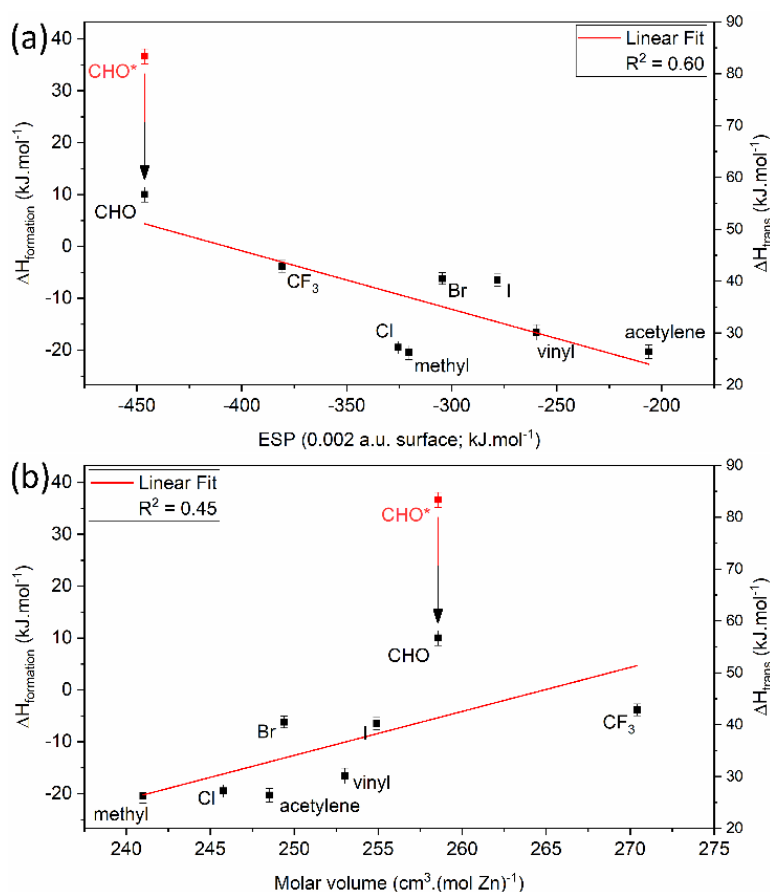
Figure 5-6. Correlation of ZIF ΔH_f and ΔH_{trans} to: (a) ESPs calculated for isolated gas-phase 2-substituted imidazolate anions and (b) ZIF molar volume. Red label and star indicate the ΔH_f and ΔH_{trans} for ZIF-90 before correction for linker dimer dissociation.

Impact of the linker substituent on ZIF stability is evident by comparing it to the effect of molar volume (MV), which is a conventional approach for comparing the stability of solid-state materials. Framework materials of higher MV, which corresponds to a lower density, are typically less thermodynamically stable than their denser counterparts.[32,91–93] Indeed, the herein explored ZIFs show a correlation of ΔH_f to MV, with R^2 of 0.45. It was shown previously that switching between the SOD- and *dia*-topology Zn(**MeIm**)$_2$ polymorphs[33], whose respective MV values are 241 and 136 cm^3·(mol Zn)$^{-1}$, leads to a ΔH_f change of ca. 11 kJ·mol^{-1} accompanied by a 44%

change in MV. In contrast, herein investigated variation of the substituent in the 2-position led to a ΔH_f variation of ca. 30 kJ·mol^{-1}, but with a MV variation of no more than 12% (30 cm^3·(mol Zn)$^{-1}$, **Figure 5-6**b).

5.5 Conclusions

We presented the first systematic and quantitative study of the effect of linker substituent on thermodynamic stability of MOFs. Using as a model a series of isomorphous sodalite-topology ZIFs based on 2-substituted linkers, we demonstrated a significant dependence of the enthalpy of formation of the MOFs from metal oxide on the choice of substituent. The calorimetric measurements were in excellent agreement with theoretically calculated values, revealing a linear correlation between MOF stability and readily calculable or tabulated properties of linker substituents, such as the Hammett σ-constants or electrostatic surface potentials. We believe that these descriptors can be used for the future design and prediction of ZIF structures with tailored stability. While periodic DFT calculation offers the most accurate prediction of ZIF energetics, they rely on the prior knowledge of crystal structure or an in-depth exploration of crystal energy landscape *via* crystal structure prediction. In contrast, this work shows that Hammett constants and electrostatic potential calculations allow for stability predictions based solely on the molecular structures of MOF linkers, proposing most feasible candidates for experimental synthesis or more in-depth computational screening.

5.6 Funding Sources

5.7   Acknowledgment

5.8   References

(1)   Li, H.; Wang, K.; Sun, Y.; Lollar, C. T.; Li, J.; Zhou, H.-C. Recent Advances in Gas Storage and Separation Using Metal–Organic Frameworks. *Mater. Today* **2018**, *21*, 108–121.

(2)   Wu, M.-X.; Yang, Y.-W. Metal-Organic Framework (MOF)-Based Drug/Cargo Delivery and Cancer Therapy. *Adv. Mater.* **2017**, *29*, 1606134.

(3)   Baumann, A. E.; Burns, D. A.; Liu, B.; Thoi, V. S. Metal-Organic Framework Functionalization and Design Strategies for Advanced Electrochemical Energy Storage Devices. *Commun. Chem.* **2019**, *2*, 86.

(4)   Furukawa, H.; Cordova, K. E.; O'Keeffe, M.; Yaghi, O. M. The Chemistry and Applications of Metal-Organic Frameworks. *Science* **2013**, *341*, 1230444.

(5)   Kirchon, A.; Feng, L.; Drake, H. F.; Joseph, E. A.; Zhou, H. C. From Fundamentals to Applications: A Toolbox for Robust and Multifunctional MOF Materials. *Chem. Soc. Rev.* **2018**, *47*, 8611–8638.

(6)   Batten, S. R.; Champness, N. R. Coordination Polymers and Metal–Organic Frameworks: Materials by Design. *Philos. Trans. R. Soc., A* **2017**, *375*, 20160032.

(7)   Connolly, B. M.; Madden, D. G.; Wheatley, A. E. H.; Fairen-Jimenez, D. Shaping the Future of Fuel: Monolithic Metal–Organic Frameworks for High-Density Gas Storage. *J. Am. Chem. Soc.* **2020**, *142*, 8541–8549.

(8)   Li, H.-Y.; Zhao, S.-N.; Zang, S.-Q.; Li, J. Functional Metal–Organic Frameworks as Effective Sensors of Gases and Volatile Compounds. *Chem. Soc. Rev.* **2020**.

(9)   Aulakh, D.; Liu, L.; Varghese, J. R.; Xie, H.; Islamoglu, T.; Duell, K.; Kung, C. W.; Hsiung, C. E.; Zhang, Y.; Drout, R. J.; Farha, O. K.; Dunbar, K. R.; Han, Y.; Wriedt, M. Direct Imaging of Isolated Single-Molecule Magnets in Metal-Organic Frameworks. *J. Am. Chem. Soc.* **2019**, *141*, 2997–3005.

(10)   Ji, Z.; Zhang, H.; Liu, H.; Yaghi, O. M.; Yang, P. Cytoprotective Metal-Organic Frameworks for Anaerobic Bacteria. *Proc. Natl. Acad. Sci. U. S. A.* **2018**, *115*, 10582–10587.

(11)   Taylor, J. M.; Dawson, K. W.; Shimizu, G. K. H. A Water-Stable Metal-Organic Framework with Highly Acidic Pores for Proton-Conducting Applications. *J. Am. Chem. Soc.* **2013**, *135*, 1193–1196.

(12)   Wang, L.; Han, Y.; Feng, X.; Zhou, J.; Qi, P.; Wang, B. Metal-Organic Frameworks for Energy Storage: Batteries and Supercapacitors. *Coord. Chem. Rev.* **2016**, *307*, 361–381.

(13)   Zou, G.; Hou, H.; Ge, P.; Huang, Z.; Zhao, G.; Yin, D.; Ji, X. Metal-Organic Framework-Derived Materials for Sodium Energy Storage. *Small* **2018**, *14*, 1702648.

(14)   Denny, M. S.; Moreton, J. C.; Benz, L.; Cohen, S. M. Metal–Organic Frameworks for Membrane-Based Separations. *Nat. Rev. Mater.* **2016**, *1*, 16078.

(15)   Cui, Y.; Li, B.; He, H.; Zhou, W.; Chen, B.; Qian, G. Metal-Organic Frameworks as Platforms for Functional Materials. *Acc. Chem. Res.* **2016**, *49*, 483–493.

(16)   Lin, R. B.; Xiang, S.; Zhou, W.; Chen, B. Microporous Metal-Organic Framework Materials for Gas Separation. *Chem* **2020**, *6*, 337–363.

(17)   Wang, Q.; Astruc, D. State of the Art and Prospects in Metal-Organic Framework (MOF)-Based and MOF-Derived Nanocatalysis. *Chem. Rev.* **2020**, *120*, 1438–1511.

(18)   Zhao, M.; Huang, Y.; Peng, Y.; Huang, Z.; Ma, Q.; Zhang, H. Two-Dimensional Metal-Organic Framework Nanosheets: Synthesis and Applications. *Chem. Soc. Rev.* **2018**, *47*, 6267–6295.

(19)   Jiao, L.; Wang, Y.; Jiang, H.-L.; Xu, Q. Metal-Organic Frameworks as Platforms for Catalytic Applications. *Adv. Mater.* **2018**, *30*, 1703663.

(20)   Ding, M.; Cai, X.; Jiang, H.-L. Improving MOF Stability: Approaches and Applications. *Chem. Sci.* **2019**, *10*, 10209–10230.

(21)   Howarth, A. J.; Liu, Y.; Li, P.; Li, Z.; Wang, T. C.; Hupp, J. T.; Farha, O. K. Chemical, Thermal and Mechanical Stabilities of Metal-Organic Frameworks. *Nat. Rev. Mater.* **2016**, *1*, 15018.

(22)   Rieth, A. J.; Wright, A. M.; Dincǎ, M. Kinetic Stability of Metal–Organic Frameworks for Corrosive and Coordinating Gas Capture. *Nat. Rev. Mater.* **2019**, *4*, 708–725.

(23)   Burtch, N. C.; Jasuja, H.; Walton, K. S. Water Stability and Adsorption in Metal–Organic Frameworks. *Chem. Rev.* **2014**, *114*, 10575–10612.

(24)   Wang, C.; Liu, X.; Keser Demir, N.; Chen, J. P.; Li, K. Applications of Water Stable Metal-Organic Frameworks. *Chem. Soc. Rev.* **2016**, *45*, 5107–5134.

(25)   Xie, L.; Xu, M.; Liu, X.; Zhao, M.; Li, J. Hydrophobic Metal–Organic Frameworks: Assessment, Construction, and Diverse Applications. *Adv. Sci.* **2020**, *7*, 1901758.

(26)   Nguyen, J. G.; Cohen, S. M. Moisture-Resistant and Superhydrophobic Metal-Organic Frameworks Obtained via Postsynthetic Modification. *J. Am. Chem. Soc.* **2010**, *132*, 4560–4561.

(27)   Liu, X.; Wang, X.; Kapteijn, F. Water and Metal–Organic Frameworks: From Interaction toward Utilization. *Chem. Rev.* **2020**, *120*, 8303–8377.

(28)   Deria, P.; Gómez-Gualdrón, D. A.; Bury, W.; Schaef, H. T.; Wang, T. C.; Thallapally, P. K.; Sarjeant, A. A.; Snurr, R. Q.; Hupp, J. T.; Farha, O. K. Ultraporous, Water Stable, and Breathing Zirconium-Based Metal-Organic Frameworks with Ftw Topology. *J. Am. Chem. Soc.* **2015**, *137*, 13183–13190.

(29)   Carter, K. P.; Ridenour, J. A.; Kalaj, M.; Cahill, C. L. A Thorium Metal-Organic Framework with Outstanding Thermal and Chemical Stability. *Chem. - Eur. J.* **2019**, *25*, 7114–7118.

(30)   Madden, D. G.; Scott, H. S.; Kumar, A.; Chen, K.-J.; Sanii, R.; Bajpai, A.; Lusi, M.; Curtin, T.; Perry, J. J.; Zaworotko, M. J. Flue-Gas and Direct-Air Capture of CO_2 by Porous Metal–Organic Materials. *Philos. Trans. R. Soc., A* **2017**, *375*, 20160025.

(31)   O'Nolan, D.; Kumar, A.; Zaworotko, M. J. Water Vapor Sorption in Hybrid Pillared Square Grid Materials. *J. Am. Chem. Soc.* **2017**, *139*, 8508–8513.

(32) Hughes, J. T.; Bennett, T. D.; Cheetham, A. K.; Navrotsky, A. Thermochemistry of Zeolitic Imidazolate Frameworks of Varying Porosity. *J. Am. Chem. Soc.* **2013**, *135*, 598–601.

(33) Akimbekov, Z.; Katsenis, A. D.; Nagabhushana, G. P.; Ayoub, G.; Arhangelskis, M.; Morris, A. J.; Friščić, T.; Navrotsky, A. Experimental and Theoretical Evaluation of the Stability of True MOF Polymorphs Explains Their Mechanochemical Interconversions. *J. Am. Chem. Soc.* **2017**, *139*, 7952–7957.

(34) Arhangelskis, M.; Katsenis, A. D.; Novendra, N.; Akimbekov, Z.; Gandrath, D.; Marrett, J. M.; Ayoub, G.; Morris, A. J.; Farha, O. K.; Friščić, T.; Navrotsky, A. Theoretical Prediction and Experimental Evaluation of Topological Landscape and Thermodynamic Stability of a Fluorinated Zeolitic Imidazolate Framework. *Chem. Mater.* **2019**, *31*, 3777–3783.

(35) Rosen, P. F.; Dickson, M. S.; Calvin, J. J.; Ross, N. L.; Friščić, T.; Navrotsky, A.; Woodfield, B. F. Thermodynamic Evidence of Structural Transformations in CO2-Loaded Metal-Organic Framework Zn(MeIm)2 from Heat Capacity Measurements. *J. Am. Chem. Soc.* **2020**, *142*, 4833–4841.

(36) Rosen, P. F.; Calvin, J. J.; Dickson, M. S.; Katsenis, A. D.; Friščić, T.; Navrotsky, A.; Ross, N. L.; Kolesnikov, A. I.; Woodfield, B. F. Heat Capacity and Thermodynamic Functions of Crystalline Forms of the Metal-Organic Framework Zinc 2-Methylimidazolate, Zn(MeIm)2. *J. Chem. Thermodyn.* **2019**, *136*, 160–169.

(37) Zhang, J. P.; Zhang, Y. B.; Lin, J. Bin; Chen, X. M. Metal Azolate Frameworks: From Crystal Engineering to Functional Materials. *Chem. Rev.* **2012**, *112*, 1001–1033.

(38) Park, K. S.; Ni, Z.; Cote, A. P.; Choi, J. Y.; Huang, R.; Uribe-Romo, F. J.; Chae, H. K.; O'Keeffe, M.; Yaghi, O. M. Exceptional Chemical and Thermal Stability of Zeolitic Imidazolate Frameworks. *Proc. Natl. Acad. Sci.* **2006**, *103*, 10186–10191.

(39) Tian, Y. Q.; Cai, C. X.; Ren, X. M.; Duan, C. Y.; Xu, Y.; Gao, S.; You, X. Z. The Silica-Like Extended Polymorphism of Cobalt(II) Imidazolate Three-Dimensional Frameworks: X-Ray Single-Crystal Structures and Magnetic Properties. *Chem. - Eur. J.* **2003**, *9*, 5673–5685.

(40) Coudert, F.-X.; Fuchs, A. H. Computational Characterization and Prediction of Metal–Organic Framework Properties. *Coord. Chem. Rev.* **2016**, *307*, 211–236.

(41) Schröder, C. A.; Baburin, I. A.; Van Wüllen, L.; Wiebcke, M.; Leoni, S. Subtle Polymorphism of Zinc Imidazolate Frameworks: Temperature-Dependent Ground States in the Energy Landscape Revealed by Experiment and Theory. *CrystEngComm* **2013**, *15*, 4036–4040.

(42) Baburin, I. A.; Leoni, S. The Energy Landscapes of Zeolitic Imidazolate Frameworks (ZIFs): Towards Quantifying the Presence of Substituents on the Imidazole Ring. *J. Mater. Chem.* **2012**, *22*, 10152–10154.

(43) Witman, M.; Ling, S.; Gladysiak, A.; Stylianou, K. C.; Smit, B.; Slater, B.; Haranczyk, M. Rational Design of a Low-Cost, High-Performance Metal-Organic Framework for Hydrogen Storage and Carbon Capture. *J. Phys. Chem. C* **2017**, *121*, 1171–1181.

(44) Galvelis, R.; Slater, B.; Chaudret, R.; Creton, B.; Nieto-Draghi, C.; Mellot-Draznieks, C. Impact of Functionalized Linkers on the Energy Landscape of ZIFs. *CrystEngComm* **2013**, *15*, 9603–9612.

(45) Galvelis, R.; Slater, B.; Cheetham, A. K.; Mellot-Draznieks, C. Comparison of the Relative Stability of Zinc and Lithium-Boron Zeolitic Imidazolate Frameworks. *CrystEngComm* **2012**, *14*, 374–378.

(46) Walker, A. M.; Civalleri, B.; Slater, B.; Mellot-Draznieks, C.; Corà, F.; Zicovich-Wilson, C. M.; Román-Pérez, G.; Soler, J. M.; Gale, J. D. Flexibility in a Metal-Organic Framework Material Controlled by Weak Dispersion Forces: The Bistability of MIL-53(Al). *Angew. Chem., Int. Ed.* **2010**, *49*, 7501–7503.

(47) Duarte Rodrigues, A.; Fahsi, K.; Dumail, X.; Masquelez, N.; van der Lee, A.; Mallet-Ladeira, S.; Sibille, R.; Filhol, J.-S.; Dutremez, S. G. Joint Experimental and Computational Investigation of the Flexibility of a Diacetylene-Based Mixed-Linker MOF: Revealing the Existence of Two Low-Temperature Phase

Transitions and the Presence of Colossal Positive and Giant Negative Thermal Expansions. *Chem. - Eur. J.* **2018**, *24*, 1586–1605.

(48)   Darby, J. P.; Arhangelskis, M.; Katsenis, A. D.; Marrett, J. M.; Friščić, T.; Morris, A. J. Ab Initio Prediction of Metal-Organic Framework Structures. *Chem. Mater.* **2020**, *32*, 5835–5844.

(49)   Arhangelskis, M.; Katsenis, A. D.; Morris, A. J.; Friščić, T. Computational Evaluation of Metal Pentazolate Frameworks: Inorganic Analogues of Azolate Metal-Organic Frameworks. *Chem. Sci.* **2018**, *9*, 3367–3375.

(50)   Yuan, S.; Feng, L.; Wang, K.; Pang, J.; Bosch, M.; Lollar, C.; Sun, Y.; Qin, J.; Yang, X.; Zhang, P.; Wang, Q.; Zou, L.; Zhang, Y.; Zhang, L.; Fang, Y.; Li, J.; Zhou, H.-C. Stable Metal-Organic Frameworks: Design, Synthesis, and Applications. *Adv. Mater.* **2018**, *30*, 1704303.

(51)   Gao, S.; Hou, J.; Deng, Z.; Wang, T.; Beyer, S.; Buzanich, A. G.; Richardson, J. J.; Rawal, A.; Seidel, R.; Zulkifli, M. Y.; Li, W.; Bennett, T. D.; Cheetham, A. K.; Liang, K.; Chen, V. Improving the Acidic Stability of Zeolitic Imidazolate Frameworks by Biofunctional Molecules. *Chem* **2019**, *5*, 1597–1608.

(52)   Tan, Y. X.; He, Y. P.; Zhang, J. Tuning MOF Stability and Porosity via Adding Rigid Pillars. *Inorg. Chem.* **2012**, *51*, 9649–9654.

(53)   Healy, C.; Patil, K. M.; Wilson, B. H.; Hermanspahn, L.; Harvey-Reid, N. C.; Howard, B. I.; Kleinjan, C.; Kolien, J.; Payet, F.; Telfer, S. G.; Kruger, P. E.; Bennett, T. D. The Thermal Stability of Metal-Organic Frameworks. *Coord. Chem. Rev.* **2020**, *419*, 213388.

(54)   Clark, S. J.; Segall, M. D.; Pickard, C. J.; Hasnip, P. J.; Probert, M. I. J.; Refson, K.; Payne, M. C. First Principles Methods Using CASTEP. *Z. Kristallogr. - Cryst. Mater.* **2005**, *220*, 567–570.

(55)   Björkman, T. CIF2Cell: Generating Geometries for Electronic Structure Programs. *Comput. Phys. Commun.* **2011**, *182*, 1183–1186.

(56)   Perdew, J. P.; Burke, K.; Ernzerhof, M. Generalized Gradient Approximation Made Simple. *Phys. Rev. Lett.* **1996**, *77*, 3865–3868.

(57)   Tkatchenko, A.; Distasio, R. A.; Car, R.; Scheffler, M. Accurate and Efficient Method for Many-Body van Der Waals Interactions. *Phys. Rev. Lett.* **2012**, *108*, 236402.

(58)   Ambrosetti, A.; Reilly, A. M.; DiStasio, R. A.; Tkatchenko, A. Long-Range Correlation Energy Calculated from Coupled Atomic Response Functions. *J. Chem. Phys.* **2014**, *140*, 18A508.

(59)   Reilly, A. M.; Tkatchenko, A. Van Der Waals Dispersion Interactions in Molecular Materials: Beyond Pairwise Additivity. *Chem. Sci.* **2015**, *6*, 3289–3301.

(60)   Monkhorst, H. J.; Pack, J. D. Special Points for Brillouin-Zone Integrations. *Phys. Rev. B* **1976**, *13*, 5188–5192.

(61)   Frisch, M. J.; Trucks, G. W.; Schlegel, H. B.; Scuseria, G. E.; Robb, M. A.; Cheeseman, J. R.; Scalmani, G.; Barone, V.; Petersson, G. A.; Nakatsuji, H.; Li, X.; Caricato, M.; Marenich, A. V.; Bloino, J.; Janesko, B. G.; Gomperts, R.; Mennucci, B.; Hratch, D. J. Gaussian 16 Rev. A.03. 2016.

(62)   Huang, X.-C.; Lin, Y.-Y.; Zhang, J.-P.; Chen, X.-M. Ligand-Directed Strategy for Zeolite-Type Metal–Organic Frameworks: Zinc(II) Imidazolates with Unusual Zeolitic Topologies. *Angew. Chem* **2006**, *118*, 1587–1589.

(63)   Morris, W.; Doonan, C. J.; Furukawa, H.; Banerjee, R.; Yaghi, O. M. Crystals as Molecules: Postsynthesis Covalent Functionalization of Zeolitic Imidazolate Frameworks. *J. Am. Chem. Soc.* **2008**, *130*, 12626–12627.

(64)   Sun, Q.; He, H.; Gao, W.-Y.; Aguila, B.; Wojtas, L.; Dai, Z.; Li, J.; Chen, Y.-S.; Xiao, F.-S.; Ma, S. Imparting Amphiphobicity on Single-Crystalline Porous Materials. *Nat. Commun.* **2016**, *7*, 1–7.

(65)   Marrett, J. M.; Mottillo, C.; Girard, S.; Nickels, C. W.; Do, J. L.; Dayaker, G.; Germann, L. S.; Dinnebier, R. E.; Howarth, A. J.; Farha, O. K.; Friščić, T.; Li, C. J. Supercritical Carbon Dioxide Enables Rapid, Clean, and Scalable Conversion of a Metal Oxide into Zeolitic Metal-Organic Frameworks. *Cryst. Growth Des.* **2018**, *18*, 3222–3228.

(66)   Titi, H. M.; Marrett, J. M.; Dayaker, G.; Arhangelskis, M.; Mottillo, C.; Morris, A. J.; Rachiero, G. P.; Friščić, T.; Rogers, R. D. Hypergolic Zeolitic Imidazolate Frameworks (ZIFs) as next-Generation Solid Fuels: Unlocking the Latent Energetic Behavior of ZIFs. *Sci. Adv.* **2019**, *5*, eaav9044.

(67)   Chaplais, G.; Fraux, G.; Paillaud, J.-L.; Marichal, C.; Nouali, H.; Fuchs, A. H.; Coudert, F.-X.; Patarin, J. Impacts of the Imidazolate Linker Substitution (CH 3 , Cl, or Br) on the Structural and Adsorptive Properties of ZIF-8. *J. Phys. Chem. C* **2018**, *122*, 26945–26955.

(68)   Li, K.; Olson, D. H.; Seidel, J.; Emge, T. J.; Gong, H.; Zeng, H.; Li, J. Zeolitic Imidazolate Frameworks for Kinetic Separation of Propane and Propene. *J. Am. Chem. Soc.* **2009**, *131*, 10368–10369.

(69)   Beldon, P. J.; Fábián, L.; Stein, R. S.; Thirumurugan, A.; Cheetham, A. K.; Friščić, T. Rapid Room-Temperature Synthesis of Zeolitic Imidazolate Frameworks by Using Mechanochemistry. *Angew. Chem., Int. Ed.* **2010**, *49*, 9640–9643.

(70)   Friščić, T.; Halasz, I.; Beldon, P. J.; Belenguer, A. M.; Adams, F.; Kimber, S. A. J.; Honkimäki, V.; Dinnebier, R. E. Real-Time and in Situ Monitoring of Mechanochemical Milling Reactions. *Nat. Chem.* **2013**, *5*, 66–73.

(71)   Stolar, T.; Užarević, K. Mechanochemistry: An Efficient and Versatile Toolbox for Synthesis, Transformation, and Functionalization of Porous Metal-Organic Frameworks. *CrystEngComm* **2020**, *22*, 4511–4525.

(72)   Brekalo, I.; Yuan, W.; Mottillo, C.; Lu, Y.; Zhang, Y.; Casaban, J.; Holman, K. T.; James, S. L.; Duarte, F.; Williams, P. A.; Harris, K. D. M.; Friščić, T. Manometric Real-Time Studies of the Mechanochemical Synthesis of Zeolitic Imidazolate Frameworks. *Chem. Sci.* **2020**, *11*, 2141–2147.

(73)   Friščić, T.; Mottillo, C.; Titi, H. M. Mechanochemistry for Synthesis. *Angew. Chem., Int. Ed.* **2020**, *59*, 1018–1029.

(74)   Mottillo, C.; Lu, Y.; Pham, M. H.; Cliffe, M. J.; Do, T. O.; Friščić, T. Mineral Neogenesis as an Inspiration for Mild, Solvent-Free Synthesis of Bulk Microporous Metal-Organic Frameworks from Metal (Zn, Co) Oxides. *Green Chem.* **2013**, *15*, 2121–2131.

(75)   Liao, Y. Te; Dutta, S.; Chien, C. H.; Hu, C. C.; Shieh, F. K.; Lin, C. H.; Wu, K. C. W. Synthesis of Mixed-Ligand Zeolitic Imidazolate Framework (ZIF-8-90) for CO2 Adsorption. *J. Inorg. Organomet. Polym. Mater.* **2015**, *25*, 251–258.

(76)   Zhang, K.; Lively, R. P.; Dose, M. E.; Brown, A. J.; Zhang, C.; Chung, J.; Nair, S.; Koros, W. J.; Chance, R. R. Alcohol and Water Adsorption in Zeolitic Imidazolate Frameworks. *Chem. Commun.* **2013**, *49*, 3245–3247.

(77)   Zhang, K.; Lively, R. P.; Zhang, C.; Chance, R. R.; Koros, W. J.; Sholl, D. S.; Nair, S. Exploring the Framework Hydrophobicity and Flexibility of Zif-8: From Biofuel Recovery to Hydrocarbon Separations. *J. Phys. Chem. Lett.* **2013**, *4*, 3618–3622.

(78)   Hachuła, B.; Nowak, M.; Kusz, J. Crystal and Molecular Structure Analysis of 2-Methylimidazole. *J. Chem. Crystallogr.* **2010**, *40*, 201–206.

(79)   Cheruzel, L. E.; Mashuta, M. S.; Buchanan, R. M. 5,10-Dihydroxy-5H,10H-Diimidazo[1,2-a:1′,2′-d]Pyrazine. *Acta Crystallogr., Sect. C: Cryst. Struct. Commun.* **2005**, *61*, o361–o362.

(80)   McDaniel, D. H.; Brown, H. C. An Extended Table of Hammett Substituent Constants Based on the Ionization of Substituted Benzoic Acids. *J. Org. Chem.* **1958**, *23*, 420–427.

(81)   Hansch, C.; Leo, A.; Taft, R. W. A Survey of Hammett Substituent Constants and Resonance and Field Parameters. *Chem. Rev.* **1991**, *91*, 165–195.

(82)   Hammett, L. P. Some Relations between Reaction Rates and Equilibrium Constants. *Chem. Rev.* **1935**, *17*, 125–136.

(83)   Hammett, L. P. The Effect of Structure upon the Reactions of Organic Compounds. Benzene Derivatives. *J. Am. Chem. Soc.* **1937**, *59*, 96–103.

(84)   Jaffé, H. H. A Reëxamination of the Hammett Equation. *Chem. Rev.* **1953**, *53*, 191–261.

(85)   Charton, M. Electrical Effects of Ortho Substituents in Imidazoles and Benzimidazoles. *J. Org. Chem.* **1965**, *30*, 3346–3350.

(86)   Ganellin, C. R. Imidazole Tautomerism of Histamine Derivatives. In *Molecular and Quantum Pharmacology*; Bergmann, E. D., Pullman, B., Eds.; Springer, Dordrecht, 1974; pp 43.

(87)   Brown, H. C.; Okamoto, Y. Electrophilic Substituent Constants. *J. Am. Chem. Soc.* **1958**, *80*, 4979–4987.

(88)   Lisac, K.; Topić, F.; Arhangelskis, M.; Cepić, S.; Julien, P. A.; Nickels, C. W.; Morris, A. J.; Friščić, T.; Cinčić, D. Halogen-Bonded Cocrystallization with Phosphorus, Arsenic and Antimony Acceptors. *Nat. Commun.* **2019**, *10*, 1–10.

(89)   Grecu, T.; Hunter, C. A.; Gardiner, E. J.; McCabe, J. F. Validation of a Computational Cocrystal Prediction Tool: Comparison of Virtual and Experimental Cocrystal Screening Results. *Cryst. Growth Des.* **2014**, *14*, 165–171.

(90)   Aakeröy, C. B.; Wijethunga, T. K.; Desper, J.; Đaković, M. Electrostatic Potential Differences and Halogen-Bond Selectivity. *Cryst. Growth Des.* **2016**, *16*, 2662–2670.

(91)   Hughes, J. T.; Navrotsky, A. MOF-5: Enthalpy of Formation and Energy Landscape of Porous Materials. *J. Am. Chem. Soc.* **2011**, *133*, 9184–9187.

(92)   Akimbekov, Z.; Navrotsky, A. Little Thermodynamic Penalty for the Synthesis of Ultraporous Metal Organic Frameworks. *ChemPhysChem* **2016**, *17*, 468–470.

(93)   Wu, L.; Hughes, J.; Moliner, M.; Navrotsky, A.; Corma, A. Experimental Energetics of Large and Extra-Large Pore Zeolites: Pure Silica Beta Polymorph C (BEC) and Ge-Containing ITQ-33. *Microporous Mesoporous Mater.* **2014**, *187*, 77–81.

Chapter 6:

Summary and Future Perspective

In this dissertation, the energetics of substitution effect on the thermodynamic stability of hybrid, dense and porous metal organic-frameworks were investigated. Different systems of hybrid materials were studied, including a system containing the organic mineral paceite and its cadmium analogue, a system of protonated-amine manganese formate perovskites and a system of zeolitic imidazolate frameworks with different polymorphs and linker substituents. The structure and property relationship within these materials were then studied to explore the role of the substitution on the resulting stability.

The formation of organic mineral paceite $CaCu(OAc)_4 \cdot 6H_2O$ from minerals such as $Cu(OAc)_2 \cdot H_2O$ (hoganite) and $CaCO_3$ (calcite) was found to be highly exothermic (-27.14 ± 0.30 kJ·mol^{-1}), explaining the driving force of its formation in nature. The substitution of Cd to the paceite structure was found to destabilize the structure, and this was expected due to the greater change in coordination that Cd undergoes compared to Cu. Additionally, the calorimetric study also revealed a possible pathway in which the paceite could be formed. It was found that the formation of $Ca(OAc)_2 \cdot H_2O \cdot AcOH$ intermediate is exothermic (-16.62 ± 0.23 kJ·mol^{-1}). Because of this, it was expected that the formation of paceite from $Cu(OAc)_2 \cdot H_2O$ and $CaCO_3$ will go through the formation of $Ca(OAc)_2 \cdot H_2O \cdot AcOH$ intermediate. The consistency of the final state on the acid calorimetry measurements was also confirmed in this study. This was important to ensure that the calculation performed to obtain the enthalpy of formations are accurate.

To explore the energetics of substitution effects on dense MOF stability, a system of protonated-amine manganese formate perovskites (AmineH$^+$-Mn-F) was studied. The thermodynamic stability decreases in the order of GUA-Mn-F, FA-Mn-F, MA-Mn-F, AZE-Mn-F and DMA-Mn-F. It was found that, unlike traditional inorganic perovskites, the stability of these hybrid perovskite samples was not governed by geometrical factors, as represented by the Goldschmidt tolerance factor. Upon further analysis, the stability was more closely related to the interaction between the A-site cation and the framework, mostly through hydrogen bonding. The relative strength of this interaction was found to be represented by the simple dissolution enthalpy measurement of the cation salts, which correlates linearly with the perovskite enthalpy of formation. It was found that the perovskite enthalpy of formation would change by 1 kJ·mol^{-1} per unit of cation salt dissolution enthalpy. This result could potentially open a way to predict the stability of other dense MOFs or other hybrid perovskites.

To understand the energetics of substitution effect on porous MOF stability, a system of zeolitic imidazolate frameworks (ZIFs) with different polymorphs and linker substituents was studied. In Chapter 4, the enthalpy of formations of fluorinated ZIF (Zn(**CF$_3$Im**)$_2$) was compared to the enthalpy of formation of Zn(**MeIm**)$_2$ and Zn(**EtIm**)$_2$. Here, a very interesting result was observed, where switching between -CH$_3$, -C$_2$H$_5$ and -CF$_3$ substituents yields sets of ZIFs with significant energy differences, albeit having similar molar volume and framework density. For example, SOD-Zn(**CF$_3$Im**)$_2$, SOD-Zn(**MeIm**)$_2$ and ANA-Zn(**EtIm**)$_2$ all have similar framework density, but their enthalpy of formations differ significantly up to 27.7 kJ mol^{-1}. Here the trend seen is also different from that has been seen with traditional porous materials such as silica zeolites and mesoporous silica, where the stability correlates linearly with the framework density.

To further investigate the role of substitution to the stability of porous metal-organic frameworks, a system of eight isostructural ZIFs with different substitutions on the 2-positions of the imidazolate linker (CH_3, $CH=CH_2$, $C\equiv CH$, CHO, CF_3, Cl, Br, I) was studied in Chapter 5. It was found that despite having the same topology, the enthalpy of formation can vary widely (~30 $kJ\cdot mol^{-1}$) simply by replacing the substituent on the linker. This confirms the significant dependence of the enthalpy of formation of the MOFs from metal oxide on the choice of substituent. Additionally, a poor correlation was observed when comparing the enthalpy of formations of the ZIFs to their framework density and molar volume. The stability trend could be explained better by relating it to readily calculable or tabulated properties of linker substituents such as electrostatic surface potential (ESP) and Hammett σ-para(+) constants. It was found that the ZIFs enthalpy of formation would change by almost 26 $kJ\cdot mol^{-1}$ per Hammett σ-para(+) unit. Similar to the case seen with hybrid perovskite earlier, this could also open a way to predict the stability of other ZIFs or other porous MOFs.

The results in Chapter 3 and Chapter 5 suggest predictive tools to predict the stability of MOFs using an easily measurable or tabulated property. These could be very powerful for use in accelerating the discovery of new MOFs. Additionally, the results showed that the MOF energetic trend behaves very differently when compared to their respective inorganic counterparts. Because of this, additional research would be necessary to test and validate the accuracy of the results and the suggested predictive tools. A further systematic thermodynamic study on other MOF systems would be beneficial. For the dense MOF group, further study could be performed on other AmineH$^+$-M-F systems, where AmineH$^+$ = GUA, FA, MA, DMA, and AZE, and M = Co, Ni and Zn. Additionally, albeit not considered as a dense MOF, methylammonium lead iodide (MAPbI$_3$) is also a hybrid organic-inorganic perovskite that gained significant attention due to its high power

conversion efficiency (PCE) for solar cell applications. A systematic study on the effect of substitution on the A-site and the B-site on the energetics has not been performed, thus it would also be interesting to study the effect of the cation substitution on the A-site, with cations such as MA and FA, and also on the B-site, with cations such as Pb and Sn, and correlate it to the result seen here with hybrid manganese formate perovskites. Similarly, in the porous MOF group, further study could be performed on other sodalite ZIFs with different metal nodes, such as Zn, Co and Cd, and with different substitutions on the 2-positions of the imidazolate linker such as $CH=CH_2$ and $C\equiv CH$. Overall, both of these studies would provide the bigger picture on the relationship between the energetics and the compositions for both dense and porous MOFs, and also provide a better understanding on how to predict the stability of other and new MOFs.

Appendix A

Supplementary Information for Chapter 2

Mechanochemical Synthesis, Accelerated Aging and

Thermodynamic Stability of the Organic Mineral Paceite

and Its Cadmium Analogue

Li, S.; Huskić, I.; Novendra, N.; Titi, H. M.; Navrotsky, A.; Friščić, T. Mechanochemical Synthesis, Accelerated Aging, and Thermodynamic Stability of the Organic Mineral Paceite and Its Cadmium Analogue. *ACS Omega* **2019**, *4*, 5486–5495.

A.1   Synthetic Procedures

Mechanochemical synthesis of calcium acetate monohydrate from calcium hydroxide

Calcium acetate was prepared by combining 37 mg (0.5 mmol) calcium hydroxide, 60 µL (~1.1 mmol) acetic acid, and 10 µL water in a milling jar. The sample was then milled for 30 minutes at 25 Hz.

Mechanochemical synthesis of calcium acetate monohydrate from calcium carbonate

The synthesis of calcium acetate monohydrate from $CaCO_3$ was accomplished by combining 100 mg (1.0 mmol) of calcium carbonate, 120 µL (~2.0 mmol) of acetic acid, and 12 µL water in a milling jar. The sample was then milled for 60 minutes at 30 Hz.

Mechanochemical two-step synthesis of synthetic paceite from calcium hydroxide

Synthetic paceite was prepared mechanochemically in a stepwise manner. First, 37 mg (0.5 mmol) calcium hydroxide, 62 µL (~1.1 mmol) acetic acid, and 10 µL water were added to a milling jar. The sample was milled for 30 minutes at 25 Hz. Subsequently, 100 mg (~0.5 mmol) copper(II) acetate monohydrate and 60 µL water were added, and the sample milled for another 30 minutes at 25 Hz.

Mechanochemical two-step synthesis of synthetic paceite from calcium carbonate

Synthetic paceite was prepared mechanochemically in a stepwise manner. First, 50 mg (0.5 mmol) calcium carbonate, 62 µL (~1.1 mmol) acetic acid, and 10 µL water were added to a milling jar. The sample was milled for 30 minutes at 25 Hz. Subsequently, 100 mg (~0.5 mmol) copper(II)

acetate monohydrate and 67 µL water were added, and the sample milled for another 30 minutes at 25 Hz.

Mechanochemical one-step synthesis of synthetic paceite from calcium hydroxide

Synthetic paceite was prepared mechanochemically in a direct one-pot method. To a milling jar were added 37 mg (0.5 mmol) calcium hydroxide, 100 mg (~0.5 mmol) copper(II) acetate monohydrate, 62 µL (~1.1 mmol) acetic acid, and 62 µL water. The sample was milled for 30 minutes at 25 Hz.

Mechanochemical one-step synthesis of synthetic paceite from calcium carbonate

Synthetic paceite was prepared mechanochemically in a direct one-pot method. To a milling jar were added 50 mg (0.5 mmol) calcium carbonate, 100 mg (~0.5 mmol) copper(II) acetate monohydrate, 62 µL (~1.1 mmol) acetic acid, and 60 µL water. The sample was milled for 30 minutes at 25 Hz.

Mechanochemical two-step synthesis of CaCd(OAc)$_4$·6H$_2$O from calcium hydroxide

The cadmium paceite analogue CaCd(OAc)$_4$·6H$_2$O was prepared mechanochemically in a stepwise manner. First, 37 mg (0.5 mmol) calcium hydroxide, 63 µL (~1.1 mmol) acetic acid, and 10 µL water were added to a milling jar. The sample was milled for 30 minutes at 25 Hz. Subsequently, 133 mg (~0.5 mmol) cadmium(II) acetate dihydrate and 60 µL water were added, and the sample milled for another 30 minutes at 25 Hz.

Mechanochemical two-step synthesis of CaCd(OAc)$_4$·6H$_2$O from calcium carbonate

The cadmium paceite analogue CaCd(OAc)$_4$·6H$_2$O was prepared mechanochemically in a stepwise manner. First, 50 mg (0.5 mmol) calcium carbonate, 62 µL (~1.1 mmol) acetic acid, and 10 µL water were added to a milling jar. The sample was milled for 30 minutes at 25 Hz. Subsequently, 133 mg (~0.5 mmol) cadmium(II) acetate dihydrate and 60 µL water were added, and the sample milled for another 30 minutes at 25 Hz.

Mechanochemical one-step synthesis of CaCd(OAc)$_4$·6H$_2$O from calcium hydroxide

The cadmium paceite analogue CaCd(OAc)$_4$·6H$_2$O was prepared mechanochemically in a direct one-pot method. To a milling jar were added 37 mg (0.5 mmol) calcium hydroxide, 133 mg (~0.5 mmol) cadmium(II) acetate dihydrate, 60 µL (~1.1 mmol) acetic acid, and 60 µL water. The sample was milled for 30 minutes at 25 Hz.

Mechanochemical one-step synthesis of CaCd(OAc)$_4$·6H$_2$O from calcium carbonate

The cadmium paceite analogue CaCd(OAc)$_4$·6H$_2$O was prepared mechanochemically in a direct one-pot method. To a milling jar were added 50 mg (0.5 mmol) calcium carbonate, 133 mg (~0.5 mmol) cadmium(II) acetate dihydrate, 62 µL (~1.1 mmol) acetic acid, and 60 µL water. The sample was milled for 30 minutes at 25 Hz.

A.2 Real-time *in situ* reaction monitoring using powder X-ray diffraction (PXRD)

In situ PXRD monitoring was performed on the PROTO AXRD Benchtop diffractometer equipped with a DECTRIS Mythen 1K strip detector. Measurements were collected using a custom designed sample holder.(ref) A homogenized mixture of $Ca(OH)_2$ and $Cu(OAc)_2 \cdot H_2O$ was placed in the middle and a 200 mL of 50% aqueous solution (by volume) of acetic acid were placed in the sample holder grooves. Consecutive powder diffractograms were collected over the course of 12 hours, with a temporal resolution of 5 min 50 seconds. Rietveld fitting was performed in TOPAZ6 analytical program.

A.3 Selected Fourier-transform infrared attenuated total reflectance (FTIR-ATR) spectra of mechanochemically prepared materials
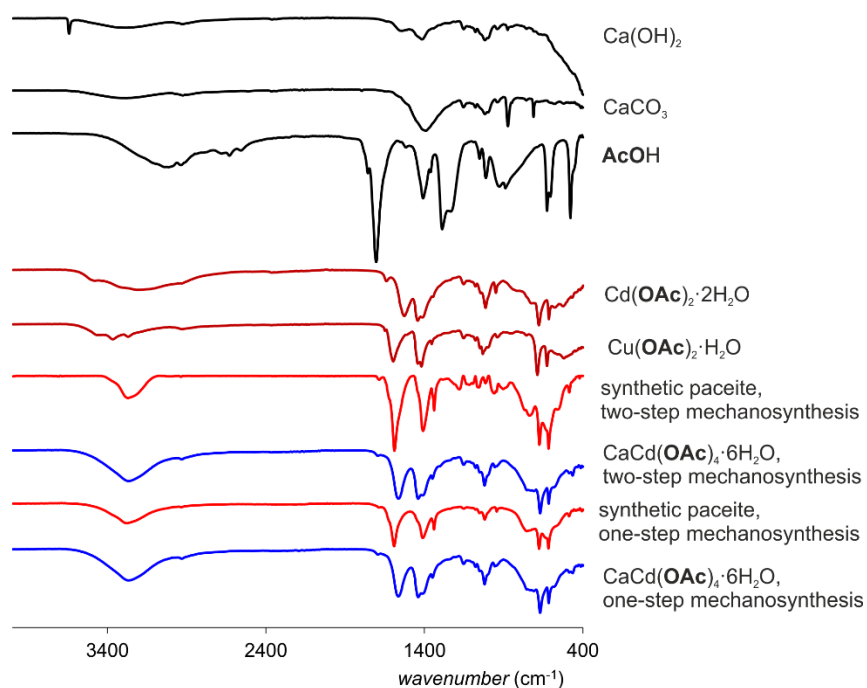
Figure A-1. Overlay of selected FTIR-ATR spectra for mechanochemical syntheses of synthetic paceite samples and its cadmium analogue $CaCd(OAc)_4 \cdot 6H_2O$.

Appendix B

Supplementary Information for Chapter 4

Theoretical Prediction and Experimental Evaluation of

Topological Landscape and Thermodynamic Stability of a

Fluorinated Zeolitic Imidazolate Framework

Arhangelskis, M.; Katsenis, A. D.; Novendra, N.; Akimbekov, Z.; Gandrath, D.; Marrett, J. M.; Ayoub, G.; Morris, A. J.; Farha, O. K.; Friščić, T.; Navrotsky, A. Theoretical Prediction and Experimental Evaluation of Topological Landscape and Thermodynamic Stability of a Fluorinated Zeolitic Imidazolate Framework. *Chem. Mater.* **2019**, *31*, 3777–3783.

B.1 Materials and methods

ZnO (≥99%), NH_4NO_3 (≥99%), Zinc carbonate basic, $[ZnCO_3]_2 \bullet [Zn(OH)_2]_3$, (technical, ≥53% Zn basis), 1–Methyl–2–pyrrolidinone (NMP) and 2,2,2-Trifluoroethanol (TFE) were purchased from Aldrich. Methanol (MeOH), N,N-Dimethylformamide (DMF) were purchased from ACP Chemicals. Ethanol (EtOH) were purchased from Commercial Alcohols. 1,4–Dioxane, Ethyl Acetate, Chloroform ($CHCl_3$), Hexane were purchased from Fisher Chemicals. All chemicals were used without further purification.

B.1.1 Thermal analysis

Thermogravimetric analyses (TGA) were performed on a TGA/DSC 1 system, which runs on a PC with STAR^e software. Samples were heated from 25 to 800 °C at a rate of 10 °C/min under flowing N_2. The balance and purge flow were 40 ml/min and 60 ml/min respectively.

B.1.2 Powder X-ray diffraction

Powder X-ray diffraction (PXRD) patterns were collected using a Bruker D2 Phaser powder diffractometer equipped with a Cu-Kα (λ=1.54060 Å) source and Lynxeye detector. The patterns were collected in the angle region between 3° and 40° (2θ) with a step size of 0.05° and 0.65 s counting per step. PXRD patterns used for structure solution-refinement were collected in the angle region between 4° and 120° (2θ) with a step size of 0.02° and 6.0 s counting per step.

B.1.3 Structure determination from powder X-ray data

Crystal structures of qtz and SOD polymorphs of Zn(**CF₃Im**)₂ were determined from powder X-ray diffraction data. Powder patterns were indexed using DICVOL06, while peak selection was made using the graphical interface of program DASH 3.3.4. For both powder patterns the indexing procedure produced unit cells very similar to those of qtz-Zn(**EtIm**)₂ (CSD EHETER) and SOD-Zn(**MeIm**)₂ (ZIF-8, CSD OFERUN03), suggesting close similarity of Zn(**CF₃Im**)₂ polymorphs with their topological analogues.

Simulated annealing structure solution and Rietveld refinement[1] were performed using TOPAS Academic 6.[2] First, Pawley refinement[3] procedure was used to refine unit cell parameters, peak shape parameters (pseudo-Voigt function) and background Chebyshev polynomial terms. The space groups $P6_4$ and $I\bar{4}3m$ were used for *qtz*- and SOD-structures, respectively.

The optimal values for unit cell, peak shape and background polynomials found in Pawley refinement were fixed during the Simulated Annealing structure solution. The only remaining variable parameters were the positions and orientations of molecular fragments, as well as the overall scale factor. In the case of the *qtz*-structure, the asymmetric unit contained an isolated Zn atom and a **CF₃Im** rigid body fragment. In the case of the SOD-structure, the rigid fragment contained half **CF₃Im** unit which was constrained to move along the crystallographic mirror plane.

Once satisfactory structural models had been found, they were subjected to Rietveld refinement. During the refinement procedure all previously constrained parameters (unit cell, peak shape and background) were allowed to refine. Atomic motion was described by a single isotropic Debye-Waller factor for non-hydrogen atoms (B_{iso}), while hydrogen atoms were assigned a Debye-Waller factor of $1.2 \times B_{iso}$.

Finally, we have investigated the possibility of CF₃ group being rotationally disordered within the experimentally established structures. While no evidence of disorder was found for the structure of *qtz*-Zn(**CF₃Im**)₂, the refinement of the corresponding SOD-polymorph produced a model with two orientations of CF₃ group related by 180° rotation, with essentially equal refined occupancies of 0.531(6) and 0.469(6). It should be noted, however, that powder X-ray diffraction is less sensitive to disorder than the single crystal measurement. In our case, however, periodic DFT calculations have shown that disorder of CF₃ group in the SOD-Zn(**CF₃Im**)₂ structure can lower the energy by approx. 5 kJ mol⁻¹ compared to a fully ordered structure (see section S4). Therefore, our experimental structural model is supported by periodic DFT calculations.

B.1.4 Thin-layer chromatography (TLC)

Thin-layer chromatography (TLC) was performed on aluminum pre-coated silica gel plates from Merck, and developed plates were visualized by UV light (254 nm), Column chromatography was performed using flash chromatography with the indicated eluent on SiliaFlash P60 40-63 µm silica gel.

B.1.5 Solution nuclear magnetic resonance (NMR) spectroscopy

1H NMR spectra (500 MHz), ¹³C NMR spectra (125 MHz) and ¹⁹F NMR were recorded on Bruker AMX300 spectrometer. Chemical shifts are reported relative to acetone-d₆ (δ 2.05 ppm) for ¹H NMR spectra and Acetone-d6 (δ 29.84 ppm) for ¹³C spectra. The ¹H NMR spectra data are presented as follows: chemical shift, multiplicity (s = singlet, br. = broad), and integration.

B.1.6 Fourier-transform infrared attenuated total reflectance (FTIR-ATR) spectroscopy

Infrared spectra were obtained using a Bruker Platinum ATR spectrometer, and are reported in wavenumber (cm^{-1}) units of significant bands.

B.1.7 Melting point

Melting point (M.P., for H**CF₃Im** ligand) was determined on a WRS-1C Melting Point Apparatus.

B.2   Synthetic Procedures

For mechanochemical experiments, reactions were conducted in a stainless steel jar of 10 mL volume, using two 7 mm (1.34 g each) diameter stainless steel balls, and a Retsch MM400 mill operating at 30 Hz. All samples of metal-organic frameworks were washed three times with methanol (MeOH) and dried under vacuum at room temperature.

B.2.1 Abbreviations

H**CF₃Im =** 2-(trifluoromethyl)-1H-imidazole; **NMP** = N-methyl-2-pyrrolidone; **EtOH** = Ethanol; **MeOH** = methanol; **CHCl₃** = chloroform; **DMF** = N,N-dimethylformamide; **TFE** = 2,2,2-trifluoroethan-1-ol; H**MeIm** = 2-methyl-1H-imidazole; H**EtIm** = 2-ethyl-1H-imidazole.

B.2.2 Synthesis of the SOD–Zn(CF₃Im)₂ framework by milling

A solid mixture of [ZnCO₃]₂ • [Zn(OH)₂]₃ (54.9 mg, 0.1 mmol) and H**CF₃Im** (136.08 mg, 1.0 mmol, 1:2 stoichiometric ratio with respect to total zinc content) were placed in a 10 ml stainless steel jar along with 70 µl of EtOH, and the reaction mixture was milled for 30 minutes.

B.2.3 Synthesis of the qtz–Zn(CF₃Im)₂ framework by milling

A solid mixture of ZnO (40.69 mg, 0.5 mmol), H**CF₃Im** (138.8 mg, 1.0 mmol) and catalyst salt NH₄NO₃ (10 mg, 0.125 mmol) were placed in a 10 ml stainless steel jar along with 50 µl of DMF and the reaction mixture was milled for 30 minutes.

B.2.4 Synthesis of the HCF₃Im ligand
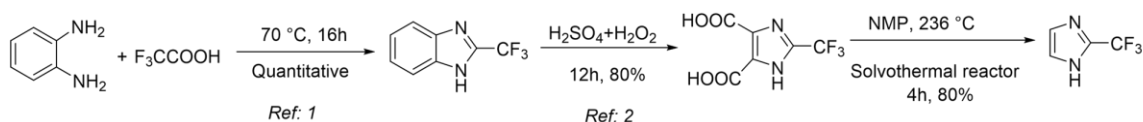
To a solution of 2-(trifluoromethyl)-1H-imidazole-4,5-dicarboxylic acid, (1.0 g, 4.46 mmol) in N-methyl-2-pyrrolidone (5 mL) was heated in hydrothermal reactor at 236 °C for 4.0 h, after this time reaction mixture diluted with H₂O (15 mL) and extracted with Ether (3 x 50 mL), combined organic layers dried over MgSO₄ and concentrated. Purification by flash chromatography on silica gel (EtOAc/Hexane: 20/80 to 30/70) afforded crystalline of 2-(trifluoromethyl)-1H-imidazole (0.382 g, 63% over two steps starting from 2-(trifluoromethyl)benzimidazole).[4] **M.P.**: 140-142 °C (145-146 °C lit.)[1]**.**). **IR (cm⁻¹):** 3022, 2922, 2797, 2612, 1661, 1568, 1476, 1420, 1334, 1188, 1099, 904, 761, 743, 728, 552. **¹H NMR**: (500 MHz, acetone-d₆): δ 12.42 (br. s, 1H), 7.27 (br.s, 2H) ppm. **¹³C NMR**: (125 MHz, acetone-d₆): δ 136.2 (q, J = 40.3), 125.6 (2C), 120.2 (q, J = 267.5 Hz). **¹⁹F NMR**: (500 MHz, acetone-d₆): δ -63.8.

B.3 Computational Methods

The topological landscape of Zn(**CF₃Im**)₂ system was explored with the aid of periodic DFT calculations. As a basis for our computational study, we have selected 8 topologically distinct structures from CSD, namely *dia*-Zn(**MeIm**)₂ (CSD OFERUN01), *kat*-Zn(**MeIm**)₂ (CSD OFERUN08), SOD-Zn(**MeIm**)₂ (CSD OFERUN03), ANA-Zn(**EtIm**)₂ (CSD MECWIB), RHO-Zn(**EtIm**)₂ (CSD MECWOH), *zni*-Zn(**HIm**)₂ (CSD IMIDZB01) and *cag*-Zn(**HIm**)₂ (CSD VEJYUF). In preparation for DFT calculations, substituents (H-, Me or Et- groups) in the 2-position were replaced by -CF₃ groups, thereby generating putative polymorphic structures of Zn(**CF₃Im**)₂. The resulting structures were geometry-optimized.

The periodic DFT calculations were performed with the plane-wave DFT code CASTEP 16.1.1.[5] The input files were prepared using cif2cell[5] program. The I-centered structures (zni, SOD, ANA and RHO topologies) were transformed to the corresponding primitive structures with the aim of reducing the cell volume and, hence, the computational cost of the DFT calculations. This transformation preserved all the symmetry operations of the original structures. The plane wave basis set was truncated at 750 eV cutoff and norm-conserving pseudopotentials were used to attenuate Coulomb potential in the core regions. The Brillouin zone was sampled with a 0.03 Å⁻¹ k-point spacing. Dispersion interactions were modelled with the aid of Grimme-D2[7] dispersion correction. As a first step the optimization procedure involved full relaxation of unit cell parameters and atomic coordinates subject to the symmetry constraints of the corresponding space groups. Subsequently, however, structures containing 4-rings in their topological nets (kat, SOD, ANA and RHO) were reoptimized in *P1* space group in order to account for the possibility of CF₃ groups being rotationally disordered. Rotational disorder of CF₃ groups is, in principle, possible for any topology. In the case of topologies containing 4-rings, CF₃ groups of neighboring **CF₃Im** are found in close proximity with each other. Consequently, the mutual orientation of these groups may have a pronounced effect on the overall lattice energy, potentially affecting the energy ranking of a particular topological polymorph. In preparation for the *P1* geometry optimization, the neighboring CF₃ groups were manually rotated in a "head-to-tail" orientation. The resulting structures were geometry-optimized without any constraints on atom coordinates or unit cell parameters. The only exception to that was the disordered RHO structure where, due to high computational cost of the calculation, we only relaxed the coordinates of atoms within the CF₃ groups. The unit cell parameters and coordinates of all remaining atoms were kept fixed at the positions, obtained from the RHO structure optimized with space group symmetry constraints.

The Grimme-D2 dispersion correction is formulated as a set of C₆ coefficients describing pairwise atom-atom interactions, ignoring all the higher order terms. As an alternative approach we have performed additional calculations with many body dispersion (MBD*)[8-10] method, which includes higher order terms beyond the pair-wise model. In addition, the dispersion coefficients in the MBD* model are calculated for each structure based on the DFT-computed electron density. The PBE-MBD* energies were obtained by performing single point calculations on the structures optimized with PBE-D2 method. Finally, electronic density of states (DOS) was calculated for the optimized crystal structures, both in the ordered and disordered configurations. CASTEP spectral calculations were performed with PBE functional, 750 eV plane-wave cutoff and 0.03 Å⁻¹ k-point spacing. The DOS plots were drawn using the adaptive broadening mode of the code OptaDOS[11,12] (**Figure B-1**-**Figure B-4**). The band gaps, determined from the DOS plots, were found to be very similar for all topological polymorphs of Zn(**CF₃Im**)₂, both experimentally observed and

hypothetical. We have excluded *zni* and *cag* structures from the DOS analysis, due to inability of these topologies to accommodate the **CF₃Im** ligand.

Table B-1. Calculated energies and band gaps of putative Zn(**CF₃Im**)₂ polymorphs.

topology/structural model		PBE-D2 total energy per formula unit		PBE-MBD* total energy per formula unit		PBE energy contribution per formula unit / eV	MBD* energy contribution per formula unit / eV	Calculated band gap / eV
		absolute / eV	relative / kJ mol^{-1}	absolute / eV	relative / kJ mol^{-1}			
qtz	*P6₄*	-7605.3131	0.00	-7605.1438	0.00	-7603.5179	-1.6259	4.551
dia	*P2₁/c*	-7605.1962	11.29	-7605.0040	13.49	-7603.3419	-1.6621	4.194
SOD	*P1*	-7605.1161	19.01	-7604.9787	15.93	-7603.6050	-1.3737	4.453
	I-43m	-7605.0523	25.17	-7604.9272	20.90	-7603.5800	-1.3472	4.447
kat	*P1*	-7605.0439	25.98	-7604.8638	27.02	-7603.2567	-1.6071	4.428
	P-42c	-7604.9443	44.31	-7604.7620	36.84	-7603.4526	-1.3443	4.391
RHO	*Im-3m*	-7604.9545	34.60	-7604.7969	33.47	-7603.4510	-1.3451	4.550
	P1	-7604.9530	34.75	-7604.7961	33.55	-7603.1919	-1.5701	4.522
ANA	*I-3ad*	-7604.8584	43.87	-7604.6748	45.25	-7603.3135	-1.3613	4.491
	P1	-7604.8539	44.31	-7604.6749	45.24	-7603.3113	-1.3636	4.491
cag	*Pbca*	-7604.0507	121.81	-7603.9313	116.99	-7602.6807	-1.2506	-
zni	*I4₁cd*	-7603.4253	182.15	-7603.2619	181.58	-7601.8157	-1.4462	-
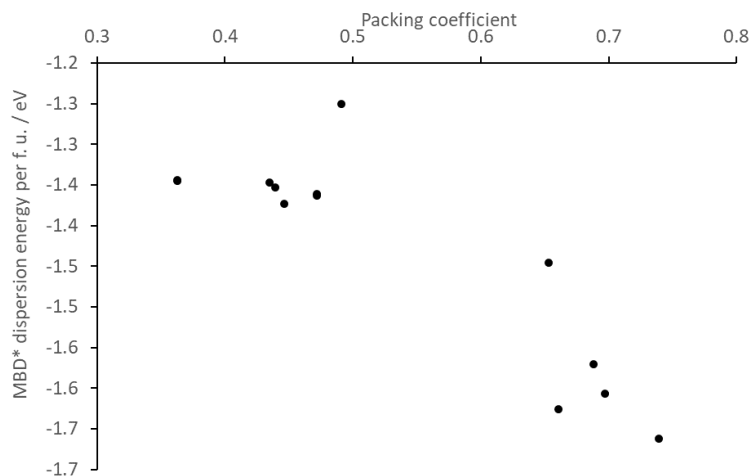
Figure B-1. The magnitude of MBD* dispersion energy as a function of framework packing coefficient. It is evident that dispersion energy decreases at high framework densities (PC>0.65), while a plateau is reached at PC< 0.5. The outlier with PC=0.49 and E(MBD*)=-1.25 eV is the cag structure which, upon optimization, had one of the Zn-N bonds replaced by Zn-F contact, ceasing to be a ZIF.

139
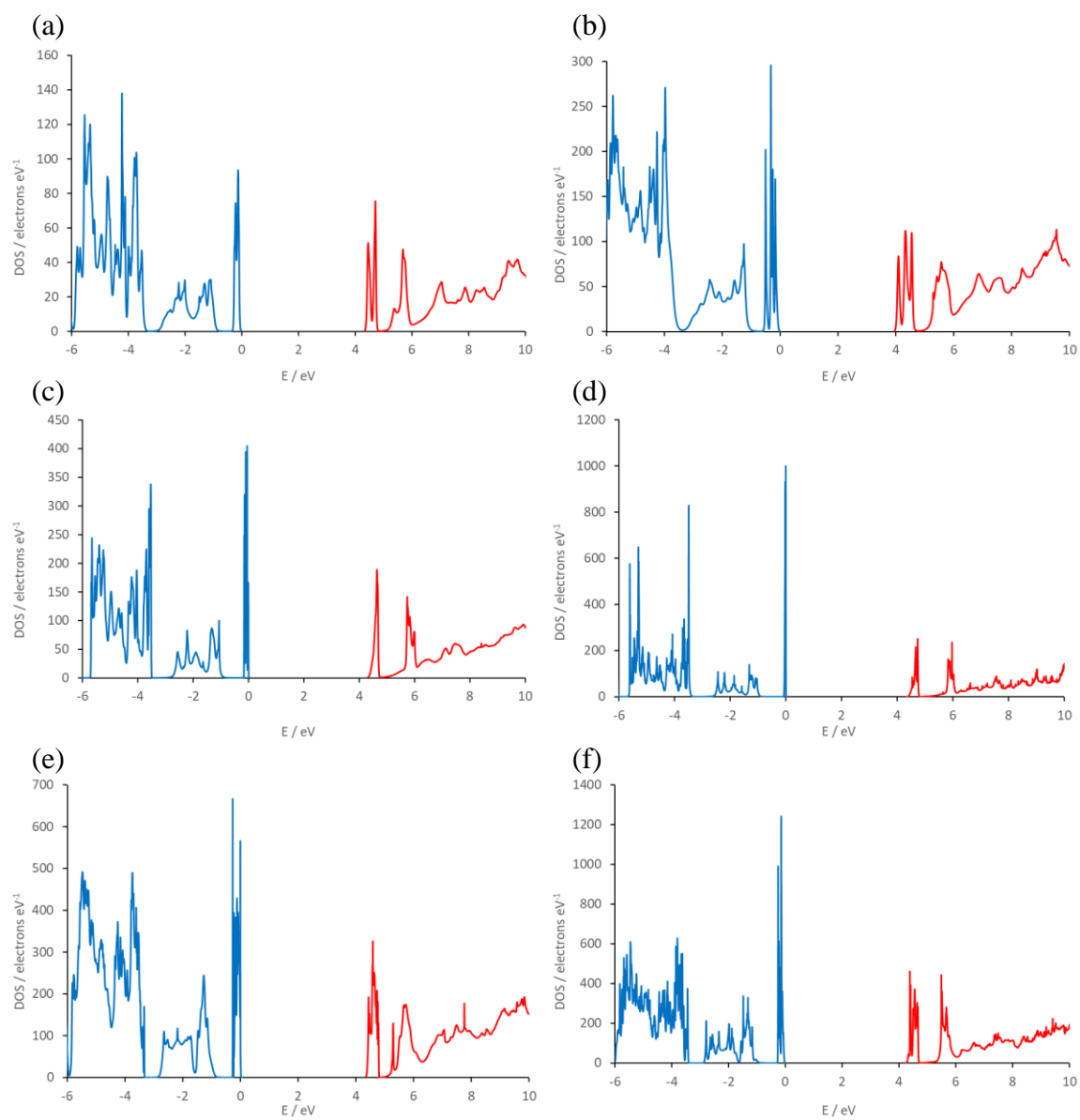
Figure B-2. DOS plot of (a) qtz-Zn(**CF₃Im**)₂, (b) dia-Zn(**CF₃Im**)₂, (c) SOD-Zn(**CF₃Im**)₂ in disordered P1 configuration, (d) SOD-Zn(**CF₃Im**)₂ in ordered I-43m configuration, (e) kat-Zn(**CF₃Im**)₂ in disordered P1 configuration, (f) kat-Zn(**CF₃Im**)₂ in ordered P-42c configuration, The valence bands are shown in blue and conduction bands are shown in red.
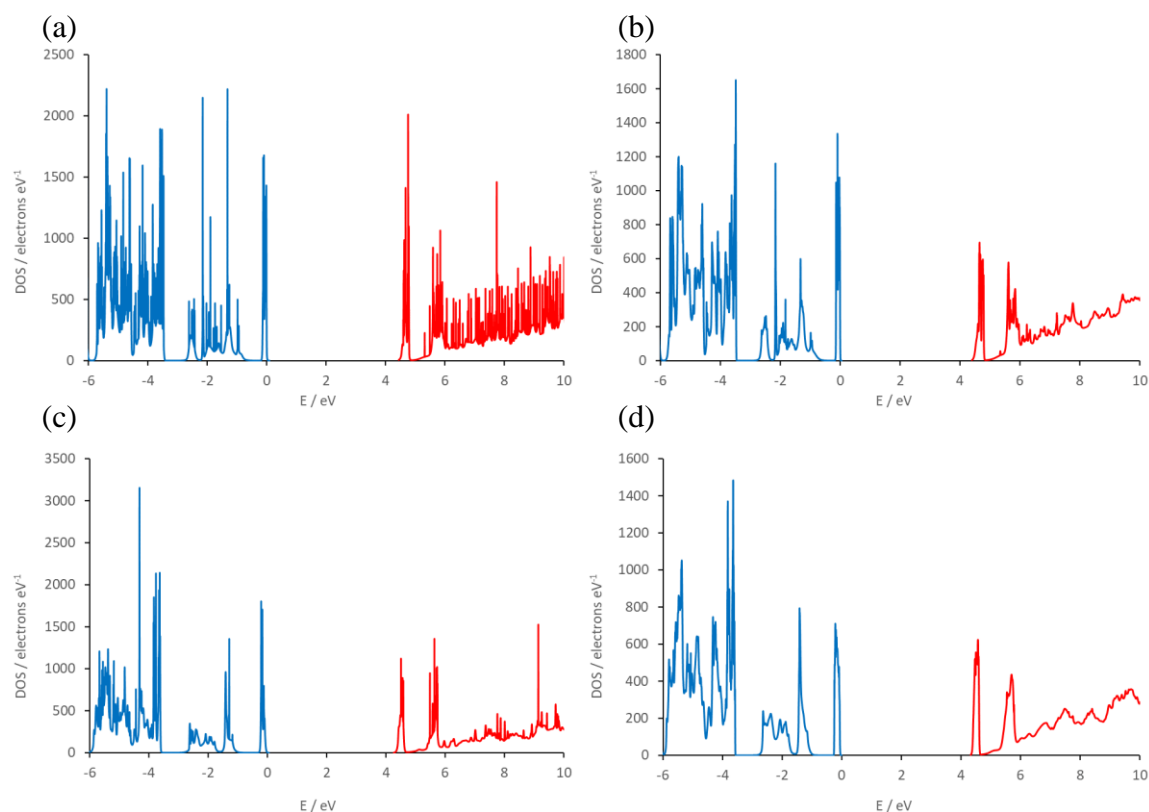
Figure B-3. DOS plot of (a) RHO-Zn(CF_3Im)$_2$ in ordered Im-3m configuration, (b) RHO-Zn(CF_3Im)$_2$ in disordered P1 configuration, (c) ANA-Zn(CF_3Im)$_2$ in disordered P1 configuration, (d) ANA-Zn(CF_3Im)$_2$ in ordered I-3ad configuration. The valence bands are shown in blue and conduction bands are shown in red.
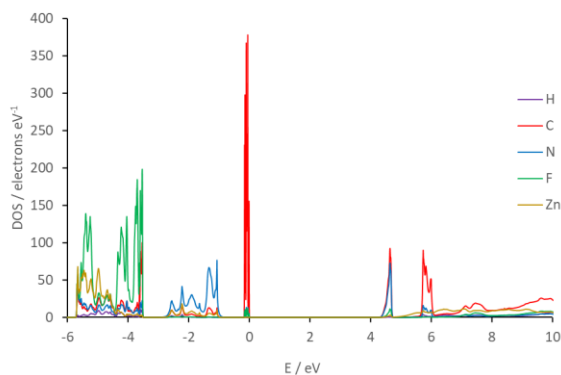
Figure B-4. Projected density of states (PDOS) plot of SOD-Zn(CF_3Im)$_2$ in disordered P1 configuration. Contributions from each element (H, C, N, F and Zn) are shown with different colors. The HOCO band is predominantly localized on the carbon atoms, while the LUCO band is distributed between carbon and nitrogen atoms. Essentially the frontier bands are localized on the CF_3Im ligands, without involvement of metal orbitals.

B.4 X-ray diffraction

B.4.1 Powder X-ray diffraction patterns
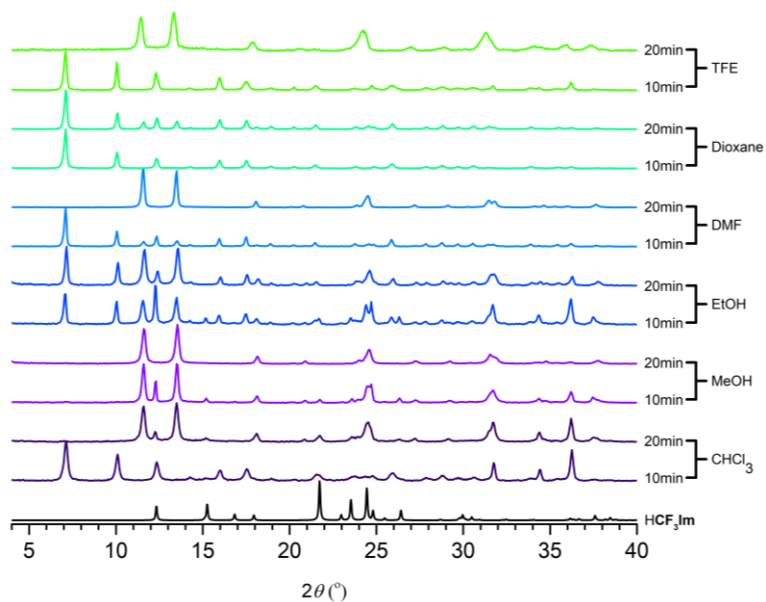
Figure B-5. Screening of the mechanochemical ILAG reaction 1 ZnO + 2 **HCF₃Im** + 10mol% NH₄NO₃ using different liquid additives and milling times.
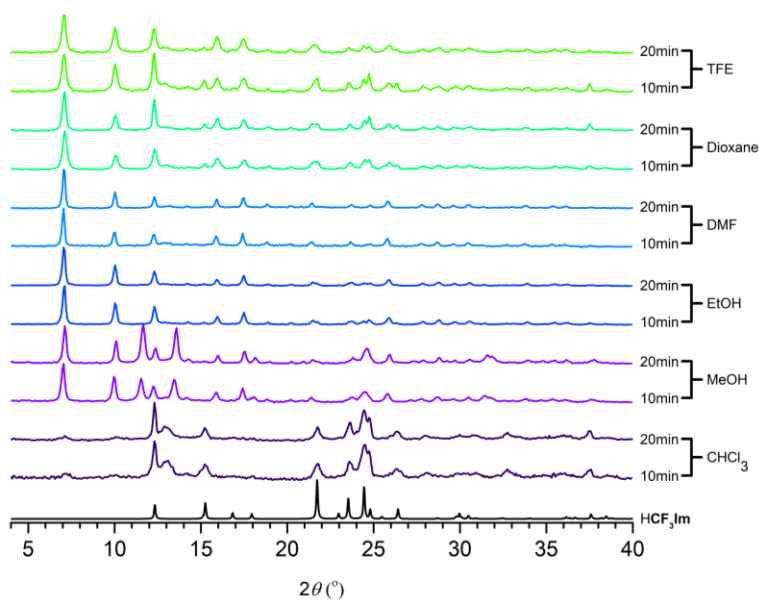
Figure B-6. Screening of the mechanochemical LAG reaction 0.2 [ZnCO₃]₂[Zn(OH)₂]₃ + 2 **HCF₃Im** using different LAG liquids and milling times.

B.4.2 Rietveld refinement of SOD- and *qtz*-Zn(CF₃Im)₂ structures
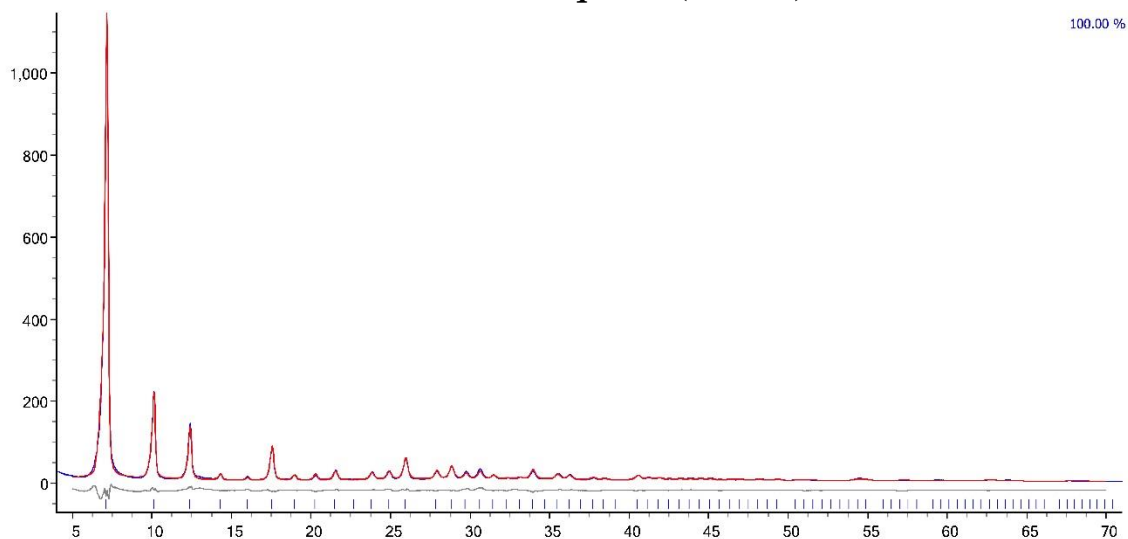
Figure B-7. The final Rietveld fit for the SOD–Zn(**CF₃Im**)₂ structure. Experimental pattern is shown in blue, calculated pattern in red, and difference curve in grey.
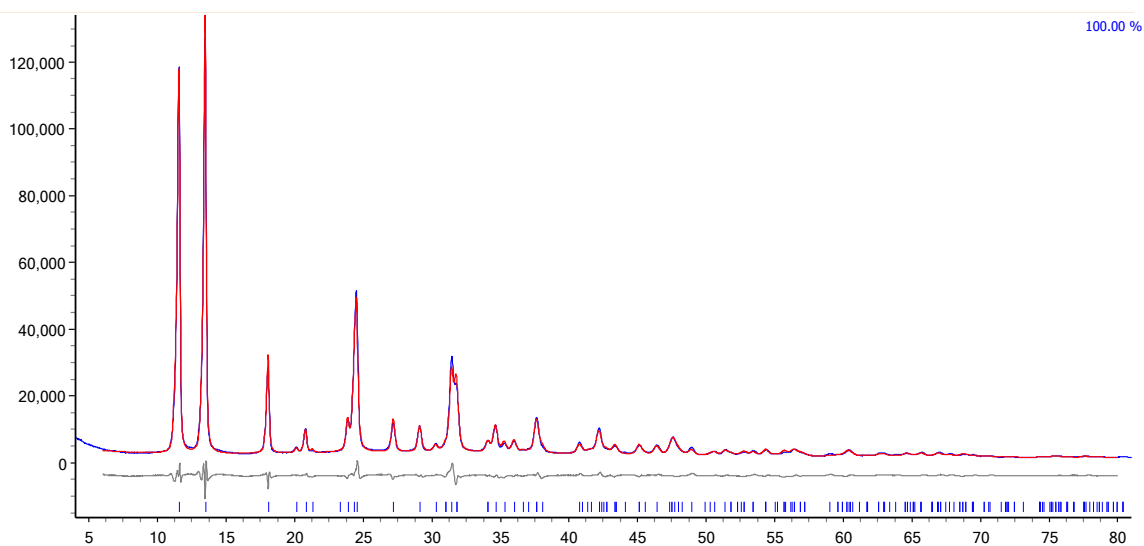
Figure B-8. The final Rietveld fit for the qtz–Zn(**CF₃Im**)₂ structure Experimental pattern is shown in blue, calculated pattern in red, and difference curve in grey.

Table B-2. Crystallographic data for structures of Zn(**CF₃Im**)₂ polymorphs determined from powder X-ray diffraction data.

	qtz–Zn(**CF₃Im**)₂	SOD–Zn(**CF₃Im**)₂
Formula	$Zn(C_4H_2F_3N_2)_2$	$Zn(C_4H_2F_3N_2)_2$
M_r (g mol⁻¹)	335.54	335.54
Crystal system	hexagonal	cubic
a / Å	8.8027(4)	17.5317(8)
b / Å	8.8027(4)	17.5317(8)
c / Å	12.7893(6)	17.5317(8)
α (°)	90	90
β (°)	90	90
γ (°)	120	90
V / Å³	858.25(9)	5388.5(7)
Space group	$P6_4$	$I\bar{4}3m$
ρ_c (g cm⁻³)	1.948	1.2408(2)
Radiation type	CuK$_\alpha$	CuK$_\alpha$
$F(000)$	492	1968
R_{wp}	0.051	0.064
R_p	0.040	0.049
R_{Bragg}	0.018	0.021
χ^2	10.224	10.727

B.4.3 Single crystal X-ray diffraction

Table B-3. Crystallographic and structure refinement data for the structure of H**CF₃Im** determined from single crystal X-ray diffraction data.

Formula	H**CF₃Im**
M_r (g mol^{-1})	136.08
Crystal system	monoclinic
Space group	$P2_1/c$
a / Å	7.5862(16)
b / Å	9.8792(18)
c / Å	7.6926(18)
β (°)	108.970(18)
V / Å^3	545.2(2)
Z	4
ρ_c (g cm^{-3})	1.658
Radiation type	CuK$_\alpha$
$F(000)$	272
Reflections measured	3499
Independent reflections	898
R_{int}	0.0991
R_1 $(I > 2\sigma(I))^{a, b}$	0.0825
$wR(F^2)$ $(I > 2\sigma(I))$ ^{c}	0.1868
R_1 (all data) ^{a}	0.1909
$wR(F^2)$ (all data) ^{c}	0.2401
S	1.031

^{a} For observed data; ^{b} $R1 = \Sigma||F_o| - |F_c||/\Sigma|F_o|$; ^{c} $wR2 = [\Sigma w(|F_o^2| - |F_c^2|)^2/\Sigma w|F_o^2|^2]^{1/2}$

B.5 Thermogravimetric analysis (TGA) of prepared ZIFs
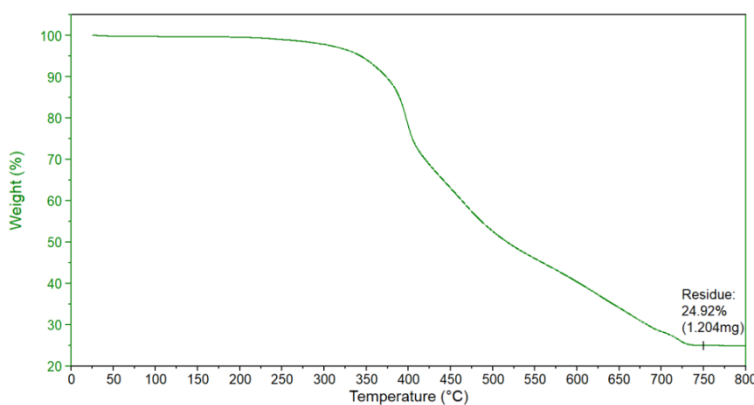
Figure B-9. TGA thermogram of SOD–Zn(**CF₃Im**)₂ framework prepared by milling, after washing with methanol and evacuation, recorded in air. Calculated ZnO residue: 24.25%; observed: 24.92%.
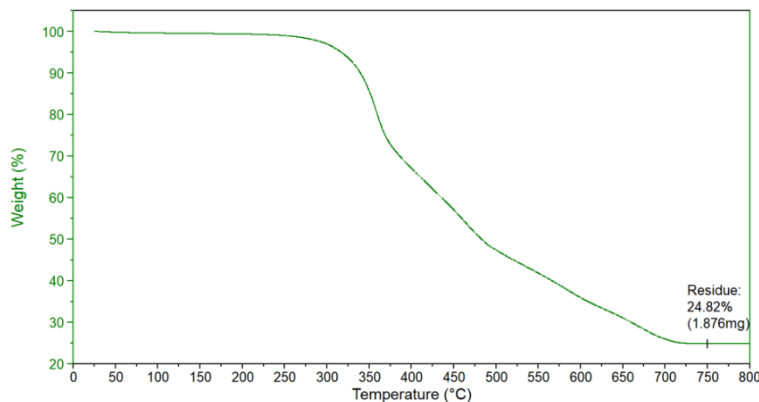
Figure B-10. TGA thermogram of qtz–Zn(**CF₃Im**)₂ framework prepared by milling, after washing with methanol, recorded in air. Calculated ZnO residue: 24.25%; observed: 24.82%.

B.6 Surface area measurements

Activation of samples prior to gas sorption measurements was done by soaking the materials in methanol for 24 hours, followed by heating at 150 °C for 8 hours under vacuum. Nitrogen isotherms were measured on a Micromeritics TriStar II 3020 at 77 K.
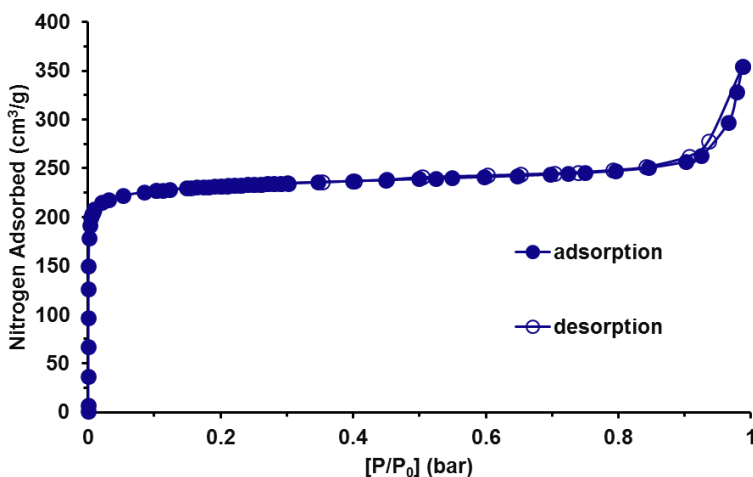
Figure B-11. N₂ isotherms for SOD–Zn(**CF₃Im**)₂ measured at 77 K. Filled and open circles represent adsorption and desorption isotherms, respectively. Connecting trace is shown as a guide for eyes.

BET surface area for SOD–Zn(**CF₃Im**)₂ = 923 m²/g

Calculated for SOD-Zn(**CF₃Im**)₂			Measured nitrogen sorption isotherm for SOD-Zn(**CF₃Im**)₂		
Accessible surface area	Pore volume	Max. pore diameter	Accessible surface area	Pore volume	Max. pore diameter
1016.5 m² / g	0.46 cm³ / g	10.9 Å	923.1 m² / g	0.384 cm³ / g	10.9 Å
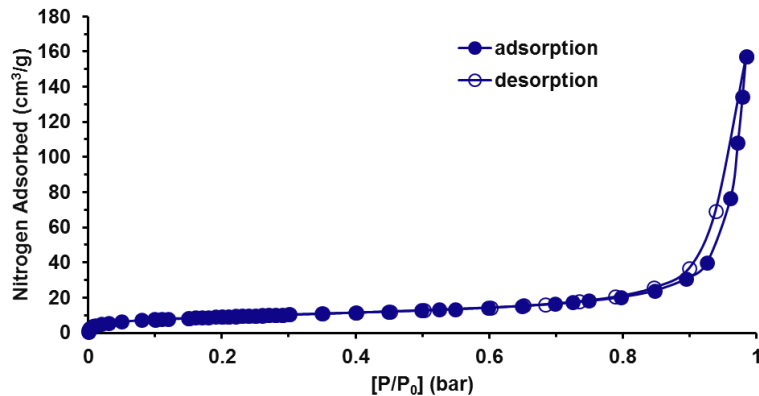
Figure B-12. N_2 isotherms for qtz–Zn(**CF₃Im**)₂ measured at 77 K. Filled and open circles represent adsorption and desorption isotherms, respectively. Connecting trace is shown as a guide for eyes.

BET surface area for *qtz*–Zn(**CF₃Im**)₂ = 29 m²/g

B.7 Fourier-transform infrared attenuated total reflectance (FTIR–ATR) spectra
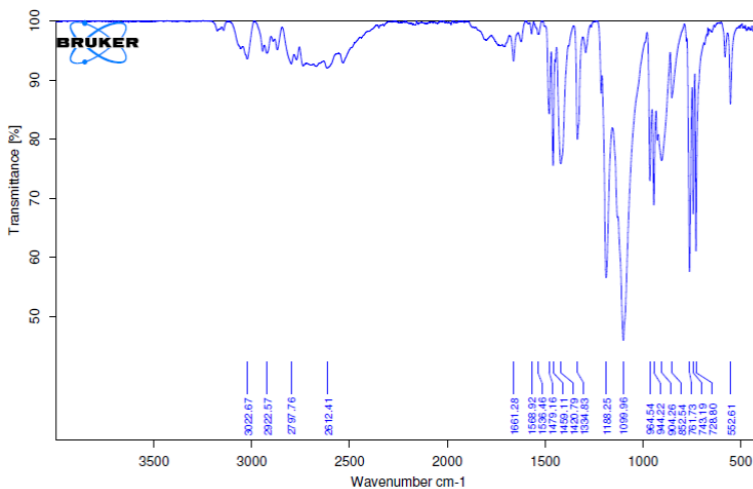
Figure B-13. FTIR–ATR spectrum of 2–(trifluoromethyl) –1H–imidazole (H**CF₃Im**).
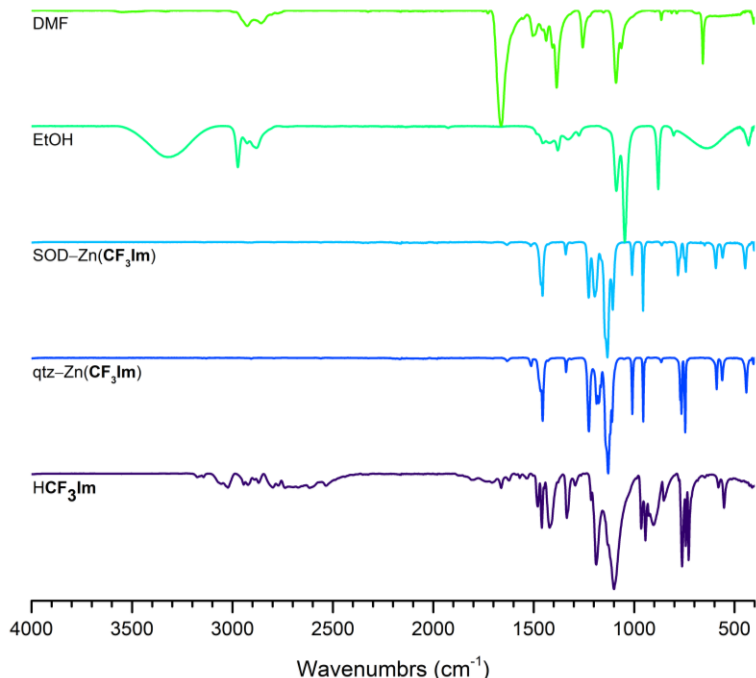
Figure B-14. FTIR–ATR spectra of Zn(**CF₃Im**)₂ products and relevant starting materials (from top to bottom): DMF (used as LAG additive); EtOH (used as LAG additive); SOD–Zn(**CF₃Im**)₂ made mechanochemically; qtz–Zn(**CF₃Im**)₂ made mechanochemically; solid H**CF₃Im** ligand.

B.8   References

(1)   Rietveld, H. M. Line profiles of neutron powder-diffraction peaks for structure refinement. *Acta Crystallogr.* **1967**, 22, 151-152.

(2)   Coelho, A. Coelho Software: Brisbane, Australia **2017**.

(3)   Pawley, G. S. Unit-cell refinement from powder diffraction scans. *J. Appl. Crystallogr.* **1981**, 14, 357-361.

(4)   René, O.; Souverneva, A.; Magnuson, S. R.; Fauber, B. P. Efficient syntheses of 2-fluoroalkylbenzimidazoles and -benzothiazoles. *Tet. Letters.* **2013**, 54, 201-204.

(5)   Clark, S. J.; Segall, M. D.; Pickard, C. J.; Hasnip, P. J.; Probert, M. I. J.; Refson, K.; Payne, M. C. First principles methods using CASTEP. *Z. Kristallogr.* **2005**, 220, 567-570.

(6)   Björkman, T. CIF2Cell: Generating geometries for electronic structure programs. *Comput. Phys. Commun.* **2011**, 182, 1183-1186.

(7)   Grimme, S. Semiempirical GGA-type density functional constructed with a long-range dispersion correction. *J. Comput. Chem.* **2006**, 27, 1787-1799.

(8)   Tkatchenko, A.; Distasio, R. A.; Car, R.; Scheffler, M. Accurate and Efficient Method for Many-Body van der Waals Interactions. *Phys. Rev. Lett.* **2012**, 108, 236402.

(9)   Reilly, A. M.; Tkatchenko, A. van der Waals dispersion interactions in molecular materials: beyond pairwise additivity. *Chem. Sci.* **2015**, 6, 3289-3301.

(10) Ambrosetti, A.; Reilly, A. M.; DiStasio, R. A.; Tkatchenko, A. Long-range correlation energy calculated from coupled atomic response functions. *J. Chem. Phys.* **2014**, 140, 18A508.

(11) Nicholls, R. J.; Morris, A. J.; Pickard, C. J.; Yates, J. R. OptaDOS - a New Tool for EELS Calculations. *J. Phys. Conf. Ser.* **2012**, 371, 012062.

(12) Morris, A. J.; Nicholls, R. J.; Pickard, C. J.; Yates, J. R. OptaDOS: A Tool for Obtaining Density of States, Core-Level and Optical Spectra from Electronic Structure Codes. *Comput. Phys. Commun.* **2014**, 185, 1477–1485.

Appendix C

Supplementary Information for Chapter 5

Linker Substituents Control the Thermodynamic Stability in

Metal-Organic Frameworks

C.1 Materials

Zinc oxide (≥99%), 2-methylimidazole (H**MeIm**) (99%), zinc basic carbonate (≥58% Zn basis), 2-chloroimidazole (H**ClIm**) (97%), 2-bromoiidazole (H**BrIm**) (97%), 2-iodoimidazole (H**IIm**) (97%), ammonium nitrate (≥99%), ammonium acetate (≥99%), and n-methyl-2-pyrrolidone (99.5%) were purchased from Sigma Aldrich and were used without any further purification. Imidazole-2-carboxaldehyde (97%) was purchased from Oakwood Chemical and was used without further purification. Methanol (99.8%) was purchased from Fischer Chemical. Dimethylformamide (99.8%) was purchased from ACP chemicals. 2-vinylimidazole[1] (H**VIm**), 2-acetyleneimidazole[2] (H**AIm**), and 2-trifluoromethylimidazole[3] (H**CF₃Im**) were prepared in-house according to previous reports.

C.2 Synthetic Procedures

All ZIFs were synthesized mechanochemically using a Retsch MM400 shaker mill (Retsch GmbH, Haan, Germany).

C.2.1 Synthesis of SOD-Zn(MeIm)₂

SOD–Zn(**MeIm**)₂ was synthesized following a previously published method[4,5]. The synthesis was performed mechanochemically by ball milling zinc oxide (1 mmol, 81 mg) with H**MeIm** (2.1 mmol, 172 mg) in the presence of ammonium nitrate (0.125 mmol, 10 mg) and 65 μl of methanol in a 10 mL stainless steel milling jar. Two 7 mm stainless steel balls were used as the milling media, and grinding proceeded at 30 Hz for 60 minutes. The product was washed with methanol then evacuated at 80°C for 12 hours.

C.2.2 Synthesis of SOD-Zn(VIm)₂

SOD-Zn(**VIm**)₂ was synthesized mechanochemically by ball milling zinc oxide (1 mmol, 81 mg) with H**VIm** (2 mmol, 188 mg in the presence of ammonium acetate (0.125 mmol, 10 mg) and 100

μl of ethanol in a 15 mL stainless steel milling jar. Two 7 mm stainless steel balls were used as the milling media, and grinding proceeded at 30 Hz for 30 minutes. The product was washed with methanol then evacuated at 80°C for 12 hours.

C.2.3 Synthesis of SOD-Zn(AIm)$_2$

SOD-Zn(**AIm**)$_2$ was synthesized mechanochemically by ball milling zinc oxide (1 mmol, 81 mg) with H**AIm** (2.4 mmol, 223 mg) with conditions identical to those of SOD–Zn(**VIm**)$_2$. Washing and evacuation also proceeded in an identical fashion. Analysis of zinc content using ICP-MS (sample size: 12.33 mg): expected 26.4%, measured 25.8%.

C.2.4 Synthesis of SOD-Zn(CHOIm)$_2$

SOD–Zn(**CHOIm**)$_2$ was synthesized mechanochemically by ball milling zinc basic carbonate ($[ZnCO_3]_2 \cdot [Zn(OH)_2]_3$) (0.2 mmol, 110 mg) with H**CHOIm** (2.2 mmol, 211 mg) in the presence of 200 μl of N-methyl-2-pyrrolidone (NMP) in a 15 mL stainless steel milling jar. Two 7 mm stainless steel milling balls were used as milling media, and milling proceeded for 90 minutes at 30 Hz. The sample was washed with methanol then evacuated at 80°C for 12 hours.

C.2.5 Synthesis of SOD-Zn(CF$_3$Im)$_2$

SOD–Zn(**CF$_3$Im**)$_2$ was synthesized mechanochemically using a previously reported method.[4] The synthesis was performed by ball milling zinc basic carbonate (0.1 mmol, 55 mg) with H**CF$_3$Im** (1.0 mmol, 136 mg) in the presence 70 μl of methanol in a 10 mL stainless steel milling jar. Two 7 mm stainless steel balls were used as the milling media, and grinding proceeded at 30 Hz for 30 minutes. The product was then washed with methanol and evacuated at room temperature.

C.2.6 Synthesis of SOD-Zn(ClIm)$_2$

SOD–Zn(**ClIm**)$_2$ was synthesized mechanochemically by ball milling zinc basic carbonate (0.1 mmol, 55 mg) with H**ClIm** (1.1 mmol, 113 mg) in the presence of 70 μl of dimethylformamide in a 15 mL stainless steel milling jar. Two 7mm stainless steel balls were used as the milling media, and milling proceeded at 30 Hz for 1 hour. The product was washed with methanol and evacuated at 80°C for 12 hours.

C.2.7 Synthesis of SOD-Zn(BrIm)$_2$

SOD–Zn(**BrIm**)$_2$ was synthesized mechanochemically by ball milling zinc oxide (0.5 mmol, 41 mg) with H**BrIm** (1.16 mmol, 170 mg) in the presence of 70 μl of N,N-dimethylformamide (DMF) and 15 mg of ammonium nitrate in a 15 mL stainless steel milling jar. Two 7mm stainless steel balls were used as the milling media, and milling proceeded at 30 Hz for 2 hours. The product was washed with methanol and evacuated at 80°C for 12 hours. Analysis of zinc content using ICP-MS (sample size: 6.35 mg): expected 18.3%, measured 18.1%.

C.2.8 Synthesis of SOD-Zn(IIm)$_2$

SOD–Zn(**IIm**)$_2$ was synthesized mechanochemically by ball milling zinc oxide (0.5 mmol, 41 mg) with H**IIm** (1.19 mmol, 230 mg) in the presence of 70 μl of DMF and 15 mg of ammonium nitrate in a 15 mL stainless steel milling jar. Two 7 mm stainless steel balls were used as the milling media, and milling proceeded at 30 Hz for 1 hour. The product was then washed with methanol and evacuated at 80°C for 12 hours. Analysis of zinc content using ICP-MS (sample size: 18.84 mg): expected 14.5%, measured 14.2%.

C.3 Calorimetric Methods

C.3.1 Room temperature solution calorimetry

Dissolution enthalpies of the samples were measured with a CSC 4400 isothermal microcalorimeter operating at 25 ℃. Small sample sizes (around 5 mg) were used to ensure that the dissolved ion concentration is low enough to avoid enthalpy contribution from ion mixing. Additionally, several experimental trials using mechanical mixture of the samples, which gave the expected enthalpy values from a mechanical mixture, confirmed that the measured enthalpies of dissolution were additive for the components so any contribution from possible ion complex formation can be neglected. In each experiment, ca. 5 mg of a sample were hand-pressed to form a pellet and dropped into 25.0 g of isothermally equilibrated 5 N HCl aqueous solution in-side a 50 mL Teflon cell of the calorimeter. All weight measurements were done using a Mettler microbalance with an accuracy of 10 µg. The solvent was isothermally equilibrated for at least 3 hours under mechanical stirring before the introduction of the sample, and the sample was allowed to dissolve in the cell for at least 3 hours, ensuring the return of baseline back to initial position. After each experiment, the cell was reassembled with fresh solvent. We have used a similar methodology in our previous thermochemical ZIF studies.[3,6,7]

C.3.2 Thermodynamic Cycles

Table C-1. Thermodynamic cycle used to calculate the formation enthalpy of ZIFs with respect to ZnO and H**RIm**.

Reactions	Enthalpy (ΔH, kJ·mol^{-1})
$Zn(\mathbf{RIm})_{2(s)} \rightarrow Zn^{2+}_{(aq)} + 2\ \mathbf{RIm}^{-}_{(aq)}$	$\Delta H_1 = \Delta H_s(Zn(\mathbf{RIm})_2)$
$ZnO_{(s)} + 2H^{+}_{(aq)} \rightarrow Zn^{2+}_{(aq)} + H_2O_{(aq)}$	$\Delta H_2 = \Delta H_s(ZnO)$
$H\mathbf{RIm}_{(s)} \rightarrow \mathbf{RIm}^{-}_{(aq)} + H^{+}_{(aq)}$	$\Delta H_3 = \Delta H_s(H\mathbf{RIm})$
$H_2O_{(l)} \rightarrow H_2O_{(aq)}$	$\Delta H_4 = \Delta H_{dil}(H_2O)$
$ZnO_{(s)} + 2H\mathbf{RIm}_{(s)} \rightarrow Zn(\mathbf{RIm})_{2(s)} + H_2O_{(l)}$	$\Delta H_5 = \Delta H_f, = -\Delta H_1 + \Delta H_2 + 2\Delta H_3 - \Delta H_4$

Table C-2. Thermodynamic cycle used to calculate the formation enthalpy of ZIF-90 with respect to ZnO and (H**CHOIm**)$_2$ dimer ligand and consequent correction with dimer dissociation enthalpy.

Reactions	Enthalpy (ΔH, kJ·mol^{-1})
Zn(**CHOIm**)$_{2(s)}$ → Zn$^{2+}_{(aq)}$ + 2 **CHOIm**$^-_{(aq)}$	$\Delta H_1 = \Delta H_s(Zn(\textbf{CHOIm})_2)$
ZnO$_{(s)}$ + 2H$^+_{(aq)}$ → Zn$^{2+}_{(aq)}$ + H$_2$O$_{(aq)}$	$\Delta H_2 = \Delta H_s(ZnO)$
(H**CHOIm**)$_{2\,(s)}$ → 2**CHOIm**$^-_{(aq)}$ + 2H$^+_{(aq)}$	$\Delta H_3 = \Delta H_s((H\textbf{CHOIm})_2)$
H$_2$O$_{(l)}$ → H$_2$O$_{(aq)}$	$\Delta H_4 = \Delta H_{dil}(H_2O)$
ZnO$_{(s)}$ + (H**CHOIm**)$_{2\,(s)}$ → Zn(**CHOIm**)$_{2(s)}$ + H$_2$O$_{(l)}$	$\Delta H_5 = \Delta H_f = -\Delta H_1 + \Delta H_2 + 2\Delta H_3 - \Delta H_4$
(H**CHOIm**)$_{2\,(s)}$ → 2H**CHOIm**$_{(s)}$	$\Delta H_6 = \Delta H_{dis}((H\textbf{CHOIm})_2)$
ZnO$_{(s)}$ + 2H**CHOIm**$_{(s)}$ → Zn(**CHOIm**)$_{2(s)}$ + H$_2$O$_{(l)}$	$\Delta H_7 = \Delta H_{f,cor} = \Delta H_5 - \Delta H_6$

C.4 Inductively coupled plasma mass spectrometry (ICP-MS) analysis

The metal content of selected ZIF samples Zn(**BrIm**)$_2$, Zn(**IIm**)$_2$ and Zn(**AIm**)$_2$ was investigated also using inductive coupled plasma mass spectrometry (ICP-MS). The ZIFs were weighed on a microbalance and dissolved in 1% trace-metals grade nitric acid in MilliQ high-purity water. Serial dilutions were performed to bring the zinc concentration to between 100 and 300 ppb in the 1% acid solution. The ICP-MS analysis was performed on these samples using a Thermo Finnigan iCap-Q ICP-MS instrument, monitoring for all isotopes of zinc.

Table C-3. Measured and theoretically calculated Zn content of selected ZIFs

Compound	Mass (mg)	Theoretical Zn (w)	Experimental Zn (w)
Zn(BrIm)$_2$	6.35	18.3%	18.1%
Zn(IIm)$_2$	18.84	14.5%	14.2%
Zn(AIm)$_2$	12.33	26.4%	25.8%

C.5 Solid-state nuclear magnetic resonance spectroscopy

To confirm the structure and composition of Zn(**CHOIm**)$_2$, a sample was investigated using 13C cross-polarization magic angle spinning (CP-MAS) solid-state nuclear magnetic resonance spectroscopy (ssNMR) Spectra were collected using a VNMRS 400 widebore spectrometer operating at 399.9 MHz for 1H and 100.5 MHz for 13C. The spectrometer was equipped with a 4mm Varian Chemagnetics double-resonance probe, and a 5 s recycle delay and 13 kHz spin rate were used. 2048 scans were collected with a cross polarization time of 2 ms.
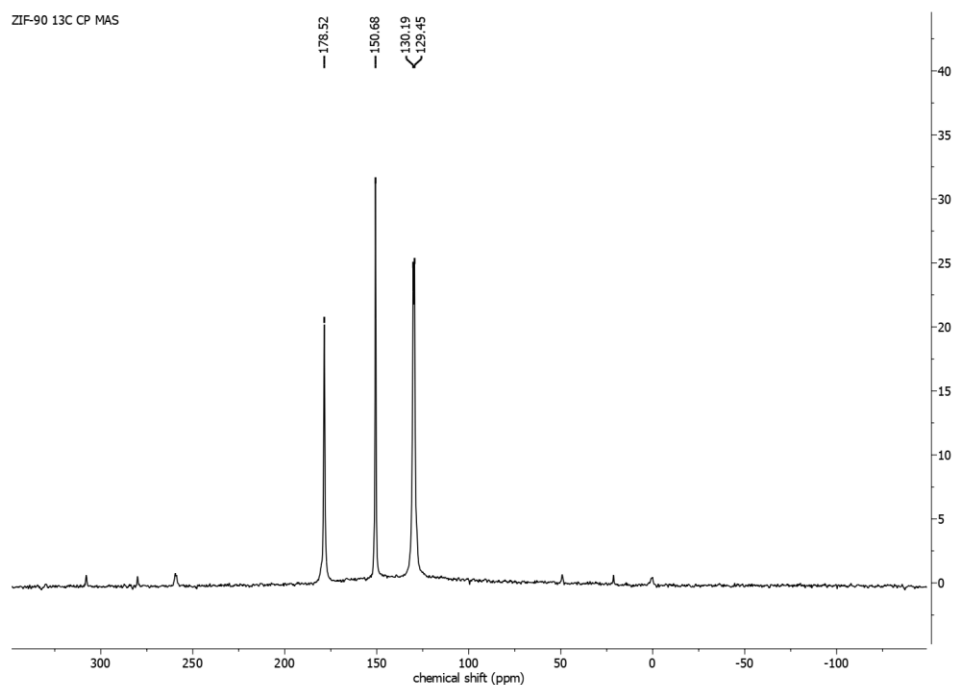
Figure C-1. ^{13}C CP/MAS NMR spectrum for Zn(**CHOIm**)$_2$

C.6 Thermogravimetric analysis (TGA) of the prepared ZIFs

Thermogravimetric analysis (TGA) was performed on a Netzsch 449 thermal balance. In each experiment, the sample (5-10 mg) was placed in a platinum crucible, and heated from 25 to $800^{\circ}C$ with a heating rate of $10^{\circ}C \cdot min^{-1}$, under a mixture of O_2 and Ar (40 ml·min^{-1} flow rate)
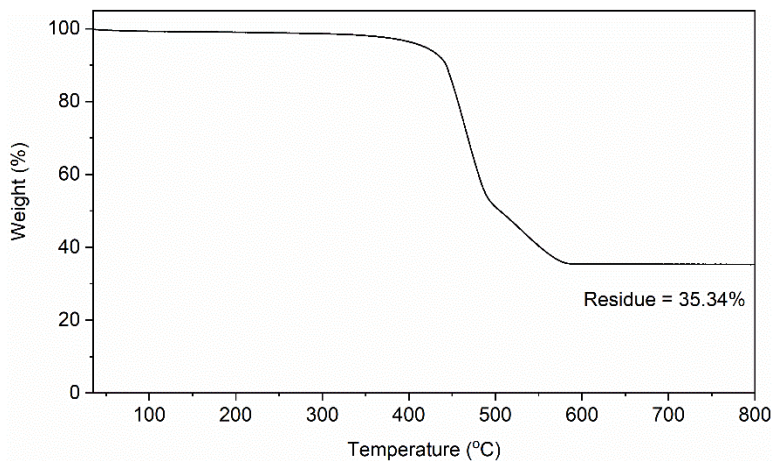
Figure C-2. TGA curve of Zn(**MeIm**)$_2$. Expected ZnO residue 35.76%, observed 35.34%
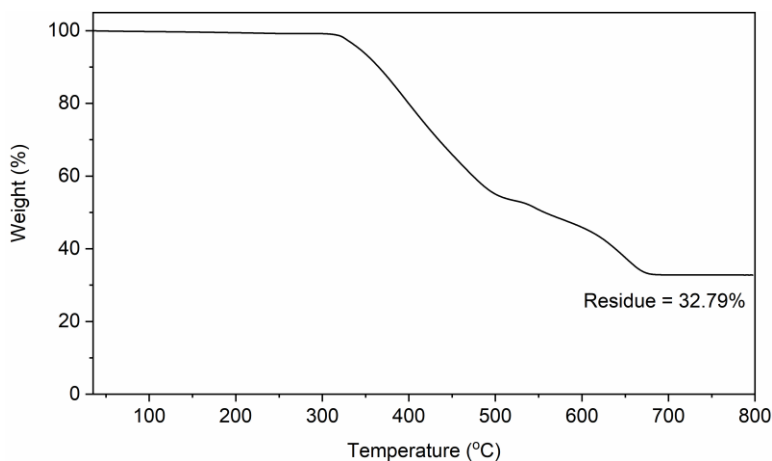
Figure C-3. TGA curve of Zn(**VIm**)$_2$. Expected ZnO residue 32.3%, observed 32.79%
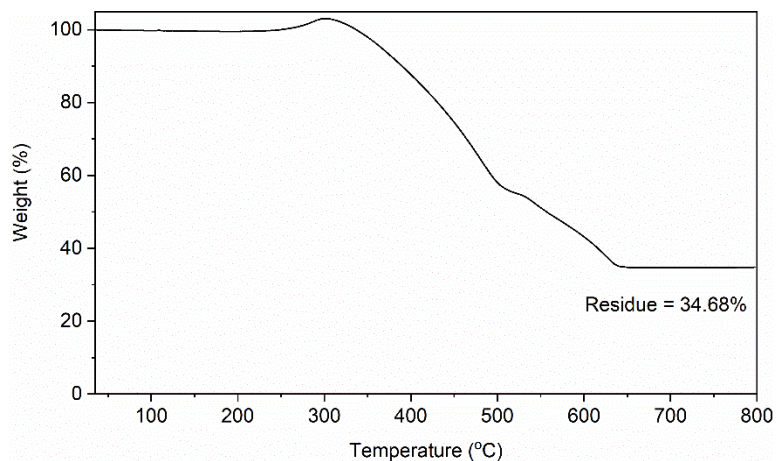
Figure C-4. TGA curve of Zn(**AIm**)$_2$. Expected ZnO residue 32.87%, observed 34.68%
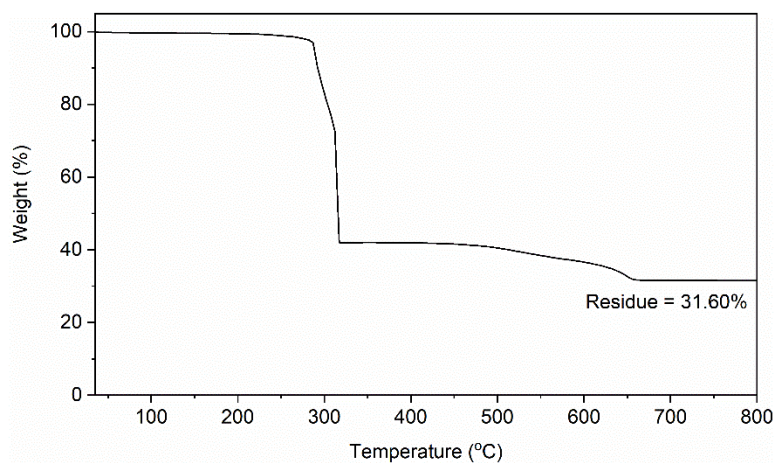
Figure C-5. TGA curve of Zn(**CHOIm**)$_2$. Expected ZnO residue 31.85%, observed 31.60%
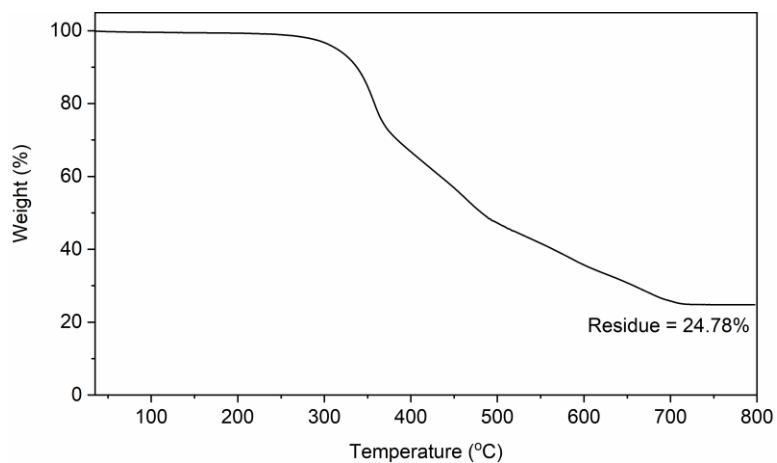
Figure C-6. TGA curve of Zn(**CF₃Im**)$_2$. Expected ZnO residue 24.25%, observed 24.78%
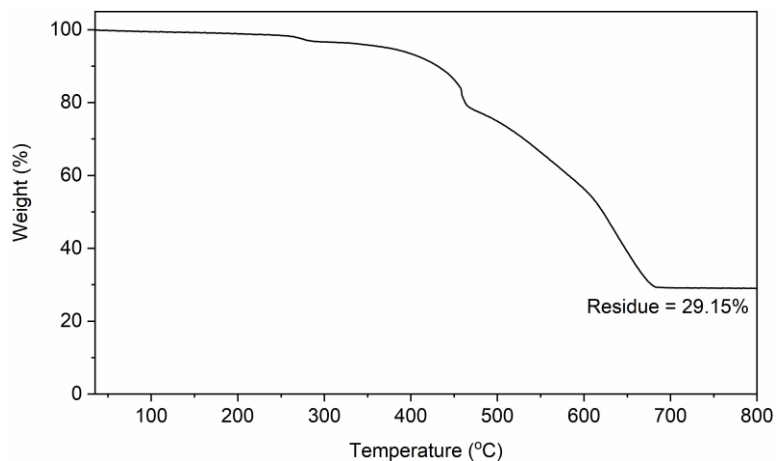
Figure C-7. TGA curve of Zn(**ClIm**)$_2$. Expected ZnO residue 30.32%, observed 29.15%
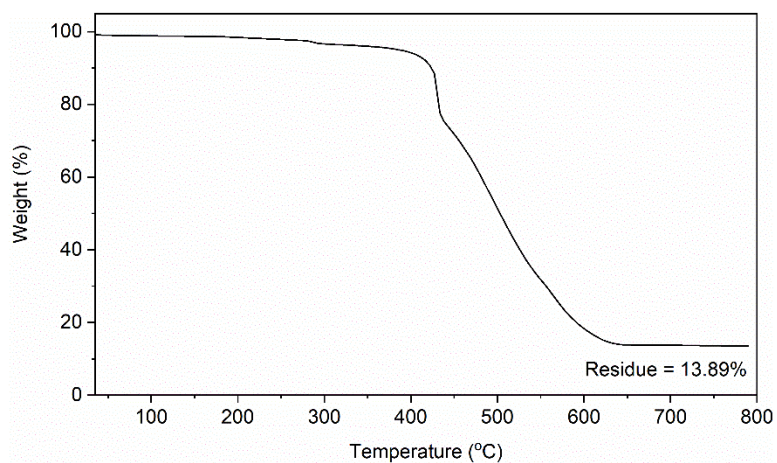
Figure C-8. TGA curve of Zn(**BrIm**)$_2$. Expected ZnO residue 22.78%, observed 13.89%
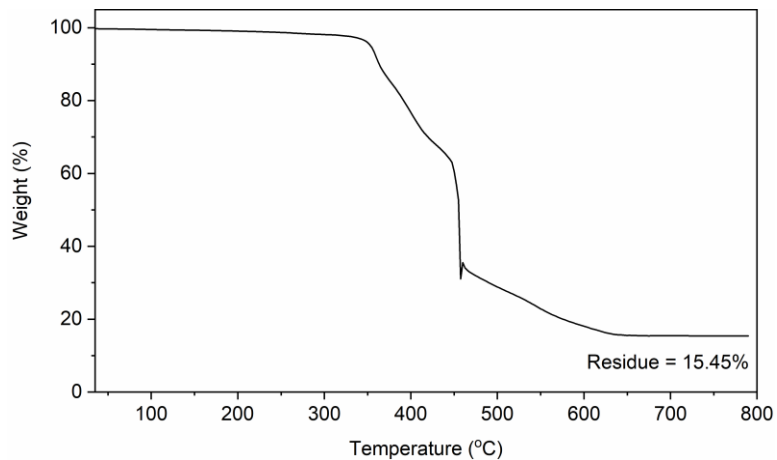
Figure C-9. TGA curve of Zn(**IIm**)$_2$. Expected ZnO residue 18%, observed 15.45%

157

C.7 Powder X-ray diffraction patterns

Powder x-ray diffractograms were collected using a Bruker D2 PHASER benchtop diffractometer fitted with a LynxEye 1-D detector (Bruker AXS, Madison, WI, USA), using Ni-filtered CuKα x-ray radiation.
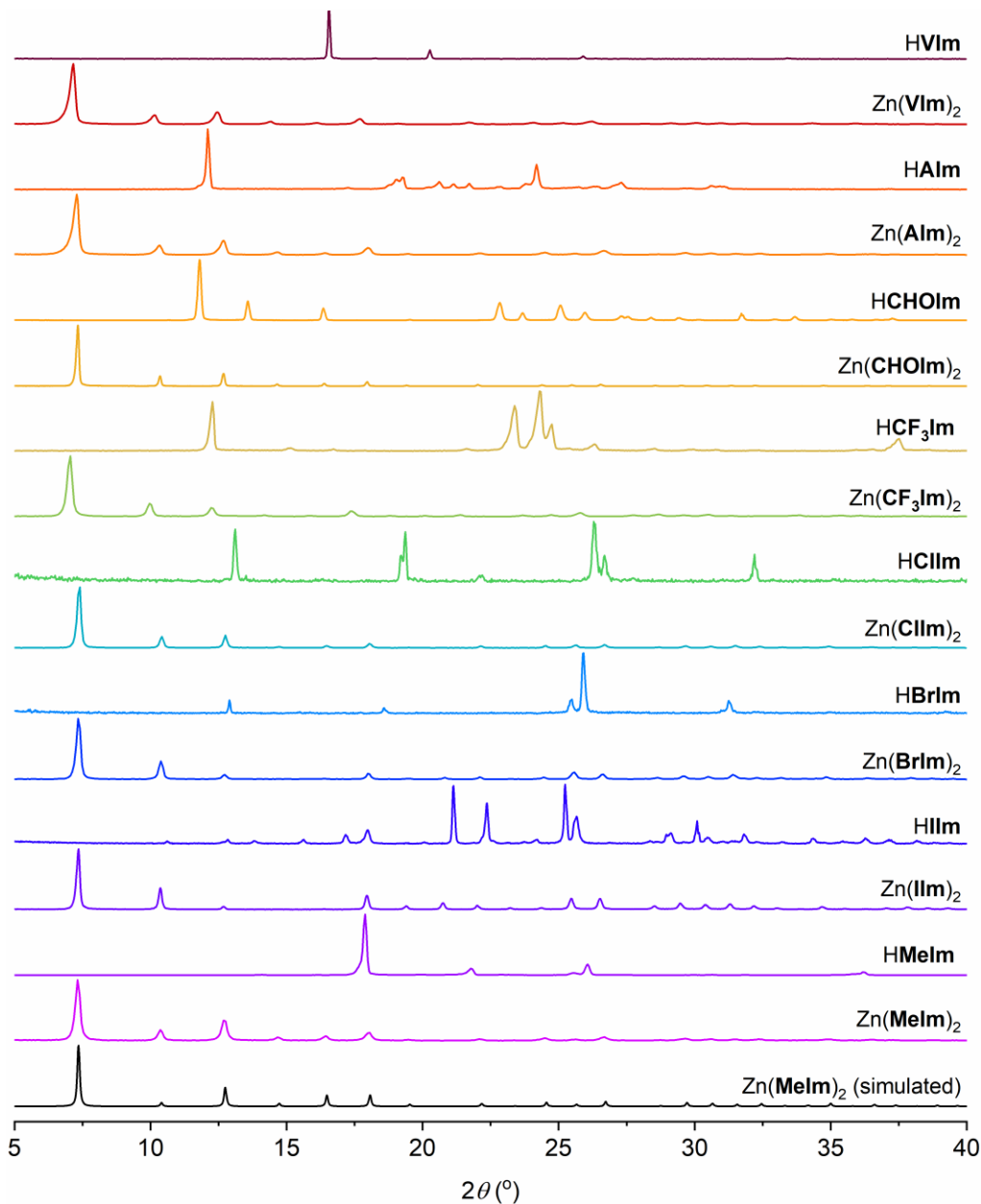
Figure C-10. PXRD patterns of the investigated ZIFs with their corresponding imidazole ligands. The simulated pattern for SOD-Zn(**MeIm**)$_2$ was based on the structure reported in the CSD (CCDC code VELVOY).

158

C.7.1 Crystal structure determination of Zn(IIm)$_2$ from powder X-ray diffraction data

Crystal structure of SOD-Zn(**IIm**)$_2$ was determined from PXRD data using the program TOPAS Academic v. 6.[8] The powder pattern of SOD-Zn(**IIm**)$_2$ was demonstrably similar to the patterns of other sodalite ZIFs, therefore it was not necessary to index the pattern, as we could assume a cubic cell with approx. 17 *Å* lattice parameter and *I-43m* space group symmetry. Pawley refinement[9] of this trial cell resulted in a lattice parameter of 17.19 Å. The Pawley procedure utilized pseudo-Voigt functions for peak shape fitting, as well as a 6th degree Chebyshev polynomial for background fitting. In addition, the instrumental offset was corrected by refining the zero-error parameter.

The Pawley refinement was followed by Rietveld refinement,[10] where the Zn atom was placed on a special position at (¾, 0, ½), while the 2-iodoimidazole linker was described with a half-molecule rigid body, constrained to lie on a mirror plane. In this refinement step, position and orientation of the imidazole rigid body was refined along with all the other parameters from the Pawley procedure. The resulting ordered structural model of SOD-Zn(**IIm**)$_2$ was isomorphous with SOD-Zn(**MeIm**)$_2$. The previously reported crystal structures of halogenated ZIFs SOD-Zn(**ClIm**)$_2$ and SOD-Zn(**BrIm**)$_2$ show rotational disorder of the imidazolate linker with respect to Zn-Zn axis.[11] In order to investigate the possibility of such a disorder in SOD-Zn(**IIm**)$_2$, a second imidazole rigid body was introduced, and the coordinates of the two imidazolate fragments were refined independently, subject to the total occupancy constraint. Indeed, the modified structural model revealed rotational disorder of the imidazolate linker, similar to that found in the structures of SOD-Zn(**ClIm**)$_2$ and SOD-Zn(**BrIm**)$_2$ The interplanar angle between the two disordered imidazolates was found to be 10(3)°, with the corresponding occupancies of 0.59(7):0.41(7). Introduction of the disordered model resulted in the improved goodness of fit (2.04 vs 2.38) and lower weighted profile R-factor (11.2% vs 13.1%).
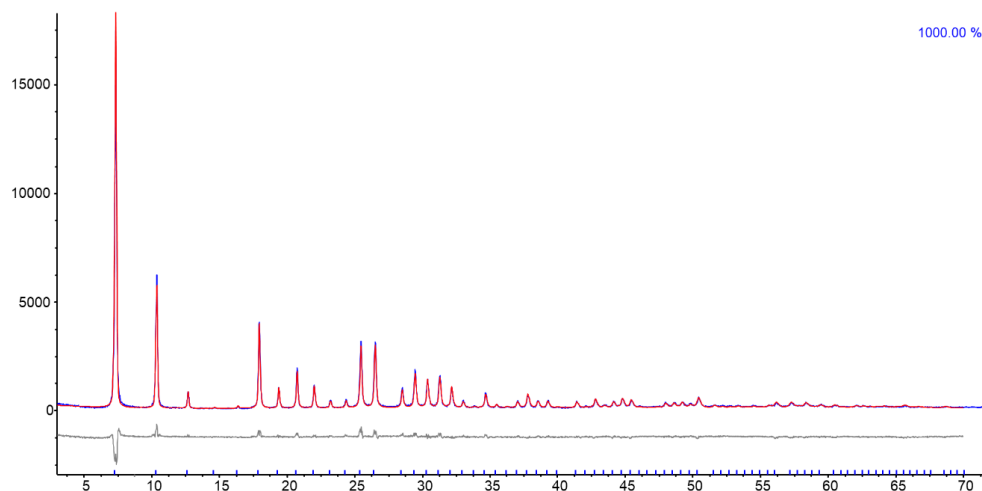
Figure C-11. The final Rietveld fit for the SOD-Zn(**IIm**)$_2$ structure. Experimental pattern is shown in blue, calculated pattern in red, and difference curve in grey.

Table C-4. Crystallographic data for the crystal structure of SOD-Zn(**IIm**)$_2$ determined from powder X-ray diffraction data.

	SOD–Zn(**IIm**)$_2$
Formula	Zn(C$_3$H$_2$IN$_2$)$_2$
M_r **(g mol^{-1})**	451.31
Crystal system	cubic
a, b, c / Å	17.1902(5)
α, β, γ (°)	90
V / Å^3	5079.8(4)
Space group	I $\bar{4}$3m
ρ_c **(g cm^{-3})**	1.7705(2)
Radiation type	CuKα
F**(000)**	2448
R_{wp}	0.112
R_p	0.091
R_{Bragg}	0.061
χ^2	2.036

C.7.2 Crystal structure determination of HVIm, HClIm, and HIIm from single crystal X-ray diffraction

Single crystal X-ray diffraction data for H**VIm**, H**ClIm**, and H**IIm** were measured on a Bruker D8 Venture diffractometer equipped with a Photon 200 area detector, and *IμS* microfocus X-ray source (Bruker AXS, Cu*K*α source). All measurements were carried out at room temperature but for H**VIm** which was measured at 150(2) K. Structure solutions were carried out using the SHELXT package from Bruker.[12] The parameters were refined for all data by full-matrix-least-squares or F^2 using SHELXL.[13] All of the nonhydrogen atoms were refined with anisotropic thermal parameters. Hydrogen atoms were placed in calculated positions and allowed to ride on the carrier atoms. All hydrogen atom thermal parameters were constrained to ride on the carrier atom. The H**IIm** materials showed a strong diffuse scattering in the form of diffuse Bragg peaks and scattering between them, twinning, and the imidazole rings were found to be heavily disorder. In addition, a major disorder was found in H**VIm** structure. Both structures were split and modeled.

Table C-5. Crystallographic data for the crystal structures of **HVIm**, **HClIm**, and **HIIm** linker precursors, determined from single crystal X-ray diffraction data.

	HVIm	HClIm	HIIm
Empirical formula	$C_5H_6N_2$	$C_3H_3ClN_2$	$C_3H_3IN_2$
Formula weight	94.12	102.52	193.97
Temperature/K	150(2)	298(2)	298(2)
Crystal system	monoclinic	monoclinic	orthorhombic
Space group	Pc	$P2_1/n$	$Pca2_1$
a/Å	8.3826(17)	9.6720(4)	17.3434(7)
b/Å	6.6386(14)	8.7035(4)	9.7088(5)
c/Å	9.7570(16)	11.2583(5)	12.3473(5)
α/°	90	90	90
β/°	90.153(7)	104.350(2)	90
γ/°	90	90	90
Volume/Å^3	542.96(18)	918.16(7)	2079.08(16)
Z	4	8	16
ρ_{calc} g·cm^{-3}	1.151	1.483	2.479
μ/mm^{-1}	0.074	5.975	47.188
F(000)	200.0	416.0	1408.0
Radiation	Mo$K\alpha$	Cu$K\alpha$	Cu$K\alpha$
$2q$ range for data collection/°	4.86 to 57.662	10.816 to 144.848	9.108 to 145.302
Reflections collected	16193	13045	28365
Independent reflections	2523 [$R_{int} = 0.1095$, $R_{sigma} = 0.0658$]	1792 [$R_{int} = 0.0806$, $R_{sigma} = 0.0524$]	4085 [$R_{int} = 0.0974$, $R_{sigma} = 0.0609$]
Data/restraints/parameters	2523/252/256	1792/0/110	4085/985/271
Goodness-of-fit on F^2	1.002	1.083	1.062
Final R indexes [I>=2σ (I)]	$R_1 = 0.0629$, $wR_2 = 0.1589$	$R_1 = 0.0938$, $wR_2 = 0.2748$	$R_1 = 0.0738$, $wR_2 = 0.1914$
Final R indexes [all data]	$R_1 = 0.1668$, $wR_2 = 0.2103$	$R_1 = 0.1028$, $wR_2 = 0.2922$	$R_1 = 0.0827$, $wR_2 = 0.2088$
Largest diff. peak/hole / e Å^{-3}	0.15/-0.13	0.49/-0.47	2.62/-3.27

C.8 Fourier transform infrared – attenuated total reflectance (FTIR-ATR) spectroscopy

A Bruker Vertex 70 FTIR spectrometer outfitted with a Bruker Platinum ATR unit was used to collect FTIR-ATR spectra.
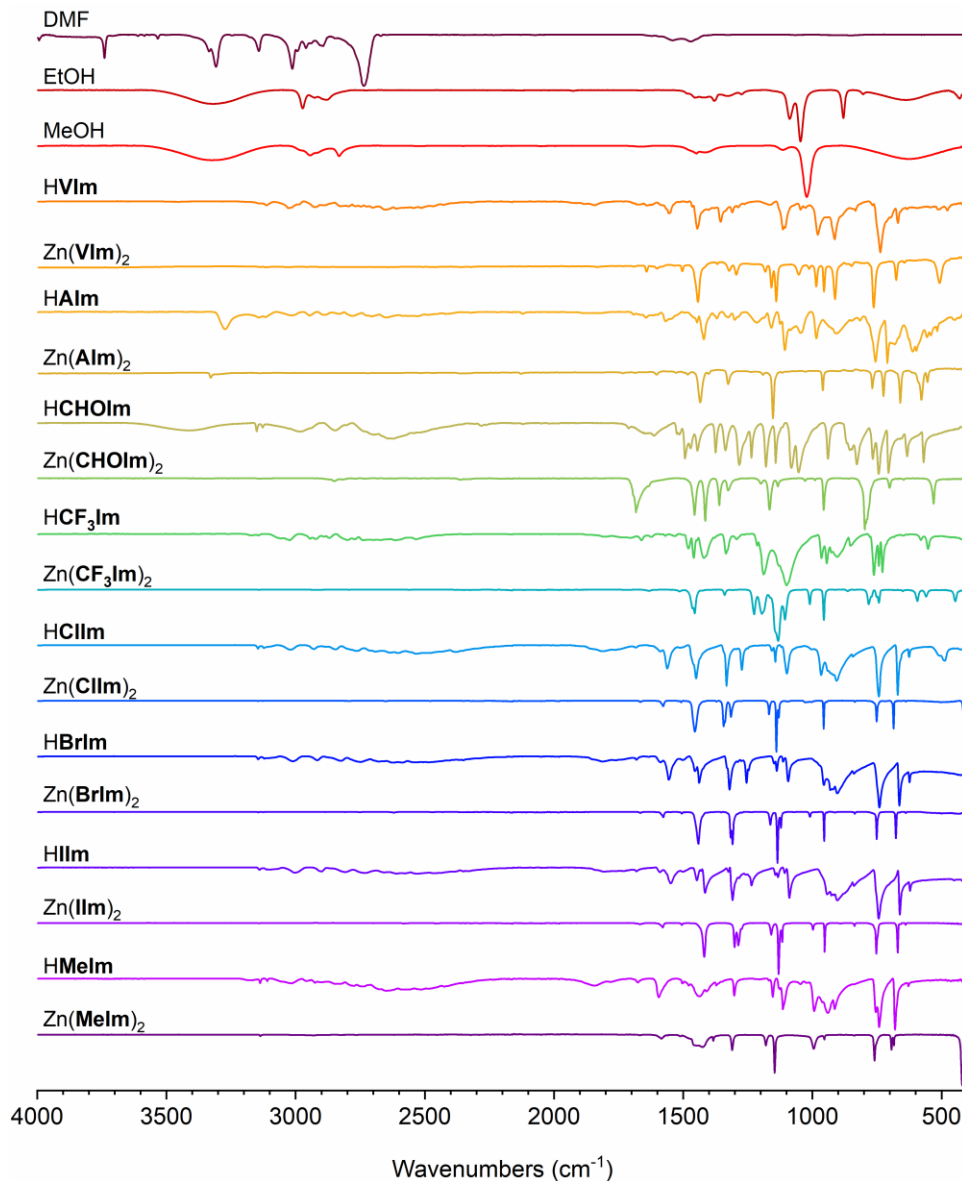
Figure C-12. Comparison of FTIR-ATR spectra for the investigated ZIFs, corresponding imidazoles and relevant liquid additives used in LAG (liquid-assisted grinding) synthesis.

C.9 Surface area measurements

The nitrogen adsorption and desorption isotherm measurements for SOD-Zn(**VIm**)$_2$, SOD-Zn(**AIm**)$_2$, and SOD-Zn(**CHOIm**)$_2$ were performed on a Quantachrome instrument at a temperature of 77 K, while measurements on SOD-Zn(**ClIm**)2, SOD-Zn(**IIm**)2, SOD-Zn(**BrIm**)2 and SOD-Zn(**MeIm**)2 were performed on a Micromeritics TriStar II Plus instrument. Samples were activated at 120°C for 4 hours prior to each measurement. The uncertainties given in the result represents 95% confidence interval.
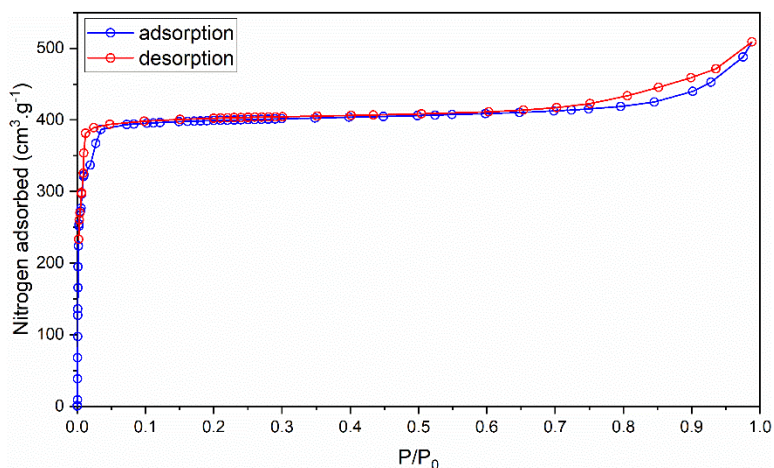
Figure C-13. The N$_2$ adsorption isotherm of SOD-Zn(**MeIm**)$_2$.
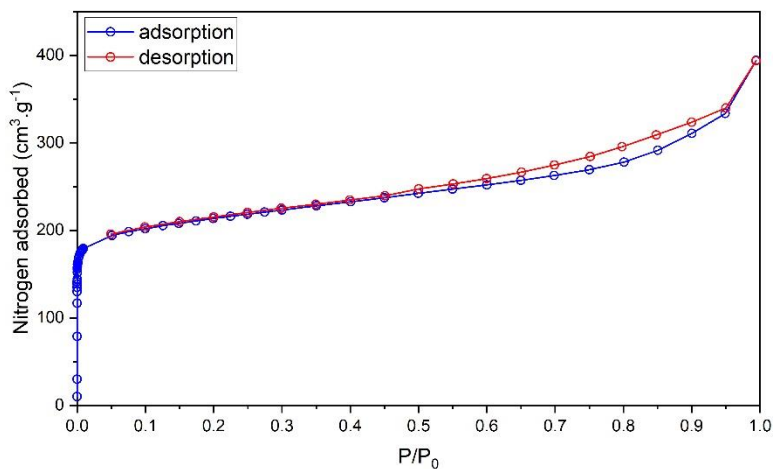
Figure C-14. The N$_2$ adsorption isotherm of SOD-Zn(**VIm**)$_2$.
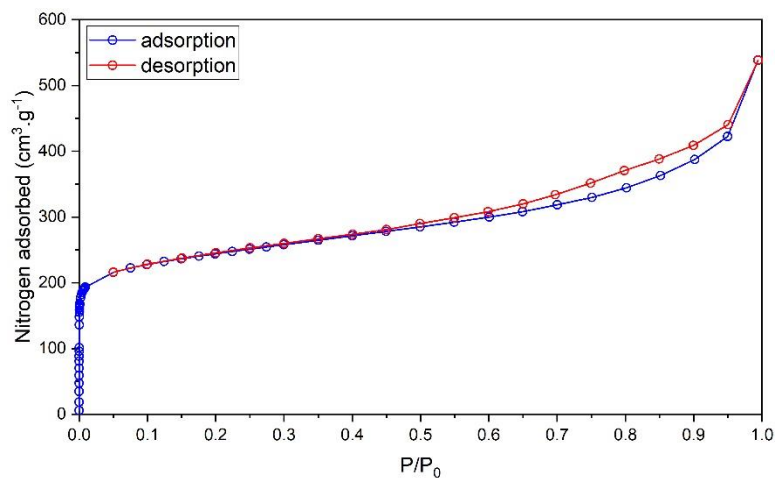
Figure C-15. The N_2 adsorption isotherm of SOD-Zn(**AIm**)$_2$.
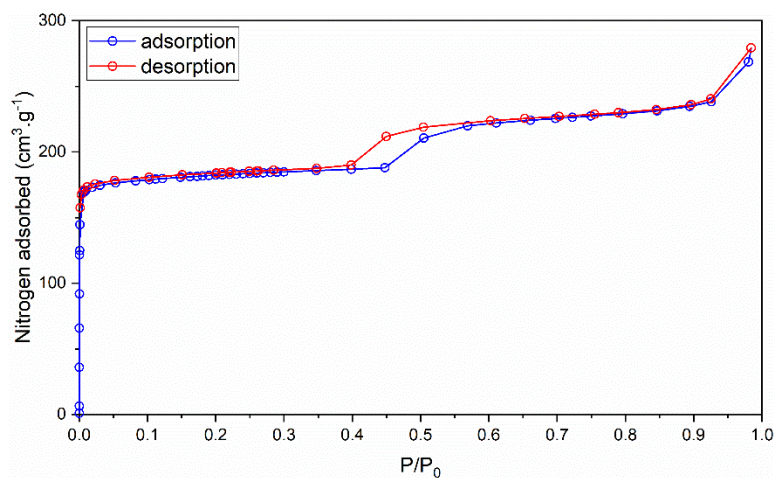
Figure C-16. The N_2 adsorption isotherm of SOD-Zn(**CHOIm**)$_2$.
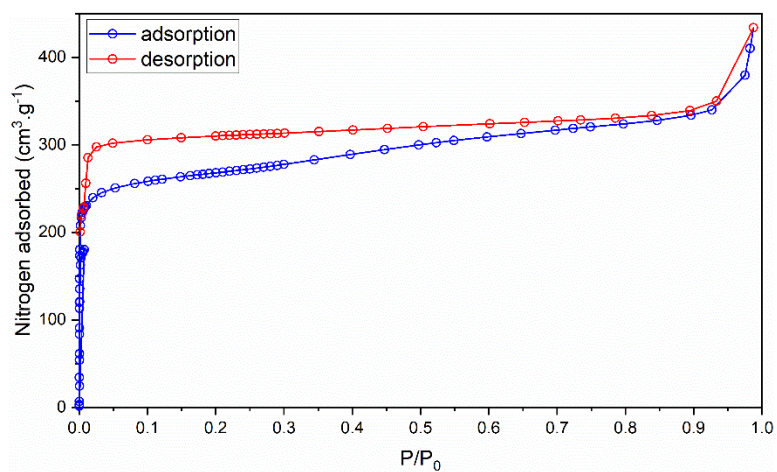
Figure C-17. The N_2 adsorption isotherm of SOD-Zn(**ClIm**)$_2$.
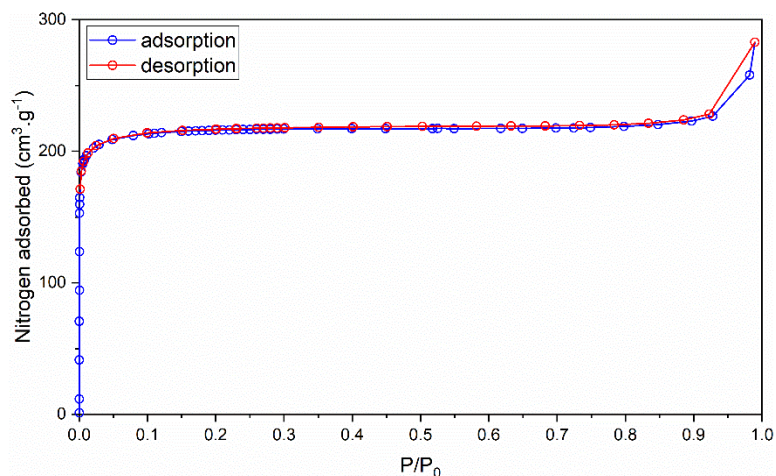
Figure C-18. The N_2 adsorption isotherm of SOD-Zn(**BrIm**)$_2$.
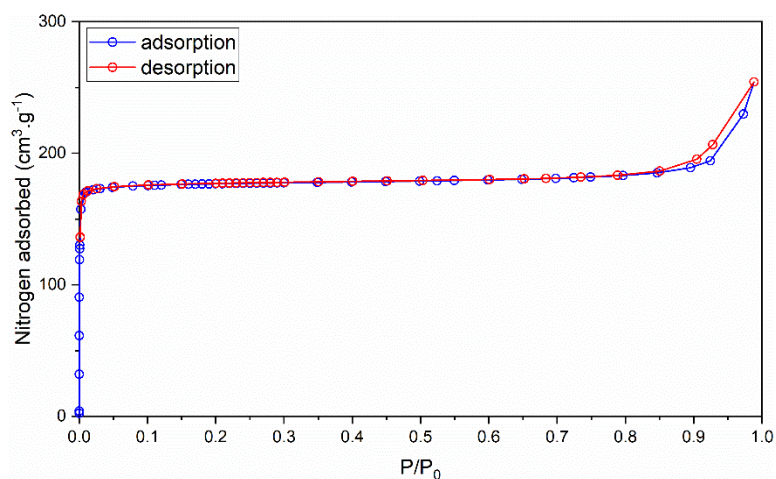
Figure C-19. The N_2 adsorption isotherm of SOD-Zn(**IIm**)$_2$.

C.10 References

(1)   Marrett, J. M.; Mottillo, C.; Girard, S.; Nickels, C. W.; Do, J. L.; Dayaker, G.; Germann, L. S.; Dinnebier, R. E.; Howarth, A. J.; Farha, O. K.; Friščić, T.; Li, C. J. Supercritical Carbon Dioxide Enables Rapid, Clean, and Scalable Conversion of a Metal Oxide into Zeolitic Metal-Organic Frameworks. *Cryst. Growth Des.* **2018**, *18*, 3222–3228.

(2)   Titi, H. M.; Marrett, J. M.; Dayaker, G.; Arhangelskis, M.; Mottillo, C.; Morris, A. J.; Rachiero, G. P.; Friščić, T.; Rogers, R. D. Hypergolic Zeolitic Imidazolate Frameworks (ZIFs) as next-Generation Solid Fuels: Unlocking the Latent Energetic Behavior of ZIFs. *Sci. Adv.* **2019**, *5*, eaav9044.

(3)   Arhangelskis, M.; Katsenis, A. D.; Novendra, N.; Akimbekov, Z.; Gandrath, D.; Marrett, J. M.; Ayoub, G.; Morris, A. J.; Farha, O. K.; Friščić, T.; Navrotsky, A. Theoretical Prediction and Experimental Evaluation of Topological Landscape and Thermodynamic Stability of a Fluorinated Zeolitic Imidazolate Framework. *Chem. Mater.* **2019**, *31*, 3777–3783.

(4)   Akimbekov, Z.; Katsenis, A. D.; Nagabhushana, G. P.; Ayoub, G.; Arhangelskis, M.; Morris, A. J.; Friščić, T.; Navrotsky, A. Experimental and Theoretical Evaluation of the Stability of True MOF Polymorphs Explains Their Mechanochemical Interconversions. *J. Am. Chem. Soc.* **2017**, *139*, 7952–7957.

(5)   Beldon, P. J.; Fábián, L.; Stein, R. S.; Thirumurugan, A.; Cheetham, A. K.; Friščić, T. Rapid Room-Temperature Synthesis of Zeolitic Imidazolate Frameworks by Using Mechanochemistry. *Angew. Chemie., Int. Ed.* **2010**, *49*, 9640–9643.

(6)   Hughes, J. T.; Bennett, T. D.; Cheetham, A. K.; Navrotsky, A. Thermochemistry of Zeolitic Imidazolate Frameworks of Varying Porosity. *J. Am. Chem. Soc.* **2013**, *135*, 598–601.

(7)   Akimbekov, Z.; Katsenis, A. D.; Nagabhushana, G. P.; Ayoub, G.; Arhangelskis, M.; Morris, A. J.; Friščić, T.; Navrotsky, A. Experimental and Theoretical Evaluation of the Stability of True MOF Polymorphs Explains Their Mechanochemical Interconversions. *J. Am. Chem. Soc.* **2017**, *139*, 7952–7957.

(8)   Coelho, A. TOPAS Academic Version 6 Technical Reference. Coelho Software: Brisbane, Australia 2017.

(9)   Pawley, G. S. Unit-Cell Refinement From Powder Diffraction Scans. *J. Appl. Crystallogr.* **1981**, *14*, 357–361.

(10)   Rietveld, H. M. A Profile Refinement Method for Nuclear and Magnetic Structures. *J. Appl. Crystallogr.* **1969**, *2*, 65–71.

(11)   Chaplais, G.; Fraux, G.; Paillaud, J.-L.; Marichal, C.; Nouali, H.; Fuchs, A. H.; Coudert, F.-X.; Patarin, J. Impacts of the Imidazolate Linker Substitution (CH_3, Cl, or Br) on the Structural and Adsorptive Properties of ZIF-8. *J. Phys. Chem. C* **2018**, *122*, 26945–26955.

(12)   Sheldrick, G. M. SHELXT - Integrated Space-Group and Crystal-Structure Determination. *Acta Crystallogr., Sect. A: Found. Adv.* **2015**, *71*, 3–8.

(13)   Sheldrick, G. M. Crystal Structure Refinement with SHELXL. *Acta Crystallogr., Sect. C: Struct. Chem.* **2015**, *71*, 3–8.